

Orbit Design of a Lunar Meteoroid Impact Flashes Observer

Master Thesis

Ana Cipriano

Technische Universiteit Delft



Orbit Design of a Lunar Meteoroid Impact Flashes Observer

Master Thesis

in fulfilment of a Master of Science in Aerospace Engineering
at Delft University of Technology,
to be defended on Friday, November 24th, 2017 at 09:30 A.M.

by

Ana Cipriano

Supervisor:	Dr. F. Topputo	
Thesis committee:	Dr. F. Topputo,	Politecnico di Milano, Delft University of Technology
	Dr. D.M. Stam,	Delft University of Technology
	Dr. A. Cervone,	Delft University of Technology
	Dr. E. Doornbos,	Delft University of Technology



Keywords: Moon, meteoroids, impact flash, orbit design, coverage, CubeSat

Front: Artist's rendering of a meteoroid impact with the lunar surface. (Steve Roy, Marshall Space Flight Center)

An electronic version of this dissertation is available at <http://repository.tudelft.nl/>.

Preface

The present thesis is a product of the work carried out as part of a Master of Science in Aerospace Engineering, at Delft University of Technology, Astrodynamics and Space Missions department. The main goal of this thesis was to determine which orbit a CubeSat, lunar meteoroid impact flashes observer should fly, in order to detect such flashes and in such a way that it contributes to the improvement of current Earth-based observation methods. The work was conducted under the supervision of Dr. Francesco Toppato, from Politecnico di Milano, to whom I thank the availability, guidance and the opportunity to contribute to ESA's Lunar CubeSats for Exploration call, as part of the LUMIO team.

I would also like to thank Gonçalo for his daily support, my family and friends for their advice and all the people from the LUMIO team who provided inputs to this work. A special thanks goes to Detlef Koschny and Chrysa Avdellidou, from the NELIOTA programme, who gave their input into the meteoroid modelling part of this thesis.

*Ana Cipriano
Delft, November 2017*

Contents

List of Figures	ix
List of Tables	xi
Acronyms	xiii
List of Symbols	xvii
Abstract	xxi
1 Introduction	1
1.1 Context	1
1.2 Objective	2
1.3 Structure	2
References	3
2 Lunar Meteoroid Impacts	5
2.1 Scientific Relevance	5
2.1.1 Near-Earth Objects	5
2.1.2 Meteoroids	6
2.2 Sun-Earth-Moon Dynamics	7
2.2.1 Meteoroid Impact Velocity	8
2.2.2 Gravitational Focusing and Acceleration	9
2.2.3 Meteoroid Impact Flux at the Moon	9
2.3 Observation and Detection	11
2.3.1 Seismic Waves	11
2.3.2 Craters	11
2.3.3 Ejecta	11
2.3.4 Radiation	12
2.3.5 Methods Comparison	12
2.4 Meteoroid Impact Flashes	12
2.4.1 The Observation Method	13
2.4.2 Detection Technology	13
2.4.3 Earth-based Monitoring Programs	14
2.4.4 Properties and Detectability of Impactors	14
2.5 Scientific Objectives	16
References	17
3 Mission Definition	21
3.1 Mission Objectives	21
3.2 Requirements and Design Drivers	22

3.3	Subsystem's Design	23
	References	25
4	Methodology	27
4.1	Orbital Design	27
4.2	Evaluation Criteria	29
	References	30
5	Lunar Remote Sensing Orbits	31
5.1	Astrodynamics	31
	5.1.1 Two-Body Problem	31
	5.1.2 Three-Body Problem	32
5.2	Orbital Geometry	34
	5.2.1 Keplerian Orbits	34
	5.2.2 Perturbed Keplerian Orbits	36
	5.2.3 Libration Point Orbits	40
5.3	Preliminary Orbital Trade-Off	46
	References	54
6	Orbit, Payload and Environment	57
6.1	Reference Frames	57
6.2	Orbit Generation	60
	6.2.1 Perturbed Two-Body Problem Orbits	60
	6.2.2 Circular Restricted Three-Body Problem Orbits	68
6.3	Payload Modelling	77
	6.3.1 Optics	77
	6.3.2 Detector	78
6.4	Meteoroid Environment	82
	6.4.1 Kinetic Energy Estimation	82
	6.4.2 Meteoroid Impact Flux Model	91
	6.4.3 Validation and Verification	93
	References	94
7	Coverage Analysis	97
7.1	Methodology	97
	7.1.1 Field-of-View Area	98
	7.1.2 Lunar Nightside Monitoring	102
	7.1.3 Number of Meteoroid Detections	104
7.2	Verification and Validation	104
7.3	Results	110
	7.3.1 Field-of-View 3.5°	110
	7.3.2 Field-of-View 6°	113
7.4	First Orbit Trade-Off	117
	References	120

8 Conclusion	121
8.1 Operative Orbit and Considerations	121
8.2 Conclusion	123
8.3 Recommendations for Future Work	125
References	126
A Constants	127

List of Figures

2.1	Moon phases and main directions of incoming meteoroids in the Earth-Moon System	8
2.2	Lunar apex/antapex asymmetry	10
2.3	Lunar meteoroid impact flashes scientific applications	17
3.1	LUMIO detector’s quantum efficiency	24
3.2	LUMIO’s configuration	24
4.1	Scheme of the experimental set-up	28
5.1	Circular Restricted Three-Body Problem reference frame	32
5.2	Forbidden regions in the Circular Restricted Three-Body Problem	33
5.3	Keplerian orbital elements	35
5.4	Lunar frozen orbits’ averaged orbital elements	38
5.5	Sun-Synchronous orbit	39
5.6	Sun-Synchronous inclination	39
5.7	Circular Restricted Three-Body Problem types of orbits	41
5.8	Northern and Southern Halo Orbits about the Earth–Moon L_2	42
5.9	Earth–Moon L_1 and L_2 Halo families becoming almost rectilinear near the Moon	43
5.10	Earth–Moon L_1 and L_2 Near-Rectilinear Orbits	43
5.11	Stable Distant-Retrograde Orbit resonant states	44
5.12	Distant-Retrograde Orbit with a 1:0:1 resonance	44
5.13	Distant-Retrograde Orbit with a 1:1:2 resonance	45
5.14	Highly eccentric lunar Frozen Orbit	47
5.15	Lunar Keplerian orbits’ lifetime	48
5.16	CRTBP orbits’ stationkeeping costs	49
5.17	Geometry of an inclination change maneuver	49
5.18	Geometry of optimal coplanar transfers	50
6.1	Mean equinox of J2000 reference frame	59
6.2	Mean Earth/Polar Axis Lunar coordinate system	60
6.3	LUMIO’s Spacecraft Bus and LUMIO-Cam reference frame	60
6.4	Spherical harmonics validation with MATLAB’s function	62
6.5	Frozen orbits’ generation software validation with GMAT	64
6.6	Lunar orbit’s osculating eccentricity and inclination maximum amplitude	65
6.7	Frozen orbits’ initial conditions	66
6.8	Frozen orbits’ osculating eccentricity and inclination maximum amplitude	66
6.9	Frozen orbit family	67
6.10	Frozen orbit’s average osculating eccentricity	68
6.11	Targeting of a perpendicular X-axis crossing to generate a planar CRTBP orbit	69

6.12	Generated Low-Prograde Orbit family	74
6.13	Validated Low-Prograde Orbit family	74
6.14	Generated CRTBP orbit families	75
6.15	CRTBP fixed orbit parameters and respective Jacobi constants	76
6.16	CRTBP orbits resonance ratios	76
6.17	CRTBP orbits' period	76
6.18	CRTBP orbits' stability index	76
6.19	CRTBP orbits' maximum and minimum distance to the Moon	77
6.20	CRTBP orbits' maximum and minimum velocity in the CRTBP reference frame	77
6.21	Geometry of an array sensor and Field-of-View projection onto the spacecraft's sky	77
6.22	Sensitivity of the Luminous Efficiency method to assumed parameters	83
6.23	Sensitivity of the Blackbody method to assumed parameters	86
6.24	Variation of the detectable kinetic energy with altitude, for low and high altitudes	87
6.25	Geometry of an off-nadir impact	88
6.26	Variation of the detectable number of impacts with altitude , for low altitudes	89
6.27	Variation of the number of impacts detectable with altitude , for high altitudes	90
6.28	Sensitivity of meteoroid mass and number of detections to assumed velocity	92
6.29	Comparison between meteoroid flux models at the Moon	93
7.1	Scheme of the coverage analysis experimental set-up	98
7.2	Instantaneous access area and footprint definition	98
7.3	Projection of an array's FOV onto the spacecraft's sky and central body's surface	99
7.4	Footprint parameters definition	99
7.5	FOV-area of a square array sensor for high altitudes	100
7.6	Scheme of the FOV-area illumination for low and high altitudes	103
7.7	Altitude and FOV-area of a Frozen Orbit	105
7.8	Frozen orbit FOV-area 2D representation	105
7.9	Frozen orbit FOV-area 3D representation	105
7.10	Altitude of a Lyapunov orbit	106
7.11	FOV-area of a Lyapunov orbit	106
7.12	Lyapunov orbit FOV-area 3D representation	107
7.13	Effective FOV-area of a Lyapunov orbit	108
7.14	Effective FOV-area of a Frozen Orbit	109
7.15	Detectable kinetic energy range from Frozen Orbits	110
7.16	Total number of meteoroid detections from Frozen Orbits	111
7.17	Detectable Kinetic energy range from CRTBP orbits (FOV = 3.5°)	112
7.18	Total number of meteoroid detections from CRTBP orbits (FOV = 3.5°)	113
7.19	Detectable Kinetic energy range from CRTBP orbits (FOV = 6°)	114
7.20	Total number of meteoroid detections from CRTBP orbits (FOV = 6°)	115
7.21	Total number of meteoroid detections from CRTBP orbits, in the desired kinetic energy range	116
7.22	Kinetic energy range detectable from NROs as function of time	119
7.23	Number of expected meteoroid detections per hour from an NRO	120

List of Tables

2.1	Trade-off between lunar meteoroid impact's observation methods	12
3.1	LUMIO top-level objectives	21
3.2	LUMIO mission objectives	22
3.3	LUMIO science requirements	22
3.4	LUMIO mission requirements	23
3.5	LUMIO-Cam parameters	24
4.1	Orbit design acceptance criteria	29
4.2	Orbit design selection criteria	29
5.1	Keplerian and Perturbed Keplerian lunar remote sensing orbits	40
5.2	CRTBP lunar remote sensing orbits	45
5.3	Trade-off between Keplerian and Perturbed Keplerian orbit types	52
5.4	Trade-off between CRTBP orbit types	53
6.1	Validation of the spherical harmonics function used to compute the Moon's NSG	62
6.2	Validation of the Frozen Orbit generation software	63
6.3	Validation of Lyapunov Orbits	72
6.4	Validation of Halo Orbits	72
6.5	Validation of Near-Rectilinear Orbits	72
6.6	Validation of Vertical Orbits	73
6.7	Validation of Distant-Retrograde Orbits	73
6.8	Validation of Low-Prograde Orbits	73
6.9	Estimated detector's noise budget	82
6.10	Assumptions of the Blackbody method in estimating the observable kinetic energy range	85
6.11	Validation of the meteoroid environment model	94
7.1	Additional LUMIO mission requirement and evaluation criteria	117
7.2	First orbit trade-off, with the Luminous Efficiency method results	117
7.3	First orbit trade-off, with the Blackbody method results	118
8.1	Operative orbit's meteoroid detection characteristics	121
A.1	Constants	127

Acronyms

- A/D** Analogue-to-Digital converter [22](#), [75](#), [76](#)
- AN** Ascending Node [31](#)
- AU** Astronomical Unit [4](#)
- BME** Body-Mean Equator [54](#), [57](#), [63](#)
- BMOP** Body-Mean Orbital Plane [54](#), [67](#)
- CCD** Charged-Coupled Device [xv](#), [12](#), [13](#), [73–75](#), [78](#), [81](#), [119–121](#)
- CK** C-matrix Kernel [98](#)
- CMOS** Complementary Metal-Oxide Semiconductor [13](#)
- CRTBP** Circular Restricted Three-Body Problem [xv](#), [29](#), [30](#), [33](#), [37–43](#), [45](#), [46](#), [48](#), [50](#), [54](#), [64–67](#), [70–73](#), [85](#), [98](#), [104](#), [107–111](#), [114](#), [119](#), [120](#)
- DC** Dark-Current [22](#), [75](#), [76](#)
- DRO** Distant-Retrograde Orbit [xv](#), [38](#), [40–43](#), [45](#), [48](#), [50](#), [65](#), [67](#), [68](#), [70](#), [72](#), [109](#), [113](#), [114](#), [118](#), [120](#), [121](#)
- ELO** Elliptical Lunar Orbit [33](#), [34](#), [44](#), [45](#), [47–49](#)
- ENF** Excess Noise Factor [22](#), [75](#)
- ESA** European Space Agency [i](#), [xv](#), [1](#), [2](#), [13](#), [19](#), [20](#), [90](#), [120](#)
- FK** Frames Kernel [54](#), [56](#)
- FO** Frozen Orbit [34](#), [43](#), [47–49](#), [56](#), [57](#), [59](#), [100](#), [101](#), [105–107](#), [113](#), [114](#)
- FOV** Field-of-View [xv](#), [9](#), [12](#), [21](#), [22](#), [43](#), [53](#), [55](#), [56](#), [73](#), [74](#), [79](#), [81](#), [82](#), [84–87](#), [89](#), [90](#), [93–107](#), [109](#), [110](#), [119](#), [120](#)
- GMAT** General Mission Analysis Tool [59](#), [60](#)
- GSD** Ground Sampling Distance [77](#), [80](#)
- HO** Halo Orbit [38](#), [43](#), [45](#), [50](#), [66](#), [67](#), [70](#), [108](#), [113](#), [114](#)
- IAA** Instantaneous Access Area [87](#), [94](#), [96–98](#), [103](#)
- IFOV** Instantaneous Field-of-View [74](#), [76](#), [77](#)

- IK** Instruments Kernel [74](#), [119](#)
- J2000** January 1st, 2000 at 12:00:00 TDB [55](#), [57](#), [67](#)
- JAXA** Japan Aerospace Exploration Agency [2](#)
- LLO** Low Lunar Orbit [33](#), [34](#), [43–45](#), [47–49](#)
- LO** Lyapunov Orbit [38](#), [43](#), [45](#), [50](#), [65](#), [67](#), [70](#), [102](#), [108](#), [113](#), [114](#), [118](#)
- LoPO** Low-Prograde Orbit [38](#), [42](#), [43](#), [45](#), [48](#), [50](#), [65](#), [68](#), [70](#), [72](#), [108](#), [113](#), [114](#)
- LUCE** Lunar CubeSats for Exploration [xv](#), [2](#)
- LUMIO** Lunar Meteoroid Impacts Observer [i](#), [xv](#), [2](#), [4](#), [19–27](#), [46](#), [48](#), [53](#), [54](#), [56](#), [74](#), [77](#), [78](#), [83](#), [84](#), [88](#), [93](#), [94](#), [98](#), [103](#), [106](#), [107](#), [109](#), [113](#), [114](#), [117–119](#), [121](#)
- ME** Mean-Earth reference frame [55–57](#), [98](#)
- NAIF** Navigation and Ancillary Information Facility [53](#)
- NASA** National Aeronautics and Space Administration [1](#), [4](#), [10](#), [13](#), [20](#), [57](#), [59](#), [118](#)
- NEA** Near-Earth Asteroid [4](#), [15](#)
- NEC** Near-Earth Comet [5](#)
- NEO** Near-Earth Object [4](#), [5](#), [119](#)
- NRO** Near-Rectilinear Orbit [38–40](#), [42](#), [43](#), [50](#), [66](#), [67](#), [70](#), [108](#), [113–117](#)
- NSG** Non-Spherical Gravity [33–36](#), [40](#), [44](#), [45](#), [55](#), [57–60](#), [68](#)
- OAR** Output Amplifier Responsivity [22](#), [76](#)
- OCN** Off-Chip Noise [75](#), [76](#)
- PA** Principal Axis reference frame [55](#), [57](#), [59](#)
- PHA** Potentially Hazardous Asteroid [5](#)
- QN** Quantisation Noise [75](#), [76](#)
- rms** root-mean-square [74](#)
- RON** Read-Out Noise [22](#), [75](#)
- SNR** Signal-to-Noise Ratio [74](#), [75](#), [77](#), [119](#)
- SPK** Spacecraft and Planets Kernel [54](#), [57](#), [67](#)
- SSO** Sun-Synchronous Orbit [34](#), [44](#), [45](#), [47](#), [49](#)
- TB** Third-Body [33–36](#), [40](#), [44](#), [45](#), [56](#), [59](#), [60](#), [68](#)

TBP Two-Body Problem [28](#), [29](#), [31](#), [46](#), [53](#), [54](#), [56](#), [98](#)

TDB Barycentric Dynamical Time [54](#), [60](#), [67](#), [104](#), [105](#)

VO Vertical Orbit [38](#), [40](#), [43](#), [45](#), [50](#), [65](#), [67](#), [70](#), [108](#), [109](#), [113](#), [114](#), [118](#)

List of Symbols

- A_{FOV} Area of an array sensor's field-of-view, projected onto the spacecraft's sky 74
- A_{eff} Effective cross sectional area of the target body 8
- A_{lens} Optics' lens area 75, 78, 84
- A_{phy} Physical cross sectional area of the target body 8
- A_x Amplitude of a CRTBP periodic orbit in the X-direction 38, 39, 67, 68, 70, 102–104
- A_y Amplitude of CRTBP a periodic orbit in the Y-direction 38
- A_z Amplitude of a CRTBP periodic orbit in the Z-direction 39, 66–68, 70
- a Semi-major axis of a Keplerian orbit 31, 32, 36, 57–61, 63, 64, 101, 105, 106
- C Jacobi constant 30, 66–68, 70, 72, 117, 120
- c Speed of light 75, 122
- cap** Detector capacity, maximum number of electrons detectable per pixel 22, 76
- d_{FL} Optics focal length 22, 73, 74
- d_θ Optics aperture 22, 75
- d_{CCD} Size of a square array sensor 73
- d_{pixel} Detector pixel size 22, 74
- d Distance to the impact flash 13, 76, 77, 79, 83–85, 90
- E_T Total (bolometric) luminous energy emitted by an impactor, across the electromagnetic spectrum 14
- E_V Luminous energy emitted by an impactor in the visible spectrum 13, 14
- E_γ Energy of the photon 76
- E Eccentric anomaly of a Keplerian elliptical orbit 32
- \mathcal{E} Specific energy, total energy of a body per unit mass, in the Two-Body Problem 28, 32
- KE** Kinetic energy of a meteoroid impact 14, 106, 113, 114, 117
- e Orbital eccentricity 29, 31, 35–37, 44, 57–60, 63
- e_R Flux of photons received at the CCD, converted to an electron flux (electrons/m²) 75

- FOV_{eff}** Effective (non-illuminated) Field-of-View area 87, 98
- FOV_{area}** Field-of-View area or footprint 96
- f_{dark} Fraction of the FOV-area not illuminated by the Sun 98
- f_{impacts} Flux of meteoroid impacts visible in the satellite's FOV-area 87, 100, 104
- f_{KE} Kinetic energy increase factor, due to gravitational acceleration 8, 85, 107
- f_{area} Effective target area increase factor, due to gravitational focusing 8, 85
- G** Gain of the CCD sensor 22, 75
- G Gravitational constant 28, 75
- H** Angular momentum, per unit mass, in the Two-Body Problem 28, 31, 54
- h_p Planck's constant 75, 122
- h Altitude with respect to the surface of a celestial body 32, 35, 37, 40, 42, 44–46, 48, 60, 77, 78, 83–85, 90, 96–98, 100, 113, 114
- i Inclination of a Keplerian circular or elliptical orbit 31, 35–37, 44, 46, 48, 57–61, 63, 101, 105
- k Boltzmann constant 75, 122
- L_F Footprint length 95
- L Lagrange or Libration point of the CRTBP 30, 37–40, 104
- M Mean anomaly of a Keplerian elliptical orbit 32
- m_V Apparent magnitude of an object in the visible spectrum 12, 76–78, 81
- m Meteoroid mass 88, 117
- N_{SM} Number of discretization points of an orbit per synodic month 100
- N_{bits} Analogue-to-Digital converter number of bits 22, 76
- N_{impacts} Number of meteoroid impacts detectable during mission lifetime 85, 100, 113, 114, 117
- N_{pixels} Detector total number of pixels 22, 76
- N_{rev} Number of discretization points of an orbit per revolution 100
- n_{crater} Ratio between diameter of impact flash and crater size 80
- n Mean angular motion of a Keplerian circular or elliptical orbit 32
- off_n** Off-chip noise of the detector, in volts per \sqrt{Hz} 22, 76
- P_E Sidereal year, orbital period of the Earth about the Sun 6, 36

- P_M Sidereal month, orbital period of the Moon about the Earth 6, 36, 37, 41, 42, 69, 70, 72, 115, 122
- P Orbital period of a Keplerian orbit (in an inertial reference frame) or CRTBP orbit (in the Earth–Moon rotating reference frame) 32, 33, 37, 40–43, 68, 69, 100, 115
- p_R Flux of photons received at the observer (photons/m²) 12, 76
- qe** Quantum efficiency of the CCD sensor 76
- R_E Radius of the Earth 86, 122
- R_M Radius of the Moon 33, 46, 47, 86, 95, 122
- r** Position vector 34
- S_M Synodic month, orbital period of the Moon about the Sun 6, 43, 57, 62, 67, 70, 72, 100, 122
- S Stability index 38–40, 42, 68–70
- s Signal received in the CCD sensor 74, 75, 77, 78
- T Effective blackbody temperature 76
- t_{exp} Exposure time of a sensor 22, 76
- v_{GC} Impactor's velocity relative to the target body, after gravitational correction 8
- v_{esc} Escape velocity at target body 8
- v Impactor's velocity relative to the target body, before gravitational correction 8, 79, 88
- x** State vector 56
- β Sun–Moon–Spacecraft phase angle 98, 99, 104, 106
- γ Photon 76
- ΔV Velocity increment xv, 45, 46, 49, 50, 114, 117–121
- Δt Duration of impact flash 77, 80, 90
- $\Delta\lambda$ Optical sensor's bandwidth 13
- ε Elevation, defined in a topocentric reference frame 95, 97
- η_T Luminous efficiency in the electromagnetic radiation spectrum 14
- η_V Luminous efficiency in the visible spectrum 14, 79
- η Off-Nadir angle, measured at the spacecraft from the subsatellite point to the target 95, 96
- θ_{FOV} Field-of-view of an array sensor projected onto the spacecraft's sky 74, 95, 96, 98, 103, 109–111
- θ_\perp Inner angle of an array sensor's field-of-view, projected onto the spacecraft's sky 74

- θ True anomaly of a Keplerian elliptical orbit 31, 32
- Λ Planetocentric longitude, defined in the Mean Earth/Polar Axis Lunar reference frame 34, 55
- λ Angle of a small circle of the central body, measured at the centre of the body 83–87, 95–98
- μ Gravitational parameter, in the Two-Body Problem, or mass parameter in the Three-Body Problem 28, 29, 34, 67, 69, 122
- ρ Angle of the true horizon's small circle of the central body, measured from the spacecraft 84
- σ Noise received or generated in the CCD sensor 22, 74–78
- τ Lens reduction factor (transmissivity, transparency and light dispersion) 22, 75, 78
- Φ Planetocentric latitude, defined in the Mean Earth/Polar Axis Lunar reference frame 34, 55
- Ω Right ascension of the ascending node of a Keplerian circular or elliptical orbit 31, 36, 57–60
- ω Argument of periapsis of a Keplerian elliptical orbit 31, 34, 35, 37, 57–61, 63, 101, 105–107

Abstract

Fragments of asteroids and comets constantly encounter the Earth and Moon in their orbits, impacting them as meteoroids. Observations of meteor showers on Earth have been studied for at least 50 years, in order to construct accurate Solar System meteoroid models. More recently, Earth-based telescopic observations of the light flashes produced by lunar meteoroid impacts have revealed useful in the validation and improvement of such meteoroid models. However, Earth-based lunar observations are restricted by weather, geometric and illumination conditions. As such, it has been proposed that a lunar orbiter could improve the detection rate of lunar meteoroid impact flashes. Assessing which orbit a spacecraft should fly in order to detect these flashes and improve current Earth-based observation methods is the aim of this thesis. The study is restricted to spacecraft with the CubeSat format and its inherent limitations, since it is also inserted in the context of the feasibility study of [LUMIO](#) and [ESA's LUCE](#) challenge.

A methodology of sequential orbital trade-offs was followed, taking into account acceptance criteria based on the mission requirements and selection criteria based on the research objective. The goal was maximize the number of meteoroid detections, during the mission lifetime, while minimizing the mission ΔV budget. Furthermore, it was required that [LUMIO](#) observed meteoroid impacts with kinetic energies between 10^{-6} and 10^{-1} kton TNT, with a [CCD](#) sensor observing in the visible spectrum. Circular Frozen Orbits, Earth–Moon L_2 Lyapunov, Halo, Near-Rectilinear, Vertical, Distant-Retrograde and Low-Prograde orbits were selected as candidate orbits, based on a preliminary orbital trade-off.

In order to determine the kinetic energy range of impacts detected, two different methods were used: the Luminous Efficiency and the Blackbody method. The methods were found to agree with respect to the minimum kinetic energy detectable and disagree with respect to the maximum kinetic energy, for high altitudes, while, for low altitudes, the contrary was verified. In order to determine the total number of meteoroid detections possible from a certain orbit, the flux was assumed uniform across the Moon surface and a coverage analysis tool was developed to determine the payload [FOV](#)-area in the lunar nightside.

Frozen Orbits were found to not allow the detection of kinetic energies larger than 10^{-6} kton TNT and, so, were eliminated from the orbital design space. On the other hand, [CRTBP](#) orbits met the meteoroid related evaluation criteria. From Lyapunov, Halo, Near-Rectilinear and Vertical Orbits it would be possible to detect between 1000 and 10000 impacts during the mission lifetime, but detections from some [DROs](#) could be one order of magnitude larger. Nonetheless, since transfer costs to [DROs](#) are known to be high, a Near-Rectilinear Orbit, with a minimal ΔV budget, was chosen as the operational orbit.

In one year, it is expected that at least 4000 meteoroid impact flashes could be detected and eventual mission extensions could triple that amount. Furthermore, new impacts in never before observed kinetic energy ranges could be detected. As such, a mission like [LUMIO](#) can not only complement Earth-based observation methods, by observing the lunar farside, but also contribute with significant statistical information to the improvement of current Solar System meteoroid models.

1

Introduction

1.1. Context

The Earth–Moon System is a rich environment for space exploration and its study can help us deepen our understanding of the Solar System. Fragments of asteroids and comets, that date back to planetary formation times, constantly encounter the Earth and Moon in their orbits, and impact them as meteoroids. Observations of meteor showers on Earth have been studied for at least 50 years ([Ceplecha et al., 1998](#)), in order to construct accurate Solar System meteoroid models. These models can be useful in, for example, predicting the small-meteoroid flux that deteriorates space equipment or when the next large meteoroid will impact Earth itself. As meteoroids originate from asteroids and comets, meteoroid models can also be used to understand the spatial distribution of those objects near the Earth–Moon System.

More recently, Earth-based telescopic observations of the light flashes produced by lunar meteoroid impacts have revealed useful in the validation and improvement of such meteoroid models. In addition, they also have many other practical applications, such as in the study of impact mechanics and seismology ([Oberst et al., 2012](#)). Monitoring the Moon for meteoroid impact flashes allows for the observation of larger areas than those covered by traditional surveys of Earth’s upper atmosphere. Thus, theoretically, more meteoroid impacts can be detected in shorter periods of time ([Bellot Rubio et al., 2000](#)). However, Earth-based lunar observations are restricted by weather, geometric and illumination conditions. As such, it has been proposed that a lunar orbiter could improve the detection rate of lunar meteoroid impact flashes, as it would allow for longer monitoring periods. Moreover, by being closer to the Moon’s surface, a lunar orbiter could also allow for the detection of meteoroids smaller than millimetres ([Koschny and McAuliffe, 2009](#)).

Given this scientific opportunity, some lunar orbiter missions for meteoroid impact flashes observation have recently been proposed. In response to [ESA’s](#) call for scientific medium-sized missions, [Wieczorek et al. \(2015\)](#) proposed a 350 kg spacecraft flying in an Earth–Moon L_2 Halo orbit with an impact flash monitoring payload. [Stone et al. \(2015\)](#), in response to [NASA’s](#) Small, Innovative Missions for Planetary Exploration call for CubeSats, proposed two identical 3U CubeSats, flying orbits at 20000 km altitude, with the dual goal of both characterising the lunar surface (dayside observations) and

detecting impact flashes (nightside observations). In response to ESA's Lunar Cubesats for Exploration challenge, [Topputo et al. \(2016\)](#) proposed a 12U CubeSat, dedicated to lunar meteoroid impact flashes observation, also flying in an Earth–Moon L_2 Halo orbit. Finally, a Lunar L_2 orbiter and 6U CubeSat by JAXA has been selected for the Exploration Mission-1 launching in 2018. The Japanese mission's main goal is to demonstrate orbit control for a CubeSat in a Earth–Moon L_2 Halo orbit, as well as detect meteoroid impact flashes on the lunar farside ([Campagnola et al., 2016](#)).

1.2. Objective

Given the recent interest in a lunar orbiter mission for meteoroid impact flashes detection, the need arises for a detailed study on which type of orbit a spacecraft should fly in order to detect these flashes and improving current Earth-based observation methods. Assessing which orbit this should be is the *aim* of this thesis.

Nonetheless, this thesis is also inserted in the context of the feasibility study of the [Lunar Meteoroid Impacts Observer \(LUMIO\)](#). This is the Cubesat proposed by [Topputo et al. \(2016\)](#) in response to the [Lunar CubeSats for Exploration \(LUCE\)](#) challenge. As such, the main *goal* of this thesis is to design the operational orbit of [LUMIO](#), given the [LUCE](#) challenge requirements. The study will thus be restricted to spacecraft with the CubeSat format and its inherent limitations.

The main research question and research objective can then be formulated as follows:

Research Question	Which is the best orbit to detect meteoroid impact flashes on the lunar surface, with a CubeSat?
Research Objective	The research objective is to help improve the detection of lunar meteoroid impact flashes, with a CubeSat. This thesis contributes to the achievement of the research objective <i>by</i> determining which <i>orbit</i> the CubeSat should fly.

1.3. Structure

This thesis is divided into 8 chapters, one of which is the Introduction here presented. The main theoretical background, related to meteoroid impact detections, is presented in Chapter 2. The [LUMIO](#) mission and methodology followed to design its operative orbit are presented in Chapters 3 and 4, respectively. The main orbit types considered in the design process and a preliminary assessment are presented in Chapter 5. Chapter 6 presents how the candidate orbits, [LUMIO](#)'s payload and the meteoroid environment have been modelled, in order to perform a lunar meteoroid detection coverage analysis and a more detailed orbital trade-off, which are, in turn, presented in Chapter 7. Finally, in Chapter 8, the operative orbit chosen, the conclusion of this thesis and recommendations for future work are presented.

References

- Z. Ceplecha, J. Borovička, W. G. Elford, D. O. ReVelle *et al.*, *Meteor Phenomena and Bodies*, *Space Science Review* **84**, 327 (1998).
- J. Oberst, A. Christou, R. M. Suggs, D. Moser *et al.*, *The present-day flux of large meteoroids on the lunar surface - A synthesis of models and observational techniques*, *Planetary and Space Science* **74**, 179 (2012).
- L. R. Bellot Rubio, J. L. Ortiz and P. V. Sada, *Luminous Efficiency in Hypervelocity Impacts from the 1999 Lunar Leonids*, *The Astrophysical Journal* **542**, L65 (2000).
- D. Koschny and J. McAuliffe, *Estimating the number of impact flashes visible on the Moon from an orbiting camera*, *Meteoritics and Planetary Science* **44**, 1871 (2009).
- M. Wieczorek, D. Mimoun, D. Baratoux, J.-L. Josset *et al.*, *A mission to the farside of the Moon*, Tech. Rep. (Institut de Physique du Globe de Paris and Institut Supérieur de l'Aéronautique et de l'Espace, 2015).
- T. Stone, J. Heynssens, P. Flikkema, I. Daubar *et al.*, *Naaki: A Twin Cubesat Mission to the Moon*, in *46th Lunar and Planetary Science Conference* (2015) p. 2875.
- F. Toppoto, J. Biggs, M. Massari, K. Mani *et al.*, *LUMIO: Lunar Meteoroid Impacts Observer*, Tech. Rep. (Politecnico di Milano, Delft University of Technology, École Polytechnique Fédérale de Lausanne, S[&]T Norway, Leonardo-Finmeccanica SpA, and The University of Arizona, 2016).
- S. Campagnola, N. Ozaki, K. Oguri, Q. Verspieren *et al.*, *Mission Analysis for EQUULEUS, JAXA's Earth-Moon Libration Orbit Cubesat*, in *67th International Astronautical Congress* (2016).

2

Lunar Meteoroid Impacts

Given the goal to determine which orbit a CubeSat should fly to detect meteoroid impact flashes, the physical phenomena must first be understood. As such, this chapter is dedicated to presenting the relevance of lunar meteoroid impacts, the required theoretical background and the description of the phenomenon itself.

Section 2.1 is dedicated to the general scientific relevance of studying lunar meteoroid impacts. In Section 2.2, the Sun-Earth-Moon dynamics that constrains the observation of lunar meteoroid impacts is described. In Section 2.3, a summary and trade-off between the main observation and detection methods of lunar meteoroid impacts is presented, while Section 2.4 is exclusively dedicated to the detection method of LUMIO: detection of impact flashes. Finally, in Section 2.5, the detailed scientific objectives of the study of lunar meteoroid impacts is presented.

2.1. Scientific Relevance

The main goal of lunar meteoroid impacts observations is related to the study of the impacting body itself: the meteoroid. However, many other scientific opportunities can arise from such studies. Namely, some related to the meteoroids' parent bodies: asteroids and comets. In the following subsections, the main scientific opportunities related to the study of lunar impacting meteoroids and their parent bodies, *Near-Earth Objects* (NEOs), will be presented.

2.1.1. Near-Earth Objects

Near-Earth Objects are asteroids or comets with a perihelion of less than 1.3 AU, whose orbits encounter the Earth's neighbourhood. As of October 2017, the Minor Planet Centre¹, a worldwide database of asteroids and comets of the Solar System, lists more than 16,500 NEOs discovered. According to NASA's Near-Earth Object Program database², it is estimated that approximately 900 of these are larger than 1 kilometre and 7500 larger than 140 metres.

Near-Earth Asteroids (NEAs) constitute the vast majority of NEOs and it is estimated that 90% of all NEAs larger than 1 kilometre have already been discovered (Mainzer *et al.*, 2011; Harris and D'Abramo,

¹<http://www.minorplanetcenter.net/> [Last accessed on: 13/10/2017]

²<https://cneos.jpl.nasa.gov/> [Last accessed on: 13/10/2017]

2015). On the other hand, *Near-Earth Comets* (NEC) are a small fraction of the NEO population. Nevertheless, both types of minor bodies are remnant debris of the Solar System formation and contain clues that are crucial to understand the composition of planets. Therefore, those asteroids and comets that reach the Earth's vicinity, i.e. NEOs, present a valuable opportunity to understand the Solar System.

Some NEOs also cross the Earth's orbit, which means that there is a probability of them colliding with Earth, with possible catastrophic consequences. Currently, it is estimated that an asteroid of approximately 1 kilometre in diameter, capable of causing a global catastrophe, collides with Earth every 500,000 years (Harris and D'Abramo, 2015) and an asteroid larger than 200 meters, capable of causing a local catastrophe, collides with Earth every 100,000 years (Lissauer and de Pater, 2013). An asteroid that passes close enough to Earth's orbit and is large enough to cause a globally-damaging impact, in the foreseeable future (Marsden, 1997), is known as a *Potentially Hazardous Asteroid* (PHA). Monitoring PHAs to predict their orbits is essential and, in the event that a PHA is discovered to be in an Earth-collision course, knowledge of its size, shape, mass and composition will also become essential to determine the best way to divert its course.

2.1.2. Meteoroids

Meteoroids are small Sun orbiting fragments of asteroids and comets, whose sizes range from micrometres to meters and masses from 10^{-15} to 10^4 kilograms (Ceplecha *et al.*, 1998). Their formation is a consequence of asteroids colliding with each other or with other bodies, comets releasing dust particles when close to the Sun and minor bodies shattering into individual fragments. Therefore, understanding meteoroids and associated phenomena can be valuable for the study of asteroids and comets themselves.

A set of meteoroids that has the same orbital motion and forms a cluster at a given orbital longitude is called a *meteoroid swarm*. However, meteoroids can also travel dispersed along the same orbit, in what is known as a *meteoroid stream*³. Nonetheless, since their orbits take between 10^3 to 10^5 years to randomise, many meteoroids still have orbits similar to their parent asteroid or comet, making it theoretically possible to associate them with the parent body (Oberst *et al.*, 2012).

When colliding with a planet or moon, swarms of meteoroids usually originate *meteoroid showers* while streams are more associated with *sporadic impacts*. It is possible to estimate the likelihood of a detected collision to have been caused by a stream or swarm meteoroid, according to the number of detected meteoroid collisions, in a certain time frame, and the models of already known showers and sporadic sources (Suggs *et al.*, 2014; Madiedo *et al.*, 2015). On the other hand, the number of detected impacts also helps to validate the current meteoroid distribution models. Therefore, studying meteoroid impacts can help deepen the understanding of the spatial distribution of NEOs in the Solar System.

The development of reliable small meteoroid's impact flux models is also critical for the sustainable design of spacecraft and space equipment. On the one hand, the consequences of meteoroid showers can be mitigated by recurring to operational procedures, such as pointing the sensitive equipments away from the main directional source of impactors. On the other hand, over the mission lifetime, the spacecraft is also impacted by the constant flux of sporadic meteoroids, and, as such, it must be shielded accordingly. If the meteoroid models used do not predict correctly the flux of meteoroids that can impact a spacecraft, the result could be either an over-conservative or ineffective shielding, affecting the mass budget and/or mission performance. (McNamara *et al.*, 2005)

³The use of these concepts is not always consistent in literature and a swarm is many times referred to as a stream. Throughout this thesis the nomenclature here defined and presented in Oberst *et al.* (2012) will be used.

The study of a range of meteoroids even smaller, known as *micrometeoroids*, can also be of interest for another reason. These meteoroids measure only between 10 micrometres and 2 millimetres (Rubin and Grossman, 2010) and, together with solar wind, cause a phenomenon known as *space weathering*. This phenomenon is responsible for the change of airless bodies' optical properties, masquerading the true optical properties of the solid body underneath. This complicates the interpretation of spectroscopic observations (Hemingway *et al.*, 2015), which are essential for the determination of the properties of an asteroid. The development of reliable meteoroid models in the micrometeoroid size range can help deepen the understanding of such phenomena and, consequently the understanding of airless bodies throughout the Solar System.

Finally, the impact of large meteoroids with Earth, even though meteoroids are smaller than asteroids or comets, can also cause severe damage. As such, it is also critical to be able to predict these impacts, by relying on accurate meteoroid impact flux models. Furthermore, understanding the dynamics of a meteoroid impact can be equally important, in order to establish impact mitigation and damage control protocols. The largest event recorded in history that is attributed to a meteoroid impact, known as the Tunguska event, occurred in 1908. The meteoroid explosion in Earth's atmosphere is estimated to have released, at least, 10 megatons of TNT (approximately 1000 times more energy than the Hiroshima atomic bomb event). According to Brown *et al.* (2002) an event like this could occur every 1,000 years. The second largest *airburst* event recorded, occurred just in 2013, in the Russian city of Chelyabinsk, causing damages over a 120 km radius and at least 374 injured (Popova *et al.*, 2013). The fragments of the meteoroid recovered, the *meteorites*, amount to 4 to 6 metric tons, which only corresponds to 0.03 to 0.05% of the original meteoroid (Popova *et al.*, 2013).

2.2. Sun-Earth-Moon Dynamics

The Earth completes one orbital revolution about the Sun, with respect to inertial space, every 365.26 days (duration of a *sidereal year*, P_E , Wakker (2015, p.257)), intercepting several meteoroid orbits along the way. When the Earth intercepts a certain meteoroid swarm, meteoroids collide with it and burn in its atmosphere, giving origin to a *meteor* shower. Since the Moon orbits the Earth, completing one revolution every 27.32 days with respect to inertial space (duration of a *sidereal month*, P_M , Wakker (2015, p.257)), it will also intercept the same meteoroid swarms at approximately the same time of the year. However, because the Moon has no significant atmosphere (Stern, 1999), the interception originates a *meteoroid* shower.

Like the Earth, the Moon also rotates about its own axis, but with the same period as it completes one revolution about the Earth, meaning that an observer on Earth always sees the same portion of the Moon (the *lunar nearside*). This characteristic, in addition to the fact that a fixed observer on Earth also moves with respect to the Moon, as the Earth rotates about its own axis, constrain the observation of the Moon from the Earth.

Since the Moon's orbital period relative to the Sun is 29.53 days (duration of a *synodic month*, S_M , Wakker (2015, p.257)), the illumination of the lunar nearside varies, which originates the Moon phases. Because lunar impact flashes can only be observed on the lunar nightside and when the lunar nearside is less than 50% illuminated (see Section 2.4.1), their detection from Earth is constrained by this Sun–Earth–Moon dynamic. It should be noted that an observer of the *lunar farside* would also be constrained by the Sun–Moon dynamic, but would see temporally opposite phases. As such, assuming that the lunar farside would also have to be less than 50% illuminated, the observations would occur during the opposite time of the month. Figure 2.1 depicts this phenomena, as well as the

main directions of incoming meteoroids in the Earth–Moon system, with respect to the Sun.

The same Sun–Earth–Moon dynamic can also indirectly constrain the observation of lunar meteoroid impacts. Firstly, the Sun, Earth and Moon’s gravity fields affect the meteoroids’ impact velocity and constrain the observable range of impact velocities, as will be explained in Subsections 2.2.1 and 2.2.2. Secondly, it is theorised that these dynamics can be the cause of an asymmetric meteoroid impact flux at the Moon, which will be addressed in Subsection 2.2.3.

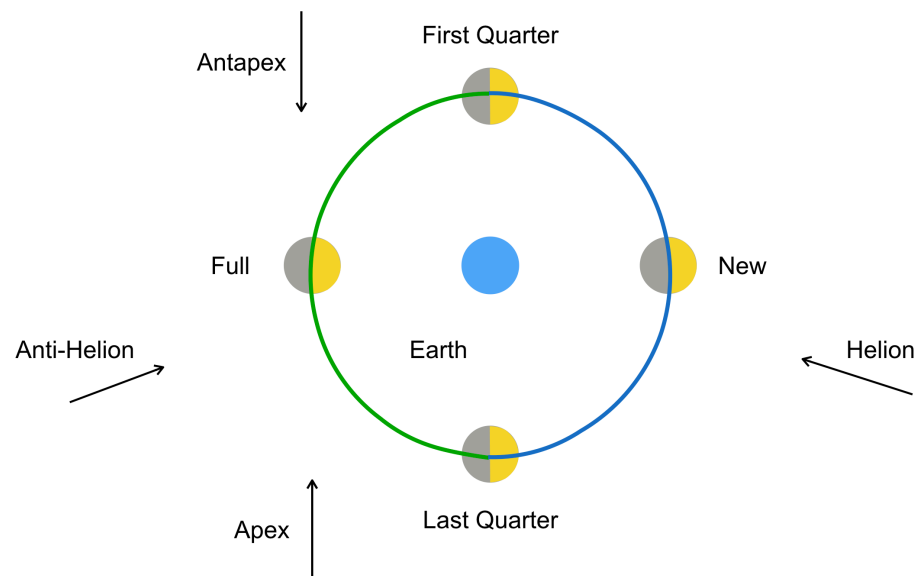


Figure 2.1: Moon phases and main directions of incoming meteoroids in the Earth-Moon System. North and South Toroidal sources are perpendicular to the plane. The blue line represents the portion of the Moon’s orbit where Earth-based impact flashes observations can be made. The green line represents the portion of the Moon’s orbit where potential lunar farside impact flashes observations could be made, assuming a less than 50% farside illumination requirement. Based on [Suggs et al. \(2008\)](#).

2.2.1. Meteoroid Impact Velocity

The meteoroid impact velocity is defined as the relative velocity of the meteoroid with respect to the impacted body. The minimum velocity of a meteoroid impact with Earth, if one neglects the gravitational effect of the Earth and assumes the impact as a pure collision between two bodies, is equal to Earth’s escape velocity: 11.2 km/s. On the other hand, a maximum impact velocity can occur when the meteoroid is in a retrograde, highly eccentric (almost parabolic) orbit about the Sun, with the Earth at its perihelion. The sum of both bodies’ velocities would give an impact velocity of 72.8 km/s ([Ceplecha et al., 1998](#)). Since the Moon has a velocity of approximately 1 km/s with respect to Earth, the lunar meteoroid impacts should be within the theoretical range of 10.2 – 73.8 km/s. The impact velocity of the fastest observed meteoroid shower actually approaches this limit, with an impact velocity of 70.7 km/s at Earth and 69.9 km/s at the Moon ([Suggs et al., 2014](#)).

Contrary to meteoroid showers, the velocity of sporadic impactors is not known and different values are assumed across the literature. [Ortiz et al. \(2006\)](#), [Oberst et al. \(2012\)](#) and [Madiedo et al. \(2015\)](#) use 17 km/s for Moon impacts, while [Suggs et al. \(2014\)](#) uses 24 km/s, which is consistent with [McNamara et al.’s](#) meteoroid engineering model.

2.2.2. Gravitational Focusing and Acceleration

When the Earth-Moon system intercepts a meteoroid swarm or stream, its gravitational force is capable of altering the course of some of those meteoroids. This perturbation leads to one or both of the following consequences: 1) a meteoroid that was not set to collide with the Earth or Moon, now collides with one of the bodies, because it is pulled by their gravitational force; and 2) the velocity of an impacting meteoroid is increased, because the meteoroid is accelerated by the Earth–Moon gravitational force. The first phenomenon described is known as *gravitational focusing* and the second as *gravitational acceleration* of meteoroids.

A consequence of the first phenomenon is that a larger number of meteoroids will impact one of the bodies. As such, when it comes to computing the probability of a meteoroid colliding with the Earth or Moon, this phenomenon is taken into account by artificially increasing the *effective target area* of the body. This is defined as the surface perpendicular to the incoming direction (*radiant*) of a meteoroid shower, representative of the body's effectiveness as an impactor collector. The area increase factor is computed as follows (Suggs *et al.*, 2014):

$$f_{area} = A_{eff}/A_{phy} = 1 + v_{esc}^2/v^2 \quad (2.1)$$

where A_{eff} is the effective cross sectional area of the target body; A_{phy} is the physical cross sectional area of the target body; v_{esc} is the escape velocity at the target body; and v is impactor's velocity, relative to the target body, before gravitational correction.

The impactor's velocity relative to the target body, taking into account the gravitational acceleration, is given by:

$$v_{GC} = \sqrt{v^2 + v_{esc}^2} \quad (2.2)$$

and the kinetic energy increase factor is given by:

$$f_{KE} = v_{GC}^2/v^2 = 1 + v_{esc}^2/v^2 \quad (2.3)$$

Both phenomena become negligible for high values of the incoming impactor's velocity, but the limit at which these phenomena can be neglected also depends on characteristics of the body itself. For example, a sporadic impactor, which is assumed to have a speed of 20 km/s with respect to Earth and 17 km/s with respect to the Moon, is accelerated 3 km/s when approaching the Earth and only 0.15 km/s when approaching the Moon. Furthermore, the radius of the target effective area is increased 14% at the Earth and only 1% at the Moon. As such, gravitational focus and acceleration of sporadic meteoroids can be significant for the Earth and negligible for the Moon. (Oberst *et al.*, 2012)

2.2.3. Meteoroid Impact Flux at the Moon

Since the Earth and Moon are impacted by the same meteoroid streams and swarms, studying the meteoroid flux at the Moon can be useful, not only to understand the meteoroid flux impacting Earth, but also to improve the meteoroid models of the Solar System. Furthermore, understanding the meteoroid flux distribution at the Moon will also be critical for future Moon surface missions, as it could help understand, for example, future lunar living areas (Rembold and Ryan, 2015).

Current estimations of the larger than 1 kilogram meteoroid flux at the Moon varies across the literature. Brown *et al.*'s model estimates 1290 impacts per year, while Ortiz *et al.*'s model estimates approximately 4000 impacts per year (Gudkova *et al.*, 2011). More recent studies, such as Suggs *et al.* (2014), suggest that the meteoroid impact flux at the Moon is approximately 6×10^{-10} per m² per

year, for meteoroids larger than 30 grams. Assuming a lunar collecting area equal to its surface area, $3.8 \times 10^{13} \text{m}^2$, this gives a larger than 30 grams meteoroid flux of approximately 23000 impacts per year.

It is also theorised that the spatial distribution of meteoroid impacts across the lunar surface has asymmetries. As summarised in [Oberst *et al.* \(2012\)](#), it is theorised that the Moon's nearside has approximately 0.1% more impacts than the lunar farside, due to the Earth's gravity field; the equatorial flux is 10% to 20% larger than at polar regions, due to the higher number of large meteoroids in low orbital inclinations; and the lunar leading side (also known as *apex*⁴ or *western hemisphere*) encounters between 37% to 80% more impactors than the lunar trailing side (also known as *antapex*⁴ or *eastern hemisphere*), due the Moon's synchronous rotation.

Figure 2.2 presents the location, on the lunar nearside, of approximately 100 detected meteoroid impact flashes. An apex/antapex asymmetry is clearly visible in these observations, but this observed asymmetry might have been caused by an observational bias. The observations on the western hemisphere were made mostly during the First Quarter Moon phase and the observations on the eastern hemisphere were made mostly during the Last Quarter Moon phase (see Figure 2.1). [Suggs *et al.* \(2014, 2008\)](#) suggests that this observed asymmetry occurs because, when observing during the Last Quarter, it is not possible to detect impactors from apex sources (which approach from the lunar far-side). Furthermore, [Oberst *et al.* \(2012\)](#) suggests that, since apex sources are easier to detect due to their large velocities, it is natural that more impacts are detected during the First Quarter. As such, observations of the lunar farside would be necessary to fully understand the lunar apex/antapex asymmetry.

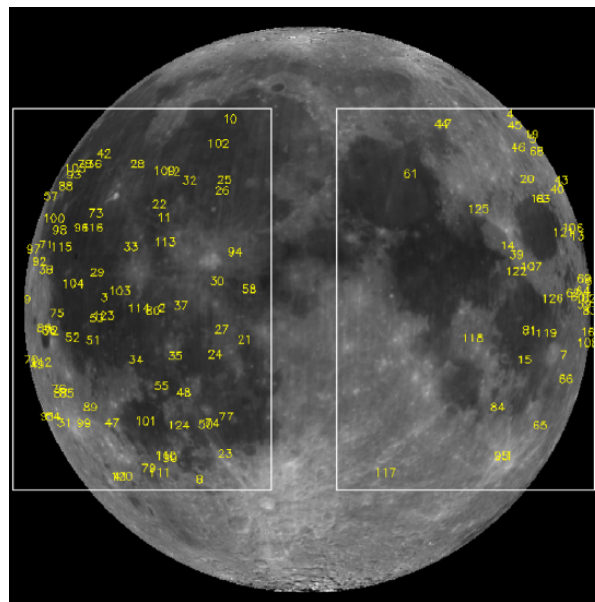


Figure 2.2: Distribution of 108 impacts observed on the lunar nearside representative of the lunar apex/antapex asymmetry. The white rectangles represent the FOV of the telescope. From [Suggs *et al.* \(2014\)](#).

⁴Note that the incoming meteoroids' apex direction depicted in Figure 2.1 is not the same as the apex direction of the Moon. The Moon's western hemisphere is known as the apex of the Moon, because it is the leading side of its motion with respect to Earth, while the apex direction of incoming meteoroids is the same as the leading direction of the Earth-Moon system in its motion about the Sun. The same can be said about the antapex direction.

2.3. Observation and Detection

The systematic detection of meteoroid impacts with the Earth has been done, at least, since 1904, twenty years after the first known photograph of a meteor was taken (Cepilecha *et al.*, 1998). Since then, numerous observations have been made, using different observation methods, such as photographic, visual, radar, infrared and infrasonic. However, these observations are acquired by monitoring portions of the Earth's atmosphere, while monitoring the Moon's surface for meteoroid impacts allows for a much larger area to be covered than these traditional methods (Ortiz *et al.*, 2006).

When a meteoroid impacts the Moon, its elevated kinetic energy originates a seismic wave, excavates a crater, accelerates ejecta particles and releases radiation. As such, any of these four phenomena can be observed in order to detect a meteoroid impact.

2.3.1. Seismic Waves

Detecting seismic waves on the lunar surface implies placing *in-situ* seismic stations on the Moon's surface, so, at the very least, it implies being close enough to the Moon's surface to deploy those instruments. This was done by four of the Apollo missions, which built a network of four seismic detectors on the Moon's nearside, covering an area approximately equivalent to that of a triangle of 1000 km side (Oberst *et al.*, 2012). The programme was operated from 1969 to 1977 and detected more than 12,000 seismic events, but these observations also included quakes and non-meteoroid impacts. In order to identify those that correspond to meteoroid impacts, it is necessary to resort to other methods capable of providing both the time and location of the impact (Gudkova *et al.*, 2011).

2.3.2. Craters

Craters on the Moon are usually observed using telescopes. By dating observed craters and studying their accumulation over time, it is possible to derive the meteoroid impact flux with the Moon, dating back to the formation of the Solar System itself. However, estimation of the current meteoroid impact flux, using crater observations, can only be done by detecting the formation of new craters. This can also be done using a telescope, but a recent lunar orbiter mission, the Lunar Reconnaissance Orbiter, used time pairs of the lunar surface (i.e. before and after pictures). The downside of this detection method is that it is time-consuming, due to the large data processing necessary (Oberst *et al.*, 2012). It is also not possible to associate an exact time-stamp to the meteoroid impact. Furthermore, regardless of the detection method, observing crater formation is always done after the impact has occurred and the final crater formed is not appropriate to directly determine certain characteristics of the meteoroid, such as kinetic energy (Holsapple, 1993). This is because the final crater can, for example, have resulted from the collapse of the crater formed immediately after the impact or have been modified by the constant flux of micrometeoroid impacts (Cudnik, 2009).

2.3.3. Ejecta

The excavation of a crater also causes a burst of particles rising above the Moon's surface. A payload recently on-board a NASA lunar orbiting mission, the Lunar Atmosphere and Dust Environment Explorer, was capable of detecting bursts of particles, generated by impacts of micrometeoroids. Szalay and Horányi (2016) proved that, from the detection of these bursts of particles, it is possible to independently determine the radiant of meteoroid showers. As such, this *in-situ* dust detector could be placed above any airless body in the Solar System to characterise the orbit of meteoroids bombarding such bodies.

2.3.4. Radiation

The release of radiation due to a meteoroid impact can be detected through observations in the visible (400–700 nm) or infrared domain (700 nm–1 mm). According to laboratory *hyper-velocity impacts* between 2 and 65 km/s, conducted by [Burchell et al. \(1996\)](#), the *effective temperature* of a *light flash* produced by an impact lies between 2000 and 6000 K ([Oberst et al., 2012](#)). As such, light flashes with lower effective temperatures (≤ 3000 K) and velocities can be better detected using infrared cameras and light flashes with higher effective temperatures (≥ 4000 K) and velocities can be better detected using visible cameras.

2.3.5. Methods Comparison

The main characteristics of each observation method presented in the previous subsections are summarised in the graphical trade-off of Table 2.1. From this trade-off it is clear that the detection of lunar impact flashes is the most advantageous method: it allows for an independent detection of meteoroid impacts, provides the most information about the impactor and allows for the monitoring of a large Moon surface area.

Table 2.1: Trade-off between lunar meteoroid impact's observation methods.

Observation	Type of method	Moon surface covered (%)	Meteoroid impacts detection	Meteoroid information obtained
Seismic waves	In-situ	red ~1.3%	red Not possible independently	red None independently
Craters	Remote sensing	green ~100%	yellow Formation of new craters; if independently, with time-consuming data processing	yellow Position of impact and crater size
Ejecta	In-situ	red ~0%	green Burst of particles; independent detection	yellow Position and time of impact
Radiation	Remote sensing	yellow up to 50%	green Observation of light flashes; independent detection	green Position and time of impact; kinetic energy (mass and/or velocity)

Legend: green Good performance yellow Acceptable performance red Unacceptable performance

2.4. Meteoroid Impact Flashes

The following section is dedicated to the phenomenon of lunar meteoroid impact flashes. The observation method and detection technology will be described in Subsections 2.4.1 and 2.4.2, respectively. Subsection 2.4.3 is dedicated to the description of the main past and present Earth-based lunar impact flashes monitoring programs. Finally, in Subsection 2.4.4 it is explained how Earth-based observations

of impact flashes' apparent magnitude are related to the impactor's kinetic energy and what the main parameters that determine the detectability of an impactor's light flash are.

2.4.1. The Observation Method

Light flashes at the Moon are typically observed by pointing a telescope at the nightside of the Moon and detecting a local spike of the *luminous energy* observed (in the visible spectrum), which is clearly above the background noise. The background noise is mainly composed, in the visible spectrum, by the *Earthshine*, which is Earth's reflected light on the Moon's surface, and, in the infrared spectrum, by thermal emissions of the Moon's surface (Bouley *et al.*, 2012). The observations need to take place in the nightside of the Moon, as opposed to the dayside, because it is where high signal-to-noise ratios can be obtained (Bellot Rubio *et al.*, 2000).

The luminous energy spike detected is quantified recurring to the concept of *apparent magnitude*. The apparent magnitude of an object quantifies the brightness of an object as seen by an observer on Earth, with respect to the brightness of a known object. In the visible range, 4×10^{10} photons per second per square meter reach Earth, from a star with 0 magnitude (Raab, 2002). By definition, a difference of +1 magnitude corresponds to a reduction of brightness by a factor of 2.5. As such, the apparent magnitude on an object in the visible spectrum can be defined as follows (Wertz, 2009, p.578):

$$m_V = 2.5 \log_{10} \left(\frac{4 \times 10^{10}}{p_R / \Delta t} \right) \quad (2.4)$$

where p_R is the flux of photons received at the observer (photons/m²) and Δt is observation time in seconds. Given this definition, a larger apparent magnitude is associated with lower brightness and, consequently, lower luminous energy. The lunar impact flashes detected from Earth-based observations have between +5 and +10.5 apparent magnitude (Oberst *et al.*, 2012), which correspond to very faint signals.

Earth-based observations of lunar impact flashes are restricted to periods when the lunar nearside is illuminated between 10%–40% or 10%–50%, according to Ortiz *et al.* (2006) or Suggs *et al.* (2008), respectively. The upper limit restriction is due to the dayside of the Moon glaring the *Field-of-View (FOV)* of the telescope. The lower limit restriction of 10% corresponds to the New Moon phase. During this phase, the observations should be made when the Moon presents itself at low elevations in the sky (morning or evening), but the observation periods turn out to be too short to be useful (Oberst *et al.*, 2012; Suggs *et al.*, 2008). On the other hand, for a lunar orbiter, the New Moon phase should be ideal for the observation of impact flashes, as there is no glare from sunlight in the *FOV*. Furthermore, when observing from the Earth, the observations are also restricted by weather conditions at the observation site.

2.4.2. Detection Technology

Coupled with a telescope, lunar impact flashes are typically recorded with a camera that contains a sensor to accurately capture the luminosity of the Moon's surface. The images recorded are then analysed by a computer program, and those containing a light flash are selected for *photometric analysis*, i.e. the determination of the apparent stellar magnitude of the flash (Suggs *et al.*, 2014). The limiting apparent stellar magnitude detectable is determined by the combination of the telescope and camera chosen (Suggs *et al.*, 2014).

Most observation programmes perform observations in the visible spectrum and use either a *Charged-*

Coupled Device (CCD) or Complementary Metal-Oxide Semiconductor (CMOS) as sensor. Both sensors are formed by an array of photo-detectors (set of capacitors) and have similar working principles: incoming photons partially discharge the capacitors and, at the end of the *exposure time*, the remaining electrons are counted and digitized. The main difference is that the photo-detectors in a CMOS can be individual read, while in a CCD the whole image must be read. (Berry and Burnell, 2000)

2.4.3. Earth-based Monitoring Programs

The first unambiguous lunar meteoroid impact flashes were detected during 1999's Leonid meteoroid showers, in the United States, and were reported by Bellot Rubio *et al.* (2000). The first redundant detection of sporadic impacts was only reported six years later by Ortiz *et al.* (2006), in Spain. These events gave origin to several monitoring programs across the globe, some of which will be briefly described in this section.

One of the first lunar impact flash surveys was conducted in two observatories in Spain, between 2001 and 2004. It covered $5.8 \times 10^6 \text{ km}^2 \pm 10\%$ of the lunar surface, and during 34 nights of observation, Ortiz *et al.* (2006) reported the detection of 3 sporadic meteoroid impact flashes.

In 2006, a lunar meteoroid impact flashes observation programme conducted by NASA's Marshall Space Flight Center was initiated. Suggs *et al.* (2008) reported the ability to monitor $4.5 \times 10^6 \text{ km}^2$ of the lunar surface, approximately 10 nights per month, but subject to weather conditions. Approximately half of the impact flashes observations occur between the Last Quarter and New Moon (0.5 to 0.1 illumination) and the other half between New Moon and First Quarter (0.1 to 0.5 illumination). The former monitoring period occurs in the morning (*waning phase*) and the latter occurs in the evening (*waxing phase*), covering the nearside part of the eastern and western hemisphere of Moon, respectively. These periods result from the illumination conditions required by the observation method (see Subsection 2.4.1) and the dynamics of the Earth–Moon motion with respect to the Sun (see Section 2.2). Suggs *et al.* (2014) reports the detection of 126 high-quality flashes (out of 240 observations, Oberst *et al.* (2012)), for 266.88 hours of monitoring, over a 5 years period. The magnitude range detected is between +10.42 and +5.07, which is estimated to correspond to an impactor's kinetic energy range between 1.67×10^{-7} and 2.31×10^{-4} kton TNT.

The most recent monitoring program, ESA's NELIOTA⁵, was initiated on February 2017 in Greece. As of October 2017, 16 validated impacts have been detected over 35 hours of observations. The programme aims to detect flashes as faint as +12 apparent visual magnitude (Bonanos *et al.*, 2015) and should be the first allowing the determination of the impact flash blackbody temperature, by observing both in the visible and infrared spectrum.

2.4.4. Properties and Detectability of Impactors

For Earth-based methods, it is possible to relate the measured impact flash's apparent stellar magnitude with the luminous energy emitted by the impactor in the visible spectrum, E_V , as follows (Suggs *et al.*, 2014):

$$\frac{E_V}{f\pi d^2} = f_V \Delta\lambda \Delta t \quad (2.5)$$

where:

- d is the distance between the lunar surface and the observer;
- $\Delta\lambda$ is the bandwidth used to perform the observations;

⁵<https://neliota.astro.noa.gr> [Last accessed on: 13/08/2017]

- f_V is the energy flux received in that bandwidth, which is a function of the measured magnitude and atmospheric properties;
- Δt is the period over which the magnitude of the impact was measured, i.e. one or more exposure times (Rembold and Ryan, 2015);
- and f is 2 or 4 if the magnitude is measured when the light flash is still close to the lunar surface (first frames) or in free space, respectively⁶

For the best kinetic energy estimation, Suggs *et al.* (2014) suggests that the shortest exposure time possible should be used and, so, the magnitude should be measured using only one frame. Furthermore, preferably, one of the first frames should be used. This is because the radiation emitted by the light flash during the first instances of the meteoroid impact is mainly due to the thermal emission of the vaporised lunar soil and could be better used to determine the rate of cooling of ejecta material (Bouley *et al.*, 2012).

The emitted luminous energy can then be related to the kinetic energy of the meteoroid, KE , using the luminous efficiency concept, η_V or η_T , as follows:

$$KE = \frac{E_V}{\eta_V} = \frac{E_T}{\eta_T} \quad (2.6)$$

where E_T represents the luminous energy emitted by the impactor across the radiation spectrum. The luminous efficiency is representative of how well an impactor converts its kinetic energy into the emission of radiation in the visible spectrum (η_V) or across the radiation spectrum (η_T). Its understanding is a key goal of impact mechanics studies.

One of the most recent studies suggests that such a parameter is independent of the impactor's mass, m , and dependent on its velocity, v , according to the following relation (Swift *et al.*, 2011):

$$\eta_V = 1.5 \cdot 10^{-3} \exp\left(\frac{9.3^2}{v}\right) \quad (2.7)$$

where v is in km/s. Nonetheless, due to the uncertainty of this parameter, Bouley *et al.* (2012) suggests that one should consider $\eta_V \in [5 \cdot 10^{-4}, 5 \cdot 10^{-3}]$.

The kinetic energy of a meteoroid can then be related to its mass and velocity as follows:

$$KE = \frac{1}{2}mv^2 \quad (2.8)$$

From Equations 2.5–2.8, and assuming a certain velocity v (see Section 2.2.1), the mass of the meteoroid can be estimated. From these equations it is also possible to conclude that:

- For a given sensor (i.e. fixed $\Delta\lambda$, Δt and minimum f_λ detectable), if the observer is closer to the lunar surface, E_V can be lower. As such, for the same impactor's velocity, smaller meteoroid masses can be detected. Furthermore, the relation between E_V and d is quadratic (e.g. if d is reduced by a factor of 2, E_V can be 4 times lower);
- A meteoroid with high velocity, even if it has a small mass, can be better detected than a massive slower meteoroid, as $KE \propto mv^2 \Rightarrow E_V \propto mv^2$ and, so, higher velocity impacts originate brighter flashes (Bouley *et al.*, 2012).

⁶This corresponds to a propagation of the emitted luminous energy over 2π steradians or 4π steradians, respectively

However, Bouley *et al.* (2012) showed that smaller impactors, even if very fast and bright, such as the Leonids, have short light flash durations. If the exposure time is not short enough, the background noise can outshine these bright impact flashes, hindering their detection. Nonetheless, these types of impacts are exceptions to the rule. In general, bright flashes are usually associated with longer light flashes and, so, can easily be detected.

2.5. Scientific Objectives

Studying lunar meteoroid impact flashes can have several scientific applications, some of which will be briefly described.

Impact mechanics The characterisation of the partition of energy during an impact is the main goal of the study of impact mechanics. The understanding of the light emission process and estimation of the luminous efficiency plays an important role in this study. This estimation is mainly done from laboratory hyper-velocity experiments, but studying lunar impact flashes of meteoroid showers, whose velocities are well known, can help validate the estimations made (Suggs *et al.*, 2008). The detection and localisation of meteoroid impacts on the lunar surface can provide essential data to seismology studies, as it can help identify those seismic waves caused by meteoroid impacts (Oberst *et al.*, 2012). Furthermore, the mass estimations that result from lunar impact flashes observations can be used to predict a crater size (Bellot Rubio *et al.*, 2000). If these observations are combined with crater detection techniques, those models can also be validated. Nonetheless, it is the combination of the three types of observations - seismic waves, crater formation and impact flashes - that will lead to the complete understanding of impact mechanics (Oberst *et al.*, 2012).

Present-day meteoroid impact flux The detection of meteoroid impact flashes on the Moon allows for the estimation of the lunar meteoroid impact flux. This flux can then be scaled to estimate the meteoroid flux on Earth, taking into account gravitational focusing and acceleration of meteoroids (Section 2.2.2). Figure 2.3a shows the estimated meteoroid flux on Earth, from different types of observations.

In this figure, the different size ranges detected by each type of observation method can be seen. Deep space telescopes monitoring of NEA's, such as LINEAR and Spacewatch, can observe meteoroids from tens of meters to kilometres (Koschny and McAuliffe, 2009); monitoring of meteor's fireballs on Earth's atmosphere, with infrared cameras, satellites or photographic observations can detect meteoroids from millimetres to tens of meters and as small as some grams (Koschny and McAuliffe, 2009; Halliday *et al.*, 1996); telescopic Earth-based observations of lunar impact flashes can detect meteoroids from tens of grams to a few kilogrammes and as small as centimetres (Suggs *et al.*, 2014). Koschny and McAuliffe (2009) estimated that a lunar orbiter at 100 km altitude could detect impact flashes of meteoroids smaller than centimetres and as small as 10^{-4} kg, which would help extend the mass/size range coverage of this method and, consequently, would increase its contribution to the validation of meteoroid models.

The current Earth-based impact flashes observations suggest that the meteoroid flux in these smaller ranges can be larger than the model predictions. However, as can also be seen in Figure 2.3a, especially in the Ortiz *et al.* (2006) observations, this estimation is highly dependent on the value of the luminous efficiency.

Temporal and spatial distribution of lunar impacts The build up of statistical observations of lunar impact flashes can also help understand the temporal and spatial asymmetries of meteoroid impacts across the Moon's surface (Section 2.2.3). Furthermore, it is possible to correlate the lunar temporal/spatial distribution of meteoroid impacts with the distribution of meteoroids in the Solar System. Suggs *et al.* (2014), for example, independently identifies meteoroid showers by studying the cumulative rate of meteoroids at each longitude of the Earth–Moon system with respect to the Sun, as seen in Figure 2.3b.

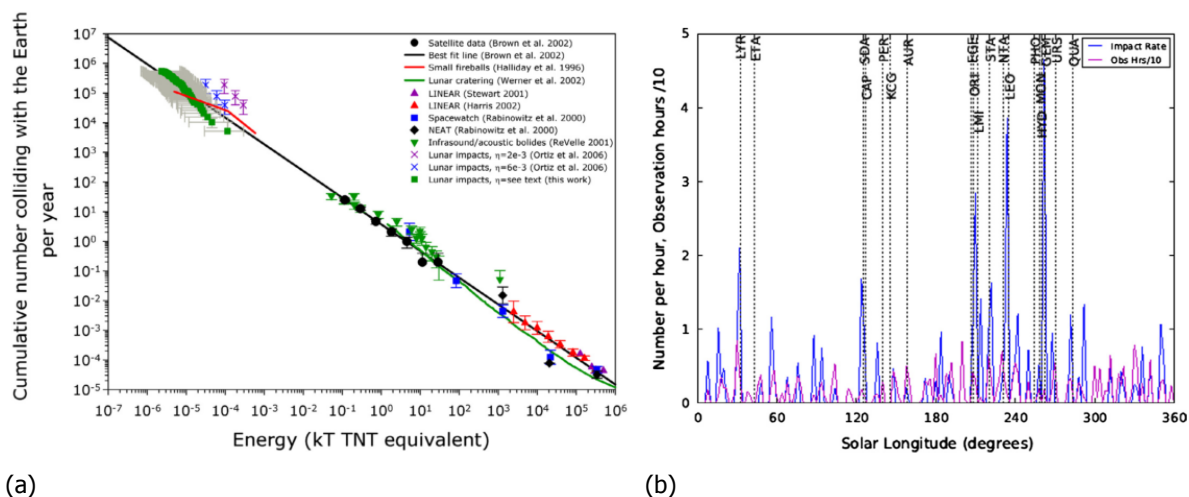


Figure 2.3: Lunar meteoroid impact flashes scientific applications: (a) Estimated meteoroid impact rate at Earth versus impactor's kinetic energy; (b) Impact flash rate in 2-degree bins of solar longitude (blue curve), with shower peak times indicated by dashed vertical lines. From Suggs *et al.* (2014).

References

- A. Mainzer, T. Grav, J. Bauer, J. Masiero *et al.*, *NEOWISE Observations of Near-Earth Objects: Preliminary Results*, *The Astrophysical Journal* **743** (2011), 10.1088/0004-637X/743/2/156.
- A. W. Harris and G. D'Abromo, *The population of near-Earth asteroids*, *Icarus* **257**, 302 (2015).
- J. J. Lissauer and I. de Pater, *Fundamental Planetary Science* (Cambridge University Press, New York, 2013).
- B. G. Marsden, *Overview of orbits*, in *Annals of the New York Academy of Sciences*, Vol. 822 (1997) pp. 52–66.
- Z. Ceplecha, J. Borovička, W. G. Elford, D. O. ReVelle *et al.*, *Meteor Phenomena and Bodies*, *Space Science Review* **84**, 327 (1998).
- J. Oberst, A. Christou, R. M. Suggs, D. Moser *et al.*, *The present-day flux of large meteoroids on the lunar surface - A synthesis of models and observational techniques*, *Planetary and Space Science* **74**, 179 (2012).
- R. M. Suggs, D. E. Moser, W. J. Cooke and R. J. Suggs, *The flux of kilogram-sized meteoroids from lunar impact monitoring*, *Icarus* **238**, 23 (2014), arXiv:1404.6458 .

- J. M. Madiedo, J. L. Ortiz, F. Organero, L. Ana-Hernández *et al.*, *Analysis of Moon impact flashes detected during the 2012 and 2013 Perseids*, *Astronomy & Astrophysics* **577**, A118 (2015), [arXiv:arXiv:1503.05227v1](https://arxiv.org/abs/1503.05227v1) .
- H. McNamara, J. Jones, B. Kauffman, R. Suggs *et al.*, *Meteoroid engineering model (MEM): A meteoroid model for the inner solar system*, *Earth, Moon and Planets* **95**, 123 (2005).
- A. E. Rubin and J. N. Grossman, *Meteorite and meteoroid: New comprehensive definitions*, *Meteoritics and Planetary Science* **45**, 114 (2010).
- D. J. Hemingway, I. Garrick-Bethell and M. A. Kreslavsky, *Latitudinal variation in spectral properties of the lunar maria and implications for space weathering*, *Icarus* **261**, 66 (2015).
- P. Brown, R. E. Spalding, D. O. ReVelle, E. Tagliaferri *et al.*, *The flux of small near-Earth objects colliding with the Earth*. *Nature* **420**, 294 (2002).
- O. P. Popova, P. Jenniskens, V. Emel'yanenko, A. Kartashova *et al.*, *Chelyabinsk Airburst, Damage Assessment, Meteorite Recovery, and Characterization*, *Science* **342**, 1069 (2013).
- K. F. Wakker, *Fundamentals of Astrodynamics* (Delft University of Technology, Institutional Repository Library, Delft, 2015).
- S. Stern, *The Lunar Atmosphere: History, Status, Current Problems, and Context*, *Reviews of Geophysics* **37**, 453 (1999).
- R. M. Suggs, W. J. Cooke, R. J. Suggs, W. R. Swift *et al.*, *The NASA lunar impact monitoring program*, in *Advances in Meteoroid and Meteor Science* (2008) pp. 293–298.
- J. L. Ortiz, F. J. Aceituno, J. A. Quesada, J. Aceituno *et al.*, *Detection of sporadic impact flashes on the Moon: Implications for the luminous efficiency of hypervelocity impacts and derived terrestrial impact rates*, *Icarus* **184**, 319 (2006).
- J. J. Rembold and E. V. Ryan, *Characterization and Analysis of Near-Earth Objects via Lunar Impact Observations*, *Planetary and Space Science* **117**, 119 (2015).
- T. V. Gudkova, P. H. Lognonné and J. Gagnepain-Beyneix, *Large impacts detected by the Apollo seismometers: Impactor mass and source cutoff frequency estimations*, *Icarus* **211**, 1049 (2011).
- K. A. Holsapple, *The scaling of impact processes in planetary sciences*, *Annual Review of Earth and Planetary Sciences* **21**, 333 (1993).
- B. Cudnik, *Lunar Meteoroid Impacts and How to Observe Them* (Springer, New York, 2009).
- J. R. Szalay and M. Horányi, *Detecting meteoroid streams with an in-situ dust detector above an airless body*, *Icarus* **275**, 221 (2016).
- M. Burchell, M. J. Cole and P. R. Ratcliff, *Light Flash and Ionization from Hypervelocity Impacts on Ice*, *Icarus* **122**, 359 (1996).
- S. Bouley, D. Baratoux, J. Vaubaillon, A. Mocquet *et al.*, *Power and duration of impact flashes on the Moon: Implication for the cause of radiation*, *Icarus* **218**, 115 (2012).
- L. R. Bellot Rubio, J. L. Ortiz and P. V. Sada, *Observation and Interpretation of Meteoroid Impact Flashes on the Moon*, *Earth* **82**, 575 (2000).

- H. Raab, *Detecting and measuring faint point sources with a CCD*, in *Proceedings of Meeting on Asteroids and Comets in Europe (MACE)* (2002).
- J. R. Wertz, *Orbit & Constellation Design & Management* (Microcosm Press; Springer, 2009).
- R. Berry and J. Burnell, *The Handbook of Astronomical Image Processing* (Willmann-Bell, Inc., 2000).
- A. Bonanos, M. Xilouris, P. Boumis, I. Bellas-Velidis *et al.*, *NELIOTA: ESA's new NEO lunar impact monitoring project with the 1.2m telescope at the National Observatory of Athens*, in *Proceedings of the International Astronomical Union*, Vol. 10 (2015) pp. 327–329.
- W. R. Swift, D. E. Moser, R. M. Suggs and W. J. Cooke, *An Exponential Luminous Efficiency Model for Hypervelocity Impact into Regolith*, in *Proceedings of the Meteoroids 2010 Conference* (2011) pp. 125–141.
- D. Koschny and J. McAuliffe, *Estimating the number of impact flashes visible on the Moon from an orbiting camera*, *Meteoritics and Planetary Science* **44**, 1871 (2009).
- I. Halliday, A. A. Griffin and A. T. Blackwell, *Detailed data for 259 fireballs from the Canadian camera network and inferences concerning the influx of large meteoroids*, *Meteoritics & Planetary Science* **31**, 185 (1996).

3

Mission Definition

Given that this thesis is inserted in the context of the [Lunar Meteoroid Impacts Observer](#) feasibility study, the following chapter is dedicated to presenting the relevant aspects of this mission to orbital design. The mission objectives and requirements are presented in Sections 3.1 and 3.2, respectively. In the latter section, a preliminary assessment of the main orbital design drivers is also presented. Section 3.3 is dedicated to the description of those [LUMIO](#) subsystems most important to orbital design, namely the payload.

3.1. Mission Objectives

The [Lunar Meteoroid Impacts Observer](#) ([LUMIO](#)) is a CubeSat mission to observe, quantify, and characterize lunar meteoroid impacts, by detecting their impact flashes with the lunar surface. [LUMIO](#)'s top-level mission objectives, which are defined by [ESA's SYSNova: R&D Studies Competition for Innovation - No.4 \(2016\)](#), are presented in Table 3.1. The specific mission objectives defined by [LUMIO](#)'s team are presented in Table 3.2.

Table 3.1: [LUMIO](#) top-level objectives.

ID	Objective
TLO.01	To perform remote sensing of the lunar surface and measurement of astronomical observations not achievable by past, current, or planned lunar missions.
TLO.02	To demonstrate deployment and autonomous operation of CubeSats in lunar environment, including localization and navigation aspects.
TLO.03	To demonstrate miniaturization of optical instrumentation and associate technology in lunar environment.
TLO.04	To perform inter-satellite link to a larger Lunar Communications Orbiter for relay of data and for telemetry, tracking, and command.
TLO.05	To demonstrate CubeSat trajectory control capabilities in lunar environment.

Table 3.2: LUMIO mission objectives.

ID	Objective
MO.01	To conduct observations of the lunar surface in order to detect meteoroid impacts and characterise their flux, flash magnitudes, luminous energies, and sizes.
MO.02	To complement observations achievable via ground-based assets in terms of space, time and quality, in order to provide a better understanding of the meteoroid environment.

3.2. Requirements and Design Drivers

In this section, the LUMIO requirements relevant for its orbit design will be presented. The scientific requirements are cited in Table 3.3 and the mission requirements are cited in Table 3.4 (Topputo *et al.*, 2017).

The first two science requirements are deduced from the data presented in Figure 2.3a. As one can conclude from this plot, Earth's meteoroid flux in the kinetic energy range of 10^{-4} to 10^{-1} kton TNT is not yet characterised with observational data. Furthermore, the characterisation of the flux in kinetic energy range of 10^{-6} to 10^{-4} kton TNT must be refined.

In requirement *SCI.05*, it is considered that the total number of observations performed by NASA's Marshall Space Flight Centre over the period of 5 years (see Chapter 2, Section 2.4.3) is enough to provide statistical information on the lunar meteoroid impact flux. In fact, Suggs *et al.* (2014) only considers about half of the 240 impacts detected for its statistical analysis, due to the photometric quality of the remaining being affected by Earth's atmosphere. As such, this requirement already includes a 50% safety margin.

Requirement *SCI.06* takes into consideration that Earth-based lunar impact flashes observation can only be done on the lunar nearside. However, a lunar orbiter can observe the lunar farside. This will complement, in space and time, ground-based assets (see Chapter 2, Section 2.2), as proposed in *MO.02*.

Finally, the first mission requirement presented, *MIS.05*, has been defined by a design choice. The last two mission requirements that define the CubeSat's injection orbit were set by ESA's *SYSNova: R&D Studies Competition for Innovation - No.4*.

Table 3.3: LUMIO science requirements.

ID	Requirement	Parent ID
SCI.01	The mission shall discover new impacts on the Moon in the equivalent kinetic energy range at Earth of 10^{-4} to 10^{-1} kton TNT.	MO.01
SCI.02	The mission shall refine the cumulative number of impacts on the Moon in the equivalent kinetic energy range at Earth of 10^{-6} to 10^{-4} kton TNT.	MO.01
	...	
SCI.05	The minimum number of detected impacts shall be 240 to provide statistical information on meteoroid impacts.	MO.01
SCI.06	The mission shall perform observations of the lunar farside	MO.02

Table 3.4: LUMIO mission requirements.

ID	Requirement	Parent ID
	...	
MIS.05	The mission shall have a minimum lifetime of 1 year	TLO.02
MIS.06	The mission shall support deployment from the Lunar Communications Orbiter into an elliptic orbit, with periselene altitude of 200 km and aposelene altitude smaller than 150000 km, or a 500 km-altitude circular orbit.	TLO.05
MIS.07	The mission shall support deployment from the Lunar Communications Orbiter into a circular or elliptical orbit with inclination between 50 and 90 degrees.	TLO.05

From these requirements, three main orbital design drivers can be identified:

Altitude Imposing a *detectable kinetic energy range* will influence the minimum and maximum altitude required, given the constraints of a certain payload (see Chapter 2, Subsection 2.4.4). The *total number of meteoroid detections* over the mission lifetime is directly related to the Moon surface area covered, i.e. the payload's FOV-area, which is also a function of altitude. On the one hand, lower altitudes should allow for the detection of less energetic meteoroids and, as these have higher impact frequencies (see Figure 2.3a), more meteoroid impacts could be detectable. On the other hand, higher altitudes allow the coverage of larger Moon surface areas and, consequently, more meteoroid impacts could also be detectable. Therefore, science requirements *SCI.01*, *SCI.02* and *SCI.05*, constrained by payload characteristics, will all dictate the satellite's orbital altitude trade-off.

Ground-track As stated in Chapter 2, Subsection 2.4.1, lunar meteoroid impact flashes are very faint and can only be detected in the lunar nightside. Furthermore, science requirement *SCI.06* stipulates that the satellite must monitor the lunar farside. As such, orbit design will have to take into account if the satellite's ground-track allows the coverage of both the lunar farside and nightside.

ΔV budget Given the limitations of Cubesat's micropropulsion systems and the need to manoeuvre the CubeSat from the orbit stated in requirements *MIS.06* and *MIS.07* to the operational orbit, the propellant budget should be taken into account in orbital design from an early stage. The propellant budget considered should also include the ΔV budget for stationkeeping, which is directly related to requirement *MIS.05*.

It should also be noted that requirements *SCI.05* and *MIS.05* might overlap. The latter imposes a minimum lifetime of 1 year, while the former indirectly imposes the minimum cumulative observation time. This cumulative time, in turn, depends on the nightside coverage allowed by the chosen orbit. As such, requirement *SCI.05* also imposes a requirement on the minimum mission lifetime itself.

3.3. Subsystem's Design

LUMIO is a 12U CubeSat (2U×2U×3U), with a wet mass of approximately 24 kg. LUMIO's only payload is the LUMIO-Cam, which is an optical instrument that observes in the visible observation spectrum (and a portion of the near-infrared) and is used to monitor and detect lunar meteoroid impact flashes. The relevant characteristics of this instrument are presented in Table 3.5 and Figure 3.1. The spacecraft

design, as defined in [Topputo et al. \(2017\)](#), is presented in Figure 3.2. LUMIO is also a Cubesat which uses chemical propulsion to autonomously perform the transfer to the operational orbit.

Table 3.5: LUMIO-Cam parameters, taken from the chosen detector's datasheet (Teledyne e2V CCD201-20*) and [Topputo et al. \(2017\)](#).

Parameter	Acronym/Symbol	Value	Units
Exposure time	t_{exp}	66	ms
Field-of-View	FOV	3.5×3.5	deg \times deg
Observation spectrum	$[\lambda_1, \lambda_2]$	400–900	nm
Optics aperture	d_ϕ	55	mm
Optics focal length	d_{FL}	217	mm
Optics lens reduction factor	τ	53.55^\dagger	%
Detector frame	N_{pixels}	1024×1024	pixels \times pixels
Detector pixel size	d_{pixel}	13×13	$\mu\text{m} \times \mu\text{m}$
Detector capacity	$cap_{(G)}$	80000 (no gain) 730000 (with gain)	electrons/pixel
Detector Dark-Current	DC	260 (at 20°C)	electrons/s/pixel
Detector Read-Out Noise	σ_{RON}	43	electrons
Detector Gain	G	2	–
Detector Excess Noise Factor	ENF	$\sqrt{2}$	–
Detector Off-chip Noise	off_n	$20 \cdot 10^{-9}$	volt/ \sqrt{Hz}
Detector Output Amplifier Responsivity	OAR	$1.4 \cdot 10^{-6}$	electrons/volt
A/D bit number	N_{bits}	14	bits

* <http://www.e2v.com/resources/account/download-datasheet/1491> [Last accessed on: 23/07/2017]

† Takes into account transmissivity, transparency and the light spreading across multiple pixels

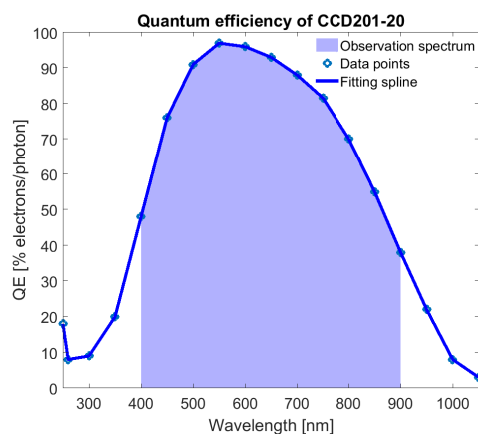


Figure 3.1: LUMIO detector's quantum efficiency. Data points were extracted from the CCD201-20 datasheet and a spline was fitted using MATLAB®'s function *spline*.

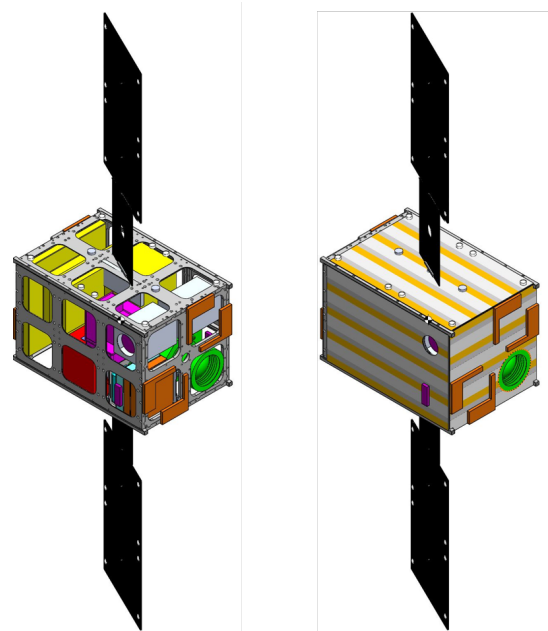


Figure 3.2: LUMIO's configuration, with (right) and without (left) external panels. From [Topputo et al. \(2017\)](#).

It should also be mentioned that the design of [LUMIO](#) was done by applying the concurrent engineering method. In concurrent engineering, all subsystems (including the orbit) are designed simultaneously and more than one iteration might be required. The requirements and subsystem design presented in this chapter refer only to the first iteration of the design process.

References

SYSNova: R&D Studies Competition for Innovation - No.4, *Lunar Cubesats for Exploration (LUCE)*, (2016), Statement of Work, Issue 1, Rev 0, TEC-SY/84/2016/SOW/RW.

F. Topputo, M. Massari, A. Cervone, P. Sundaramoorthy *et al.*, *LUMIO: Lunar Meteoroids Impact Observer, A Cubesat at Earth-Moon L2, Challenge Analysis*, Tech. Rep. (Politecnico di Milano, Delft University of Technology, École Polytechnique Fédérale de Lausanne, The University of Arizona, S[&]T Norway, and Leonardo SpA, 2017).

R. M. Suggs, D. E. Moser, W. J. Cooke and R. J. Suggs, *The flux of kilogram-sized meteoroids from lunar impact monitoring*, *Icarus* **238**, 23 (2014), [arXiv:1404.6458](#) .

4

Methodology

In this chapter, the orbital design methodology applied in this thesis will be explained. In Section 4.1, the methodology steps and the experimental set-up used are introduced. Section 4.2 is dedicated to establishing the evaluation criteria used throughout the design process.

4.1. Orbital Design

The main objective of orbital design is to determine which orbit a spacecraft should fly, in order to meet the mission objectives, requirements and budgets. Usually, several types of orbits are assessed and a trade-off between orbital parameters leads to a final operational orbit. In traditional (large) satellite missions, the ΔV budget is then computed, a launcher is selected and, if needed, iterations to the design process are made. It is also typical to assess the need for single satellite or a constellation and its replenishment, replacement, retrieval or disposal options (Wertz, 2009, p.591).

When designing the orbit of a CubeSat, some steps of the general orbital design guide might not apply. CubeSats, for example, usually do not have a dedicated launcher. Instead, they “piggy-back ride” with a larger satellite mission, which drives the launcher selection process. This is the case of LUMIO, which will be released by the Lunar Communications Orbiter into lunar orbit. CubeSats also have restricted ΔV budgets, given their limited propulsion systems and mass. In addition, it is the main mission that dictates the departure orbit. As such, the CubeSat is limited to those operational orbits that are accessible from the departure orbit imposed. This is why, in the present thesis, the ΔV budget will be taken into account in the orbital trade-off from an early stage, and not just after a preferential operational orbit has been found. For this mission, assessment of the need for a constellation is out of the scope of orbital design, because LUMIO has already been defined as a single satellite mission (Toppato *et al.*, 2017).

Taking into account these considerations, the outline of the methodology used is as follows:

1. Definition of the evaluation criteria, based on requirements and research objective;
2. Establishment of the relevant orbit types for lunar remote sensing;
3. Preliminary trade-off between these orbit types, taking only into account their main characteristics and eliminating clearly non-feasible options;

4. First orbital trade-off, between orbital parameters of *candidate orbits*. In this step, only evaluation criteria related to lunar meteoroid impacts will be considered. For that purpose a lunar meteoroid impact flashes coverage analysis will be performed, taking into account the meteoroid flux at the Moon and the non-illuminated lunar surface area observable by the LUMIO-Cam. Candidate orbits that are non-feasible according to these criteria will be eliminated. The remaining – *partly-feasible orbits* – move on to the next orbital trade-off;
5. Second orbital trade-off, between partly-feasible orbits. In this step, evaluation criteria related to the ΔV budget, determined by optimising the transfer trajectory, will be taken into account. The result of this orbital trade-off should be the chosen operational orbit or a set of preferred operational orbits.

The experimental set-up, taking into account the described methodology, is presented in Figure 4.1. The preliminary orbit trade-off will mainly use available data from literature. The first and second orbital trade-offs use the results obtained from custom developed computer programs, that make use of external toolkits. The program developed for the first orbital trade-off is part of the work carried out for this thesis and is described in detail in Chapters 6 and 7. The second orbit trade-off and development of the associated trajectory optimisation software was carried out by LUMIO's Mission Analysis team. As such, a detailed description of this trade-off and corresponding tools will not be part of this thesis. Nonetheless, the results obtained will be addressed in Chapter 8.

It should be noted that the chosen approach of performing sequential trade-offs, eliminating candidate orbits in between, can falsely lead to the discovery of only non-feasible operational orbits at the last step. This can happen if, for example, the evaluation criteria and assumptions defined are too strict with respect to the requirements. In this case, at least one iteration back to step one might have to occur. On the other hand, eliminating candidate orbits increases the efficiency of the design process, since it reduces the complexity and execution time of the following steps, some of which rely on computationally heavy methods. Nonetheless, in order for this method to lead to a valid conclusion on whether the research objective has been achieved, the definition of the evaluation criteria and assumptions is critical.

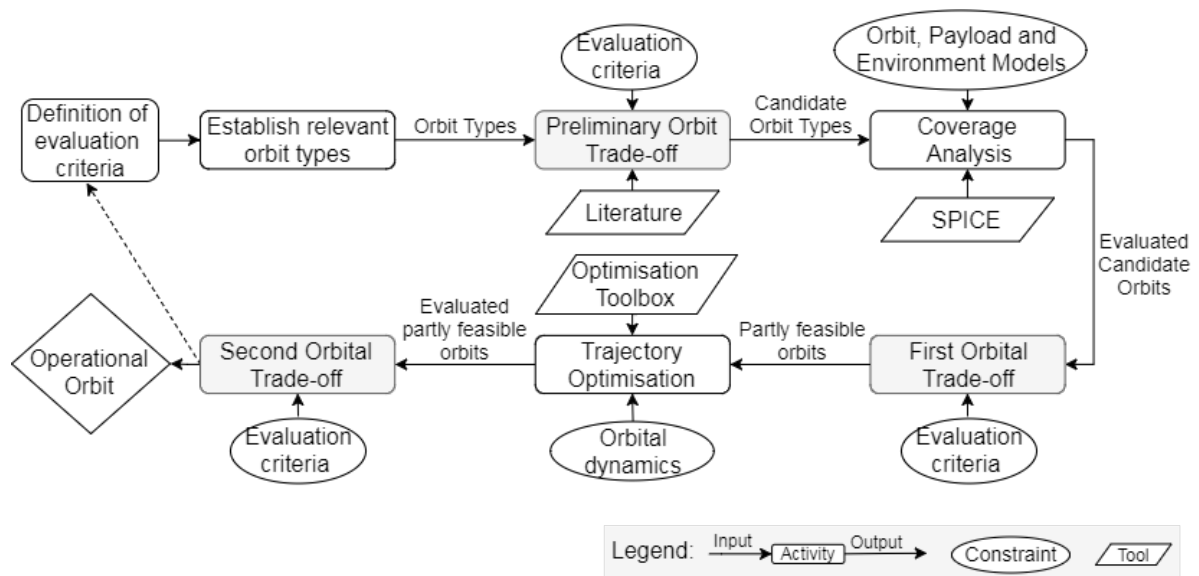


Figure 4.1: Scheme of the experimental set-up used.

4.2. Evaluation Criteria

The evaluation criteria will be divided into two types: *acceptance criteria* and *selection criteria*. The former are defined based on the science and mission requirements (see Chapter 3, Section 3.2). The latter are defined based on orbital performance parameters and will allow the selection of the final orbit, from a set of candidate orbits that meet the acceptance criteria. The acceptance and selection criteria are presented in Tables 4.1 and 4.2, respectively. The reasoning behind the definition of these criteria will be explained in the following paragraphs.

Table 4.1: Orbit design acceptance criteria.

ID	Criteria	Parent ID
EC.A.01	The operational orbit shall allow the detection of meteoroids in the equivalent kinetic energy range at Earth of 10^{-6} to 10^{-1} kton TNT.	SCI.01 SCI.02
EC.A.02	The operational orbit shall allow the detection of at least 240 meteoroid impacts during the mission lifetime.	SCI.05
EC.A.03	The operational orbit shall allow the detection of at least 2 meteoroid impacts in the in the equivalent kinetic energy range at Earth of 10^{-4} to 10^{-1} kton TNT.	SCI.01
EC.A.04	The operational orbit shall allow the detection of at least 100 meteoroid impacts in the in the equivalent kinetic energy range at Earth of 10^{-6} to 10^{-4} kton TNT.	SCI.02
EC.A.05	The operational orbit shall allow monitoring of the lunar farside at night.	SCI.06
EC.A.06	The operational orbit shall support a minimum mission lifetime of 1 year, with a maximum total ΔV budget of 200 m/s.	MIS.05
EC.A.07	The operational orbit shall be accessible from the departure orbit, with a maximum total ΔV budget of 200 m/s.	MIS.06 MIS.07

Table 4.2: Orbit design selection criteria.

ID	Criteria
EC.S.01	The total number of meteoroids detected during the mission lifetime shall be maximised.
EC.S.02	The total ΔV budget shall be minimised.

Acceptance Criteria The first three acceptance criteria and *EC.A.05* follow directly from their parent science requirements. There is a need to define two separate criteria regarding SCI.01, because this requirement affects two different orbital parameters. First, it defines a kinetic energy range to be observed (10^{-4} to 10^{-1} kton TNT), which is a function of altitude, hence, the definition of EC.A.01. Second, it implies that the cumulative observation in this range should be long enough to allow the detection of at least 2 meteoroid impacts, hence, the definition of EC.A.03. Analogously, for requirement SCI.02, criteria EC.A.01 and EC.A.04 were defined. In the latter, the approximate number of meteoroid impact flashes used by [Suggs et al. \(2014\)](#), to estimate the lunar impact flux in this range, has been considered reasonable for a “refinement”.

In the last two acceptance criteria, a total ΔV budget of 200 m/s as been considered reasonable to support a minimum mission lifetime of 1 year and deployment from the Lunar Communications Orbiter. This is based on LUMIO’s preliminary ΔV estimated in [Topputo et al. \(2016\)](#) for a transfer to

an Earth-Moon L2 Halo orbit. [Campagnola et al. \(2016\)](#), for example, estimates a much smaller ΔV of approximately 80 m/s for a transfer to an Earth-Moon L2 Halo orbit. However, the CubeSat EQUULEUS is departing from an Earth-escape orbit and performing two flybys to reduce its energy, while LUMIO is already departing from a lunar-captured state.

Selection Criteria The selection criteria presented were defined in view of the research question and objective. As such, in order to know what is the *best* orbit to *improve* current Earth-based lunar impact flashes observation, the selection criteria have been defined taking into account the *performance* of the orbit. This performance will be assessed based on two parameters: the total number of meteoroids detected over the mission lifetime and the total ΔV budget.

The first has been chosen because one of the main goals of lunar impact flashes monitoring is to improve the current Solar System meteoroid models and a larger number of observations, in the same time period, can contribute towards this goal. Moreover, if the ΔV budget for 1-year lifetime of some of the candidate orbits turns out to be smaller than 200 m/s, selecting the one with the minimum ΔV budget can also contribute towards the same goal. This is because the stationkeeping ΔV could be increased, allowing for a larger mission lifetime and, so, the possibility of detecting more meteoroid impact flashes. On the other hand, a smaller ΔV budget and propellant mass can give more flexibility to the design of other subsystems.

References

- J. R. Wertz, *Orbit & Constellation Design & Management* (Microcosm Press; Springer, 2009).
- F. Topputo, M. Massari, A. Cervone, P. Sundaramoorthy et al., *LUMIO: Lunar Meteoroids Impact Observer, A Cubesat at Earth-Moon L2, Challenge Analysis*, Tech. Rep. (Politecnico di Milano, Delft University of Technology, École Polytechnique Fédérale de Lausanne, The University of Arizona, S[&]T Norway, and Leonardo SpA, 2017).
- R. M. Suggs, D. E. Moser, W. J. Cooke and R. J. Suggs, *The flux of kilogram-sized meteoroids from lunar impact monitoring*, *Icarus* **238**, 23 (2014), [arXiv:1404.6458](#) .
- F. Topputo, J. Biggs, M. Massari, K. Mani et al., *LUMIO: Lunar Meteoroid Impacts Observer*, Tech. Rep. (Politecnico di Milano, Delft University of Technology, École Polytechnique Fédérale de Lausanne, S[&]T Norway, Leonardo-Finmeccanica SpA, and The University of Arizona, 2016).
- S. Campagnola, N. Ozaki, K. Oguri, Q. Verspieren et al., *Mission Analysis for EQUULEUS, JAXA's Earth-Moon Libration Orbit Cubesat*, in *67th International Astronautical Congress* (2016).

5

Lunar Remote Sensing Orbits

This chapter concerns Steps 2 and 3 of the methodology presented in Chapter 4. Section 5.1 introduces relevant concepts of orbital dynamics, regarding the Two and Three-Body Problem. The establishment and description of the relevant orbit types for lunar remote sensing are presented in Section 5.2. Finally, the preliminary trade-off between these orbit types, taking only into account their main characteristics, is presented in Section 5.3.

5.1. Astrodynamics

5.1.1. Two-Body Problem

Given two bodies, i and k , with a radially-symmetric mass density distribution, Newton's law of gravitation dictates that the motion of body i , with respect to body k , when only the mutual gravitational attractions of the two bodies are present, is given by:

$$\frac{d^2 \mathbf{r}}{dt^2} = -\frac{\mu}{r^3} \mathbf{r} \quad \text{with:} \quad \mu = G m_k \left(1 + \frac{m_i}{m_k} \right) \quad (5.1)$$

where \mathbf{r} is the position of body i in a non-rotating reference frame, centered at body k , and G is the *gravitational constant*, $6.674 \times 10^{-11} \text{ m}^3 \text{ kg}^{-1} \text{ s}^{-2}$. If m_i is the mass of the spacecraft and m_k is the mass of the central body, then $m_k \gg m_i$ and $\mu \approx G m_k$, which is known as the *gravitational parameter* of body k . Equation 5.1 then represents the *Restricted Two-Body Problem (TBP)*, as body k suffers no gravitational attraction from body i .

The TBP has two conservation laws: the conservation of *energy* (\mathcal{E}) and *angular momentum* (\mathbf{H}), per unit mass of body i . From these laws, it is possible to determine the analytical solution of the TBP, which describes a conic section with one of the foci located at the origin of the reference frame (body k). The following types of orbits can be distinguished, according to the type of conic section:

- $e = 0$: circular
- $0 < e < 1$: elliptical
- $e = 1$: parabolic
- $e > 1$: hyperbolic

where e is the eccentricity of the orbit.

5.1.2. Three-Body Problem

The Three-Body Problem concerns the study of the motion of three bodies under the influence of their mutual gravitational attractions. If the mass of two bodies, P_1 and P_2 , is much larger than the mass of the third, P_3 , the motion of the first two is given by the solution of the TBP. Therefore, the problem is *restricted* to the motion of the third body, the spacecraft, as it does not influence the motion of the *primaries*. Furthermore, if the primaries move about each other in circular orbits, then the problem is known as the **Circular Restricted Three-Body Problem (CRTBP)**.

For the dynamic system to be time independent (*autonomous*), the equations of motion can be defined in a frame that rotates with the motion of the primaries, centred at the *barycentre* of the system. Furthermore, it is conventional to adimensionalise the equations by setting the primaries' angular velocity, the distance between them and the sum of their masses equal to the unity. The mentioned referential is presented in Figure 5.1, where μ , known as the *mass parameter*, is defined as $\mu = m_2/(m_1 + m_2)$.

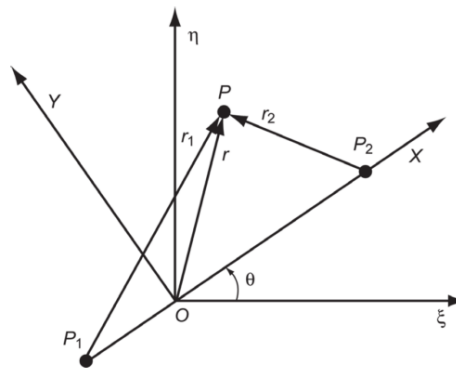


Figure 5.1: CRTBP reference frame (XYZ), with $OP_1 = \mu$ and $OP_2 = 1 - \mu$. From Wakker (2015, p.56).

The equations of motion defined in the mentioned reference frame are (Wakker, 2015, p.59):

$$\begin{aligned}\ddot{x} - 2\dot{y} &= U_x \\ \ddot{y} - 2\dot{x} &= U_y \\ \ddot{z} &= U_z\end{aligned}\tag{5.2}$$

where the subscripts denote the partial derivative of the function:

$$U(x, y, z) = \frac{1}{2}(x^2 + y^2) + \frac{1 - \mu}{r_1} + \frac{\mu}{r_2}\tag{5.3}$$

with:

$$\begin{aligned}r_1 &= \sqrt{(x + \mu)^2 + y^2 + z^2} \\ r_2 &= \sqrt{(x + \mu - 1)^2 + y^2 + z^2}\end{aligned}\tag{5.4}$$

The CRTBP has only one integral of motion, known as the *Jacobi integral*, which is given by (Wakker, 2015, p.60):

$$C = 2 \left(\frac{1}{2}(x^2 + y^2) + \frac{1 - \mu}{r_1} + \frac{\mu}{r_2} \right) - (\dot{x}^2 + \dot{y}^2 + \dot{z}^2) = 2U - V^2\tag{5.5}$$

and does not have an analytical solution. This integral only constrains the 6-dimensional phase space to 5 dimensions, but it provides useful information about the CRTBP dynamics.

Since $V^2 = \dot{x}^2 + \dot{y}^2 + \dot{z}^2 \geq 0$, Equation 5.5 gives $2U(x, y, z) \geq C$. This means that, for a certain initial condition and correspondent value of C , the Jacobi integral gives information about the regions of space accessible or not to body P_3 . The latter are known as the *forbidden regions*. These regions are delimited by the *surfaces of Hill*, given by $2U(x, y, z) = C$, where body P_3 has null velocity. Figure 5.2 shows the forbidden regions in the XY-plane, for decreasing values of the *Jacobi constant* (C). Since the Jacobi constant is also related to the energy of the spacecraft by $C = -2(V^2/2 - U) = -2E$, smaller values of C mean larger values of energy and larger accessible regions in space, as can be seen in Figure 5.2. (Wakker, 2015, p.60-64)

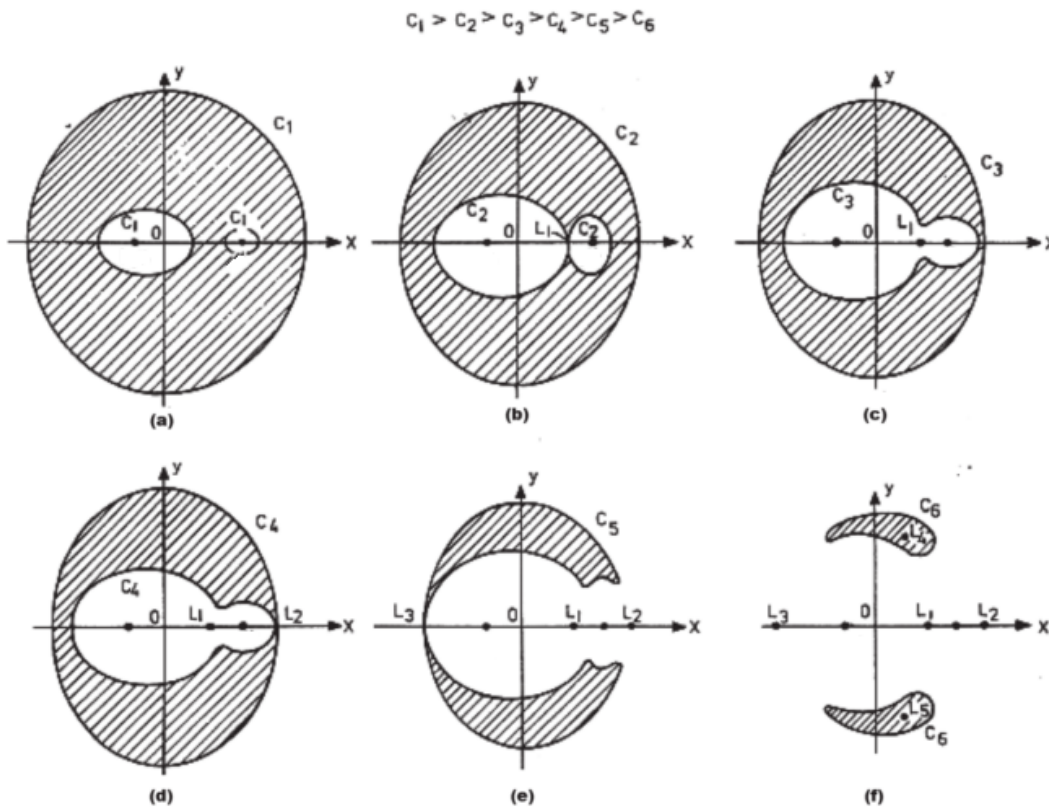


Figure 5.2: Forbidden regions (striped pattern) and surfaces of Hill (outer black lines) for decreasing values of the Jacobi constant. The Lagrangian points are denoted by L_i . From Wakker (2015, p.63).

For increasing values of energy, these forbidden regions gradually open up through the *Lagrangian points*. These are equilibrium points of the dynamical system and are also known as *libration points*. There are five Lagrangian points, three of which are in the X-axis (L_1 , L_2 and L_3) and are known as the *collinear* libration points. The remaining two (L_4 and L_5), known as the *triangular* libration points, are in the XY-plane and are the third vertex of an equilateral triangle formed with the two primaries. The Lagrangian points are also presented in Figure 5.2.

Since the Jacobi integral provides little information, the study of the phase space about the equilibrium points can be useful (Topputo et al., 2005). From linearising the dynamical system, the triangular equilibrium points are found to be stable only for $\mu < 0.0385$ (Wakker, 2015, p.74). The collinear points' linear analysis shows that these are unstable for any value of μ . Furthermore, they are a saddle

point (two real opposite-signed eigenvalues) and a 4D *center* (periodic motion given by two pairs of imaginary eigenvalues) (Musielak and Quarles, 2014).

5.2. Orbital Geometry

This section is dedicated to the description of *lunar remote sensing orbits*. Only orbits that allow a *periodic or repetitive motion with respect to the Moon's surface* will be considered as lunar remote sensing orbits. Orbits whose range to the lunar surface exceeds more than 1/3 of the Earth-Moon distance (≈ 100000 km) will also not be considered lunar remote sensing orbits. Three different classes of orbits are distinguished: Keplerian; Perturbed Keplerian and Libration Point Orbits. These classes and respective orbit types will be described in the following subsections.

5.2.1. Keplerian Orbits

The orbit a body describes in the TBP, represented by a conic section, is known as a *Keplerian orbit*. Of the conic sections presented in Section 5.1.1, only circular and elliptical orbits allow the monitoring of the central body, the Moon. Parabolic and hyperbolic orbits lead the spacecraft to escape the body's Sphere of Influence. Therefore, they will not be considered as lunar remote sensing orbits.

The shape, size and orientation of an elliptical orbit, with respect to a non-rotational reference frame centred at the primary focus, do not change in the TBP (Wakker, 2015, p.260). Therefore, it is possible to characterise the satellite's orbit by a set of fixed parameters, known as the *orbital elements*. The position and velocity of a satellite in its orbit are represented by six state variables, and so, there are also six orbital elements, which are interchangeable with the state variables. The six orbital elements used in this thesis are as follows (see also Figure 5.3):

- the semi-major axis (a) of the ellipse that describes the orbit;
- the eccentricity (e) of the ellipse that describes the orbit;
- the inclination (i), which is the angle between the orbital plane and a reference plane (e.g. the equatorial plane) or the angle between the Z-axis and \mathbf{H} . It is measured between 0° and 180° , in the counter-clockwise direction, when looking from the [Ascending Node \(AN\)](#) to the origin of the reference frame;
- the right ascension of the ascending node (Ω), which is the angle measured along the reference plane, between the X-axis and the [AN](#) direction, from 0° to 360° in the counter-clockwise direction;
- the argument of periapsis (ω), which is the angle measured along the orbital plane, between the [AN](#) and the periapsis, from 0° to 360° , in the direction of motion of the spacecraft;
- the true anomaly (θ) at epoch, which is the angle measured along the orbital plane, between the periapsis and the spacecraft, from 0° to 360° , in the direction of motion of the spacecraft, at a certain epoch.

The first two orbital elements define the size and shape of the orbit; i and Ω define the orientation of the orbit plane; ω defines the orientation of the orbit within the orbital plane; and θ defines the position of the satellite within the orbit (Wertz, 2009, p.46). Satellites with $i < 90^\circ$ are said to move in *prograde* orbits, while satellites with $90^\circ < i < 180^\circ$ move in *retrograde* orbits.

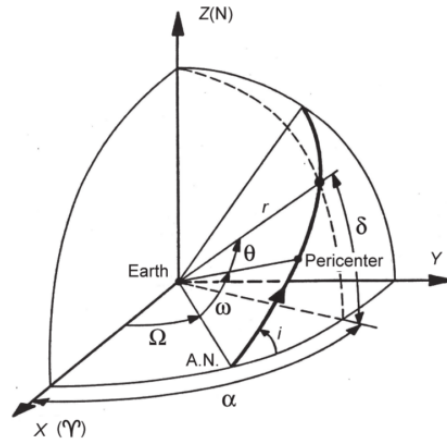


Figure 5.3: Orbital elements of a Keplerian elliptical orbit. From Wakker (2015, p.261).

The semi-major axis (a) of a Keplerian orbit is related to the *specific energy* of the body (\mathcal{E}) through the *vis-viva* equation (Wertz, 2009, p.40):

$$\mathcal{E} = \frac{1}{2}v^2 - \frac{\mu}{r} = -\frac{\mu}{2a} \Leftrightarrow v = \sqrt{\mu \left(\frac{2}{r} - \frac{1}{a} \right)} \quad (5.6)$$

From Equation 5.6, it can be concluded that, when the body is at the *periapsis* (smallest altitude, h_p) its velocity is maximum and at the *apoapsis* (largest altitude, h_a) is minimum. Furthermore, since the angular momentum is constant, a line joining the primary focus and the body will swipe out equal areas in equal units of time. In terms of coverage, this means that a spacecraft on an elliptical orbit covers for a longer period regions directly below its apoapsis and for a shorter period regions directly below its periapsis. For circular orbits, $r = a$, and so, Equation 5.6 becomes $v = \sqrt{\mu/r}$, meaning that the velocity in a circular orbit is constant. As such, a spacecraft in a circular orbit covers all regions below its orbit with the same period.

The time it takes for the body to complete one revolution in its orbit, known as the *orbital period* (P), is given by:

$$P = 2\pi \sqrt{\frac{a^3}{\mu}} \quad (5.7)$$

for both elliptical and circular orbits. From Equation 5.7 it is also possible to define the *mean angular motion* (n) as follows:

$$n = \frac{2\pi}{P} = \sqrt{\frac{\mu}{a^3}} \quad (5.8)$$

The true anomaly of a satellite is difficult to compute, so the concept of mean anomaly (M) was introduced (Wertz, 2009, p.49). The mean anomaly is given by $M = n(t - t_0)$, where t_0 is the time of passage at the periapsis (Wakker, 2015, p.169). To relate M with θ , the concept of eccentric anomaly (E) is introduced. The true anomaly is related with the eccentric anomaly through the *Gauss equation*, as follows (Wertz, 2009, p.49):

$$\tan\left(\frac{E}{2}\right) = \left(\frac{1-e}{1+e}\right)^{1/2} \tan\left(\frac{\theta}{2}\right) \quad (5.9)$$

and the eccentric anomaly relates with the mean anomaly through the *Kepler equation*:

$$M = E - e \sin E \quad (5.10)$$

It should be noted that Equations 5.9 and 5.10 are only valid for circular and elliptic orbits.

From an orbital design perspective, when defined about the Moon, a Keplerian circular or elliptical orbit is known as a **Low Lunar Orbit (LLO)** or an **Elliptical Lunar Orbit (ELO)**, respectively (Whitley and Martinez, 2016). These types of orbits are briefly described below.

Low Lunar Orbit A **LLO** has a constant low altitude with respect to the Moon's surface and has a short period of $P \approx 2$ hours, for $h = 100$ km (Equation 5.7). For altitudes larger than 100 km, Earth's gravitational field affects the satellite's motion in such a way that the orbit can no longer be considered as only under the influence of the Moon's gravity field (Abad *et al.*, 2009; Carvalho *et al.*, 2010).

Elliptical Lunar Orbit An **ELO** usually has a low altitude at the perilune and a relatively large altitude at the apolune. This means that the distance between the satellite and the Moon's surface can vary significantly in one orbital revolution and so can the coverage periods of certain lunar regions.

For altitudes between 500 and 20000 km, a lunar orbiter's motion is mainly dominated by perturbations caused by the Earth's gravity field (Ely, 2005). As such, the limit altitude for **ELOs** considered in this analysis will be 10000 km (Whitley and Martinez, 2016). For altitudes larger than that, the orbit will be considered an orbit of the **CRTBP**. This altitude limit also imposes a limit to the eccentricity of **ELOs**, given by (Wakker, 2015, p.681):

$$\begin{cases} r_p = a(1 - e) > R_M \\ r_a = a(1 + e) < 10000 \text{ km} \end{cases} \Leftrightarrow e < \frac{r_a - r_p}{r_p + r_a} = 0.74 \quad (5.11)$$

where R_M is the radius of the Moon and r_p and r_a are the radius of the periapsis and apoapsis, respectively. Otherwise, the spacecraft would crash into the lunar surface when at the periapsis.

For both types of orbit, lunar surface coverage also depends on the inclination of the orbit, as larger inclinations allow the coverage of higher latitudes. An orbit with $i = 90^\circ$, known as a *polar orbit*, would allow coverage of all latitudes. Furthermore, it should be noted that, in the true Earth-Moon environment, these orbits are perturbed and not purely Keplerian. As such, mitigation measures must be taken into account to maintain the Keplerian properties of the orbit, as will be briefly explain in the following subsection.

5.2.2. Perturbed Keplerian Orbits

In Subsection 5.1.1, it was assumed that the spacecraft was only under the influence of one gravitational field, generated by a central body that had a radially symmetric mass distribution. However, other celestial bodies, besides the central body, can also influence the motion of a satellite. These are known as **Third-Body (TB)** perturbations (Russell, 2012). Furthermore, celestial bodies' mass distribution is not perfectly radially symmetric. As such, depending on the position of a spacecraft above the celestial body's surface, it will experience a different gravitational acceleration, which will cause the spacecraft to deviate from the nominal Keplerian orbit. These are known as **Non-Spherical Gravity (NSG)** perturbations (Russell, 2012). Perturbing forces, such as the **TB** or **NSG**, originate what is known as a *perturbed Keplerian orbit* (Wakker, 2015, p.527).

The equations of motion of a lunar satellite, perturbed by the NSG of the Moon and by the Earth as a TB, can be written as (Wakker, 2015, p.32, 528, 549):

$$\begin{aligned} \frac{d^2 \mathbf{r}}{dt^2} + \frac{\mu_M}{r^3} \mathbf{r} &= f_{TB} - C \nabla U_{NSG} \\ f_{TB} &\equiv -\mu_E \left(\frac{\mathbf{r}_E}{r_E^3} - \frac{\mathbf{r}_E - \mathbf{r}}{\|\mathbf{r}_E - \mathbf{r}\|^3} \right) \\ U_{NSG} &\equiv \frac{\mu_M}{r} \left[\sum_{n=2}^{\infty} J_n \left(\frac{R_M}{r} \right)^n P_n(\sin \Phi) - \sum_{n=2}^{\infty} \sum_{m=1}^n J_{n,m} \left(\frac{R_M}{r} \right)^n P_{n,m}(\sin \Phi) \cos[m(\Lambda - \Lambda_{n,m})] \right] \end{aligned} \quad (5.12)$$

where f_{TB} is the Third-Body perturbation force, μ_M and μ_E are the gravitational parameters of the Moon and Earth, respectively, and \mathbf{r}_E is the position vector of Earth, in a non-rotating Moon-centred reference frame. U_{NSG} is the perturbing potential of the Moon's Non-Spherical Gravity field; r , Φ and Λ are planetocentric coordinates, defined in a body-fixed reference frame (see Chapter 6, Subsection 6.1); $P_{n,m}$ are associated Legendre polynomials of the first kind, of degree n and order m ; $J_{n,m}$ and $\Lambda_{n,m}$ are the coefficients of the model; and C is a transformation matrix from the body-fixed to inertial Moon-centred reference frame.

These perturbations also mean that the orbital elements, presented as fixed parameters in Section 5.2.1, in reality, are not constant and vary during one orbital revolution. Therefore, if one wants to maintain the Keplerian orbital elements of orbits such as a LLO and ELO constant, the perturbations must be countered, usually by spending propellant.

Nonetheless, there are certain types of orbits that take advantage of the perturbed gravity field characteristics, in such a way that their orbital elements remain approximately constant, and, so, require very little propellant to be maintained. This stable type of orbits is known as a Frozen Orbit (FO) (Wertz, 2009, p.90). It is also possible to take advantage of the perturbed gravity field characteristics in such a way that the orbital plane remains nearly fixed with respect to the Sun, as the Earth–Moon system moves in its orbit (Wertz, 2009). This type of orbit is known as a Sun-Synchronous Orbit (SSO). Both types of orbits have been discovered for the Moon and will be detailed in the paragraphs below.

Frozen Orbits A lunar FO is an orbit whose orbital elements remain constant, on average, during one orbital revolution. They usually exist only for certain combinations of a , e , i and ω , which makes their design restrict (Whitley and Martinez, 2016). However, the altitude of the satellite in a frozen orbit is constant over each latitude, which makes the coverage pattern repetitive. Two different types of lunar frozen orbits have been found. The first take only into account perturbations by the zonal terms of the lunar NSG field (J_n -terms) and have low altitudes ($h < 100$ km). The second also take into account perturbations of Earth's gravity field and have higher altitudes ($h > 100$ km).

Elife and Lara (2003) numerically found two families of stable, low altitude, quasi-circular lunar orbits, considering 7 terms of the lunar zonal harmonics. The first have inclinations between 0° and 63° (critical inclination), and the second between 73° and 86.5° . Orbits with inclinations in between and high eccentricities were found to be unstable (see Figure 5.4, top-left plot). The argument of periapsis for either family can be 90° or 270° and varies at most by 3° , near the critical inclination. For other ω values, no stable frozen orbits can exist, according to the analytical study performed by Abad et al. (2009). Furthermore, Abad et al. (2009) also demonstrated that analytically computed frozen initial conditions, using only the J_2 and J_7 terms, could remain periodic using a more realistic gravity field model (up to $n = 9$), if a corrector method is used. Using the averaged orbital elements as initial

conditions can lead to a non-frozen orbit in less than one year.

Ely (2005) designed a high-altitude, lunar quasi-frozen orbit, with $h_a = 9382$ km, $e = 0.6$, $i = 63^\circ$ and $\omega = 90^\circ$, taking into account only Earth TB perturbations. The oscillations around the average value could reach $\Delta e \approx 0.15$, $\Delta i \approx 4^\circ$ and $\Delta \omega \approx 20^\circ$, considering the true ephemeris of Earth. Including the Moon's NSG field up to $n = 50$ and the Sun's TB perturbation, in a 1 year simulation, only $\Delta \omega$ increased to $\approx 30^\circ$. Abad *et al.* (2009) later performed an analytical study for moderate altitude orbits ($100 < h < 3500$ km), considering both the J_2 and J_7 -terms of the Moon's NSG and Earth TB perturbations. The results obtained are presented in Figure 5.4. From these plots, it can be concluded that the unstable inclination region found for lower altitudes, decreases for larger altitudes. Moreover, for even larger altitudes, high eccentricity frozen orbits become a possibility.

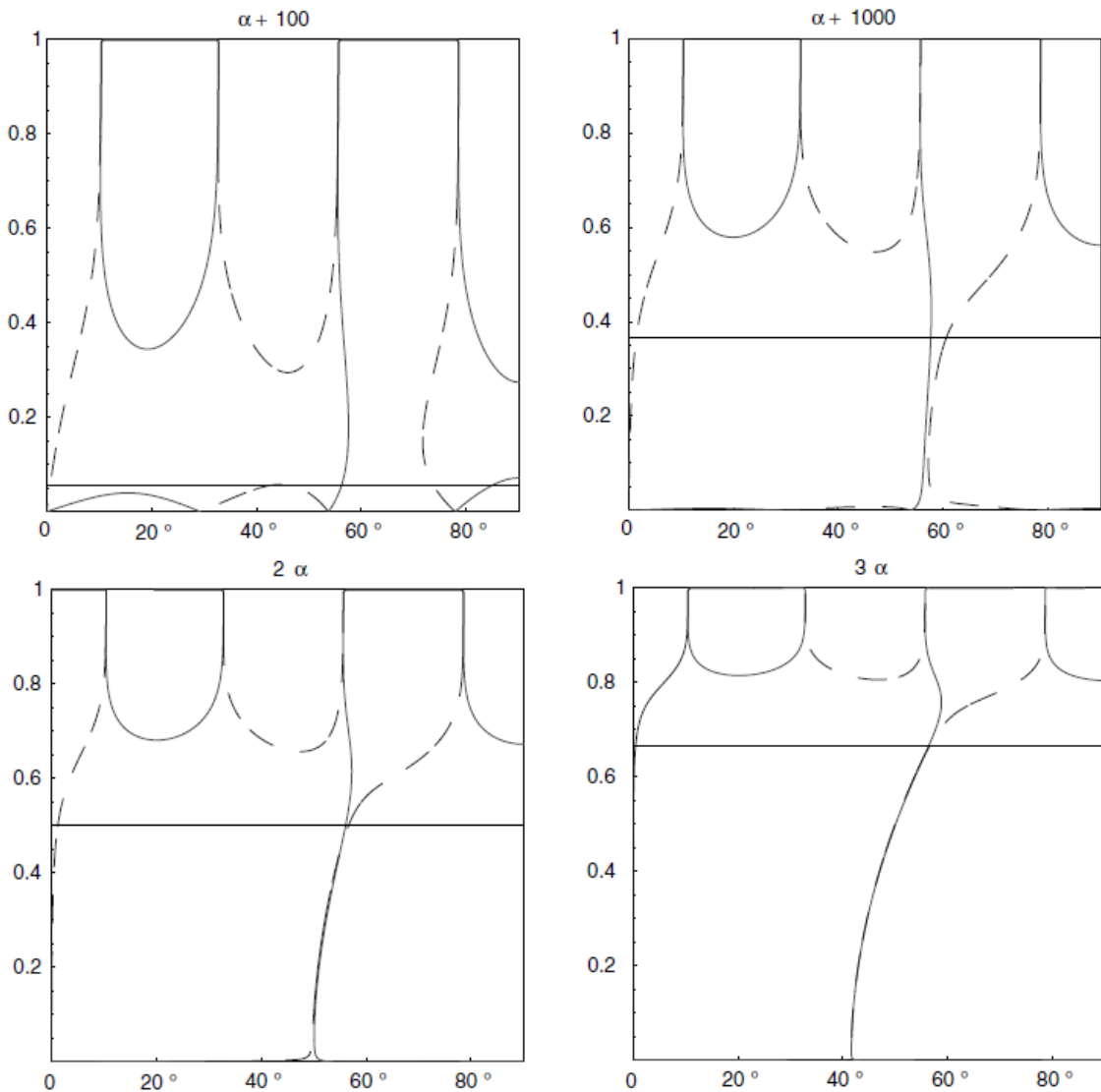


Figure 5.4: Lunar frozen orbits' averaged orbital elements: inclination, eccentricity and semi-major axis (denoted as $\alpha + h_0$) and argument of periapsis. The constant eccentricity line denotes the eccentricity above which the satellite crashes. The four semi-major axis presented are 1838, 2738, 3476 and 5217 km (left to right and top to bottom). Dashed lines correspond to $\omega = 90^\circ$ and solid lines to $\omega = 270^\circ$. From Abad *et al.* (2009).

Sun-Synchronous Orbits A Sun-Synchronous orbit is an orbit whose line of nodes rotates in such a way that the orbital plane orientation is fixed relative to the Sun. Figure 5.5 depicts this situation. From this figure, one can observe that the orbital plane needs to rotate an angle $\theta = 2\phi$, as the Earth–Moon system also rotates the same angle θ about the Sun. The Earth–Moon system completes one revolution about the Sun in $P_E = 365.26$ days, so the line of nodes needs to rotate $\dot{\theta} = 360^\circ/P_E \approx 0.9856^\circ/\text{day}$. Considering the duration of a sidereal month ($P_M = 27.32$ days), the precession rate of the line of nodes must equal $\dot{\theta}$ as follows (Park and Junkins, 1994):

$$\dot{\Omega} = \frac{360}{P_E} S_M = \frac{360}{365.26} \cdot 27.32 = 26.9266^\circ/\text{sidereal month} \quad (5.13)$$

The natural precession of the line of nodes, taking into account the J_2 and J_{22} terms of the Moon's NSG perturbation potential, is a function of the type: $\dot{\Omega} = f(a, e, i, \Omega_0)$, where Ω_0 denotes the longitude of the ascending node at time zero (Carvalho et al., 2009). Taking into account 5.13, this function gives the following Sun-Synchronous inclination (i_{SS}) (Carvalho et al., 2009):

$$i_{SS} = \pi - \cos^{-1} \left(\frac{1.327307409 \cdot 10^{-7} a^2 (1 - e^2)^{3/2}}{n(613.573 + 67.496(-2 - e^2 + 3e^4) \cos(2\Omega_0))} \right) \quad (5.14)$$

The variation of i_{SS} with a, e and Ω_0 is depicted in Figure 5.6. From these plots, it can be concluded that, for $a = 1838$ km, lunar Sun-Synchronous orbits exist for inclinations between $\approx 132^\circ$ and 176° , for $\Omega_0 \in [20, 160] \cup [200, 340]^\circ$ (Carvalho et al., 2009). For this semi-major axis, the eccentricity is restricted to $e < 0.05$, otherwise the satellite would crash. For circular orbits and $a < 1838$ km, the Sun-synchronous inclination range tends towards $[125, 170]^\circ$, while $\Omega_0 \in [0, 360]^\circ$. For $a > 1838$ km, Earth's TB perturbation needs to be taken into account and Equation 5.14 no longer applies.

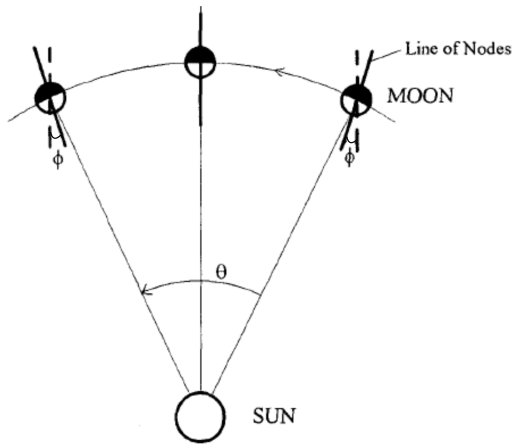


Figure 5.5: Sun-Synchronous orbit: the line of nodes rotates an angle $\theta = 2\phi$ to maintain a relative position between the orbital plane and the Sun. From Park and Junkins (1994).

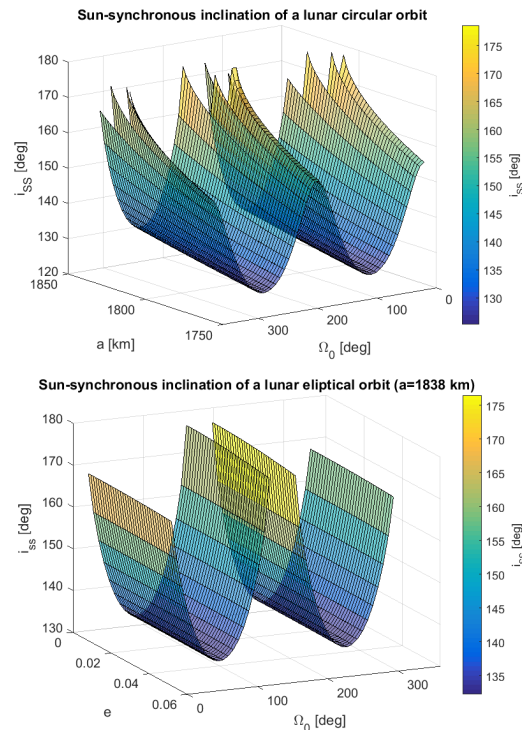


Figure 5.6: Sun-Synchronous inclination. Computed with Equation 5.14 from Carvalho et al. (2009).

Table 5.1 summarizes the main characteristics of Keplerian and Perturbed Keplerian orbits, as presented in Subsections 5.2.1 and 5.2.2.

Table 5.1: Characteristics of Keplerian and Perturbed Keplerian lunar remote sensing orbits. The information within parentheses denotes the conditions correspondent to interval limits.

Orbit	h (km)	e	i ($^\circ$)	ω ($^\circ$)	P (h)	Coverage characteristics
Low Lunar Orbit	$< 100^{a,b}$	0	$[0, 180[$	–	< 2	Constant altitude
Elliptical Lunar Orbit	$< 10000^c$ (apoapsis altitude)	< 0.74 (crash)	$[0, 180[$	$[0, 360[$	< 27 ($e = 0.1$; $h_a = 10000$ km)	Variable altitude; possible to cover more extensively certain regions
Frozen Orbit	$< 100^a$ (only Moon zonal harmonics)	$[0, 0.1]^{a,d}$	$[0, 63] \cup$ $[73, 86.5]^{*,a,d}$	90 or 270 ± 3^a	< 2 ($e = 0.01$; $h_a = 100$ km) ^a	Possibly variable altitude, but constant over each latitude ^b
	$[100, 9000]^{a,e}$ (Moon zonal harmonics and Earth)	$[0, 0.7]^\dagger$ ($h = 3700$ km)	0 or $[40, 70]^a$	90 or 270^a	< 24 ($e = 0.6$; $h_a = 9000$ km) ^e	
Sun-synchronous Orbit	$< 100^b$ (only Moon's J_2 and C_{22})	< 0.05 (crash)	$[125, 170]$ (from Fig. 5.6)	$[0, 360[$	< 2	Approximately constant altitude and illumination angles

^a Abad *et al.* (2009) ^b Carvalho *et al.* (2010) ^c Whitley and Martinez (2016) ^d Elipe and Lara (2003) ^e Ely (2005)

* Symmetric intervals with respect to 90° also exist (Park and Junkins, 1994)

† Smaller interval for lower altitudes (Abad *et al.*, 2009)

5.2.3. Libration Point Orbits

Given that the CRTBP does not have an analytical solution, the analytical or numerical exploration of the dynamic phase space is a must to understand its dynamics. This has led to the discovery of *periodic orbits* in the CRTBP, about all Libration points, the Moon and Earth. If about L_1 and L_2 , these orbits can serve the purpose of lunar monitoring, since these points are closer to the Moon ($\approx 60,000$ km) than L_3 , L_4 and L_5 ($> 300,000$ km). Therefore, only orbits about L_1 and L_2 will be considered as lunar remote sensing orbits.

Folta *et al.* (2015) groups CRTBP orbits in three main categories: *Libration Point Orbits*, *Resonant Orbits* and *Moon-centred Orbits* (see Figure 5.7). The first category contains orbits whose motion revolves (mostly) about one of the Earth–Moon Libration points. The second category contains orbits whose periods are resonant with the lunar orbital period (P_M). These can be either *interior* or *exterior* if they remain interior to the Moon's orbit or cross it to higher altitudes. Finally, Moon-centred Orbits are exterior resonant orbits that appear to orbit the Moon in the CRTBP reference frame.

It should be noted that Interior Resonant Orbits lead to very large ranges with respect to the Moon and do not allow monitoring of the lunar farside (Requirement SCI.06), so they will not be considered as candidate orbits. Axial and Distant Prograde orbits will also not be considered, since their irregular shape can lead to a complex coverage pattern, with no added benefits. Therefore,

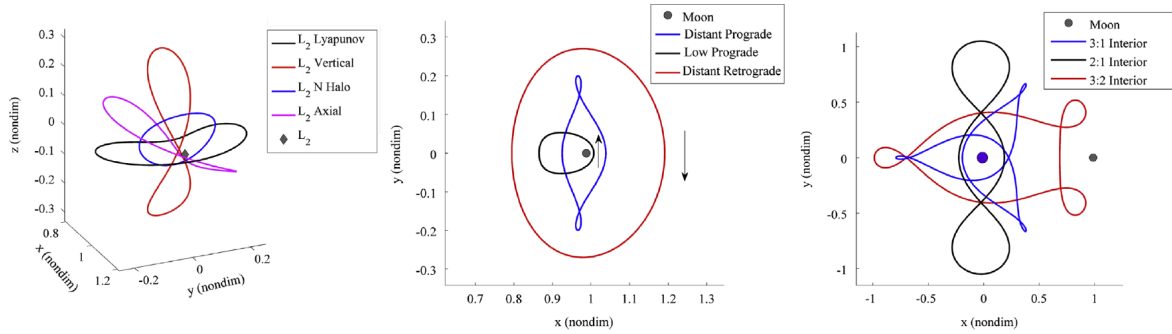


Figure 5.7: CRTBP orbit types grouped into three main families: Libration Point Orbits (left); Moon-centred Orbits, which are also Exterior Resonant Orbits (center) and Interior Resonant Orbits (right). The orbits are represented in the CRTBP reference frame, centred at Earth (blue circle), and the arrows denote the direction of motion. From [Folta et al. \(2015\)](#).

only six types of periodic orbits that exist in the CRTBP – the Lyapunov Orbit (LO), the Halo Orbit (HO), the Near-Rectilinear Orbit (NRO) (which are part of the Halo family), the Vertical Orbit (VO), the Distant-Retrograde Orbit (DRO) and the Low-Prograde Orbit (LoPO) – will be considered for orbital design. These orbits are presented in detail in the following paragraphs and Table 5.2 (at the end of the section) summarizes their main characteristics. They will be collectively referred to as either CRTBP orbits or Libration Point Orbits.

Compared with Keplerian orbits, these orbits can be more easily accessible from Earth, have more favourable thermal environments, few or no lunar eclipses and infrequent Earth shadowing ([Whitley and Martinez, 2016](#)). It should be noted, nonetheless, that, since these orbits are associated with unstable Lagrangian points, they are all inherently unstable. In order to characterise the stability of the orbit, the concept of stability index is introduced (S). The mathematical definition is as follows ([Folta et al., 2015](#); [Grebow et al., 2008](#)):

$$S = \frac{1}{2} \left(|v| + \frac{1}{|v|} \right) \quad (5.15)$$

where v denotes the (reciprocal) pair of eigenvalues associated with the stable/unstable subspace of the orbit. $S > 1$ indicates instability of the orbit, while $S < 1$ indicates stability. Furthermore, a larger stability index is usually associated with larger stationkeeping costs, but lower transfer costs ([Grebow et al., 2008](#)).

Lyapunov Orbits A LO is a periodic orbit in the CRTBP XY-plane, about L_1 or L_2 . They are typically characterised by the amplitude in the X-axis direction (A_x). For very large A_x amplitudes it is even possible to observe the lunar apex and antapex. Their orbital periods range from approximately 15 to 30 days and their stability index is relatively high ($S \sim 300$).

Halo Orbits A HO is also a periodic orbit about L_1 and L_2 , but has an out-of-plane component in the direction of the Z-axis. The frequency of the out-of-plane motion matches the in-plane motion, giving origin to a 3D periodic orbit¹. Based on this premise, [Farquhar and Kamel \(1973\)](#) concluded that the amplitude of L_2 3D periodic orbits, in the Y-direction (A_y), would have to be larger than 32379 km, meaning that Halo orbits are inherently large.

As with any other Libration Point Orbit, one does not have an exact analytical solution for Halo

¹If the in-plane and out-plane frequencies do not match, a small-sized *Lissajous* quasi-periodic orbit is originated

orbits. Analytical approximations are typically used as a first guess for their numerical computation. [Thurman and Worfolk \(1996\)](#), for example, use a third-order analytical solution for Halo orbits, developed by [Richardson \(1980\)](#). Richardson's first-order approximation, written in coordinates of the [CRTBP](#) reference frame, centred at the Libration point, is given by:

$$\begin{aligned}x &= -A_x \cos(\lambda t + \phi) \\y &= kA_x \sin(\lambda t + \phi) \\z &= A_z \sin(\nu t + \psi)\end{aligned}\tag{5.16}$$

where ν is forced equal to λ , A_x and A_z are constrained by a non-linear algebraic relation and ϕ and ψ by a linear relation.

The solutions of the [CRTBP](#) are symmetric with respect to the XY-plane. As such, if the sign of z is inverted, another family of orbits appears as mirror reflections of the first family, about the XY-plane ([Richardson, 1980](#)). These two branches of Halo orbits are known as the Northern Halo family, if z is in phase with x , or as the Southern Halo family, if z and x are 180° out-of-phase ([Breakwell and Brown, 1979](#)). In the Earth–Moon L_2 , a satellite in a Northern Halo Orbit moves in the clockwise direction, when seen from Earth, while a satellite in a Southern Halo Orbit moves in the counter-clockwise direction, as depicted in [Figure 5.8](#).

[Breakwell and Brown \(1979\)](#) also showed that both Earth–Moon L_1 and L_2 Halo orbits grow larger in size as they approach the Moon, until about halfway of the distance, but their periods (≈ 14 days) become slightly shorter. [Figure 5.8](#) also shows this growth of (L_2) Halo Orbits towards the Moon. Furthermore, these orbits are relatively stable ($S \sim 150$) and have the advantage of allowing constant Earth visibility ([Farquhar, 1972](#)).

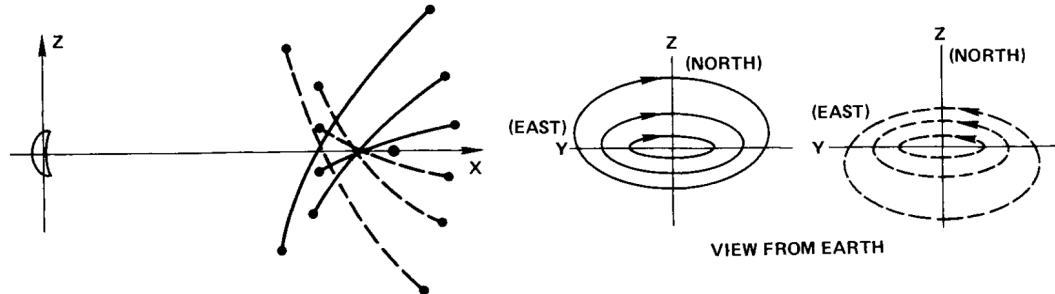


Figure 5.8: Northern and Southern Halo Orbits about the Earth–Moon L_2 . Projection onto the XZ-plane (left) and YZ-plane (right). Southern Halo Orbits are represented by dashed lines and Northern Halo Orbits by solid lines. From [Breakwell and Brown \(1979\)](#).

Near-Rectilinear Orbits A survey of Halo orbits by [Breakwell and Brown \(1979\)](#) showed that both Halo families at the Earth–Moon L_1 and L_2 become almost rectilinear when close to the Moon. Furthermore, the L_2 Halo Orbits become smaller in size when getting closer to the Moon, while the L_1 Halo Orbits increase in size, as depicted in [Figure 5.9](#). These almost rectilinear orbits, that are part of the Halo family, are known as Near-Rectilinear Orbits.

When very close to the Moon, they appear to be large elliptical orbits. As such, just as Halo Orbits, they remain relatively fixed with respect to the Earth–Moon direction and are always visible from Earth. [Figure 5.10](#) presents four different types of [NROs](#), according to the family of Halo Orbits that belong to. In this figure, it is possible to observe that the different types of [NRO](#) families appear to intersect

near the Moon, establishing a connection between the L_1 and L_2 families of Halo Orbits, phenomenon which [Howell and Breakwell \(1984\)](#) called the “ L_1 - L_2 bridge”.

These orbits can have a much shorter period than traditional Halo Orbits ($P > 4$ days) and the stability index can also be much lower ($S \sim 1$). Furthermore, it is possible to cover more extensively certain parts of the lunar surface. For example, an L_2 NRO orbit can be useful for the coverage of the lunar farside and a Southern NRO for the coverage of the lunar south pole, while for an L_1 Northern NRO the opposite is verifiable.

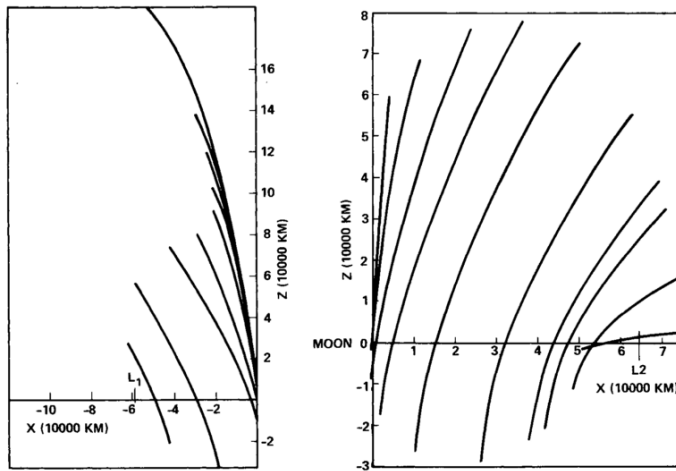


Figure 5.9: Earth–Moon L_1 (left) and L_2 (right) Halo families becoming almost rectilinear near the Moon. From [Breakwell and Brown \(1979\)](#).

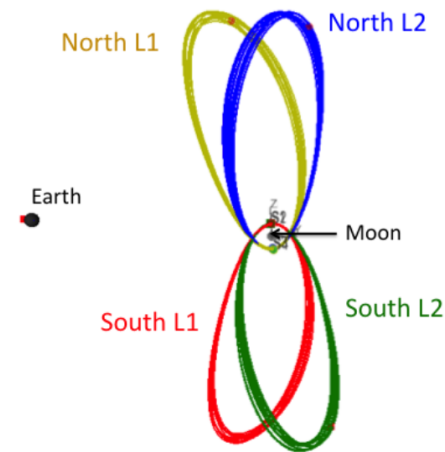


Figure 5.10: Types of Earth–Moon L_1 and L_2 NRO families. From [Whitley et al. \(2016\)](#).

Vertical Orbits A VO is also another periodic orbit about L_1 and L_2 that has motion component out of the XY-plane. However, while Halo orbits have a circular shape, Vertical orbits are shaped as an eight (see Figure 5.7). This is because they cross the X-axis twice in one orbital period. Their orbital periods range from approximately 10 to 20 days and their stability index is in between that of Halo and Lyapunov orbits ($S \sim 200$). Given their shape, these orbits can be used to monitor both lunar poles in one orbital revolution.

Distant-Retrograde Orbits A numerical survey of non-periodic orbits of the CRTBP by [Hénon \(1970\)](#) lead to the discovery of quasi-periodic retrograde orbits at large distances from the primary bodies (see Figure 5.7). Furthermore, these orbits have no apparent size limit, so they can even encompass both L_1 and L_2 . A large sized retrograde quasi-periodic in the CRTBP is known as a **Distant-Retrograde Orbit**, while a small retrograde quasi-periodic orbit can be considered as a perturbed lunar Keplerian orbit ([Ming and Shijie, 2009](#)).

[Turner \(2016\)](#) studied the stability of DROs for 30 years, taking into account the Moon’s NSG and the Sun, Venus and Jupiter’s TB perturbation. He concluded that low-altitude DROs ($h < 45000$ km) tend to be stable, while high-altitude DROs ($h > 50000$ km) only tend to be stable if near-resonant with the Moon. The resonant state can be described by the coefficient $m:n:p$, where:

- m denotes the number of times the Moon revolves around the Earth in inertial space;
- n denotes the number of times the spacecraft revolves around the Moon in inertial space;
- p denotes the number of times the spacecraft revolves around the Moon in the CRTBP frame.

It is also common to represent the resonant state using the ratio $p/m = P_M/P$, since $p = m + n$ (Turner, 2016).

Figure 5.11 shows the regions of stable DROs, as function of the initial distance and velocity relative to the Moon. There are two distinct regions: the first is a large region that corresponds to lower altitudes, higher p/m ratios and a broad range of initial velocities ($x_0 = [20, 50] \cdot 10^3$ km; $v_{y,0} = [375, 575]$ m/s $\Rightarrow p/m = [3, 6]$); the second is a small region that corresponds to higher altitudes and velocities and lower p/m ratios ($x_0 = [60, 80] \cdot 10^3$ km; $v_{y,0} = [500, 575]$ m/s $\Rightarrow p/m = [1.6, 2]$).

There are two resonant states that could be specially interesting for the mission in question: 1:0:1 and 1:1:2. Figure 5.12 depicts the former and Figure 5.13 the latter. In the first resonant state, $P_M = P$, and the spacecraft does not complete any revolution with respect to the Moon, in inertial space. From Figure 5.12, one can observe that this would lead the spacecraft and the Moon to be almost always aligned with respect to the AE-direction. In the time of the year where the incoming light direction is from E to A (≈ 1 month), this would mean that the spacecraft would permanently be able to observe the nightside of the Moon. However, Turner (2016) reports that no stable initial conditions for this type of orbit have been found.

In the second resonant state, $P_M = 2P$, and, so, the spacecraft completes one revolution with respect to the Moon, in inertial space, and two revolutions, in the CRTBP reference frame, in one sidereal month. From Figure 5.13, one can observe that this would lead the spacecraft to observe twice the lunar farside and nearside. Depending on the time of the year, the incoming light direction would either be approximately aligned with the orbit's minor axis (left plot) or major axis (right plot). For the first case, this means that both Earth and space-based observations could be done simultaneously in time and, for the lunar nearside, also in space. As such, this configuration could be an opportunity to validate the mission concept with Earth-based observation. For the second case, however, observations would be complementary in both space and time. A similar situation should also occur for the resonant state of 1:3:4.

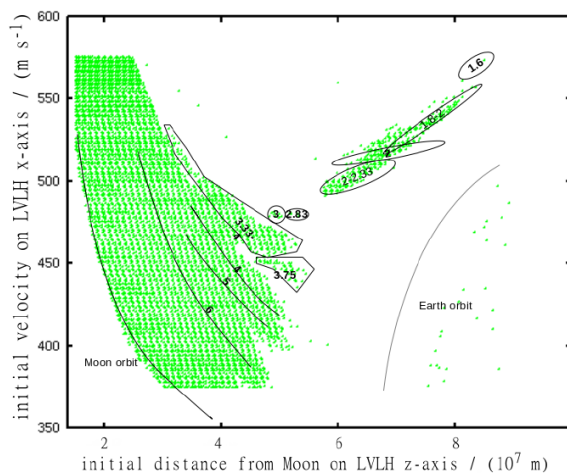


Figure 5.11: Stable Distant-Retrograde Orbit resonant states p/m . Function of the initial distance to the Moon (in the negative direction of the CRTBP reference frame X-axis) and initial velocity relative to the Moon (in the positive direction of the CRTBP reference frame Y-axis). The "Moon" and "Earth orbit" lines delimit the region of DROs initial conditions. From Turner (2016).

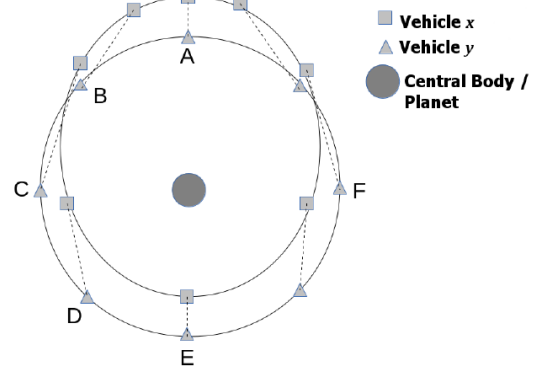


Figure 5.12: Distant-Retrograde Orbit with a 1:0:1 resonance, in an inertial Earth-centred reference frame. "Vehicle x" is the spacecraft, "Vehicle y" is the Moon and "Central Body" is the Earth. From Turner (2016).

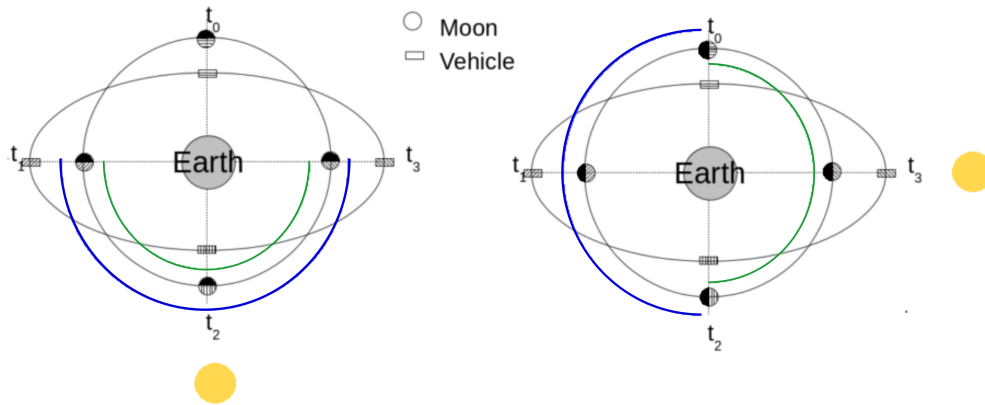


Figure 5.13: Distant-Retrograde Orbit with a 1:1:2 resonance, in an inertial, Earth-centred reference frame. The yellow circle denotes the incoming light direction: aligned with the minor axis (left) or major axis (right). The green line represents the portion of the Moon's orbit where Earth-based impact flashes observations can be made and the blue line where potential lunar DRO impact flashes observations could be made, assuming less than 50% full-disk illumination. Adapted from Turner (2016).

Low-Prograde Orbits LoPO are another family of CRTBP orbits that have been found numerically. Their motion is prograde and can allow much smaller ranges to the Moon than DROs, hence the name. Their orbital periods range from approximately 2 to 14 days and their stability index is comparable with those of DROs or NROs ($S \sim 4$). Given their shape (see Figure 5.7, centre plot), these orbits can be used to cover more extensively the nearside of the Moon.

Table 5.2: Characteristics of CRTBP lunar remote sensing orbits. The information within parentheses identifies the type of information being presented.

Orbit	Geometry	h (10^3 km)	P (days)	S^*	Coverage characteristics	Earth Visibility
Lyapunov Orbits	2D	$[40, 78]^a$ ($A_x = 20000$ km, $P = 15.5$ days)	$L_1: [12, 32]$ $L_2: [14, 36]^b$	$L_1: 350$ $L_2: 300^b$	Lunar nearside or farside and possibly lunar apex and antapex ^c	Occultation can occur
Halo Orbits (including NROs)	3D	$L_1: [20, 65]$ $L_2: [10, 75]^d$ (Maximum distance)	$L_1: [7, 13]$ $L_2: [4, 15]^d$	$L_1: 175$ $L_2: 100^b$ NRO: $\sim 1^d$	Lunar nearside or farside and possibly north or south pole	Always visible
Vertical Orbits	3D	$L_1: [50, 60]$ $L_2: [50, 65]^d$ (Maximum distance)	$L_1: [10, 18]$ $L_2: [14, 18]^{b,d}$	$L_1: 250$ $L_2: 200^b$	Lunar nearside or farside and both poles	Occultation can occur
Distant-Retrograde Orbits	2D	$[20, 50] \cup [60, 80]^e$ (Initial distance to the Moon)	$[4, 16]^e$ (resonant state $P_M/P \in [1.6, 6]$)	1^b	Variable altitude; lunar nearside and farside	Occultation can occur
Low-Prograde Orbits	2D	$[38, 50]^f$ (Maximum range in X-axis)	$[2, 14]^b$	4^b	Lunar nearside covered more extensively	Occultation can occur

^a Bernelli-Zazzera et al. (2004) ^b Folta et al. (2015) ^c Doedel et al. (2007) ^d Grebow et al. (2008) ^e Turner (2016)

^f Guzzetti et al. (2016) * Average over orbit family

5.3. Preliminary Orbital Trade-Off

The goal of the preliminary orbital trade-off is to assess and compare the main characteristics of the candidate orbit types presented in the previous sections and eliminate clearly non-feasible options. Of the evaluation criteria defined in Chapter 4, Section 4.2, only 5 will be taken into account: *EC.A.05*, *EC.A.06*, *EC.A.07*, *EC.S.01* and *EC.S.02*. The remaining refer to the kinetic energy range and number of impacts detectable, which imply modelling both the impact phenomenon and payload (see Chapter 6).

Compliance with criteria will be categorised as one of the following: meets evaluation criteria; can meet evaluation criteria during the detailed analysis, at later stages in the design process; or does not meet the evaluation criteria. The following paragraphs detail the methodology used and the results obtained for each orbit type, per evaluation criteria. Tables 5.3 and 5.4 (at the end of the section) summarise the results found in a graphical trade-off between the orbit types.

Farside monitoring at night (*EC.A.05*) All orbital families presented in Section 5.2 have orbits which allow the monitoring of the lunar farside, at night, at least once per synodic month. The only type of orbit which not allow it are L_1 Lyapunov, Halo or Vertical orbits and, thus, will no be considered.

Nightside observation time per synodic month (*EC.S.01*) Selection criteria *EC.S.01* requires the maximisation of the total number of impacts detected, for which detailed modelling will be required. However, it is possible to directly relate this criteria with the total lunar nightside observation time, per synodic month. This can more easily be estimated than the total number of meteoroid detections, recurring to orbital dynamics, and, so, it is used to assess preliminary performance with respect to *EC.S.01*.

For orbits of the CRTBP two cases can be distinguished: L_2 orbits (LO, HO, NRO and VO) and Moon-centred orbits (DRO, LoPO). The first, if not too close to the Moon, observe mostly the lunar farside and opposite lunar phases than an observer on Earth. As such, assuming that less than 50% illumination is required for impact flashes detection, these orbits can only observe 50% of the time the lunar nightside, per synodic month. Moon-centred orbits can observe both the lunar nearside and farside. However, as can be seen in Figure 5.13, for a resonant DRO, the sequence of lunar phases observed by the spacecraft can be very similar to those of L_2 orbits. As such, one can estimate that these orbits also allow a lunar nightside observation time of $\approx 50\%$, per synodic month. An analogous reasoning can be made for resonant LoPOs.

For Keplerian or Perturbed Keplerian orbits, two cases can also be distinguished: circular and elliptical orbits. Since these orbits have smaller FOV-areas, it will be assumed that the FOV-area is either 100% or 0% illuminated, if the spacecraft is between the Sun and Moon or between the Moon and outer-space, respectively.

For low-altitude circular orbits with a small period, the orientation of the orbital plane with respect to the Sun does not vary much in one orbital revolution. Thus, the incoming sunlight direction can be considered constant during one orbital revolution. This means that 50% of the orbital period the FOV-area is 100% illuminated and the other 50% is 0% illuminated (see, for example, Figure 5.5). As such, since $P \ll S_M$, it can be extrapolated that it is possible to observe the lunar nightside $\approx 50\%$ of the time, per synodic month. This would be the best case scenario for either LLOs or circular FOs.

For elliptical orbits, a fixed incoming sunlight direction during one orbit revolution can also be assumed, if P is small enough. However, in an elliptical orbit, the satellite is at the apoapsis for longer

periods than at the periapsis. Thus, the variation of the incoming sunlight direction throughout the year must be taken into account and, so, the elliptic case is more complex.

Figure 5.14 depicts the incoming sunlight direction of a Frozen Orbit, with $h_a = 10000$ km, $i = 0^\circ$ and $e = 0.74$, throughout the year. From this figure, one can conclude that the lunar nightside observation time, per synodic month, varies throughout the year: it is maximum when the apoapsis is directly above the lunar nightside and minimum when it is directly above the lunar dayside. Recurring to Equations 5.9 and 5.10, it can be concluded that the spacecraft is about the periapsis ($|\theta| < 90^\circ$) approximately 8% of the orbital period and is about the apoapsis ($|\theta| > 90^\circ$) approximately 92% of the orbital period. As such, the nightside observation time per synodic month can range between these two values, throughout the sidereal year.

This variation of nightside observation time per synodic month could lead to the detection of less meteoroids, since part of the yearly meteoroid showers would most likely not be detectable. Furthermore, for a large part of the year, the mission would hardly complement lunar impact flashes' ground-based observations, as defined in Mission Objective *MO.02* (see Chapter 3, Section 3.1). Ideally, the incoming sunlight direction would be constant throughout the year (and the apoapsis always above the nightside of the Moon), but there are no elliptical SSOs (see Table 5.1). As such, elliptical orbits, including frozen elliptical orbits, will not be considered as candidate orbits.

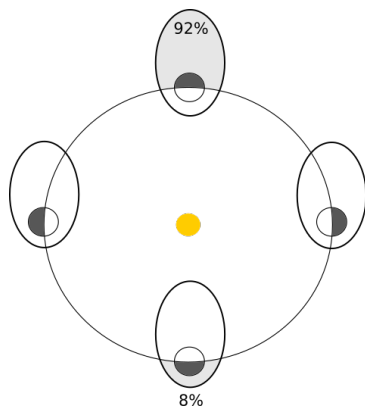


Figure 5.14: Highly eccentric lunar Frozen Orbit and the variation of the lunar nightside observation time, throughout the sidereal year. Drawing not to scale.

Lifetime (EC.A.06) The orbital lifetime is given by the time it takes the satellite to crash onto the lunar surface and is typically defined for Keplerian or Perturbed Keplerian orbits. Since a mission lifetime larger than 1 year is required, this characteristic can be useful in assessing if that requirement is met. Nonetheless, if the natural lifetime of an orbit is smaller than 1 year, it is its maintenance ΔV that determines the compliance with *EC.A.06* (see next paragraph).

Figure 5.15 shows the orbital lifetime for LLOs, taking into account the lunar NSG (left plot), and ELOs, taking into account Earth's TB perturbations (right plot). From Ramanan and Adimurthy's study (left plot) it can be concluded that LLOs typically have an orbital lifetime smaller than 200 days, the exception being inclinations for which the orbit is frozen. For an inclination closer to Sun-Synchronous, $i = 100^\circ$, the orbital lifetime would be ≈ 300 days. From de Almeida Prado's study (right plot) it can be concluded that the lifetime of ELOs can vary from 140 days, for $e = 0.45$, to 1000 days, for $e = 0.01$. Furthermore, a lifetime larger than 1 year is only possible for a low-eccentricity orbit of $e < 0.15$. On the other hand, Frozen Orbits have been estimated to last more than 3 years (Elipse and Lara, 2003).

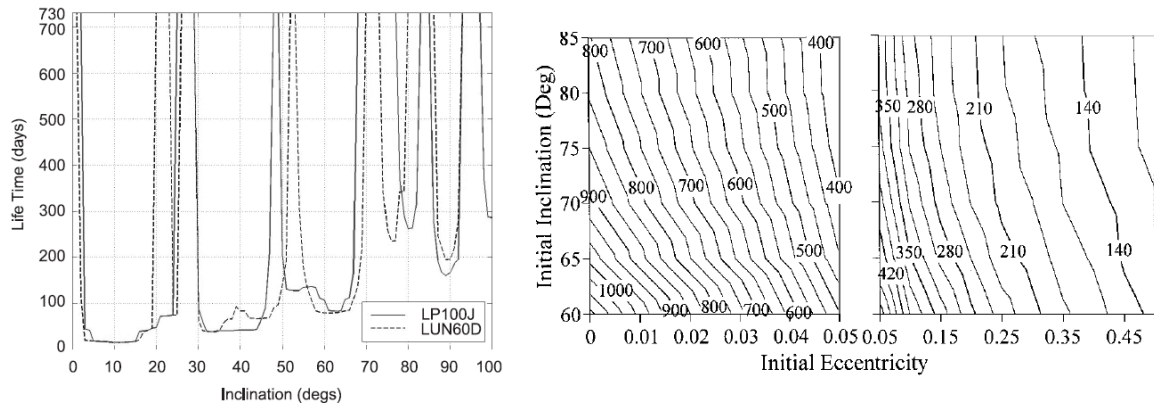


Figure 5.15: Lifetime of lunar Keplerian orbits. Left: Low Lunar Orbit with $h = 100$ km, taking into account two different models of the Moon's NSG; from Ramanan and Adimurthy (2005). Right: Elliptical Lunar Orbit with $a = 7000$ km, taking into account Earth's TB perturbations; from de Almeida Prado (2003).

Total ΔV budget (EC.A.06, EC.A.07 and EC.S.02) The amount of propellant spend in reaching the operational orbit and maintaining it are two quantities that should be assessed together, given that there is only a limit for their sum: the total ΔV budget. This should be less than 200 m/s to comply with EC.A.06 or EC.A.07 and should be the smallest possible to comply with EC.S.02. As such, the evaluation presented in the last two columns of Tables 5.3 and 5.4 refer to the total ΔV budget. The individual contributions of maintenance and transfer ΔV will be detailed in the following paragraphs.

Maintenance ΔV (EC.A.06) Assuming that the operational orbit is reachable with enough margin relative to the 200 m/s ΔV -limit, it is the amount of propellant spent in maintaining the orbit that dictates if the mission can last 1 year. As such, it is mainly the maintenance ΔV that dictates compliance with EC.A.06. The exception to this rule are Frozen Orbits, which have orbital lifetimes larger than one year and, theoretically, do not need to be maintained recurring to propellant (Whitley and Martinez, 2016). There are some ELOs with low eccentricities which also have orbital lifetimes larger than 1 year, but their coverage characteristics quickly degenerate with time, and, so, maintenance is required. The same applies to SSOs.

For highly elliptical ELOs, the stationkeeping ΔV can be larger than 300 m/s, while for SSOs and LLO ($h = 100$ km) can be larger than 50 m/s per year (Whitley and Martinez, 2016). For low-eccentricity orbits no values of stationkeeping ΔV have been found in literature. Nonetheless, an estimation can be made recurring to the right-side plot on Figure 5.15, as follows: knowing that 1) a highly elliptical orbit has a lifetime larger than 140 days and requires 300 m/s per year; it can be estimated that 2) a low eccentricity orbit ($e \approx 0.1$), which has a lifetime of ≈ 350 days, should require $\Delta V > \frac{140}{350} \cdot 300 = 120$ m/s per year.

The maintenance ΔV budget for most of the CRTBP orbits has been estimated from Figure 5.16, with the exception of VOs and LoPOs. This plot indicates, in the X-axis, a representative order of magnitude of the stationkeeping ΔV for an LO, HO and DRO. These were computed with a long-term strategy of 12 orbital revolutions as nominal guidance, including random errors in position, velocity and impulsive correction manoeuvres, for an average of 500 trials. For VOs, a not optimised value of 88 m/s stationkeeping ΔV per year has been found in literature (Grebow et al., 2008), while for LoPOs no information regarding their maintenance has been found.

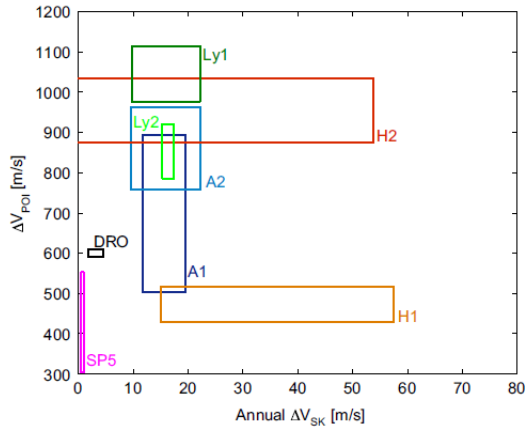


Figure 5.16: Stationkeeping costs of CRTBP orbits (X-axis). The Y-axis refers to the transfer ΔV from an Earth parking orbit, which does not apply to LUMIO. Legend: Ly_i – Lyapunov for L_i ; Hi – Halo for L_i ; Ai – Axial for L_i ; SP_i – Short Period for L_i ; DRO – Distant Retrograde Orbit. From [Folta et al. \(2015\)](#).

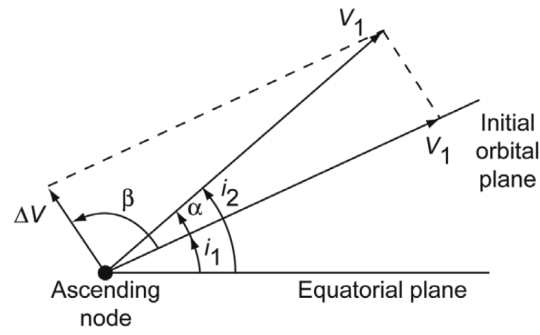


Figure 5.17: Geometry of an inclination change maneuver between two circular orbits with the same radius. From [Wakker \(2015, p.318\)](#).

Accessibility from injection orbit (EC.A.07) The accessibility from the injection orbit is measured in terms of the ΔV spent in the transfer to the operational orbit. The ΔV is evaluated as: Low, if < 200 m/s; Medium, if in between 200 and 600 m/s; or High, if > 600 m/s. For Keplerian orbits, the optimal transfer ΔV can easily be estimated resorting the orbital dynamics knowledge of the TBP. For CRTBP orbits, the optimal transfer ΔV needs to be computed numerically, using optimisation methods. As such, in this preliminary trade-off, only optimal transfers between Keplerian orbits will be computed. For CRTBP orbits, the values found in literature, most representative of LUMIO's transfer, will be assumed.

The injection orbit can either be: (A) a circular orbit with $h = 500$ km and $i \in [50, 90]^\circ$; or (B) an elliptical orbit with $h_p = 200$ km, $h_a < 15000$ km and $i \in [50, 90]^\circ$. So, in order to reach a Keplerian operational orbit, it might be required to perform an inclination change manoeuvre and/or a coplanar transfer between orbits with different altitudes and/or eccentricities.

The geometry of an inclination change between two circular orbits with the same altitude is depicted in Figure 5.17. The change of velocity is given by ([Wakker, 2015, p.317](#)):

$$\Delta V_i = 2v_1 \sin\left(\frac{i_2 - i_1}{2}\right) \quad (5.17)$$

where $v_1 = \sqrt{\mu_M/r_1}$ denotes the velocity of the circular orbit with radius $r_1 = h_1 + R_M$ and i_1 and i_2 denote the inclination of the orbit before and after the manoeuvre, respectively. The geometry of an optimal transfer between two circular orbits of different altitudes (Hohmann transfer) is presented on the left-side of Figure 5.18. The total velocity change required to transfer from orbit I to III, or

vice-versa, is given by (Wertz, 2009, p.93):

$$\Delta V_c = |\Delta V_1 + \Delta V_2| \quad (5.18)$$

$$\Delta V_1 \equiv \sqrt{\mu_M} \left(\sqrt{\frac{2}{r_p} - \frac{1}{a_T}} - \sqrt{\frac{1}{r_1}} \right) \quad (5.19)$$

$$\Delta V_2 \equiv \sqrt{\mu_M} \left(\sqrt{\frac{1}{r_2} - \frac{1}{a_T}} - \sqrt{\frac{2}{r_a} - \frac{1}{a_T}} \right) \quad (5.20)$$

where $r_a = r_2$, $r_p = r_1$ and $a_T = (r_1 + r_2)/2$ are the radius of apoapsis, periapsis and semi-major axis of the transfer orbit (II), respectively; $r_1 = h_1 + R_M$ and $r_2 = h_2 + R_M$ are the orbital radius of the initial and final circular orbits, respectively. Equation 5.19 can also be used to compute the transfer ΔV from a circular orbit with radius r_1 to elliptical orbit with semi-major axis $a = (r_1 + r_a)/2$, as depicted on the right-side of Figure 5.18 (from orbit I to II). The transfer between two elliptical orbits, with the same periapsis radius (r_1) is depicted in the same figure. For a transfer from II to III, or vice-versa, the ΔV_e is given by:

$$\Delta V_e = \left| \sqrt{\mu_M} \left(\sqrt{\frac{2}{r_1} - \frac{1}{a_2}} - \sqrt{\frac{2}{r_1} - \frac{1}{a_1}} \right) \right| \quad (5.21)$$

where $a_1 = (r_1 + r_a)/2$ and $a_2 = (r_1 + r_2)/2$ are the semi-major axis of initial and final orbit, respectively.

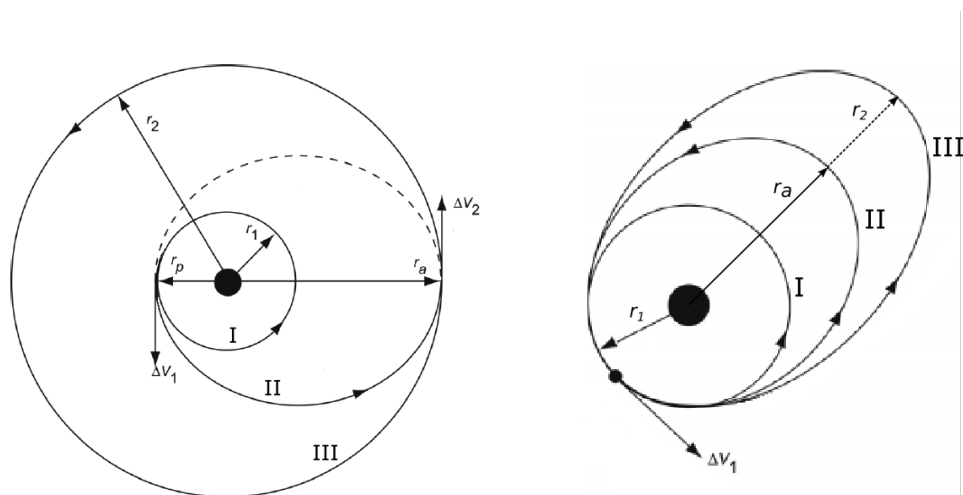


Figure 5.18: Geometry of optimal coplanar transfers: between two circular orbits (left) and between a circular and elliptical orbit or between two elliptical orbits, with the same periapsis radius (right). Adapted from Wakker (2015, p.295-296).

In order to assess the range of ΔV required for each orbital family, the following cases were studied:

- $(A)_{i=90} \rightarrow \text{SSO}$: plane change from a circular injection orbit, with $h_1 = 500$ km and $i_1 = 90^\circ$, to an **SSO**, with $h_2 = 100$ km and $i_2 > 125^\circ$. The limit inclination represents the best case scenario, in terms of ΔV , to reach an **SSO** from the injection orbit. The inclination change would have to be carried out while still in the injection orbit (A), since this orbit is larger than the largest **SSO**, and, so, v_1 in Equation 5.17 is minimal. As such, taking just into account the inclination change manoeuvre, the ΔV required to obtain an **SSO** would be > 890 m/s. Therefore, this orbit does meet evaluation criteria *EC.A.07*.
- $(A)_{i=50} \rightarrow \text{LLO, ELO or FO}$: plane change from a circular injection orbit, with $h_1 = 500$ km and

$i_1 = 50^\circ$, to a circular LLO, ELO or FO, with $i_2 = 0^\circ$ and $h_2 < 500$ km. From Equation 5.17, $\Delta V_i = 1.2$ km/s, if the orbital manoeuvre is performed when in the injection orbit. Hence, the cost to reach these orbits can also be high, which indicates that not all orbital inclinations are feasible.

- (A) →LLO: altitude change from a circular injection orbit, with $h_1 = 500$ km to a LLO, with $h_2 < 100$ km. The limiting altitude represents the best case scenario, in terms of ΔV , to reach an LLO from the injection orbit. From Equation 5.18, the transfer requires $\Delta V_c > 150$ m/s. Taking also into account the maintenance cost of at least 50 m/s, leads LLOs to not meet evaluation criteria EC.A.07.
- (A) →ELO _{$e > 0.1$} : altitude change from a circular injection orbit, with $h_1 = 500$ km to a low-eccentricity ELO, with $h_p = 500$ km and $e > 0.1$ (i.e. $h_a > 3581$ km). The limiting eccentricity represents the best case scenario to obtain an eccentric orbit, when departing from orbit (A). From Equation 5.19, the transfer requires $\Delta V > 72$ m/s. Taking also into account a maintenance cost larger than 120m/s, this leads low-eccentricity ELOs to not meet evaluation criteria EC.A.07.
- (B) →ELO _{$e < 0.7$} : altitude change from a highly eccentric injection orbit, with $h_p = 200$ km and $h_a = 15000$ km, to a highly eccentric ELO, with $h_p = 200$ km and $h_a < 10000$ km. From Equation 5.21, the transfer requires $\Delta V > 4$ m/s. However, taking into account a maintenance cost larger than 300m/s, leads highly eccentric ELOs to not meet evaluation criteria EC.A.07.
- (A) →FO: altitude change from a circular injection orbit, with $h_1 = 500$ km to a circular FO, with $h_2 = 1000$ km. From Equation 5.18, the transfer requires $\Delta V_c = 142$ m/s. As such, including a 40% margin for a small inclination change ($\approx 2^\circ$, if at 1000 km altitude), the feasibility of circular FOs ($h < 9000$ km, Table 5.1) is restricted to altitudes approximately smaller than 1000 km.

Finally, it should be noted that Elliptical Frozen Orbits could be reached with low ΔV budgets (cases (A) →ELO _{$e > 0.1$} and (B) →ELO _{$e < 0.7$}). However, as previously mentioned, these will not be considered as candidate orbits due to the variations of the lunar nightside observation time, per synodic month, typical for elliptical orbits.

Regarding CRTBP orbits, Halo L_2 orbits have been found to be the most accessible. Campagnola *et al.* (2016) has estimated $\Delta V \approx 60$ m/s, departing from an Earth-escape trajectory and performing two lunar fly-bys. A study conducted by Pontani and Teofilatto (2013) found an optimal transfer to a Lyapunov L_2 orbit with $\Delta V = 561$ m/s, using an Earth manifold to reach the cislunar space. An additional 20 m/s would be required to reach a LoPO from a Lyapunov L_2 orbit. Ozimek and Howell (2010) optimised a transfer from a high-altitude Earth parking orbit to a Vertical L_2 orbit, using low-thrust, resulting in $\Delta V \approx 600$ m/s. Finally, a transfer to a DRO can cost between 600 to 1000 m/s, departing from Earth (Ming and Shijie, 2009; Haapala *et al.*, 2014). However, these cases are not identical to the case of LUMIO, which departs from a lunar orbit. Therefore, none of these orbit types can be said compliant or non-compliant with EC.A.07 and further analysis is required.

In conclusion, the candidate orbit types that move on to the detailed evaluation are:

- **Circular Frozen Orbits**, with $h \in [100, 1000]$ km and $i \in [50, 90]^\circ$. This range of inclinations is chosen in order to avoid expensive plane change manoeuvres.
- **CRTBP L_2 Orbits**: Lyapunov, Halo, Near-Rectilinear and Vertical Orbits.
- **CRTBP Moon-centred orbits**: Distant and Low-Prograde Orbits.

Table 5.3: Trade-off between Keplerian and Perturbed Keplerian orbit types. The information within parentheses denotes the conditions correspondent to the evaluation made and the coloured assessment made in the last two columns refers to the total ΔV budget.

Orbit Type	Farside monitoring at night	Nightside observation time per synodic month (%)	Lifetime (days)	Total ΔV budget (EC.S.02)	
				Maintenance ΔV (m/s per year)	Accessibility from injection orbit
	EC.A.05	EC.S.01	EC.A.06	EC.A.06	EC.A.07
LLO	<u>green</u> Possible	<u>green</u> < 50 (best case scenario)	<u>red</u> [16, 160] ^a ($i < 90^\circ$, $h = 100$ km orbit, NSG: $n = 100$)	<u>red</u> > 50 ^b ($i \in [0, 360]^\circ$, $h = 100$ km)	<u>red</u> Low — High (> 150 m/s, from circular $h = 500$ km to $h = 100$ km)
ELO	<u>green</u> Possible	<u>red</u> [8, 92] (function of line of nodes angle with Sun direction; $h_a = 10000$ km, $i = 0^\circ$ and $e = 0.74$)	<u>yellow</u> [140; 1000] ^c (function of decreasing e , from 0.45 to 0; $a = 7000$ km)	<u>red</u> > [120, 300] ^b ($i = 0^\circ$, $e = [0.1, 0.73]$, $a \approx 7000$ km)	<u>red</u> Low — High (> 72 m/s, from circular to elliptical; or > 4 m/s, between elliptic)
FO	<u>green</u> Possible	<u>green</u> If circular: < 50 (best case scenario: low-altitude)	<u>green</u> > 1000 ^d ($e = 0$, $i = 78^\circ$, $h = 100$ km)	<u>yellow</u> 0 ^b ($i = 40^\circ$, $e = 0.6$, 880×8800 km)	<u>yellow</u> Low — High (> 142 m/s, from circular $h = 500$ km to $h = 1000$ km)
SSO	<u>green</u> Possible	<u>green</u> < 50	<u>yellow</u> ≈ 300 ^a ($i = 100^\circ$, $h = 100$ km)	<u>red</u> > 50 ^b ($i \in [0, 360]^\circ$, $h = 100$ km)	<u>red</u> High (> 890 m/s, from $i = 90^\circ$ to $i = 125^\circ$, at circular $h = 100$ km)

^aRamanan and Adimurthy (2005) ^bWhitley and Martinez (2016) ^cde Almeida Prado (2003) ^dElpe and Lara (2003)

Legend: green Meets evaluation criteria yellow Can meet evaluation criteria during detailed analysis red Does not meet evaluation criteria

Accessibility ΔV : Low \rightarrow < 200 m/s Medium \rightarrow [200, 600] m/s High \rightarrow > 600 m/s

Table 5.4: Trade-off between CRTBP orbit types. The information within parentheses denotes the conditions correspondent to the evaluation made and the coloured assessment made in the last two columns refers to the total ΔV budget.

Orbit Type	Farside monitoring at night	Nightside observation time per synodic month (%)	Total ΔV budget (EC.S.02)	
			Maintenance ΔV (m/s per year)	Accessibility from injection orbit
	EC.A.05	EC.S.01	EC.A.06	EC.A.07
LO	<u>green</u> Possible if L_2 orbit	<u>green</u> < 50 (small orbit)	<u>yellow</u> [15; 18] ^a (L_2 orbit)	<u>yellow</u> Medium ^b (561 m/s coming from Earth manifold)
HO (including NROs)	<u>green</u> Possible if L_2 orbit	<u>green</u> < 50 (Halo or NROs not too close to the Moon)	<u>yellow</u> [0; 55] ^a (L_2 orbit, smaller for orbits closer to the Moon)	<u>yellow</u> Low ^c (\approx 60 m/s, departing from Earth-escape trajectory)
VO	<u>green</u> Possible if L_2 orbit	<u>green</u> < 50 (small orbit)	<u>yellow</u> \sim 88 ^d (L_2 orbit, not optimised)	<u>yellow</u> Low – Medium ^e (\approx 600 m/s from high-altitude Earth parking orbit, with low-thrust engine)
DRO	<u>green</u> Possible	<u>green</u> < 50 (resonant state)	<u>yellow</u> [3, 5] ^a (large orbit)	<u>yellow</u> Medium – High ^{f,g} ([600, 1000] m/s from Earth, not optimised)
LoPO	<u>green</u> Possible	<u>green</u> < 50 (resonant state)	<u>yellow</u> Unknown	<u>yellow</u> Medium ^b (\approx 20 m/s from Lyapunov Orbit)

^a Folta *et al.* (2015) ^b Pontani and Teofilatto (2013) ^c Campagnola *et al.* (2016) ^d Grebow *et al.* (2008) ^e Ozimek and Howell (2010) ^f Haapala *et al.* (2014)

^g Ming and Shijie (2009)

Legend: green Meets evaluation criteria yellow Can meet evaluation criteria during detailed analysis red Does not meet evaluation criteria

Accessibility ΔV : Low \rightarrow < 200 m/s Medium \rightarrow [200, 600] m/s High \rightarrow > 600 m/s

References

- K. F. Wakker, *Fundamentals of Astrodynamics* (Delft University of Technology, Institutional Repository Library, Delft, 2015).
- F. Topputo, M. Vasile and A. E. Finzi, *An approach to the design of low energy interplanetary transfers exploiting invariant manifolds of the restricted three-body problem*, *Advances in the Astronautical Sciences* **119**, 2229 (2005).
- Z. E. Musielak and B. Quarles, *The three-body problem*, *Reports on Progress in Physics* **77**, 065901 (2014), [arXiv:1508.02312](https://arxiv.org/abs/1508.02312) .
- J. R. Wertz, *Orbit & Constellation Design & Management* (Microcosm Press; Springer, 2009).
- R. Whitley and R. Martinez, *Options for Staging Orbits in Cislunar Space*, in *IEEE Aerospace Conference Proceedings* (2016).
- A. Abad, A. Elipe and E. Tresaco, *Analytical Model to Find Frozen Orbits for a Lunar Orbiter*, *Journal of Guidance, Control, and Dynamics* **32**, 888 (2009).
- J. P. S. Carvalho, R. Vilhena de Moraes and A. F. B. A. Prado, *Some orbital characteristics of lunar artificial satellites*, *Celestial Mechanics and Dynamical Astronomy* **108**, 371 (2010).
- T. A. Ely, *Stable constellations of frozen elliptical inclined lunar orbits*, *Journal of the Astronautical Sciences* **53**, 301 (2005).
- R. P. Russell, *Survey of Spacecraft Trajectory Design in Strongly Perturbed Environments*, *Journal of Guidance, Control, and Dynamics* **35**, 705 (2012).
- A. Elipe and M. Lara, *Frozen Orbits About the Moon*, *Journal of Guidance, Control, and Dynamics* **26**, 238 (2003).
- S. Park and J. Junkins, *Orbital mission analysis for a lunar mapping satellite*, *AAS/AIAA Astrodynamics Specialist Conference* (1994), [doi:10.2514/6.1994-3717](https://doi.org/10.2514/6.1994-3717).
- J. P. D. S. Carvalho, R. V. De Moraes and A. F. B. De Almeida Prado, *Nonsphericity of the moon and near sun-synchronous polar lunar orbits*, *Mathematical Problems in Engineering* **2009** (2009), [10.1155/2009/740460](https://doi.org/10.1155/2009/740460).
- D. C. Folta, N. Bosanac, D. Guzzetti and K. C. Howell, *An earth-moon system trajectory design reference catalog*, *Acta Astronautica* **110**, 341 (2015).
- D. J. Grebow, M. T. Ozimek, K. C. Howell and D. C. Folta, *Multi-body orbit architectures for lunar south pole coverage*, *Journal of Spacecraft and Rockets* **45**, 334 (2008).
- R. W. Farquhar and A. A. Kamel, *Quasi-periodic orbits about the translunar libration point*, *Celestial Mechanics* **7**, 458 (1973).
- R. Thurman and P. A. Worfolk, *The geometry of halo orbits in the circular restricted three-body problem*, Tech. Rep. (The Geometry Center, University of Minnesota, 1996).
- D. L. Richardson, *Analytic construction of periodic orbits about the collinear points*, *Celestial Mechanics* **22**, 241 (1980).

- J. V. Breakwell and J. Brown, *The halo family of 3-dimensional periodic orbits in the Earth-Moon restricted 3-body problem*, *Celestial Mechanics* **20**, 389 (1979).
- R. W. Farquhar, *A halo-orbit lunar station*, *Astronautics and Aeronautics* **10**, 59 (1972).
- K. C. Howell and J. V. Breakwell, *Almost rectilinear halo orbits*, *Celestial Mechanics* **32**, 29 (1984).
- R. Whitley, R. Martinez, G. Condon, J. Williams *et al.*, *Cislunar Near Rectilinear Halo Orbits for Human Space Exploration*, in *AIAA SPACE 2016* (NASA Johnson Space Center, 2016).
- M. Hénon, *Numerical exploration of the restricted problem*, *Astronomy and Astrophysics* **9**, 24 (1970).
- X. Ming and X. Shijie, *Exploration of distant retrograde orbits around Moon*, *Acta Astronautica* **65**, 853 (2009).
- G. Turner, *Results of Long-Duration Simulation of Distant Retrograde Orbits*, *Aerospace* **3**, 37 (2016).
- F. Bernelli-Zazzera, F. Topputo and M. Massari, *Assessment of mission design including utilization of libration points and weak stability boundaries*, Tech. Rep. (Ariadna Study, ESA, 2004).
- E. J. Doedel, V. A. Romanov, R. C. Paffenroth, H. B. Keller *et al.*, *Elemental periodic orbits associated with the libration points in the circular restricted 3-body problem*, *International Journal of Bifurcation and Chaos* **17**, 2625 (2007).
- D. Guzzetti, N. Bosanac, A. Haapala, K. C. Howell *et al.*, *Rapid trajectory design in the Earth-Moon ephemeris system via an interactive catalog of periodic and quasi-periodic orbits*, *Acta Astronautica* **126**, 439 (2016).
- R. V. Ramanan and V. Adimurthy, *An analysis of near-circular lunar mapping orbits*, *Journal of Earth System Science* **114**, 619 (2005).
- A. F. B. de Almeida Prado, *Third-Body Perturbation in Orbits Around Natural Satellites*, *Journal of Guidance, Control, and Dynamics* **26**, 33 (2003).
- S. Campagnola, N. Ozaki, K. Oguri, Q. Verspieren *et al.*, *Mission Analysis for EQUULEUS, JAXA's Earth-Moon Libration Orbit Cubesat*, in *67th International Astronautical Congress* (2016).
- M. Pontani and P. Teofilatto, *Low-energy Earth-Moon transfers involving manifolds through isomorphic mapping*, *Acta Astronautica* **91**, 96 (2013).
- M. Ozimek and K. C. Howell, *Low-thrust transfers in the earth-moon system including applications to libration point orbits*, *Journal of Guidance, Control, and Dynamics* **33**, 533 (2010).
- A. F. Haapala, M. Vaquero, T. a. Pavlak, K. C. Howell *et al.*, *Trajectory Selection Strategy for Tours in the Earth-Moon System*, *Advances in the Astronautical Sciences* **150**, 1151 (2014).

6

Orbit, Payload and Environment

This chapter is dedicated to introducing the models that will be used for the lunar meteoroid impact flashes' coverage analysis (Chapter 7), as well as how they have been implemented. First, it is necessary to generate the candidate orbits, which have been determined from the Preliminary Orbital Trade-off (see Chapter 5, Section 5.3). For that purpose, the astrodynamics models presented in Chapter 5 will be used. Their implementation, validation and results obtained are discussed in Section 6.2. Second, it is necessary to model the payload, the LUMIO-Cam, as will be presented in Section 6.3. This includes modelling both optics and detector, in order to determine the instrument's FOV and the ranges of signals it can detect. Finally, it is necessary to relate the detectable signal range with the kinetic energy range of the impactors and the instrument's FOV-area with the total number of meteoroid impacts that can be observed. This requires modelling both the impact phenomenon and the meteoroid flux environment, as will be detailed in Section 6.4. The reference frames that will be used are introduced in Section 6.1.

6.1. Reference Frames

The position and velocity of a spacecraft are always determined with respect to a certain *reference frame*. The classification of reference frames adopted is the same as the one defined in SPICE, a toolkit developed by NAIF¹ with a MATLAB® interface. This toolkit is used widely for Solar System geometry computations and includes the functionality to compute transformations between all of the reference frames presented in this section. The two main classes of reference frames defined in SPICE are: inertial and non-inertial.

Inertial Reference Frames

An *inertial* reference frame is fixed with respect to the stars, as it does not rotate, and its origin has none (or negligible) acceleration. Inertial reference frames are typically used to describe the motion of spacecraft about a body. For example, in the TBP, an Earth-centred non-rotating reference frame can be considered inertial when used to describe the motion of a spacecraft about the Earth, while a Sun-centred non-rotating frame can be considered inertial when used to describe the motion of a spacecraft (or planet) about the Sun.

¹<https://naif.jpl.nasa.gov/naif/> [Last accessed on: 12/08/2017]

The *Earth mean equator and equinox of J2000 reference frame* (also known as the *J2000 reference frame*) is a commonly used non-rotating inertial reference frame. The reference frame is defined when centred at Earth, but its origin can be placed where most appropriate (in LUMIO's case, it shall be the Moon). As depicted in Figure 6.1, the XY-plane is coincident with Earth's equatorial plane, the Z-axis is approximately the Earth's spin axis and the X-axis points to the *First Point of Aries* (or *vernal equinox*), at epoch J2000 TDB². The Y-axis completes the right-handed reference frame. The First Point of Aries is not fixed with respect to the stars, due to the motion of the equator and ecliptic, caused by the gravitational attraction of other bodies of the Solar System. Therefore, an epoch, the J2000 TDB, is necessary to define the inertial reference frame. This reference frame is already implemented in the toolkit SPICE. It will be used to integrate the TBP equations of motion and store all the orbits generated in a *Spacecraft and Planets Kernel (SPK)*, SPICE's file type used to store ephemerides.

The *Body Mean Equator of Date frame* (BME_{t_0}) is another inertial reference frame, with respect to which Keplerian orbital elements will be defined. The XY-plane is defined by the body's (Moon) equator of date and the +Z axis is approximately the body's rotation axis of date. The X-axis is defined by the intersection of the body's equator of date with the Earth Mean Equator of J2000 and the Y-axis completes the right-handed frame. The reference frame is used centred at the Moon and the epoch chosen to fix it, t_0 , is the starting date of the operational mission. This reference frame is not implemented in SPICE, but can be defined using a *Frames Kernel (FK)*. The FK used is the same that was used for the lunar SMART-1 mission, and is publicly available in SPICE's database¹.

Finally, the *Body-Mean Orbital Plane of Date frame* ($BMOP_{t_0}$) will be used to define CRTBP orbits, with respect to inertial space. The XY-plane is defined by the body's orbital plane of date and the X-axis points from the central body to the orbiting body. The component orthogonal to the X-axis of the inertially referenced velocity of the body, with respect the central body, defines the Y-axis direction. The Z-axis is in the direction of the body's angular momentum vector (\mathbf{H}) and completes the right-handed frame. If the Moon is the orbiting body and the Earth is the central body, this reference frame is identical to the Earth-Moon CRTBP reference frame (Chapter 5, Figure 5.1), fixed at an epoch t_0 . Once again, the reference frame is used centred at the Moon and the epoch chosen is the starting date of the operational mission. The FK used is adapted from a Geocentric Solar Ecliptic reference frame, publicly available in SPICE's website¹.

As depicted in Figure 6.1, the orbital plane of the Moon is approximately 5° inclined with respect to the ecliptic, which in turn is 23° inclined with respect to Earth's equator. This means that the inclination of the XY-plane of $BMOP_{t_0}$ with respect to the J2000's XY-plane varies between 18° and 28°, as the Moon's line of nodes precesses. The XY-plane of BME_{t_0} (lunar equator) is inclined with respect to the XY-plane of $BMOP_{t_0}$ (lunar orbital plane) by a constant value of approximately 7°. (Wakker, 2015, p.412)

Non-Inertial Reference Frames

A *non-inertial* reference frame has an accelerated origin and/or a rotational motion with respect to the stars. Two types of non-inertial reference frames will be briefly described: the *body-fixed* reference frame and the *spacecraft* reference frame.

Body-Fixed Reference Frame Usually centred at a natural body, the body-fixed reference frame rotates with the same angular velocity as the body to which it is attached. It is used to describe the position of a spacecraft relative to the body's surface. Two body-fixed frames defined by the **Lunar**

²January 1st, 2000 at 12:00:00 [Barycentric Dynamical Time](#)

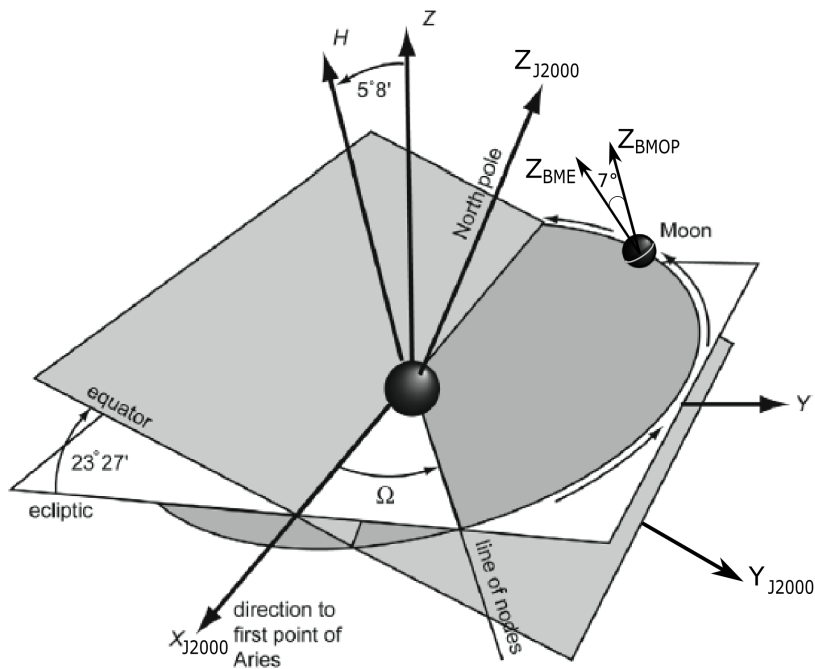


Figure 6.1: Mean equinox of J2000 reference frame. Adapted from Wakker (2015, p.411).

Geodesy and Cartography Working Group and Lunar Reconnaissance Orbiter Project (2008) will be used.

The first, is the Moon-centred *Mean Earth/Polar Axis Lunar reference frame (ME)*. The Z-axis is defined as the mean lunar axis of rotation and the reference great circle passing through the poles (i.e. the *Prime Meridian*) is defined by the Earth's mean direction, which is fixed, due to the Moon being tidally locked to the Earth. The point at which the lunar equator and the Prime Meridian intersect is called the *mean sub-Earth point*. The X-axis points to the mean sub-Earth point and the Y-axis completes the right-handed frame.

However, the actual lunar sub-Earth point varies on the lunar surface, due to the *geometric lunar libration* phenomena (see Wakker, 2015, p.413). Nonetheless, this reference frame is implemented in SPICE with a high precision lunar orientation model, and will be used to project the spacecraft's FOV onto the lunar surface.

The spherical coordinate system in the Mean Earth/Polar Axis Lunar reference frame is depicted in Figure 6.2 and is given by:

- the planetocentric *longitude* (Λ) - angle measured along the lunar equator, between the mean sub-Earth point and the spacecraft, from 0° to 360° , in the eastward direction;
- the planetocentric *latitude* (Φ) - angle measured between the lunar equatorial plane and the spacecraft, from -90° to 90° , positive north of the equator and negative south;
- the distance between the lunar centre of mass and the spacecraft.

The second body-fixed frame is the Moon-centred *Principal Axis reference frame (PA)*, whose axes are defined by the principal axes of the Moon. This reference frame would coincide with the ME reference frame if the Moon were a truly synchronously rotating triaxial ellipsoid. The PA is also implemented in SPICE and will be used to compute the Moon's NSG perturbation.

Spacecraft Reference Frame The spacecraft reference frame is a spacecraft-fixed frame which is centred at its structure. LUMIO's spacecraft bus reference frame has been defined as depicted in Figure 6.3. The X-axis points in the direction of the main engine. The Y-axis points normal to a side panel and its direction will coincide with the direction of motion. The Z-axis points to the top panel, completing the right-handed reference frame. It is also possible to define a LUMIO-Cam fixed reference frame, with respect to the spacecraft bus frame. The instrument is mounted along the negative direction of the spacecraft X-axis and its frame is rotated -90 degrees about spacecraft Y-axis, as depicted in Figure 6.3. Both of these frames will be used to define the spacecraft's attitude and have been implemented in SPICE using an FK. The latter will also be used to define the instrument's FOV.

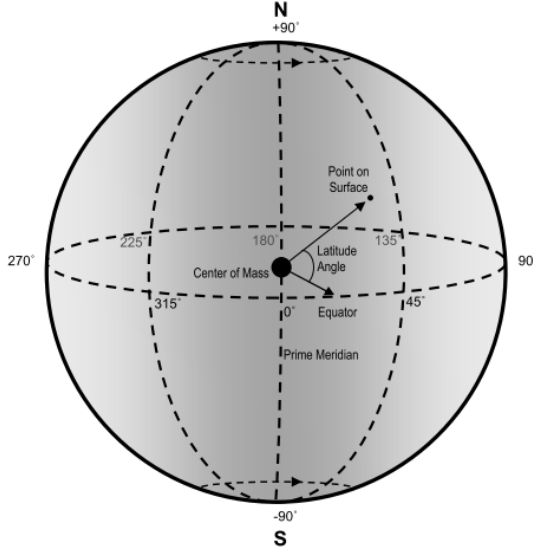


Figure 6.2: Mean Earth/Polar Axis Lunar (ME) coordinate system. From the Lunar Geodesy and Cartography Working Group and Lunar Reconnaissance Orbiter Project (2008).

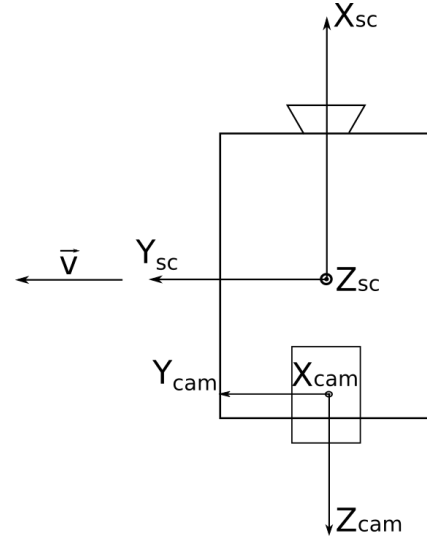


Figure 6.3: LUMIO's Spacecraft Bus and LUMIO-Cam reference frame.

6.2. Orbit Generation

6.2.1. Perturbed Two-Body Problem Orbits

In order to generate the candidate Frozen Orbits (FOs), the equations of motion for a perturbed TBP orbit (Equation 5.12) are integrated as a first order system:

$$\dot{\mathbf{x}} = \begin{bmatrix} v_x \\ v_y \\ v_z \\ -\frac{x}{r^3} - \mu_E \left(\frac{x_E}{r_E^3} - \frac{x_E - x}{||r_E - r||^3} \right) - C\nabla_x U_{NSG} \\ -\frac{y}{r^3} - \mu_E \left(\frac{y_E}{r_E^3} - \frac{y_E - y}{||r_E - r||^3} \right) - C\nabla_y U_{NSG} \\ -\frac{z}{r^3} - \mu_E \left(\frac{z_E}{r_E^3} - \frac{z_E - z}{||r_E - r||^3} \right) - C\nabla_z U_{NSG} \end{bmatrix} \quad (6.1)$$

where $\mathbf{x} = [x, y, z, v_x, v_y, v_z]^T$ is the state vector, $r = \sqrt{x^2 + y^2 + z^2}$ and $r_E = \sqrt{x_E^2 + y_E^2 + z_E^2}$.

In order to compute Earth's Third-Body perturbation, the position of the Earth with respect to the

Moon, for a certain epoch t , is computed using function *cspice_spkpos* of SPICE. Furthermore, the planetary ephemerides used are the *de430* (SPK-file). These are not the latest ephemerides available in SPICE's database, but are the ephemerides with which the lunar **ME** and **PA** references frames have been implemented in the toolkit.

The spacecraft's acceleration due to the Moon's **Non-Spherical Gravity** is computed using a MATLAB[®] user developed function (Aguiar, 2017), based on Gottlieb (1993), and will be validated against MATLAB[®]'s own spherical harmonics function (*gravitysphericalharmonic*). The former has been chosen due to its higher computational speed. Nonetheless, computing the Moon's spherical harmonics still is the most computationally expensive part of the Frozen Orbit's generation code. For that reason, the model is restricted to a low order and degree: 7. Furthermore, most lunar **FOs** have been computed taking only into account zonal terms up to degree 7 (see Chapter 5, Subsection 5.2.2). Sectorial and tesseral harmonics ($m = n \neq 0$ and $m \neq n \neq 0$, respectively) have also been included, because a study by Carvalho *et al.* (2010) has shown that they can influence significantly the satellite's motion, to the point that it could collide with the lunar surface or not. The gravity model used is the GL0660B. This model is derived in Konopliv *et al.* (2013), with data from the GRAIL mission, and has been made publicly available by NASA³.

Methodology

The initial conditions to generate a frozen orbit will be computed numerically, following a method similar to the one applied in Ely (2005). As such, in order to determine the initial eccentricity, $e_{0,\text{frozen}}$, of a Frozen Orbit with semi-major axis a_0 and inclination i_0 , the following methodology will be followed:

1. Define N guesses of frozen initial conditions as orbital elements, in the BME_{t_0} reference frame, one for each of N possible eccentricities $e_0 = [e_{0,1}, \dots, e_{0,j}, \dots, e_{0,N}]$;
2. Transform the initial conditions to Cartesian coordinates, in the **J2000** reference frame;
3. Adimensionalize and propagate the initial conditions for 14.5 days, in the Moon-centred **J2000** reference frame, with the dynamics given by Equation 6.1;
4. Compute the osculating orbital elements, in the BME_{t_0} reference frame;
5. Determine the maximum (peak-to-peak) amplitude of the osculating eccentricity, for each initial condition:

$$\Delta e_j = \max_t(e_j(t)) - \min_t(e_j(t))$$

6. Determine the frozen eccentricity e_0 that leads to the minimum Δe :

$$e_{0,\text{frozen}} = \arg \min_{e_{0,j}}(\Delta e)$$

The frozen initial conditions found are then propagated again in the **J2000** reference frame, but now for $S_M = 29.5$ days, in order to perform the coverage analysis that will follow. The determination of the frozen initial conditions is only done with a shorter propagation period to speed up the algorithm. Furthermore, it should be noted that this methodology does not guarantee the boundedness of i , a , ω or Ω . As such, it will be necessary to verify if the orbits found are frozen for these orbital elements. Finally, the orbits are stored in an **SPK**, using the SPICE utility *mkspk.exe*.

³GL0660B model, version of 6/13/2013, available at: http://pds-geosciences.wustl.edu/grail/grail-1-lgrs-5-rdr-v1/grail_1001/shadr/jggrx_0660b_sha.tab [Last accessed on: 31/05/2017]

Verification

In order to verify the correct implementation of the MATLAB[®] user developed function that computes the Moon's **Non-Spherical Gravity**, MATLAB[®]'s *gravitysphericalharmonic* has been used. An orbit with initial orbital elements $a = 1873$ km, $i = 90^\circ$, $e = 0$ and $\Omega = \omega = 0^\circ$ has been propagated for 1 day, taking only into account the Moon's **NSG** up to degree and order 7. The final state obtained, using each function to compute the Moon's **NSG**, is presented in Table 6.1 and the osculating orbital elements are presented in Figure 6.4. It can be concluded that the results obtained with the user developed function do not differ significantly from MATLAB[®]'s function: the error in the final position is $\sim 10^{-5}$ meters and the error in velocity $\sim 10^{-8}$ meters per second. As such, the user developed function can be considered correctly implemented. Furthermore, the user developed function's calls took 0.561 s, while MATLAB[®]'s function's calls took 12.32 s, which proves that the former can be 95% less computationally expensive.

Table 6.1: Validation of the spherical harmonics function used to compute the Moon's **Non-Spherical Gravity**. The initial state corresponds to a lunar orbit with orbital elements $a = 1873$ km, $i = 90^\circ$, $e = 0$ and $\Omega = \omega = 0^\circ$. The final state corresponds to a propagation of 1 day, taking only into account the Moon's **NSG** up to degree and order 7. The first digit for which the user developed function and MATLAB[®]'s *gravitysphericalharmonic* differ is denoted in bold.

		Initial State	Final State		
			MATLAB [®] 's	User Developed	Difference
r (km)	x	1838	332.7398832 6 52	332.7398832 7 80	$1.28 \cdot 10^{-8}$
	y	0	3.898869052 7 04	3.898869052 7 53	
	z	0	1803.7122086 4 9	1803.7122086 4 7	
v (km/s)	v_x	0	-1.609878766 7 22	-1.609878766 7 19	$1.15 \cdot 10^{-11}$
	v_y	$1.00006955149 \cdot 10^{-16}$	$-6.256845259438 \cdot 10^{-3}$	$-6.256845259413 \cdot 10^{-3}$	
	v_z	1.633237521524	0.2926391928 0 41	0.2926391928 1 55	

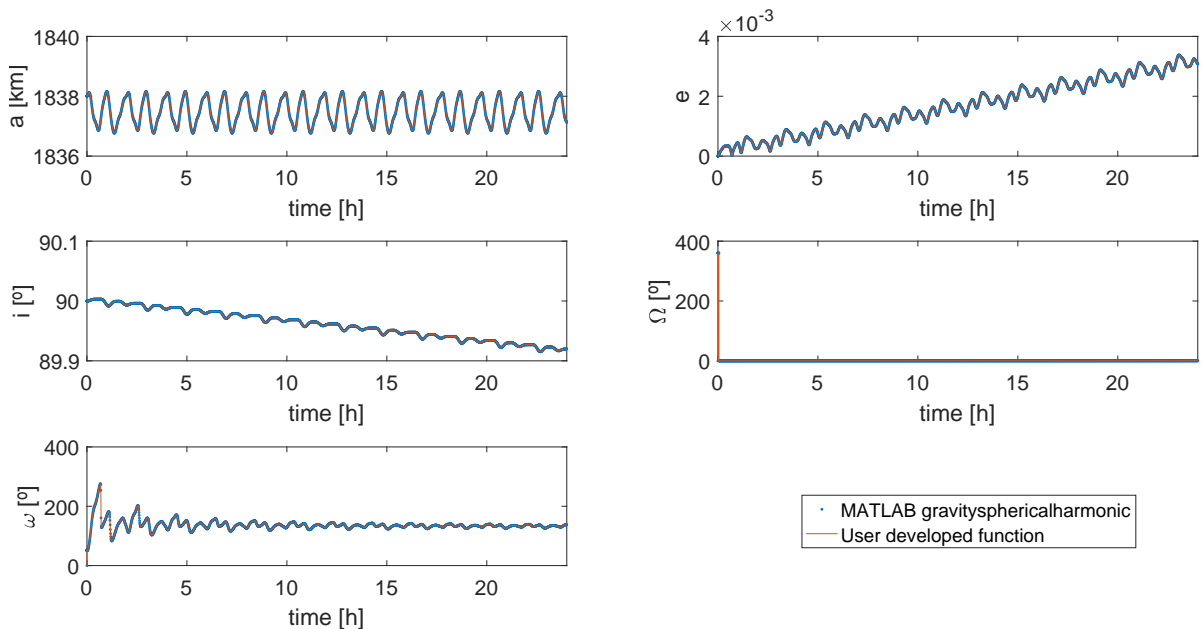


Figure 6.4: Validation of the spherical harmonics function used to compute the Moon's **Non-Spherical Gravity**. The initial orbital elements correspond to $a = 1873$ km, $i = 90^\circ$, $e = 0$ and $\Omega = \omega = 0^\circ$. These have been propagated for 1 day, taking only into account the Moon's **NSG** up to degree and order 7.

In order to verify the correct implementation of the Frozen Orbit generation code, a [NASA](#) software, the [General Mission Analysis Tool \(GMAT\)](#), has been used. An orbit with initial orbital elements $a = 1973$ km, $i = 45^\circ$, $e = 0.05$, $\Omega = 0^\circ$ and $\omega = 90^\circ$ has been propagated for 28 days, taking into account the Moon's [NSG](#) up to degree and order 7 and the Earth's [TB](#) perturbation. For the validation only, a different lunar [NSG](#) model and body-fixed frame have been used. The lunar gravity model used was the LP165P ([Konopliv, 2001](#)), which is already implemented in [GMAT](#). Furthermore, the body-fixed frame used was the IAU_MOON, which is less precise than the [PA](#) reference frame. However, [GMAT](#) does not allow the implementation of body-fixed frames as precise as the [PA](#) reference frame.

The final state obtained with [GMAT](#) and the developed code is presented in Table 6.2. The osculating orbital elements for the last day of propagation are presented in Figure 6.5. In Table 6.2, one should notice that the initial conditions provided to [GMAT](#) and the MATLAB[®] code are not identical. This is due to the transformations between reference frames internal to [GMAT](#). Nonetheless, the results obtained with the developed code do not differ significantly from those of [NASA's](#) validated software: the error in the final position is ~ 1 meter and the error in velocity $\sim 10^{-3}$ meters per second. As such, the developed software can be considered correctly implemented.

Table 6.2: Validation of the [Frozen Orbit](#) generation software. The initial state corresponds to a lunar orbit with orbital elements $a = 1973$ km, $i = 45^\circ$, $e = 0.05$, $\Omega = 0^\circ$ and $\omega = 90^\circ$. The final state corresponds to a propagation of 28 days, taking into account the Moon's [NSG](#) up to degree and order 7 and the Earth's [TB](#) perturbation. The first digit for which the [GMAT](#) and the MATLAB[®] developed code differ is denoted in bold.

		Initial State		
		GMAT	MATLAB	Difference
r (km)	x	6.01663836 27 $\cdot 10^{-2}$	6.01663836 30 $\cdot 10^{-2}$	$7.85 \cdot 10^{-12}$
	y	675.937223818910	675.937223818903	
	z	1712.52972991303	1712.52972991303	
v (km/s)	v_x	-1.672161016096	-1.672161016096	$3.34 \cdot 10^{-17}$
	v_y	1.4884204870124 8 $\cdot 10^{-4}$	1.4884204870121 8 $\cdot 10^{-4}$	
	v_z	1.11022302462516 $\cdot 10^{-16}$	9.52400673290954 $\cdot 10^{-17}$	

		Final State		
		GMAT	MATLAB	Difference
r (km)	x	478.997664837545	478.99 8 975276827	$1.39 \cdot 10^{-3}$
	y	600.179744592635	600.179 2 86521803	
	z	1686.79629586614	1686.79613797141	
v (km/s)	v_x	-1.55821773562385	-1.55821742517637	$1.20 \cdot 10^{-6}$
	v_y	0.545172219475365	0.545172607369548	
	v_z	0.188863455197148	0.188864547571678	

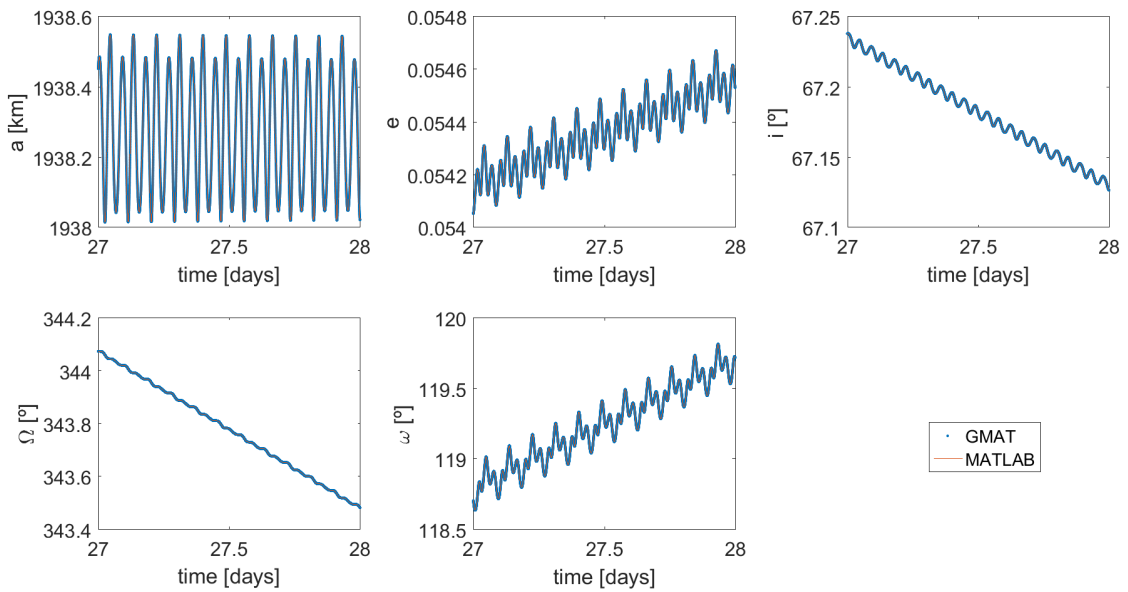


Figure 6.5: Validation of the frozen orbits' generation software with **GMAT**. The initial orbital elements correspond to $a = 1973$ km, $i = 45^\circ$, $e = 0.05$, $\Omega = 0^\circ$ and $\omega = 90^\circ$. These have been propagated for 28 days, taking into account the Moon's **NSG** up to degree and order 7 and the Earth's **TB** perturbation.

Results and Validation

The Frozen Orbits chosen as candidates were:

- $\omega = 90^\circ$ or $\omega = 270^\circ$;
- a between 1838 and 2738 km ($100 < h_0 < 1000$ km), with a step size of 100 km;
- i between 50° and 90° , with a step size of 10° ;
- $\Omega = 0^\circ$.

For each of these orbits, the initial guess for a frozen eccentricity ranged from $1 \cdot 10^{-6}$ to 0.06 ([Abad et al., 2009](#)), with $N = 10$ (step size ≈ 0.0067). Higher eccentricities are not tested because the preliminary trade-off of Chapter 5 showed that circular orbits are preferred. Furthermore, a minimum desired periaxis altitude has been set as $h_p = 30$ km. The starting epoch for the operational mission has been chosen as $t_0 = 01$ Jan 2020 12:00:00.000 (**TDB**).

Figure 6.6 shows the maximum amplitude of the osculating eccentricity and inclination, for some of the candidate orbits. These are representative of the results obtained at the end of Step 5 of the methodology presented. From these results it can be concluded that:

- Frozen orbits are more stable for higher altitudes, as Δe and Δi are lower;
- Slightly eccentric orbits are more stable than almost circular orbits, as Δe is lower, especially for $i = 80^\circ$ (bottom-left plot). However, for lower altitudes, Frozen Orbits need to be almost circular ($e < 0.027$), otherwise $h_p < 30$ km;
- Orbits with $i_0 = 50^\circ$ have $\Delta e < 0.01$, while orbits with $i_0 = 80^\circ$ have $\Delta e < 0.025$. So, the latter are less stable. This is due to the fact that $i_0 = 80^\circ$ is approximately a critical inclination of both low and high altitude frozen orbits (see Table 5.1);
- The inclination of the orbits can be considered frozen, as $\Delta i \in [0.5, 1.4]^\circ$.

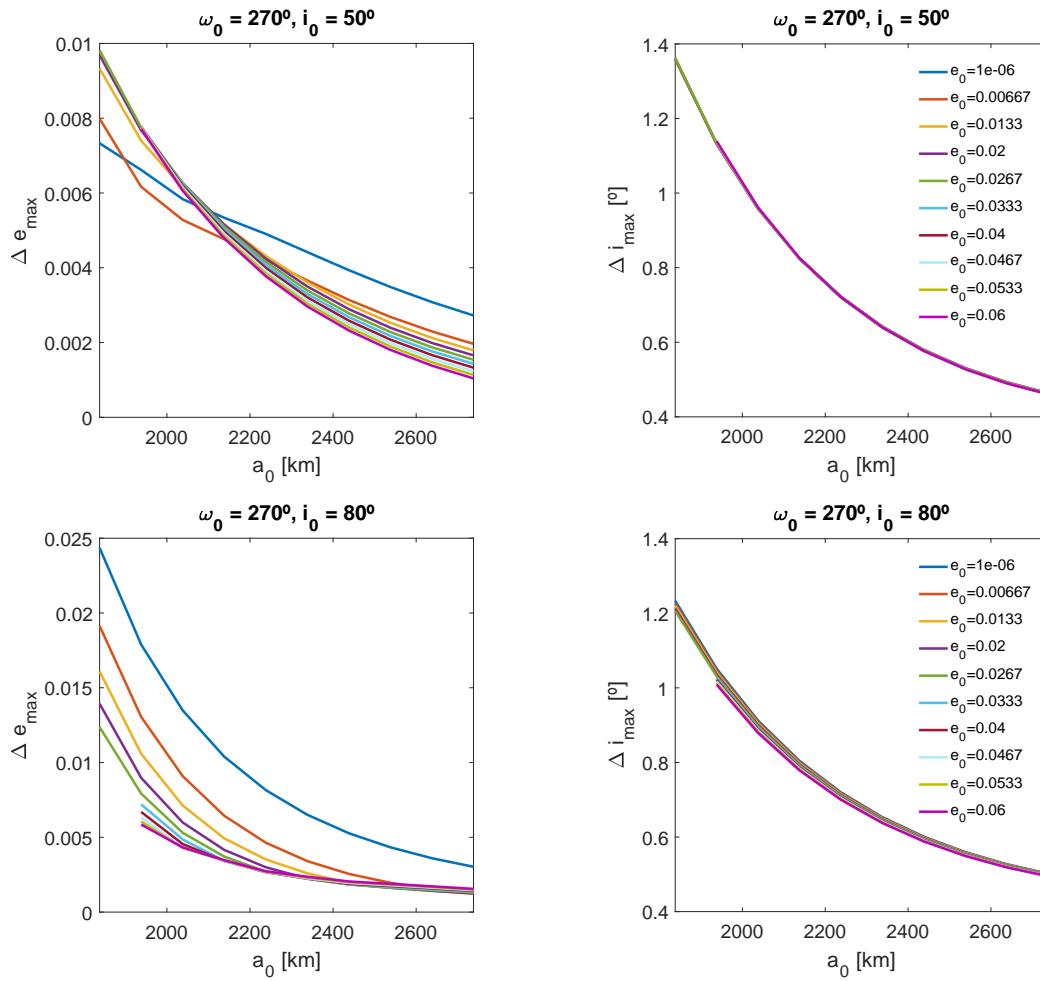


Figure 6.6: Maximum amplitude of the osculating eccentricity and inclination, for $1838 \leq a \leq 2738$ km, $\omega = 270^\circ$ and $i = 50^\circ$ (top) or $i = 80^\circ$ (bottom). The orbits have been propagated for 14.5 days and orbits whose periapsis lowers to < 30 km altitude are not represented.

Figure 6.7 shows the frozen eccentricity obtained with the methodology presented, for each combination of a_0 , i_0 and ω_0 . Figure 6.8 shows the maximum amplitude of the osculating eccentricity and inclination for these orbits, integrated for a longer period (29.5 days). From these plots, and in agreement with the previously stated, it can be concluded that:

- Frozen Orbits are more stable for higher altitudes, as Δe and Δi are lower (Figure 6.8);
- For $60^\circ < i < 80^\circ$ and $\omega = 90^\circ$ or $50^\circ < i < 70^\circ$ and $\omega = 270^\circ$, the frozen orbits are indeed slightly more eccentric orbits. The exception are lower altitude orbits ($h = 100$ km), which are almost circular ($e < 0.02$) due to the $h_p > 30$ km limit. Furthermore, for $i = 90^\circ$, Frozen Orbits are also almost circular, for all altitudes (Figure 6.7);
- Orbits with $i_0 = 50^\circ$, $i_0 = 60^\circ$ or $i_0 = 90^\circ$ have $\Delta e < 0.015$, while orbits with $70^\circ < i < 80^\circ$ have $\Delta e < 0.035$. So, once again, the latter are less stable, due to the proximity to the critical inclination (Figure 6.8);
- The inclination of the orbits can also be considered frozen for almost one month, as $\Delta i \in [0.5, 1.5]^\circ$ (Figure 6.8).

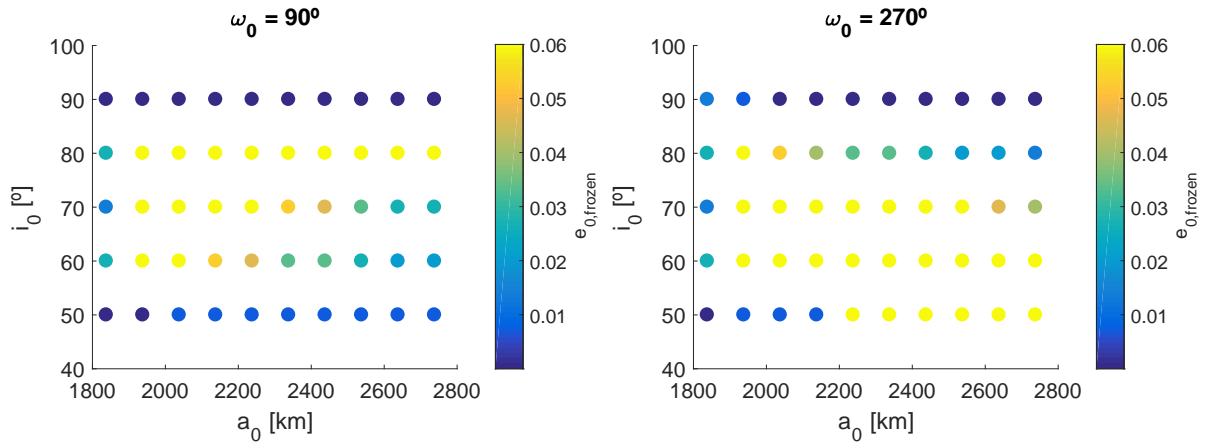


Figure 6.7: Frozen orbits' initial conditions obtained with the methodology presented. Orbits have been propagated for 14.5 days.

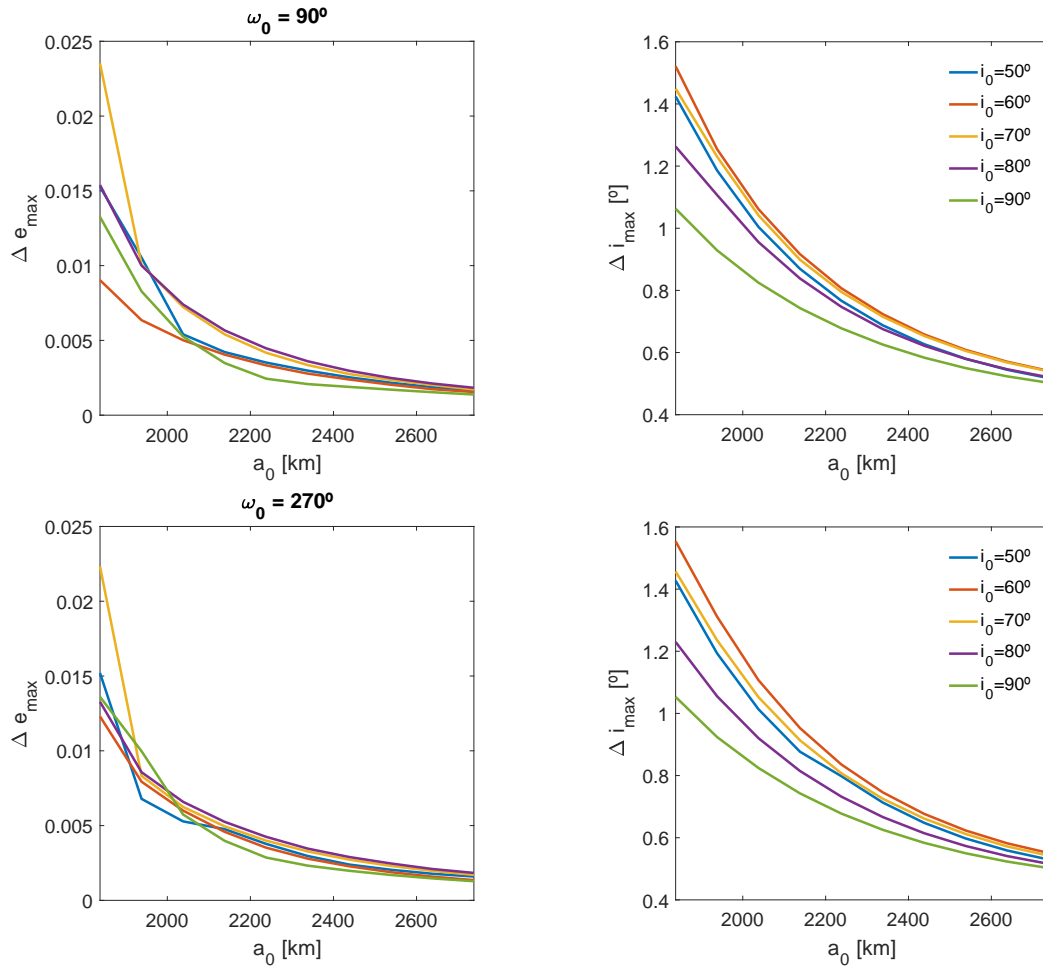


Figure 6.8: Frozen orbits' osculating eccentricity and inclination maximum amplitude. Orbits have been propagated for $S_M \approx 29.5$ days.

As one can observe, the order of magnitude of the bounds of Δe and Δi do not differ significantly from an integration period of 14.5 to 29.5 days: the Δi range increases from $[0.5, 1.4]^\circ$ to $[0.5, 1.5]^\circ$ and Δe remains < 0.025 . Additionally, Figure 6.9 shows some representative Frozen Orbits, where it

can also be verified that Δa is bounded, while $\Delta \Omega$ is not. For a Frozen Orbit with $\omega_0 = 90^\circ$, $a_0 = 1837$ km and $i_0 = 50^\circ$, for example, it has been verified that $\Delta a \approx 1$ km, while $\Delta \Omega \approx 25^\circ$. It was also verified that the majority of the orbits have a large $\Delta \omega$ over the integration period of 29.5 days. Orbits with $i_0 = 50^\circ$ or $i_0 = 90^\circ$ have specially large $\Delta \omega$, but, since these Frozen Orbits are almost circular, the definition of the argument of periapsis loses its meaning anyhow. As such, the orbits can be considered frozen only with respect to a , e and i . Nonetheless, this frozen state might not hold for longer periods, especially for the mission duration of 1 year. As such, in case one of these orbits is chosen as the operational orbit, a refinement of the frozen orbit initial conditions is required. This can be done, for example, using a corrector method, as mentioned in Chapter 5, Subsection 5.2.2.

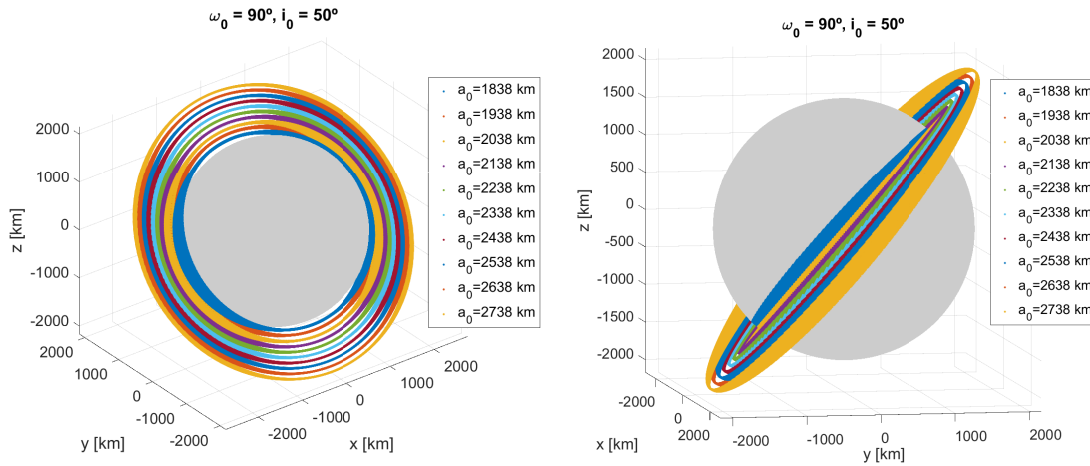


Figure 6.9: Frozen orbit family represented in the BME_{t_0} reference frame, propagated over 29.5 days.

Figure 6.10 shows the average osculating eccentricity as a function of the average osculating inclination, for two semi-major axis values. These plots can be compared directly with the plots in Figure 5.4, from *Abad et al. (2009)*, for validation purposes. For $a = 1838$ km, one can observe that Frozen Orbits have been found in the unstable region $i \in [63, 73]^\circ$ or $i > 86.5^\circ$ (see Table 5.1) and the average eccentricities obtained are smaller than those in *Abad et al. (2009)*. This is most likely due to the limit imposed on the periapsis altitude, which restricted the eccentricity to almost circular. The short propagation period can also have prevented the instability of these inclinations to manifest itself. For $a = 2738$ km, low eccentricities were also expected, except for $i \approx 60^\circ$. In fact, at least for $\omega = 270^\circ$, slightly higher eccentricities were found for $i \approx 60^\circ$. Nevertheless, these are restricted due to the maximum eccentricity imposed of 0.06. Furthermore, *Abad et al. (2009)* has only found frozen orbits with $\omega = 90^\circ$ for $i \approx 60^\circ$, while the methodology applied has led to frozen orbits with $\omega = 90^\circ$ for all inclinations tested. Once again, the short propagation period could have prevented the instability of orbits with $\omega = 90^\circ$ to manifest itself. Alternatively, the lunar sectorial and tesseral spherical harmonics terms might have stabilized the orbits, but the validation of this hypothesis would require further analysis.

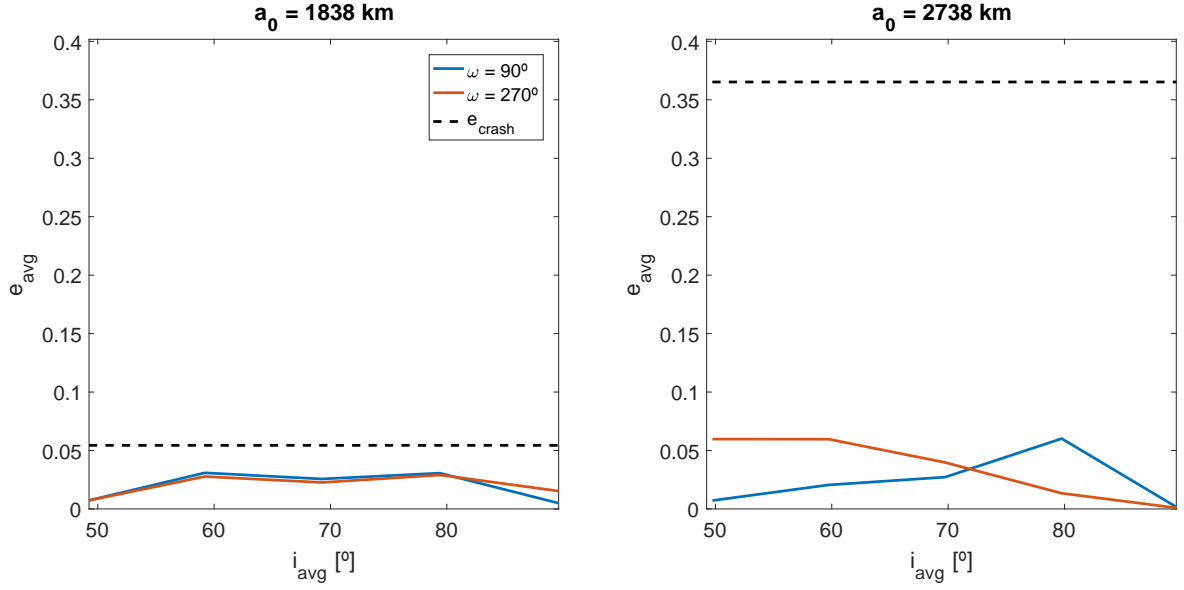


Figure 6.10: Frozen orbit's average osculating eccentricity as function of the average osculating inclination, over 29.5 days, for $a = 1873$ km (left) and $a = 2738$ km (right).

6.2.2. Circular Restricted Three-Body Problem Orbits

In order to generate the candidate **CRTBP** orbits, the equations of motion of the **CRTBP** (Equation 5.2) are integrated as a first order system (Zhang *et al.*, 2015):

$$\dot{\mathbf{x}} = \begin{bmatrix} \dot{\mathbf{r}} \\ \dot{\mathbf{v}} \end{bmatrix} = \begin{bmatrix} \mathbf{v} \\ \mathbf{g}(\mathbf{r}) + \mathbf{h}(\mathbf{v}) \end{bmatrix} \quad (6.2)$$

where the functions $\mathbf{g}(\mathbf{r})$ and $\mathbf{h}(\mathbf{v})$ are defined as follows:

$$\mathbf{g}(\mathbf{r}) = \begin{bmatrix} x - (1 - \mu)(x + \mu)/r_1^3 - \mu(x + \mu - 1)/r_2^3 \\ y - (1 - \mu)y/r_1^3 - \mu y/r_2^3 \\ -(1 - \mu)z/r_1^3 - \mu z/r_2^3 \end{bmatrix} \quad \mathbf{h}(\mathbf{v}) = \begin{bmatrix} 2v_y \\ -2v_x \\ 0 \end{bmatrix} \quad (6.3)$$

with $r_1 = [(x + \mu)^2 + y^2 + z^2]^{1/2}$ and $r_2 = [(x + \mu - 1)^2 + y^2 + z^2]^{1/2}$.

Methodology

In order to compute the initial conditions of a **CRTBP** orbit, a time-varying targeting scheme is used (see e.g. Ozimek, 2006). The goal is to iteratively adjust the initial conditions at t_0 ($\mathbf{x}_0^{k+1} = \mathbf{x}_0^k + \delta\mathbf{x}_0$), such that certain constraints on the state are met at t_f (e.g. $\delta\mathbf{x}_f = \mathbf{a} - \mathbf{x}_f = 0$). The general mathematical formula for a time-varying targeting scheme is as follows (Grebow *et al.*, 2008):

$$\begin{bmatrix} \delta\mathbf{r}_f \\ \delta\mathbf{v}_f \end{bmatrix} = \begin{bmatrix} \Phi(t_0, t_f) & \dot{\mathbf{r}}_f \\ & \dot{\mathbf{v}}_f \end{bmatrix} \begin{bmatrix} \delta\mathbf{r}_0 \\ \delta\mathbf{v}_0 \\ \delta(t_f - t_0) \end{bmatrix} \quad (6.4)$$

where δ denotes the variation with respect to the reference and $\Phi(t_f, t_0)$ is the state transition matrix, associated with Equation 6.2, that maps a variation at t_0 to a variation at t_f . In order to define constraints at t_f , the symmetric behaviour of periodic orbits can be explored (Ozimek, 2006). As such, Equation 6.4 is adapted to the type of symmetry of the orbit. Three types of symmetry which will be

used to determine CRTBP orbits' initial conditions will be explained with more detail in the following paragraphs.

2D X-axis symmetry Lyapunov, Distant-Retrograde and Low-Prograde Orbits (LO, DRO and LoPO) are all planar orbits that are symmetric about the X-axis of the CRTBP reference frame. Given an initial guess state:

$$\mathbf{x}_0 = [x_0 \ 0 \ 0 \ \dot{y}_0]^T$$

the orbit can be propagated until $y_f = 0$ and $\dot{y}_f < 0$, as depicted in Figure 6.11 by the dashed line, thereby providing an initial guess for half the orbital period, τ . However, to obtain a symmetric orbit, the crossing at the X-axis must be perpendicular, i.e. $\dot{x}_f = 0$. As such, a correction of the initial conditions is required.

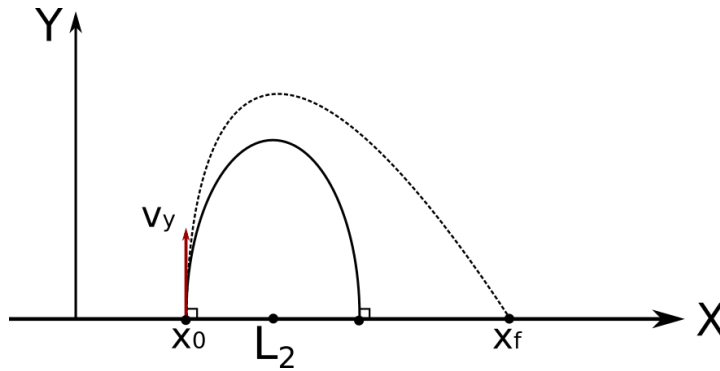


Figure 6.11: Targeting of a perpendicular X-axis crossing to generate a planar periodic orbit in the CRTBP, symmetric about the X-axis. The dashed line represents the propagation of initial conditions not yet converged and the solid line represents the desired orbit. The orbits are represented in the CRTBP reference frame, not to scale.

For that purpose, the first three state variables are fixed, i.e. $\delta x_0 = \delta y_0 = \delta \dot{x}_0 = 0$ and, so, x_0 determines the size of the orbit. On the other hand, \dot{y}_0 is allowed to vary. As such, the corrections that must be made to the initial state and (half) period of the orbit can be computed by solving the following equation (Ozimek, 2006):

$$\begin{bmatrix} 0 \\ -\dot{x}_f \end{bmatrix} = \begin{bmatrix} \frac{\partial y}{\partial \dot{y}_0} & \dot{y} \\ \frac{\partial \dot{x}}{\partial \dot{y}_0} & \dot{x} \end{bmatrix} \begin{bmatrix} \delta \dot{y}_0 \\ \delta \tau \end{bmatrix} \quad (6.5)$$

The first constraint corresponds to $y_f = 0$, which is automatically satisfied, since the propagation of the orbit is stopped when at the X-axis. The final orbit is then obtained by propagating the corrected initial conditions for $P = 2\tau$.

3D X-axis symmetry A Vertical Orbit is 3-Dimensional and symmetric about the X-axis of the CRTBP reference frame. Given an initial guess state:

$$\mathbf{x}_0 = [x_0 \ 0 \ 0 \ 0 \ \dot{y}_0 \ \dot{z}_0]^T$$

the orbit can be propagated until $y_f = 0$ and $z_f > 0$, providing an initial guess for one-quarter of the orbital period, τ . However, to obtain a symmetric orbit, $\dot{x}_f = 0$ and $\dot{z}_f = 0$ must be enforced at t_f .

Four state variables are fixed at t_0 : $\delta y_0 = \delta z_0 = \delta \dot{x}_0 = \delta \dot{y}_0 = 0$ and, so, \dot{y}_0 determines the size

of the orbit. On the other hand, x_0 and \dot{z}_0 are allowed to vary. As such, the corrections that must be made to the initial state and (one-quarter) period of the orbit can be computed solving the following equation (Grebow, 2006):

$$\begin{bmatrix} 0 \\ -\dot{x}_f \\ -\dot{z}_f \end{bmatrix} = \begin{bmatrix} \frac{\partial y}{\partial x_0} & \frac{\partial y}{\partial \dot{z}_0} & \dot{y} \\ \frac{\partial \dot{x}}{\partial x_0} & \frac{\partial \dot{x}}{\partial \dot{z}_0} & \ddot{x} \\ \frac{\partial \dot{z}}{\partial x_0} & \frac{\partial \dot{z}}{\partial \dot{z}_0} & \ddot{z} \end{bmatrix} \begin{bmatrix} \delta x_0 \\ \delta \dot{z}_0 \\ \delta \tau \end{bmatrix} \quad (6.6)$$

The final orbit is then obtained by propagating the corrected initial conditions for $P = 4\tau$.

3D XZ-plane symmetry Halo and Near-Rectilinear orbits are 3-Dimensional and symmetric about the XZ-plane of the CRTBP reference frame. Given an initial guess state:

$$\mathbf{x}_0 = [x_0 \quad 0 \quad z_0 \quad 0 \quad \dot{y}_0 \quad 0]^T$$

the orbit can be propagated until $y_f = 0$ and $\dot{y}_f < 0$, providing an initial guess for half orbital period, τ . However, once again, to obtain a symmetric orbit, $\dot{x}_f = 0$ and $\dot{z}_f = 0$ must be enforced at t_f .

Four state variables are fixed at t_0 : $\delta y_0 = \delta z_0 = \delta \dot{x}_0 = \delta \dot{z}_0 = 0$ and, so, z_0 determines the size of the orbit. On the other hand, x_0 and \dot{y}_0 are allowed to vary. As such, the corrections that must be made to the initial state and (half) period of the orbit can be computed solving the following equation (Grebow, 2006):

$$\begin{bmatrix} 0 \\ -\dot{x}_f \\ -\dot{z}_f \end{bmatrix} = \begin{bmatrix} \frac{\partial y}{\partial x_0} & \frac{\partial y}{\partial \dot{y}_0} & \dot{y} \\ \frac{\partial \dot{x}}{\partial x_0} & \frac{\partial \dot{x}}{\partial \dot{y}_0} & \ddot{x} \\ \frac{\partial \dot{z}}{\partial x_0} & \frac{\partial \dot{z}}{\partial \dot{y}_0} & \ddot{z} \end{bmatrix} \begin{bmatrix} \delta x_0 \\ \delta \dot{y}_0 \\ \delta \tau \end{bmatrix} \quad (6.7)$$

The final orbit is then obtained by propagating the corrected initial conditions for $P = 2\tau$. However, Equation 6.7 does not converge for orbits larger with $A_z \approx 32000$ km. As such, another targeting scheme must be employed.

Given the same initial state, only three state variables are fixed at t_0 : $\delta y_0 = \delta \dot{x}_0 = \delta \dot{z}_0 = 0$ and the size of the orbit is determined by the desired Jacobi Constant (C). On the other hand, x_0 , z_0 and \dot{y}_0 are allowed to vary. As such, the corrections that must be made to the initial state and (half) period of the orbit can be computed solving the following equation (adapted from Topputo, 2016):

$$\begin{bmatrix} 0 \\ -\dot{x}_f \\ -\dot{z}_f \\ C - C_0 \end{bmatrix} = \begin{bmatrix} \frac{\partial y}{\partial x_0} & \frac{\partial y}{\partial z_0} & \frac{\partial y}{\partial \dot{y}_0} & \dot{y} \\ \frac{\partial \dot{x}}{\partial x_0} & \frac{\partial \dot{x}}{\partial z_0} & \frac{\partial \dot{x}}{\partial \dot{y}_0} & \ddot{x} \\ \frac{\partial \dot{z}}{\partial x_0} & \frac{\partial \dot{z}}{\partial z_0} & \frac{\partial \dot{z}}{\partial \dot{y}_0} & \ddot{z} \\ \frac{\partial C}{\partial x_0} & \frac{\partial C}{\partial z_0} & \frac{\partial C}{\partial \dot{y}_0} & 0 \end{bmatrix} \begin{bmatrix} \delta x_0 \\ \delta z_0 \\ \delta \dot{y}_0 \\ \delta \tau \end{bmatrix} \quad (6.8)$$

An orbit generated with the correction scheme of Equation 6.7 or 6.8 will be referred to as an Halo Orbit or a Near-Rectilinear Orbit, respectively.

It should also be noted that the method presented requires an initial guess for each candidate orbit. Halo and Lyapunov orbits were generated with the same MATLAB[®] code used in [Topputo \(2016\)](#), which had already implemented an analytical first guess determination procedure, based on [Thurman and Worfolk \(1996\)](#). The MATLAB[®] code for the remaining orbits was developed, based on the one provided, but a *continuation procedure* was implemented to determine the first guess. This means that the initial guess state for each orbit j is based on the converged initial state of the previously generated orbit $j - 1$, as follows ([Grebow, 2006](#)):

$$\mathbf{x}_0^j = \mathbf{x}_0^{j-1} + s \Delta \mathbf{x}_0 \quad (6.9)$$

where s is the step size and $\Delta \mathbf{x}_0$ is the direction of the continuation. For a [DRO](#), for example, the continuation is done along the X-axis, so, $\Delta \mathbf{x}_0 = [1, 0, 0, 0]^T$, and the step size is a fixed value $s = \Delta x_0$. Nonetheless, the first orbit of the family generated ($j = 1$) still requires a “manual” initial guess. For [NROs](#) this initial guess comes from the last Halo Orbit generated, while for the remaining orbits the initial guesses were taken from the literature.

Once the initial conditions of a [CRTBP](#) orbit is determined, the orbit is propagated for $S_M = 29.5$ days and, similarly to a Frozen Orbit, is stored in an [SPK](#). In order to do so, the orbits are first transformed to the Moon-centred [BMOP](#) _{t_0} fixed at $t_0 = 01 \text{ Jan } 2020 \text{ 12:00:00.000}$ ([TDB](#)), as follows:

$$\mathbf{x}_{\text{BMOP}_{t_0}} = \begin{bmatrix} \cos t & -\sin t & 0 & & & & \\ \sin t & \cos t & 0 & & 0 & & \\ 0 & 0 & 1 & & & & \\ & & & -\sin t & -\cos t & 0 & \\ & 0 & & \cos t & -\sin t & 0 & \\ & & & 0 & 0 & 0 & \end{bmatrix} \mathbf{x} \quad (6.10)$$

and then to the Moon-centred [J2000](#) frame using SPICE.

Validation and Verification

In order to validate the initial conditions determined for [LO](#), [HO](#), [NRO](#) and [VO](#), data from [Grebow \(2006\)](#) was used. The results obtained are presented in Tables [6.3](#) to [6.6](#). For the first three types of orbit, the fixed variable was A_x , A_z and C , respectively, while [Grebow \(2006\)](#) fixed instead values of x and z . Nonetheless, the results obtained with the MATLAB[®] code do not differ significantly from [Grebow's](#): the error in the final position is at most $\sim 10^{-3}$ (adimensional), the error in velocity and orbital period $\sim 10^{-4}$ (adimensional) and the error in the stability index $\sim 10^{-1}$. For Vertical Orbits, the fixed variable was $v_{y,0}$ in both cases. Furthermore $x_0 = 1.1119$ and $v_{z,0} = 0.4358$ have been used as first guess, before initiating the continuation procedure ([Grebow, 2006](#)). The results obtained in this case present a lower error: in the final position and velocity is at most $\sim 10^{-5}$ (adimensional), in the orbital period $\sim 10^{-4}$ (adimensional) and in the stability index $\sim 10^{-3}$. As such, the MATLAB[®] code that generates [LO](#), [HO](#), [NRO](#) or [VO](#) can be considered validated.

In order to validate the initial conditions determined for [DROs](#), data from [Turner \(2016\)](#) was used. The results obtained are presented in Tables [6.7](#) to [6.6](#). The fixed variable was the initial distance with respect to the Moon: $r_0 = 1 - \mu - x_0$. Furthermore, $v_{y,0} = 0.350$ km/s has been used as first guess, before initiating the continuation procedure ([Turner, 2016](#)). The results obtained with the MATLAB[®] code do not differ significantly from [Turner's](#): the error in the final velocity is at most $\sim 10^{-2}$ kilometres per second and the error in the orbital period $\sim 10^5$ seconds. It should be noted that [Turner \(2016\)](#) integrated the orbits for 30 years, using a more precise model, including the Moon and Earth's

NSG and the Sun, Venus and Jupiter's TB perturbation. As such, the MATLAB® code that generates DROs can be considered validated.

Regarding the validation of LoPOs, no numerical data has been found in the literature, so, an analogous validation could not be made. Table 6.8 presents the results obtained with the developed MATLAB® code. Once again, the fixed variable was the initial distance with respect to the Moon (r_0) and $v_{y,0} = -0.1$ km/s has been used as first guess. The orbital periods determined are in accordance with the range presented in Table 5.2 of [2, 14] days (Folta *et al.*, 2015). The orbits generated are also presented in Figure 6.12. Comparing these orbits with the LoPOs generated in Guzzetti *et al.* (2016) (Figure 6.13), one can conclude that the two families are very similar. As such, the MATLAB® code that generates LoPOs will be considered validated.

Table 6.3: Validation of Lyapunov Orbits with Grebow (2006). The state variable fixed during the targeting scheme is denoted in bold. Regarding the initial conditions fixed in MATLAB®, x_0 corresponds to $A_x = 9150$ km and $A_x = 20000$ km, for orbits #1 and #2, respectively.

	#	x_0 (adim)	x_f (adim)	$v_{y,f}$ (adim)	P (adim)	S
MATLAB®	1	1.1290	1.1761	-0.1226	3.3978	651.565
	2	1.0920	1.1924	-0.2505	3.5133	434.971
Grebow	1	-	1.1762	-0.1231	3.3981	651.010
	2	-	1.1924	-0.2502	3.5128	435.772
Difference	1	-	$2.95 \cdot 10^{-5}$	$-4.66 \cdot 10^{-4}$	$2.45 \cdot 10^{-4}$	-0.555
	2	-	$-8.24 \cdot 10^{-5}$	$3.94 \cdot 10^{-4}$	$-5.88 \cdot 10^{-4}$	0.801

Table 6.4: Validation of Halo Orbits with Grebow (2006). The state variable fixed during the targeting scheme is denoted in bold. Regarding the initial conditions fixed in MATLAB®, z_0 corresponds to $A_z = 1000$ km and $A_z = 30400$ km, for orbits #1 and #2, respectively.

	#	z_0 (adim)	x_f (adim)	z_f (adim)	$v_{y,f}$ (adim)	P (adim)	S
MATLAB®	1	$-2.2784 \cdot 10^{-3}$	1.1808	$3.1388 \cdot 10^{-3}$	-0.1556	3.4154	605.655
	2	$-6.5371 \cdot 10^{-2}$	1.1652	0.1098	-0.2008	3.3065	239.519
Grebow	1	-	1.1809	0	-0.1559	3.4155	606.113
	2	-	1.1654	0.1099	-0.2011	3.3066	239.574
Difference	1	-	$9.91 \cdot 10^{-5}$	$-3.13 \cdot 10^{-3}$	$-2.86 \cdot 10^{-4}$	$4.28 \cdot 10^{-5}$	0.458
	2	-	$1.17 \cdot 10^{-4}$	$7.12 \cdot 10^{-5}$	$-2.84 \cdot 10^{-4}$	$2.42 \cdot 10^{-5}$	0.055

Table 6.5: Validation of Near-Rectilinear Orbits with Grebow (2006). The variable fixed during the targeting scheme is denoted in bold.

	#	C	x_f (adim)	z_f (adim)	$v_{y,f}$ (adim)	P (adim)	S
MATLAB®	1	3.0738	1.1434	0.1576	-0.2216	3.1400	76.9712
	2	3.0614	1.1350	0.1700	-0.2245	3.0625	49.5041
Grebow	1	-	1.1435	0.1579	-0.2220	3.1393	76.6589
	2	-	1.1354	0.1699	-0.2247	3.0645	50.0298
Difference	1	-	$3.09 \cdot 10^{-5}$	$2.30 \cdot 10^{-4}$	$-3.22 \cdot 10^{-4}$	$-7.01 \cdot 10^{-4}$	-0.3123
	2	-	$3.16 \cdot 10^{-4}$	$-1.62 \cdot 10^{-4}$	$-1.81 \cdot 10^{-5}$	$1.90 \cdot 10^{-3}$	0.5256

Table 6.6: Validation of Vertical Orbits with Grebow (2006). The state variable fixed during the targeting scheme is denoted in bold.

	#	x_0 (adim)	$v_{y,0}$ (adim)	$v_{z,0}$ (adim)	P (adim)	S
MATLAB®	1	1.1003	-0.3217	0.5973	5.6754	204.315
	2	1.0905	-0.4317	0.7416	6.0172	240.740
	3	1.0841	-0.5417	0.8415	6.1304	236.034
	4	1.0796	-0.6517	0.9128	6.1847	217.804
Grebow	1	1.1003	-0.3217	0.5973	5.6753	204.308
	2	1.0906	-0.4317	0.7416	6.0172	240.742
	3	1.0842	-0.5417	0.8415	6.1305	236.038
	4	1.0796	-0.6517	0.9128	6.1848	217.809
Difference	1	$-3.15 \cdot 10^{-5}$	0	$-7.45 \cdot 10^{-5}$	$-1.03 \cdot 10^{-4}$	$-6.69 \cdot 10^{-3}$
	2	$1.44 \cdot 10^{-5}$	0	$-3.51 \cdot 10^{-5}$	$-7.58 \cdot 10^{-7}$	$2.11 \cdot 10^{-3}$
	3	$4.18 \cdot 10^{-5}$	0	$-5.82 \cdot 10^{-5}$	$3.08 \cdot 10^{-5}$	$4.43 \cdot 10^{-3}$
	4	$-2.61 \cdot 10^{-5}$	0	$-8.99 \cdot 10^{-6}$	$3.97 \cdot 10^{-5}$	$4.95 \cdot 10^{-3}$

Table 6.7: Validation of Distant-Retrograde Orbits with Turner (2016). The variable fixed during the targeting scheme is denoted in bold. $r_0 = 1 - \mu - x_0$ denotes the initial distance with respect to the Moon.

	#	r_0 (km)	$v_{y,0}$ (km/s)	P (10^6 s)	P_M/P	S
MATLAB®	1	60000	0.503	1.005	2.34	1
	2	64500	0.515	1.096	2.15	1
	3	69500	0.529	1.194	1.97	1
	4	70750	0.533	1.218	1.93	1
	5	77250	0.556	1.339	1.76	1
Turner*	1	60000	0.498	1.028	2.3	–
	2	64500	0.507	1.105	2.13	–
	3	69500	0.519	1.191	2	–
	4	70750	0.529	1.274	1.85	–
	5	77250	0.539	1.271	1.86	–
Difference	1	0	$-5.88 \cdot 10^{-3}$	0.0222	$-4.70 \cdot 10^{-2}$	–
	2	0	$-8.22 \cdot 10^{-3}$	0.0088	$-2.35 \cdot 10^{-2}$	–
	3	0	$-1.08 \cdot 10^{-2}$	-0.0033	$2.34 \cdot 10^{-2}$	–
	4	0	$-4.78 \cdot 10^{-3}$	0.5561	$-8.74 \cdot 10^{-2}$	–
	5	0	$-1.71 \cdot 10^{-2}$	-0.0687	$9.80 \cdot 10^{-2}$	–

* The orbital period is an average over a 30-year propagation time

Table 6.8: Validation of Low-Prograde Orbits. The variable fixed during the targeting scheme is denoted in bold. $r_0 = 1 - \mu - x_0$ denotes the initial distance with respect to the Moon.

	#	r_0 (km)	$v_{y,0}$ (km/s)	r_f (km)	P (days)	P_M/P	S
MATLAB®	1	50000	-0.0974	5487	9.029	3.02	1
	2	47000	-0.1169	7630	7.648	3.57	1
	3	44000	-0.1417	9459	6.829	4.00	1
	4	41000	-0.1700	11305	6.258	4.365	1
	5	38000	-0.2019	13274	5.842	4.676	1

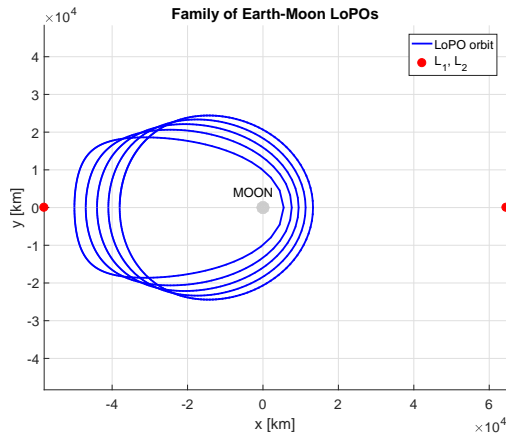


Figure 6.12: Low-Prograde Orbits generated with the developed MATLAB[®] code, represented in the Moon-centred CRTBP reference frame.

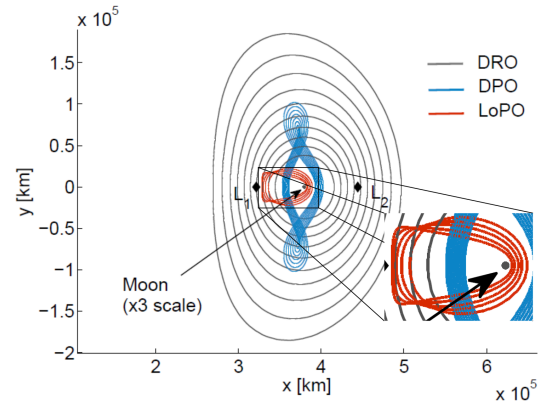


Figure 6.13: Low-Prograde Orbit family from Guzzetti *et al.* (2016), represented in the CRTBP reference frame.

Results

The CRTBP orbits chosen as candidates were:

- Lyapunov Orbits: A_x between 7800 and 21000 km, with a step size of 600 km;
- Halo Orbits: A_z between 1000 and 32000 km, with a step size of 1000 km;
- Near-Rectilinear Orbits: C between ≈ 3.0273 and ≈ 3.1068 , with a step size ≈ 0.0026 ;
- Vertical Orbits: $v_{y,0}$ between -0.03 and -0.23 with a step size of 0.01;
- Distant-Retrograde Orbits: r_0 between 20000 and 80000 km, with a step size of 2000 km;
- Low-Prograde Orbits: r_0 between 38000 and 50000 km, with a step size of 3000 km.

The orbits have been propagated for $S_M = 29.5$ days in the CRTBP reference frame. The LO, HO, NRO, VO and DRO family are presented in Figure 6.14. The LoPO family has already been presented in Figure 6.12.

In order to be able to compare the characteristics of CRTBP orbits, the Jacobi Constant (C), associated to the initial conditions of each orbit, will be used. Figure 6.15 shows the correspondence between the Jacobi Constant and the fixed parameter, for each candidate orbit, except for NROs. In general, it can be concluded that a larger (absolute) value of the fixed parameter, and thus, a larger orbit, corresponds to a lower C .

Figures 6.16 and 6.17 show the resonance ratio and orbital period of each orbit type, as function of C . Two resonance ratios are presented: the first with respect to the sidereal month ($P_M \approx 27$ days) and the second with respect to the synodic month ($S_M \approx 29.5$ days). From Figure 6.17 it can be concluded that the orbital period increases with orbit size and decreasing C , except for the Halo Orbit family. On the other hand, from Figure 6.18, one can conclude that the stability index decreases with C and increasing orbit size, except for DROs and LoPO which have $S = 1$.

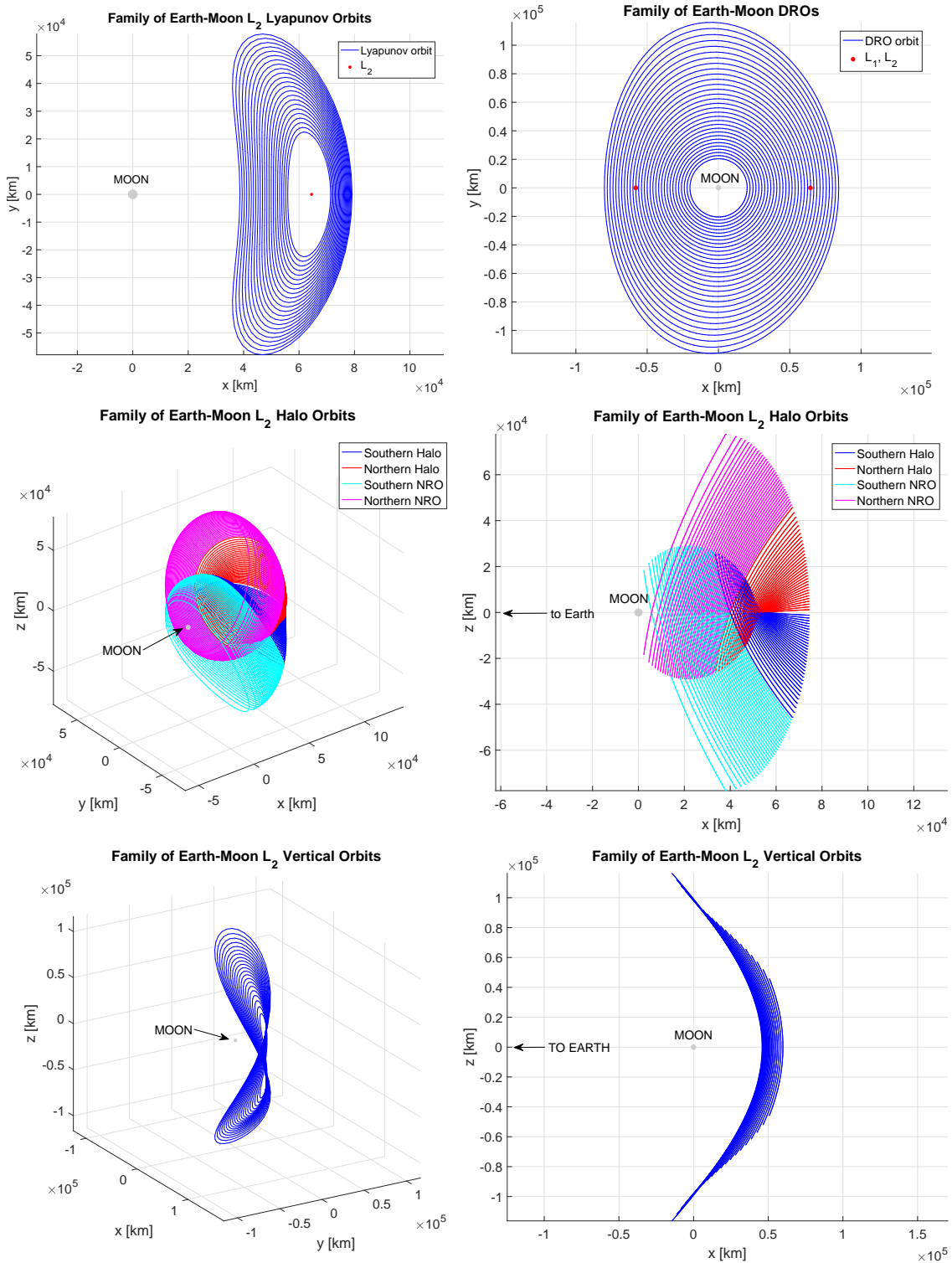


Figure 6.14: Generated CRTBP orbit families, represented in the Moon-centered CRTBP reference frame.

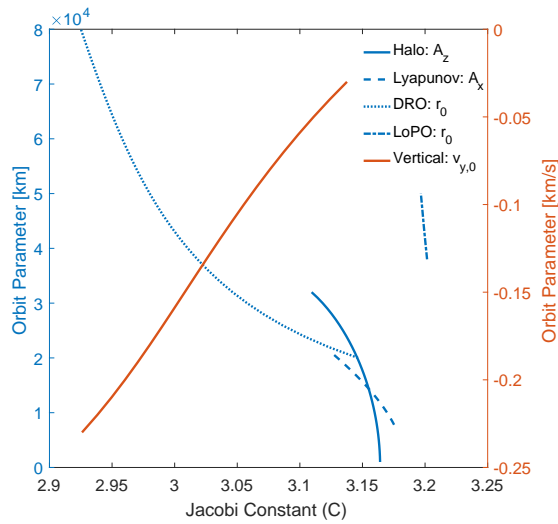


Figure 6.15: CRTBP fixed orbit parameters as function of the respective Jacobi Constant. Parameters which are distances are represented on the left-axis and those that are velocities are represented on the right-axis.

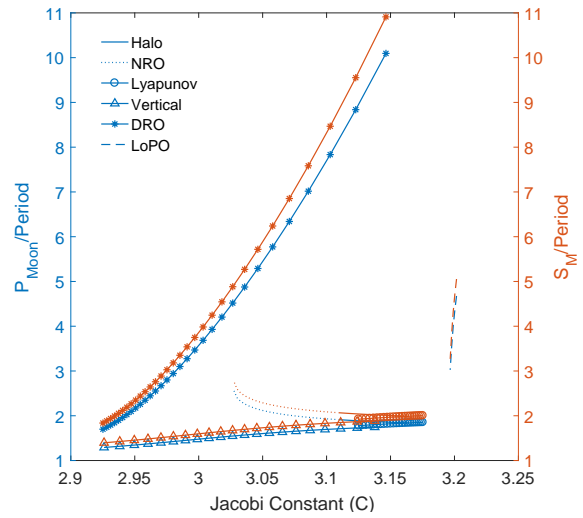


Figure 6.16: CRTBP orbits resonance ratio, with respect to the lunar orbital period, P_M (left-axis) and the synodic month, S_M (right-axis).

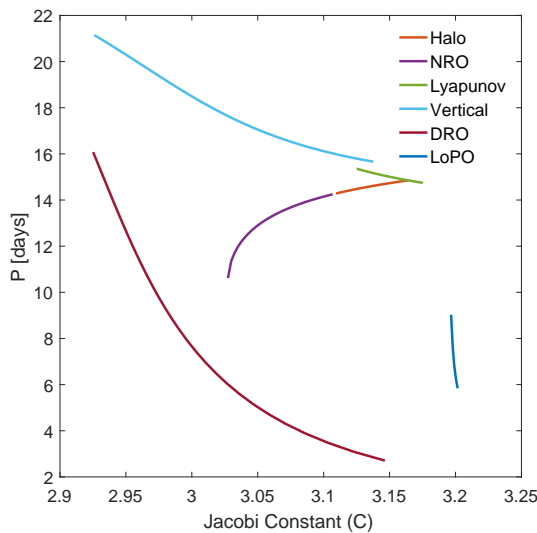


Figure 6.17: CRTBP orbits' period.

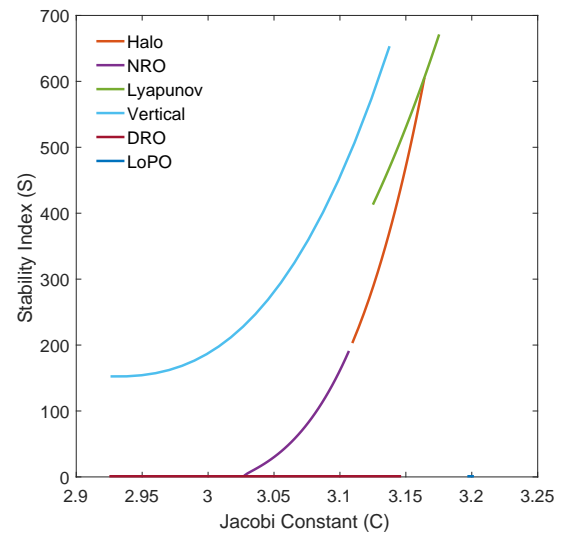


Figure 6.18: CRTBP orbits' stability index.

Figures 6.19 and 6.20 show the minimum and maximum distance and velocity with respect to the Moon for each of the candidate orbits, as function of C . It should be noted that all CRTBP orbits, with the exception of some DROs, have a Moon range variation of at least 10000 km, in one orbital revolution. Furthermore, this value increases for orbits that go closer to the Moon (smaller C). In terms of meteoroid detections, this means that orbits with smaller minimum distances to the Moon are not necessarily better, as long observation periods at larger distances could cancel out the advantage. LoPOs, for example, have the lowest minimum distances to the Moon (≈ 10000 km), which can be beneficial for meteoroid detection. However, when closest to the Moon, LoPOs have the highest maximum velocities (≈ 1 km/s), and, so, a short observation period at this range. All other orbits have orbital velocities smaller than ≈ 0.7 km/s and a smaller velocity variation in one orbital revolution.

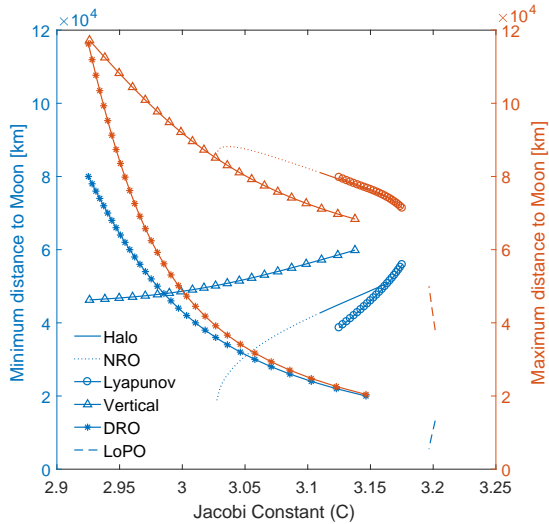


Figure 6.19: CRTBP orbits' maximum and minimum distance to the Moon.

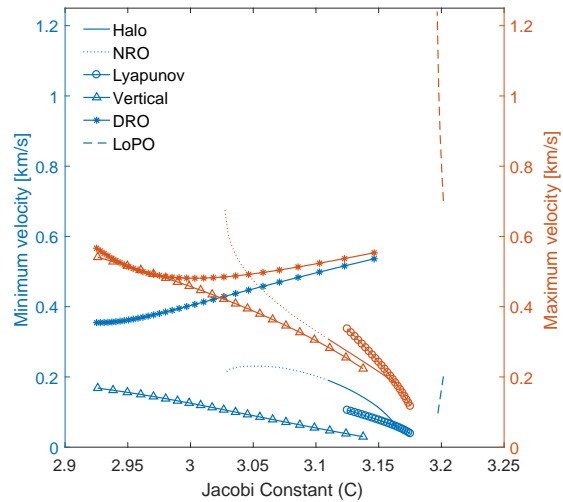


Figure 6.20: CRTBP orbits' maximum and minimum velocity in the CRTBP reference frame.

6.3. Payload Modelling

6.3.1. Optics

An array sensor, such as a CCD sensor, captures an image by absorbing the light that enters the instrument through an optical system, as depicted in Figure 6.21 (left). In this figure, the plane where the real image is projected is known as the *image plane* or *FOV* and the *optic* or *focal point* represents the aperture of a perfect optical system. The distance between the focal point and the array sensor is known as the *focal length* (d_{FL}). Given a square array of side d_{CCD} , the *FOV* of the instrument is given by:

$$FOV = 2 \tan^{-1} \left(\frac{d_{CCD}}{2 d_{FL}} \right) \tag{6.11}$$

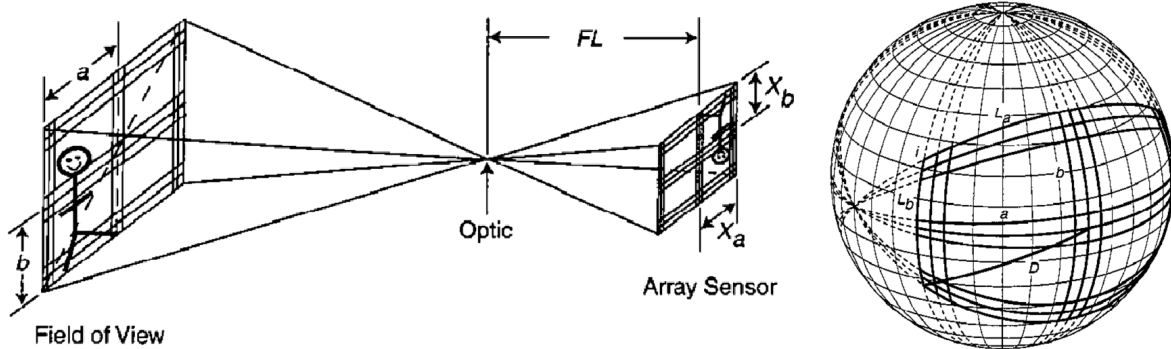


Figure 6.21: Geometry of an array sensor (left) and respective Field-of-View projection onto the spacecraft's sky (right). Notation used in the text for a square array: $FOV/2 = a = b$ (which are angles); $d_{CCD}/2 = x_a = x_b$; $d_{FL} = FL$; $\theta_{FOV}/2 = L_a = L_b$; $\theta_L = i$. From Wertz (2009, p. 354).

The spacecraft's perspective of the instrument's *FOV* is defined in a spacecraft centred sphere of unitary radius, known as the *spacecraft's celestial sphere*. As can be seen in Figure 6.21 (right), the instrument's *FOV* is distorted in the spacecraft's celestial sphere. In fact, the straight lines that define

the instrument's **FOV** are projected onto the spacecraft's sky as great circle arcs. As such, it is possible to compute the length (θ_{FOV}), inner angles (θ_{\angle}), and area (A_{FOV}) of the projected spacecraft's **FOV** recurring to spherical geometry, as follows:

$$\theta_{FOV} = 2 \tan^{-1} \left[\sin \left(\frac{FOV}{2} \right) \tan \left(\frac{\pi}{4} \right) \right] \quad (6.12)$$

$$\theta_{\angle} = 2 \cos^{-1} \left[\cos \left(\frac{FOV}{2} \right) \sin \left(\frac{\pi}{4} \right) \right] \quad (6.13)$$

$$A_{FOV} = 4\theta_{\angle} - 2\pi \quad (6.14)$$

For a small **FOV**, $\theta_{FOV} \approx FOV$ and $\theta_{\angle} \approx 90^\circ$, so there is almost no distortion of the instrument's **FOV** projection onto the spacecraft's sky, as it approximately maintains a squared shape. In this case, a planar approximation is sufficient, and there is no need to use spherical geometry (Wertz, 2009, p.305-308).

The **Instantaneous Field-of-View (IFOV)** of an array sensor is defined analogously to the **FOV** of the instrument, but corresponds to only one pixel of the array. For a squared pixel of dimension d_{pixel} , Equation 6.11 can be used to compute the instrument's **IFOV** in the optical axis direction. The **IFOV** is usually small, so, when projected onto the spacecraft's celestial sphere, suffers almost no distortion. However, this assumption might not be reasonable for pixels near the sensor edges, specially when the **FOV** of the instrument is large. Figure 6.21 (right) also depicts this situation. It can be observed that the pixels at nadir maintain their squared shape, while pixels near the edges of the (large) **FOV** projection are distorted.

For the case of **LUMIO**, $d_{FL} = 217 \text{ mm} \Rightarrow FOV \approx 3.5^\circ$ (see Table 3.5), which leads to $\theta_{FOV} \approx 3.498^\circ$ and $\theta_{\angle} \approx 90.05^\circ$. As such, **LUMIO-Cam's FOV** will be assumed planar when projected onto the spacecraft's sky. Furthermore, a pixel size of $d_{pixel} = 13 \text{ } \mu\text{m} \Rightarrow IFOV \approx 0.0034^\circ \ll FOV$, so, the projection of all pixel's **IFOV** will also be considered planar.

The optical geometry of the **LUMIO-Cam**, as depicted in Figure 6.21 (left), was implemented in SPICE resorting to an **Instruments Kernel (IK)**. An **IK** is a SPICE file that allows the implementation of an instrument's **FOV** size, shape and orientation. These were defined in the instrument's fixed reference frame (see Figure 6.3) with four vectors pointing to the corners of the **FOV**, centred at the focal point. The **IK** was then successfully validated with SPICE's function *cspice_getfov*.

6.3.2. Detector

The **CCD** sensor collects photons emitted by the impact flash, but also some undesired signals, which are considered as noise. As such, in order to determine if the signal of an impact flash is detectable, the concept of **Signal-to-Noise Ratio (SNR)** must first be introduced.

Given the signal of the impact (s_{impact}) and the Poisson noise associated with all signals (σ), the **SNR** is defined as follows (Raab, 2002):

$$SNR = \frac{s_{impact}}{\sigma} \quad (6.15)$$

where s_{impact} is measured in electrons generated in the **CCD**, per pixel ($e^-/pixel$), and σ is measured in electrons **root-mean-square (rms)**. The Poisson noise of a signal is defined as $\sigma_i = \sqrt{s_i}$ and the total

Poisson noise is given by (Raab, 2002):

$$\sigma = \sqrt{\sum_i \sigma_i^2} \quad (6.16)$$

Seven noise sources will be taken into account for the computation of σ :

- σ_{impact} , the noise associated with the impact flash signal itself;
- σ_M , the Moon's surface background noise;
- σ_C , the cosmic background noise;
- σ_{DC} , the CCD's internal noise, known as **Dark-Current**;
- σ_{RON} , the CCD's **Read-Out Noise**;
- σ_{OCN} , the CCD's **Off-Chip Noise**;
- σ_{QN} , the A/D converter's noise, known as **Quantisation Noise**.

How each of these noise sources is estimated is detailed in the following subsection.

Finally, the CCD sensor chosen also has the possibility of amplifying the incoming signals by a factor G (gain), at the cost of an **Excess Noise Factor (ENF)**. As such, when computing the **SNR**, all signals generated in the detector, before the multiplication register (s_{impact} , s_M , s_C and s_{DC}), must be multiplied by G and the corresponding noises by **ENF**, as follows (Topputo *et al.*, 2017):

$$\text{SNR} = \frac{G \cdot s_{\text{impact}}}{\sqrt{\text{ENF}^2 \cdot G \cdot (s_{\text{impact}} + s_M + s_C + s_{DC}) + \sigma_{RON}^2 + \sigma_{OCN}^2 + \sigma_{QN}^2}} \quad (6.17)$$

where $\sigma_i^2 = G \cdot s_i$, for the impact flash, dark current and Moon and cosmic background signals.

Methodology

In order to determine the range of signals the CCD can detect, the following methodology is followed:

1. Estimation of the squared Moon's background noise, σ_M^2 , as follows (Raab, 2002):

$$\sigma_M^2 = G \cdot s_M = G \cdot e_{RM} \cdot A_{\text{lens}} \cdot \tau \quad \left[\frac{e^-}{\text{pixel}} \right] \quad (6.18)$$

where $A_{\text{lens}} = \pi(d_\phi/2)^2$ is the area of the optics' lens, τ is a constant that takes into account the lens transmissivity, transparency and the light spreading across multiple pixels; e_{RM} is the flux of photons received, due to the Moon's background light emission, converted to an electron flux and computed as follows (based on Bouley *et al.* (2012)):

$$e_{RM} = \frac{S_{\text{Moon}} t_{\text{exp}}}{2\pi d^2} \int_{\lambda_1}^{\lambda_2} L(\lambda, T_M) \frac{qe(\lambda)}{E_\gamma(\lambda)} d\lambda \quad \left[\frac{e^-}{m^2} \right] \quad (6.19)$$

$$L(\lambda, T) \equiv \pi \frac{2h_p c^2}{\lambda^5 \left[\exp\left(\frac{h_p c}{\lambda k T}\right) - 1 \right]} \quad \left[\frac{W}{m^2 \text{ nm}} \right] \quad (6.20)$$

$$E_\gamma(\lambda) \equiv \frac{hc}{\lambda} \quad \left[\frac{J}{\gamma} \right] \quad (6.21)$$

where $\lambda \in [\lambda_1, \lambda_2]$ is the observed wavelength, $T_M \approx 150$ K is the assumed (constant) blackbody temperature of the Moon (Bouley *et al.*, 2012), t_{exp} is the exposure time of the sensor and d is the distance to the impact flash. $L(\lambda, T)$ is given by Planck's law, $qe(\lambda) [e^-/\gamma]$ is the quantum efficiency of the sensor and $E_\gamma(\lambda)$ is the energy of the photon, where γ denotes the photon. Finally, S_{Moon} is the emitting surface of the Moon, which will be assumed equal to the Moon surface area observed by one pixel, i.e. the IFOV-area;

2. Estimation of the squared cosmic noise, σ_C^2 , as follows (Raab, 2002):

$$\sigma_C^2 = G \cdot s_C = G \cdot p_{RC} \cdot A_{lens} \cdot \tau \cdot \overline{qe} \left[\frac{e^-}{pixel} \right] \quad (6.22)$$

where $\overline{qe} \equiv \left[\int_{\lambda_1}^{\lambda_2} qe(\lambda) d\lambda \right] / (\lambda_2 - \lambda_1)$ is the mean quantum efficiency over the observation spectrum and p_{RC} is the flux of photons received at the sensor, computed as follows:

$$p_{RC} = 2748 \cdot t_{exp} \cdot A_{IFOV} \left[\frac{\gamma}{m^2} \right] \quad (6.23)$$

where it was assumed that the cosmic background noise corresponds to $m_\gamma = +18$, so, 2748 $\gamma/s/m^2$ per square arc second are received by the sensor (Raab, 2002). A_{IFOV} is the IFOV area in square arc seconds;

3. Estimation of the squared dark current noise, σ_{DC}^2 , as follows (Raab, 2002):

$$\sigma_{DC}^2 = G \cdot s_{DC} = G \cdot DC \cdot t_{exp} \left[\frac{e^-}{pixel} \right] \quad (6.24)$$

where DC is the number of electrons generated in the sensor per second and pixel, at a certain temperature;

4. Estimation of the Off-Chip Noise of the sensor, σ_{OCN} , as follows (Topputo *et al.*, 2017):

$$\sigma_{OCN} = \frac{\text{off}_n}{OAR} \sqrt{\frac{\pi N_{pixels}}{t_{exp}}} \quad (6.25)$$

where off_n denotes the off-chip noise in volts per \sqrt{Hz} , OAR denotes the Output Amplifier Responsivity, in electrons per volt, and N_{pixels} denotes the total number of pixels of the sensor;

5. Estimation of Quantisation Noise noise, σ_{QN} , as follows (Topputo *et al.*, 2017):

$$\sigma_{QN} = \frac{0.7 \text{ cap}_G}{2^{N_{bits}} \sqrt{12}} \quad (6.26)$$

where cap is the detector capacity and N_{bits} is the A/D converter number of bits;

6. Assuming that the impact flash can be detected for $SNR > SNR_{min}$, the determination of the

minimum signal detectable is made, by solving Equation 6.17 for $s_{impact} = s_{min}$, as follows:

$$\begin{aligned} \text{SNR}_{min} &= \frac{G \cdot s_{min}}{\sqrt{\text{ENF}^2 \cdot G \cdot s_{min} + \text{Noise}}} \Rightarrow \\ \Rightarrow s_{min} &= \frac{(\text{SNR}_{min} \cdot \text{ENF})^2 + \sqrt{(\text{SNR}_{min} \cdot \text{ENF})^4 + 4\text{Noise} \cdot \text{SNR}_{min}^2}}{2G} \quad \left[\frac{e^-}{\text{pixel}} \right] \end{aligned} \quad (6.27)$$

with:

$$\text{Noise} \equiv \text{ENF}^2 (\sigma_M^2 + \sigma_C^2 + \sigma_{DC}^2) + \sigma_{RON}^2 + \sigma_{OCN}^2 + \sigma_{QN}^2 \quad (6.28)$$

7. Determination of the maximum impact flash signal detectable, as follows:

$$s_{max} = \text{cap} \quad \left[\frac{e^-}{\text{pixel}} \right] \quad (6.29)$$

It should be noted that, given the estimation of σ_M^2 made in Step 1, s_{min} is a function of the distance to the impact flash (d). This parameter, in turn, is a function of the orbital altitude (h). However, in order to simplify the analysis that will follow, it will be assumed that the impact flash occurs at nadir, and, so, $d = h$. As such, $S_{Moon} \approx \text{IFOV-area}$ can be reasonably approximated by:

$$\text{IFOV-area} = \left[2h \tan\left(\frac{\text{IFOV}}{2}\right) \right]^2 \equiv \text{GSD}^2 \quad (6.30)$$

where **GSD** denotes the **Ground Sampling Distance**.

Finally, the corresponding visual apparent magnitude detectable can be estimated from Equation 2.4, as follows:

$$m_V = 2.5 \log\left(\frac{4 \times 10^{10}}{p_R/\Delta t}\right) = 2.5 \log\left(4 \times 10^{10} \frac{\Delta t \cdot A_{\text{lens}} \cdot \tau \cdot \bar{q}e}{s_{\text{impact}}}\right) \quad (6.31)$$

where Δt is the duration of the impact.

Validation and Verification

The validation of the methodology presented with data from the literature is not possible, due to the particular nature of the problem. However, the implementation of each formula has been validated against data presented in the corresponding reference sources (Raab, 2002; Bouley et al., 2012; Harding et al., 2015). Furthermore, LUMIO's noise budget and SNR estimation was also independently carried out by its payload engineer, in an analogous fashion to what has been presented in this section. Since the results obtained in this independent analysis are in alignment with the presented in the next subsection, the methodology will be considered validated.

It should be noted that the analysis conducted does not take into account motion blur, which should be significant for high orbital velocities. Earthshine on the the Moon's surface is also not taken into account in the noise budget, but only orbits that observe the lunar nearside should be affected. Finally, stray-light has also been neglected and the optics are assumed to be always perfectly focused.

Results

Given the payload characteristics presented in Chapter 3 (Table 3.5) and the methodology previously described, the noise budget estimated is detailed in Table 6.9. As can be observed, the variation of

σ_M with h is not significant in the computation of the noise budget, due to the small value of σ_M . As such, and considering that a signal is detectable for $\text{SNR}_{\min} = 5^4$, the range of signals detectable by the CCD is given by:

$$s = [s_{\min}, s_{\max}] = [290, 80000] e^- / \text{pixel}$$

for all altitudes. From Equation 6.31, the corresponding range of impact flash apparent magnitudes detected is:

$$m_V = [+1.759, +7.891]$$

Table 6.9: Estimated detector's noise budget.

Noise	Value	Reference
σ_M	$\approx 6.9 \cdot 10^{-18}^*$	Eqs. 6.18–6.21, 6.30
σ_C	7.5	Eqs. 6.22–6.23
σ_{DC}	5.9	Eq. 6.24
σ_{RON}	43	Table 3.5
σ_{OCN}	101	Eq. 6.25
σ_{QN}	9	Eq. 6.26
Noise	$\approx 12297^*$	Eq. 6.28

* for $h \in [100, 100000]$ km

6.4. Meteoroid Environment

6.4.1. Kinetic Energy Estimation

In order to determine the kinetic energy range the LUMIO-Cam can detect from a certain orbit, two different methods will be employed. These are the *Luminous Efficiency method* and the *Blackbody method*. The first assumes a directly proportional relation between light emitted in the visible spectrum and the impactor's kinetic energy, given by the luminous efficiency coefficient. On the other hand, the second assumes that the impact flash emits radiation as a blackbody and the emitting surface scales with the size of the impact crater. Both methods will be detailed in the following subsections.

Luminous Efficiency method

The methodology employed in the Luminous Efficiency method is as follows:

1. Estimation of received energy flux in the visible spectrum (based on Raab, 2002):

$$E_R = \frac{s_{\text{impact}} \overline{E_\gamma}}{\tau A_{\text{lens}} \overline{q_e}} \quad \left[\frac{\text{J}}{\text{m}^2} \right] \quad (6.32)$$

where $s_{\text{impact}} \in [290, 80000] e^- / \text{pixel}$, assuming that the impact is only detected by one pixel; and $\overline{q_e}$ and $\overline{E_\gamma}$ are the mean quantum efficiency and photon energy over the sensor's observation spectrum, respectively;

2. Estimation of the total emitted energy in the visible spectrum:

$$E_T^V = 2\pi d^2 E_R \quad [\text{J}] \quad (6.33)$$

⁴Threshold defined in the Negotiation Meeting for the ITT 8643–Lunar Cubesats for Exploration (2017)

where d is the distance between the sensor and the impact flash and the radiation as been assumed emitted into 2π steradians (Suggs *et al.*, 2014);

3. Estimation of the meteoroid's kinetic energy:

$$\text{KE} = \frac{E_T^V}{\eta_V} \quad [\text{J}] \quad (6.34)$$

where η_V is the luminous efficiency in the visible spectrum.

In order to use this method some parameters need to be assumed, namely d and η_V . The luminous efficiency parameter will be assumed given by the following relation (Swift *et al.*, 2011):

$$\eta_V = 1.5 \cdot 10^{-3} \exp\left(\frac{9.3^2}{v}\right) \quad (2.7)$$

where v is in km/s and within the range $\eta_V \in [5 \cdot 10^{-4}, 5 \cdot 10^{-3}]$ (see Chapter 2, Subsection 2.4.4). The distance to the impact will be assumed equal to the satellite's altitude, meaning that *the impact is assumed to occur at nadir*. Finally, the impact velocity will be assumed as $v = 17$ km/s, which is the minimum assumed velocity found in literature, for a sporadic lunar impact (Oberst *et al.*, 2012).

The sensitivity of the model to v and η_V is presented in Figure 6.22 (left plot), for a fixed altitude of 60000 km (approximately the Earth-Moon L_2 distance to the Moon). The minimum and maximum detectable kinetic energy (KE_{min} and KE_{max}) correspond to $s_{min} = 290 e^-$ and $s_{max} = 80000 e^-$, respectively. Furthermore, the maximum value tested of v , 24 km/s, is found in Suggs *et al.* (2014). By assuming the lower bound of the impact velocity, the estimation of KE_{min} is the most conservative and KE_{max} is the least conservative, but as can be seen on the left-side plot of Figure 6.22, the model is practically non-sensitive to the tested range of v . The largest uncertainty of the model comes instead from the uncertainty in η_V . The right-side plot of Figure 6.22 shows the consequence of such sensitivity with respect to the number of impacts detected in the satellite's FOV. How these types of plots have been generated will be explained in Section 6.4.2. The sensitivity of the number of impacts detected with respect to the assumed impact velocity comes from the gravitational corrections made to the meteoroid flux model used and not from the relation $\eta_V(v)$.

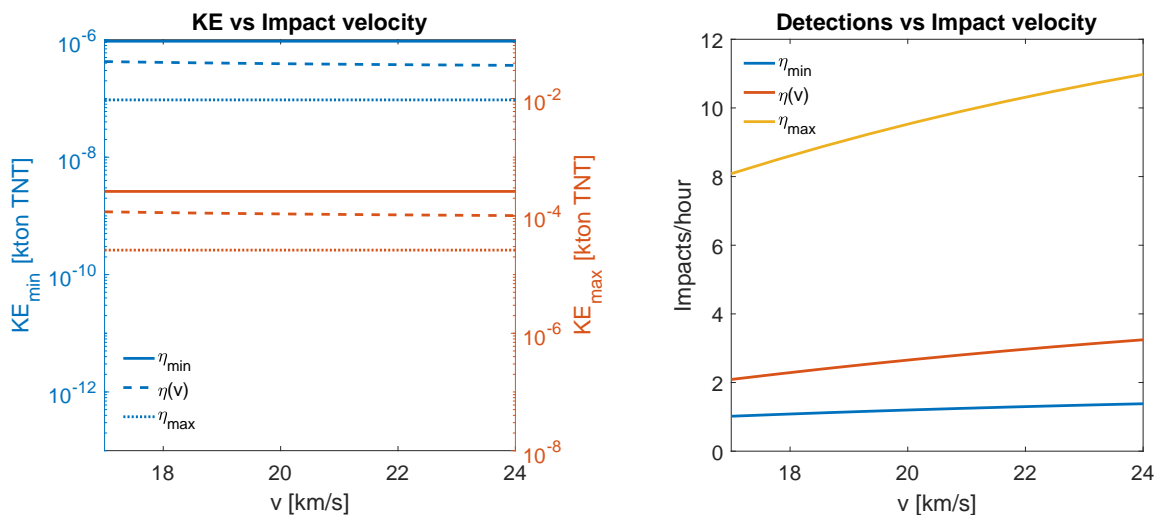


Figure 6.22: Sensitivity of the luminous efficiency method to assumed parameters, in the estimation of the kinetic energy range detected (left) and flux of meteoroids visible in the satellite's FOV (right).

Blackbody method

The methodology employed in the Blackbody method is as follows:

1. Estimation of the flux of electrons generated in the sensor [Raab \(2002\)](#):

$$e_R = \frac{S_{\text{impact}}}{\tau A_{\text{lens}}} \left[\frac{e^-}{m^2} \right] \quad (6.35)$$

2. Estimation of the total flux of photons emitted in the visible, converted to an electron flux (based on [Bouley et al., 2012](#)):

$$e_T = \Delta t \int_{\lambda_1}^{\lambda_2} L(\lambda, T_F) \frac{qe(\lambda)}{E_\gamma(\lambda)} d\lambda \left[\frac{e^-}{m^2} \right] \quad (6.36)$$

where Δt is the assumed duration of the impact, which should be smaller than the exposure time, and T_F is the assumed (constant) blackbody temperature of the impact flash. $L(\lambda, T_F)$ is given by Equation 6.20 and $E_\gamma(\lambda)$ by Equation 6.21;

3. Estimation of the emitting surface area, i.e the effective area of the impact flash ([Bouley et al., 2012](#)):

$$S = 2\pi d^2 \frac{e_R}{e_T} \quad [m^2] \quad (6.37)$$

4. Estimation of the impact's crater diameter:

$$D = \frac{2\sqrt{S/\pi}}{n_{\text{crater}}} \quad [m] \quad (6.38)$$

where n_{crater} is the ratio between the diameter of the impact flash and respective crater, as has been assumed in [Bouley et al. \(2012\)](#). Assuming that the impact is only detected by one pixel, D should smaller than GSD .

5. Estimation of the meteoroid's kinetic energy, from Gault's law ([Bouley et al., 2012](#)):

$$KE = \left(\frac{D}{0.25\rho_p^{0.167}\rho_t^{-0.5}g^{-0.165}(\sin\theta_i)^{1/3}} \right)^{1/0.29} \quad [J] \quad (6.39)$$

where ρ_p and ρ_t are the projectile and target densities, g is the gravitational acceleration at the Moon (see Appendix A) and θ_i is the impact angle with respect to the horizontal.

The nominal parameters assumed in this study are presented in Table 6.10. The distance to the impact will also be assumed equal to the satellite's altitude. Furthermore, Δt , T_M and n_{crater} are assumed not a function of the impactor's kinetic energy. Nonetheless, it is stipulated that there is a correlation between Δt and KE ([Rembold and Ryan, 2015](#)), as brighter flashes are usually longer (see Chapter 2, Subsection 2.4.4). Additionally, the flash temperature is also assumed to be constant during the impact flash emission.

Contrary to the former model, KE_{min} and KE_{max} can vary by more than one order of magnitude, depending on the assumed parameters. The left-side plots on Figure 6.23 demonstrate the sensitivity of the model to three of the parameters assumed: Δt , T_F and n_{crater} , for a fixed satellite altitude of 60000 km. The maximum values tested are the exposure time, for Δt , and for T_F and n_{crater} are taken from [Koschny and McAuliffe \(2009\)](#) and [Bouley et al. \(2012\)](#), respectively. A 1σ -error related to the

Table 6.10: Assumptions of the Blackbody method in estimating the observable kinetic energy range.

Parameter	Symbol	Value	Units	Reasoning
Impact duration	Δt	10	ms	Lower bound of the impact flashes detected on Earth (Bouley <i>et al.</i> , 2012)
Flash temperature	T_F	2700	K	Within the interval mentioned in Suggs <i>et al.</i> (2017)
Diameter ratio	n_{crater}	1	–	Minimum ratio assumed in Bouley <i>et al.</i> (2012)
Projectile's density	ρ_p	2000	kg/m ³	From Bouley <i>et al.</i> (2012)
Target's density	ρ_t	3000	kg/m ³	From Bouley <i>et al.</i> (2012)
Incidence angle	θ_i	45	deg	From Bouley <i>et al.</i> (2012)

magnitude measured by the CCD sensor, computed as follows (Raab, 2002):

$$\sigma_{m_V} = \log_{2.5} \left(1 + \frac{1}{\text{SNR}} \right) \quad (6.40)$$

is also presented. This error is clearly less significant than the possible error associated with the estimation of Δt , T_F or n_{crater} .

By assuming the lower bounds of Δt , T_F and n_{crater} , from the plots of Figure 6.23, it can also be concluded that:

- the estimation of KE_{min} is the most conservative possible, while the estimation of KE_{max} is the least conservative possible;
- the estimation of the number of meteoroid impacts visible in the satellite's FOV is the most conservative possible;

It should be noted that, if KE_{min} is not the most conservative assumption, the number of meteoroids detected in the satellite's FOV can increase exponentially (see Section 6.4.2). Overestimating KE_{max} does not affect as much the estimated number of meteoroid detections, because more energetic impacts are less likely to occur. As such, in order to conservatively estimate the number of meteoroid impacts detectable, also KE_{min} must be estimated conservatively.

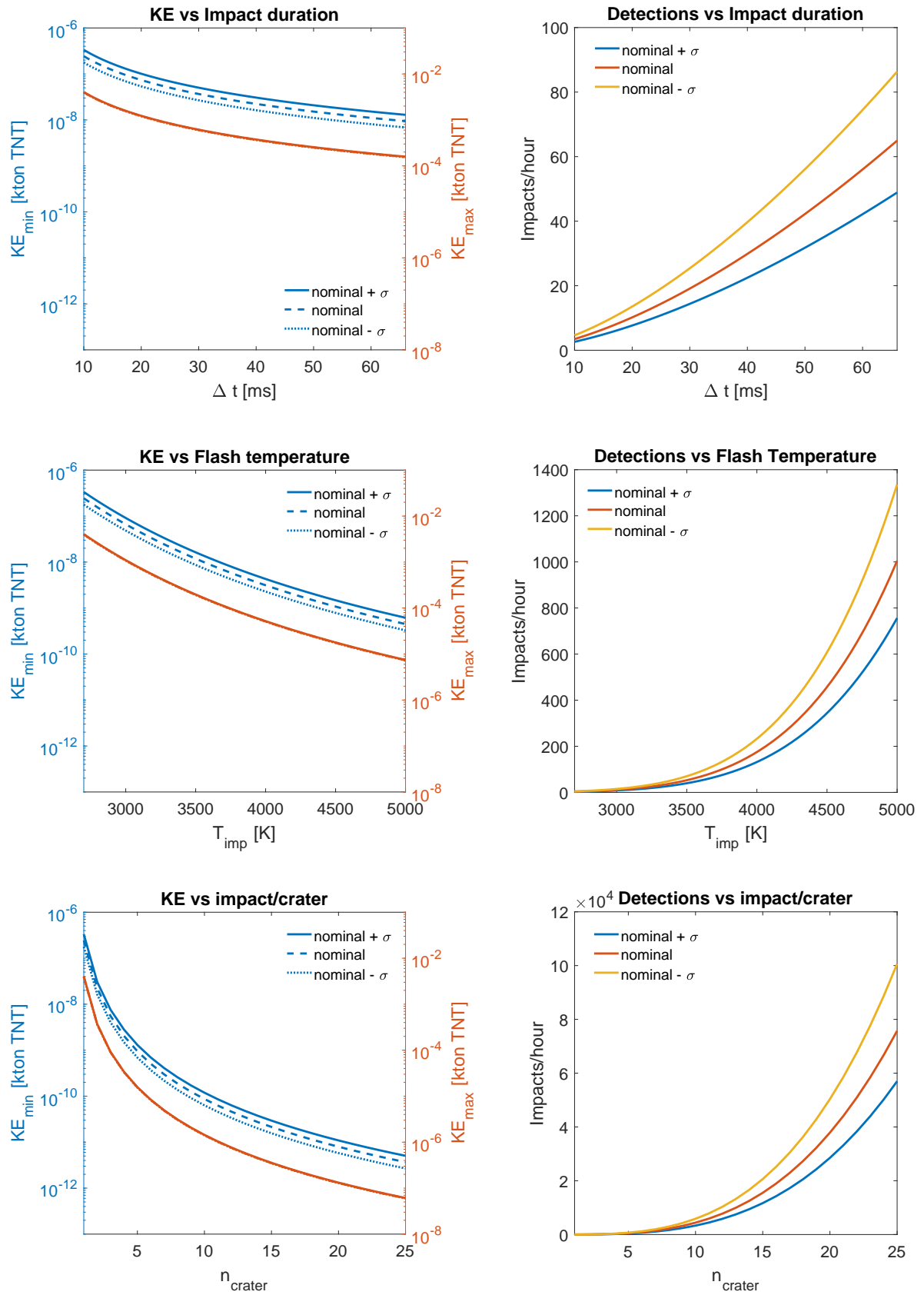


Figure 6.23: Sensitivity of the Blackbody method to assumed parameters (Table 6.10), in the estimation of the kinetic energy range detected (left) and flux of meteoroids visible in the satellite's FOV (right).

Method comparison and sensitivity to position of impact

Both methods presented reasonably agree with respect to the minimum kinetic energy detectable, given the nominal assumptions ($v = 17$ km/s and Table 6.10) and taking into account their respective error margins. The first estimates that $KE_{min} \in [9 \cdot 10^{-8}; 9 \cdot 10^{-7}]$ kton TNT (η_V -error, see Figure 6.22), while the second estimates that $KE_{min} \in [1 \cdot 10^{-7}; 3 \cdot 10^{-7}]$ kton TNT ($1\sigma_m$ -error, see Figure 6.23). However, the methods can disagree by at least two orders of magnitude when it comes to the maximum kinetic energy. The Luminous Efficiency method estimates $KE_{max} \in [2 \cdot 10^{-5}; 2 \cdot 10^{-4}]$ kton TNT (η_V -error, see Figure 6.22), while the Blackbody method estimates $KE_{max} \approx 4 \cdot 10^{-3}$ kton TNT ($1\sigma_m$ -error, see Figure 6.23). These kinetic energy ranges translate into 1 to 8 detections per hour, for the Luminous Efficiency method and 3 to 5 impact flashes detections per hour, for the Blackbody method. Nonetheless, this comparison only holds for the assumption $d = h = 60000$ km.

The top-plots of Figure 6.24 show the variation of KE_{min} and KE_{max} with $h = d$ ($\lambda_{imp} = 0^\circ$ curve), for low altitudes ($100 < h < 1000$ km), using the Luminous Efficiency method and the Blackbody method (left and right-side plot, respectively). The bottom-plots of Figure 6.24 depict the same variation, but for high altitudes ($h > 55000$ km, limit for which the LUMIO-Cam has a full disk view of the Moon – see Chapter 7, Subsection 7.1.1). In fact, for high altitudes the methods reasonably agree with respect to KE_{min} and disagree with respect to KE_{max} , while for low altitudes the opposite is verifiable.

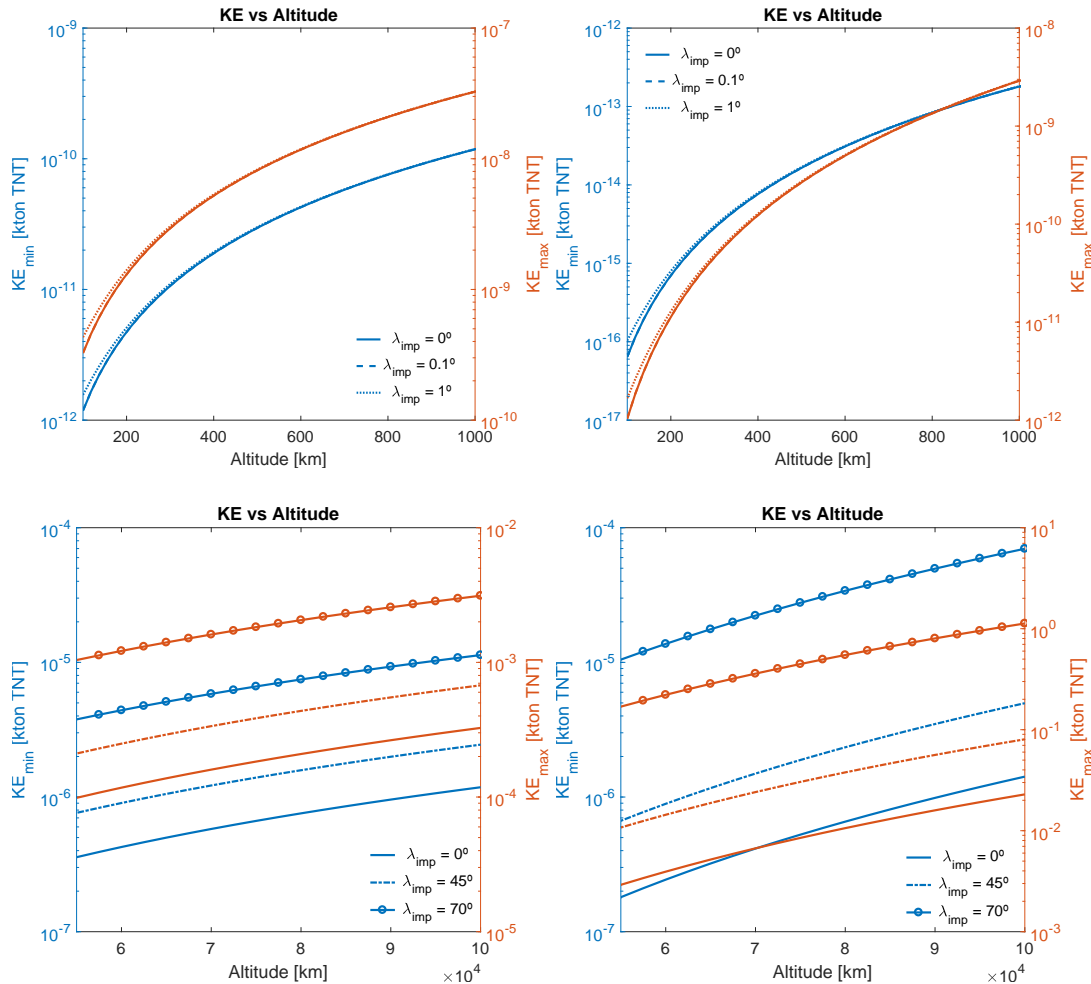


Figure 6.24: Variation of the detectable minimum and maximum kinetic energy with altitude and distance to the impact, for low (top) and high (bottom) altitudes, and the Luminous Efficiency method (left) or Blackbody method (right).

In both figures, the $\lambda_{imp} \neq 0^\circ$ curves represent impacts that are an angle ρ_{imp} off-nadir, assuming $d \neq h$. Figure 6.25 depicts the geometry of an off-nadir impact.

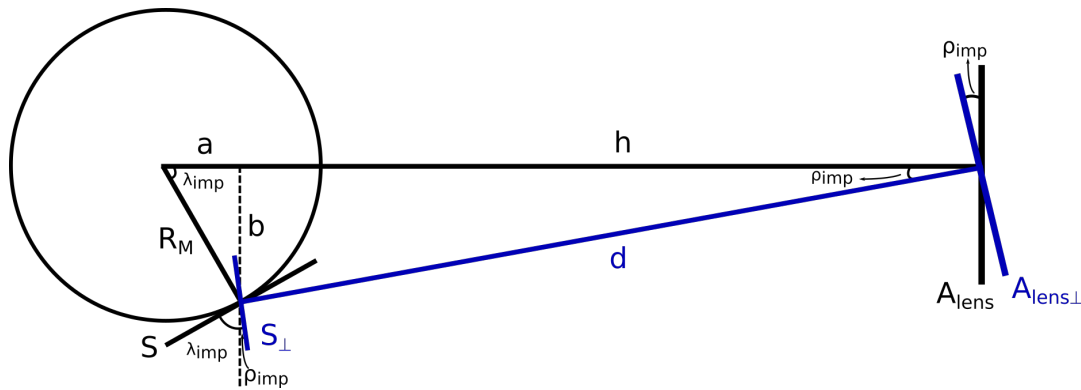


Figure 6.25: Geometry of an off-nadir impact.

From this figure it can be deduced that:

1. The distance to the impact is given by:

$$d = \sqrt{(R_M + h - a)^2 + b^2} \quad (6.41)$$

$$a \equiv R_M \cos \lambda_{imp} \quad (6.42)$$

$$b \equiv R_M \sin \lambda_{imp} \quad (6.43)$$

2. The effective area of the lens (perpendicular to the impact direction) is given by:

$$A_{lens\perp} = A_{lens} \cos^2(\rho_{imp}) \quad (6.44)$$

$$\rho_{imp} \equiv \tan^{-1} \left(\frac{b}{R_M + h - a} \right) \quad (6.45)$$

3. The effective area of the impact is given by:

$$S_{\perp} = S \cos^2(\rho_{imp} + \lambda_{imp}) \quad (6.46)$$

For both methods, the $\lambda_{imp} \neq 0^\circ$ curves are computed using $A_{lens\perp}$, given by Equation 6.44, in Equations 6.32 and 6.35, instead of A_{lens} . In Equations 6.33 and 6.36, d is given by Equation 6.41, and not by the satellite's altitude. For the Blackbody method, S in Equation 6.37 is replaced by S_{\perp} , as given in Equation 6.46. Finally, Equation 6.33 of the Luminous Efficiency method is multiplied by the ratio $A_{lens}/A_{lens\perp}$, given by Equation 6.44.

For low-altitudes, the λ_{imp} tested are 0.1° and 1° , which correspond to the edge of LUMIO-Cam's FOV-area for an altitude of 100 km and 1000 km, respectively. From the top-plots of Figure 6.24, it can then be concluded that, for low altitudes, the assumption that the impact occurs at nadir is reasonable, regardless of the method used. However, the same cannot be said for higher altitudes. Observing the bottom-plots of Figure 6.24, it can be concluded that, for the Luminous Efficiency method, both KE_{min} and KE_{max} would be estimated one order of magnitude higher, if the impact were assumed to occur closer to the edge of the FOV-area. For the Blackbody method the estimations would be almost two orders higher.

Figures 6.26 and 6.27 show the variation of the number of impacts detectable in the instrument's FOV-area with respect to altitude and distance to the impact, for low and high altitudes, respectively. The left-side plots in both figures show absolute values, while the right-side plots are normalised by the nominal case: impacts assumed to occur at nadir ($\lambda_{imp} = 0^\circ$). For low altitudes, as expected, the relative error with respect to the nominal case is small (less than 5% at 1000 km altitude), for both methods. However, for high altitudes the error is $\sim 90\%$, if the impact occurs almost at the edge of the FOV-area ($\lambda_{imp} = 70^\circ$). As such, for CRTBP orbits, the assumption that the impact occurs at nadir is not as reasonable as it is for Frozen Orbits. Hence, for the assessment of the latter, *the impact will be assumed to occur at the midpoint between the sub-satellite point and the closest edge of the FOV-area*. For high altitudes, for example, the FOV-area is the entire full-disk of the Moon ($\lambda_{max} \approx 90^\circ$), so, the midpoint corresponds to $\lambda_{imp} \approx 45^\circ$. Nonetheless, the detectable signal range ($s = [290, 80000]e^{-/pixel}$) will be assumed constant and, so, not a function of the impact's position.

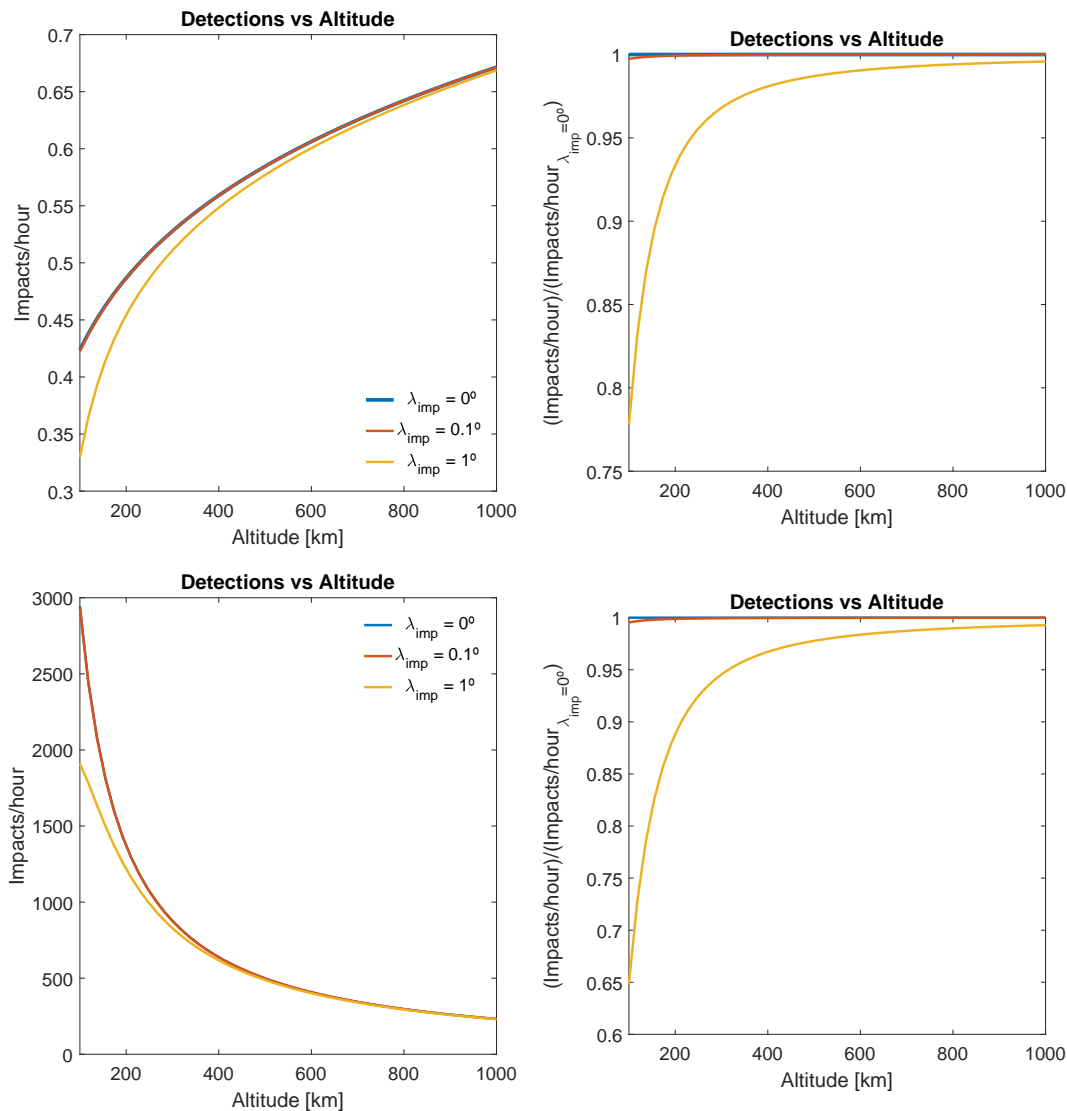


Figure 6.26: Variation of the detectable number of impacts with altitude and distance to the impact (λ_{imp}), for low altitudes and the Luminous Efficiency method (top) or Blackbody method (bottom). The right-side plots present the same results but normalised by the number of impacts detectable at nadir.

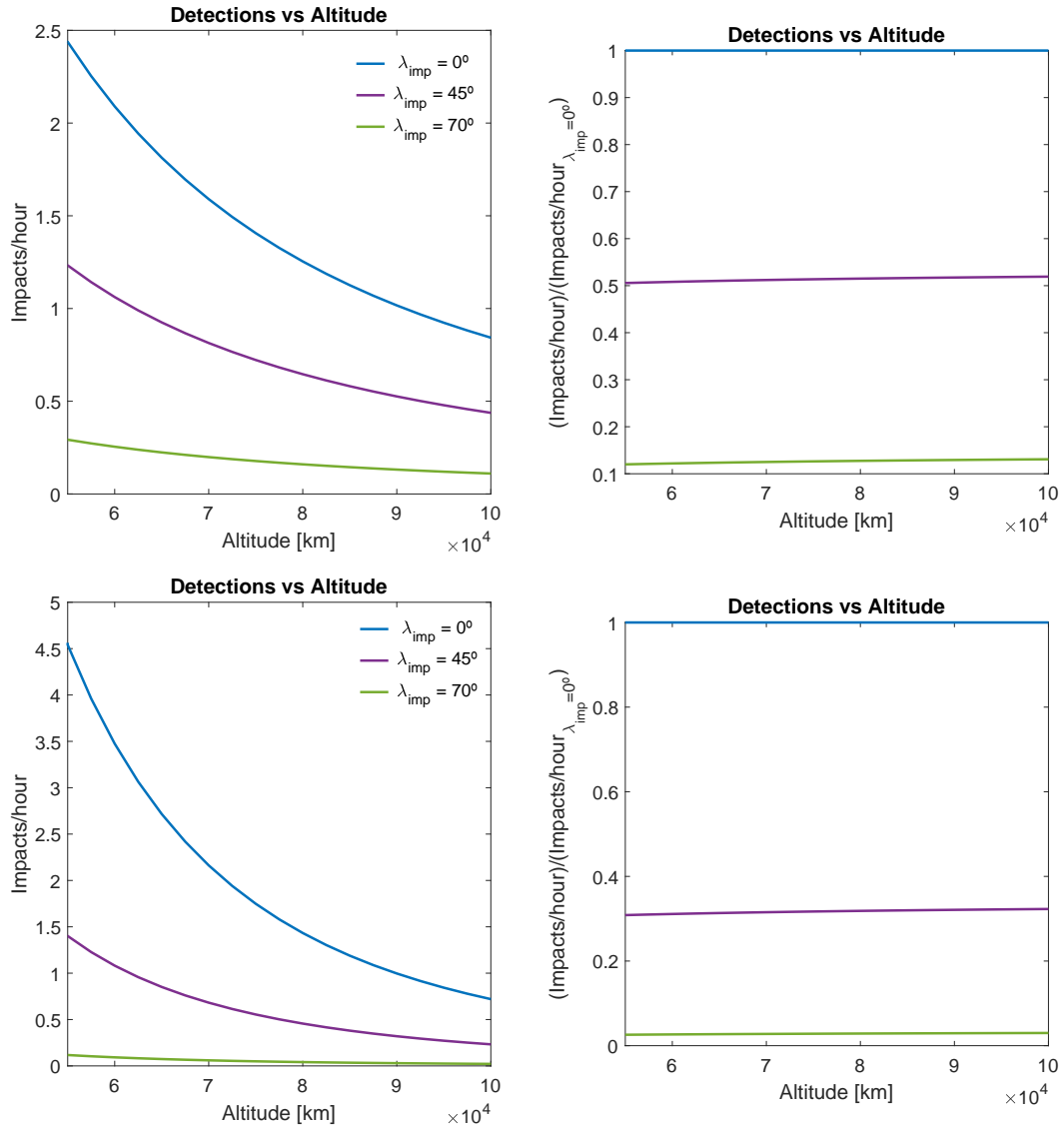


Figure 6.27: Variation of the number of impacts detectable with altitude and distance to the impact (λ_{imp}), for high altitudes and the Luminous Efficiency method (top) or Blackbody method (bottom). The right-side plots present the same results but normalised by the number of impacts detectable at nadir.

Finally, it should also be noted that, while for high altitudes both methods predict that a higher altitude leads to less meteoroid detections, for low altitudes the methods are contradictory. Combining Equations 6.32 to 6.34, it can be concluded that, in the Luminous Efficiency method, $KE \propto d^2$. On the other hand, from Equations 6.35 – 6.39, it can be concluded that, in the Blackbody method, $KE \propto d^{1/0.29}$. From the meteoroid flux used model (see Section 6.4.2), $N_{impacts} \propto KE^{-0.9} \times FOV_{area}$. Since for low altitudes, $FOV_{area} \propto h^2$ (see Equation 7.21) and assuming that $d = h$, this leads to:

$$\text{Luminous Efficiency method: } N_{impacts} \propto h^{0.2} \quad (6.47)$$

$$\text{Blackbody method: } N_{impacts} \propto h^{-1.1} \quad (6.48)$$

As such, the Luminous efficiency method predicts that the number of detections increases with altitude, while the Blackbody method predicts that it decreases. For higher altitudes ($h > 55000$ km), the FOV-

area is approximately constant, so:

$$\text{Luminous Efficiency method: } N_{\text{impacts}} \propto h^{-1.8} \quad (6.49)$$

$$\text{Blackbody method: } N_{\text{impacts}} \propto h^{-3.1} \quad (6.50)$$

6.4.2. Meteoroid Impact Flux Model

The meteoroid impact flux model used in the previous sections is the following (Brown *et al.*, 2002):

$$\log_{10}[f_E(\geq KE_E)] = 0.5677 - 0.9 \log_{10}(KE_E) \quad \left[\frac{\text{impacts}}{\text{year}} \right] \quad (6.51)$$

where f_E is the cumulative number of meteoroid impacts with Earth, per year, for kinetic energies larger than KE_E .

In order to translate this flux at Earth into a meteoroid flux at the Moon, a gravitational correction term must be introduced. Following the method presented in Suggs *et al.* (2014), due to the gravitational attraction of the Earth, both the target's collecting area and impactor's kinetic energy increase by a factor of (see Chapter 2, Subsection 2.2.2):

$$f_{\text{area}} = f_{KE} = 1 + v_{\text{esc}}^2/v^2 = 1 + \frac{11.09^2}{17^2} = 1.4256 \quad (6.52)$$

The cumulative meteoroid impact flux at the Moon, per year, is then:

$$f_M(\geq KE_M) = \frac{f_E(f_{KE} \cdot KE_M)}{f_{\text{area}}} \frac{R_M^2}{R_E^2} \quad \left[\frac{\text{impacts}}{\text{year}} \right] \quad (6.53)$$

where KE_M is the kinetic energy estimation obtained from one of the two methods presented in the last section and R_M and R_E are the radius of the Moon and Earth, respectively. Gravitational corrections regarding the Moon have been neglected (Oberst *et al.*, 2012).

The estimated number of meteoroid impacts in the spacecraft's FOV, presented in Figures 6.22–6.23 and 6.26–6.27, has been computed using this model, as follows:

$$f_{\text{impacts}}(t) = \frac{1}{2} \frac{\text{FOV}_{\text{eff}}}{4\pi R_M^2} [f_M(\geq KE_{\text{min}}) - f_M(\geq KE_{\text{max}})] \quad \left[\frac{\text{impacts}}{\text{year}} \right] \quad (6.54)$$

where FOV_{eff} is the Moon surface area observable by the payload, not illuminated by the Sun. All results presented in the previous section were computed assuming that the entire FOV-area was not illuminated and, so, $\text{FOV}_{\text{eff}} = \text{FOV}_{\text{area}}$. For high altitudes, the area was assumed equal to the Instantaneous Access Area and for low altitudes was given by the *tangent approximation* (see Chapter 7, Section 7.1.1). Furthermore, in the above formula, the number of meteoroid detections per hour has been reduced by a factor of 50%, to take into account possible occultations by lunar mountains (Koschny and McAuliffe, 2009).

The coloured lines on the right-side plots of Figure 6.28 show the sensitivity of using Brown's meteoroid impact flux model (Equation 6.53) in predicting the number of meteoroid detections, with respect to v . The black dotted lines show the sensitivity of using Grün's interplanetary meteoroid flux

model (Grün *et al.*, 1985):

$$f_M(\geq m) = \frac{1}{2} [(2.2 \cdot 10^3 m^{0.306} + 15)^{-4.38} +$$
 (6.55)

$$1.3 \cdot 10^{-9} (m + 1 \cdot 10^{11} m^2 + 1 \cdot 10^{27} m^4)^{-0.36} +$$
 (6.56)

$$1.3 \cdot 10^{-16} (m + 1 \cdot 10^6 m^2)^{-0.85}]$$
 (6.57)

where m is the meteoroid mass in grams. A 1/2 constant has been introduced because the flux given by this model is for a rotating plate with a size of the unit area, and only particles from one half sphere can impact the surface of the Moon (Koschny and McAuliffe, 2009). Furthermore, instead of requiring a kinetic energy estimation, this model requires a meteoroid mass. As such, the sensitivity of this model to the impact velocity assumed comes from $m = 2KE/v^2$. The minimum and maximum mass detectable by LUMIO (m_{min} and m_{max} , respectively) are presented on the left-side plots of Figure 6.28, assuming a distance to the impact flash of $h = 60000$ km.

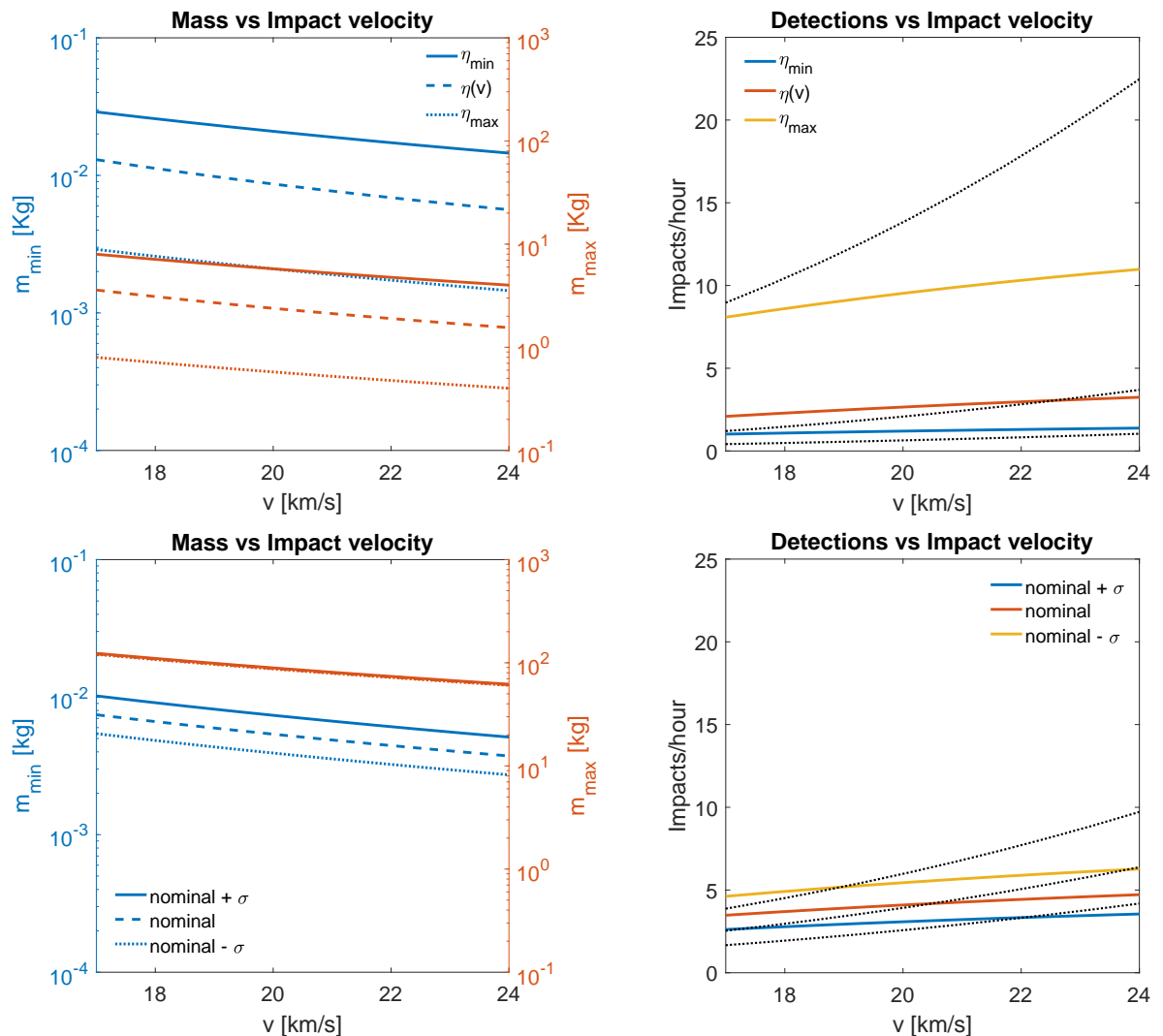


Figure 6.28: Sensitivity of meteoroid mass estimation to the assumed velocity impact (left) and flux of meteoroids visible in the satellite's FOV (right), for both the Luminous Efficiency method (top) and Blackbody method (bottom). The black dotted lines on the right plots were computed using Grün's interplanetary meteoroid flux model, while the coloured lines were computed using Brown's Earth meteoroid flux model, gravitationally corrected.

Comparing both meteoroid detections predictions, one can conclude that Brown's model sensitivity to the impact velocity is less significant than Grün's model. Furthermore, using Brown's model, both methods lead to a number of detections that falls (approximately) within the expected, according to Grün's model (at least for $h = 60000$ km). As such, and since the science requirements have been deduced from the plot of Figure 2.3a, for the remaining analysis, Brown's model will be used. Nonetheless, it should be noted that for $KE > 10^{-7}$ kton TNT Brown's model may overestimate the lunar meteoroid flux, according to Grün's model (see Figure 6.29).

Finally, it should be noted that, by using Brown's model, the meteoroid impact flux asymmetries discussed in Chapter 2, Subsection 2.2.3 will not be taken into account in this study, as the *flux will be assumed uniform across the Moon's surface*. Furthermore, the flux will also be considered evenly distributed throughout the year, meaning that *peaks related to meteoroid showers, will not be taken into account*. Nonetheless, it should be noted that Brown's model includes both the flux of sporadic meteoroids and showers. As such, the flux presented in Figure 6.29, should be seen as an *average flux per unit area and time*.

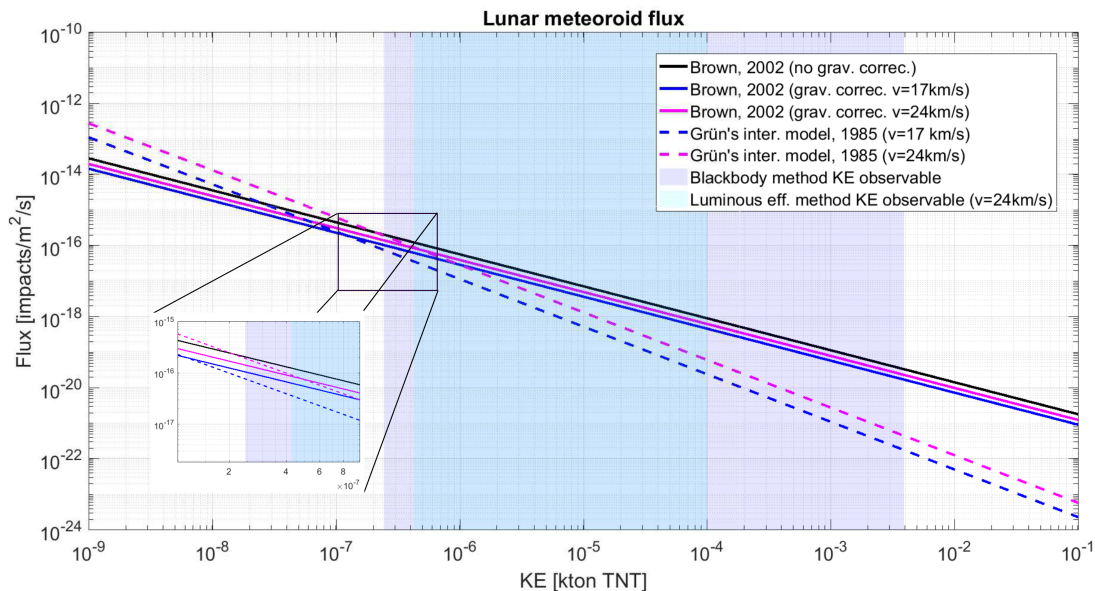


Figure 6.29: Comparison between meteoroid flux models at the Moon. The kinetic energy ranges presented are the nominal values obtained with either the Blackbody or Luminous efficiency method and are valid for a distance to the impact flash of 60000 km.

6.4.3. Validation and Verification

In order to validate the meteoroid environment model, data from a current ESA Earth-based meteoroid impact flashes monitoring program, NELIOTA (see Chapter 2, Subsection 2.4.3), has been used. The programme consists of a telescope with 1.2 m diameter, capable of performing observations in the R-band ($\lambda \in [520, 796]$ nm). Based on data provided on the programme's website⁵, the exposure time has been assumed 33 ms, the lens transmissivity 60% and the average quantum efficiency has been computed as 53%. The programme typically detects 0.46 impacts per hour (16 impacts in 35 hours observation time), with visual magnitudes ranging from +11 to +6. Assuming that these values correspond to the limiting capacity of the detector, it is possible to estimate the minimum and maximum signal received at the detector from Equation 6.31. Then, it is possible to apply both kinetic energy

⁵<https://neliota.astro.noa.gr> [Last accessed on: 13/08/2017]

estimation methods and predict the total number of impacts detectable from Earth ($d = h = 384401$ km). For that purpose, and since no information is available on the area monitored by the telescope, the FOV-area has been assumed as 1/3 of the entire (dark) Moon disk. The results obtained are presented in Table 6.11.

Table 6.11: Validation of the meteoroid environment model with data from the NELIOTA programme⁵. The range presented for the Luminous Efficiency method corresponds to $\Delta t \in [10, 33]$ ms. The FOV-area has been assumed 1/3 of the entire (dark) Moon disk.

Method	KE_{min} (kton TNT)	KE_{max} (kton TNT)	Impacts/hour
Luminous Efficiency	$[0.922, 3.043] \cdot 10^{-6}$	$[0.922, 3.043] \cdot 10^{-4}$	[0.35, 0.12]
Blackbody	$2.774 \cdot 10^{-6}$	$7.787 \cdot 10^{-3}$	0.13

Since the results obtained, with both methods, are the same order of magnitude as the detected in the NELIOTA programme, the methodology applied can be considered validated.

References

- K. F. Wakker, *Fundamentals of Astrodynamics* (Delft University of Technology, Institutional Repository Library, Delft, 2015).
- Lunar Geodesy and Cartography Working Group and Lunar Reconnaissance Orbiter Project, *A Standardized Lunar Coordinate System for the Lunar Reconnaissance Orbiter*, Tech. Rep. (Goddard Space Flight Center, NASA, Greenbelt, Maryland, 2008).
- G. Aguiar, *Earth-Mars low-thrust transfers with ballistic capture and real-Solar System dynamics*, Master thesis (unpublished), Delft University of Technology (2017).
- R. G. Gottlieb, *Fast gravity, gravity partials, normalized gravity, gravity gradient torque and magnetic field: derivation, code and data*, Tech. Rep. (Nasa, Lyndon B. Johnson Space Center, 1993).
- J. P. S. Carvalho, R. Vilhena de Moraes and A. F. B. A. Prado, *Some orbital characteristics of lunar artificial satellites*, *Celestial Mechanics and Dynamical Astronomy* **108**, 371 (2010).
- A. S. Konopliv, R. S. Park, D. N. Yuan, S. W. Asmar et al., *The JPL lunar gravity field to spherical harmonic degree 660 from the GRAIL Primary Mission*, *Journal of Geophysical Research: Planets* **118**, 1415 (2013).
- T. A. Ely, *Stable constellations of frozen elliptical inclined lunar orbits*, *Journal of the Astronautical Sciences* **53**, 301 (2005).
- A. Konopliv, *Recent Gravity Models as a Result of the Lunar Prospector Mission*, *Icarus* **150**, 1 (2001).
- A. Abad, A. Elipe and E. Tresaco, *Analytical Model to Find Frozen Orbits for a Lunar Orbiter*, *Journal of Guidance, Control, and Dynamics* **32**, 888 (2009).
- C. Zhang, F. Topputo, F. Bernelli-Zazzera and Y. Zhao, *Low-Thrust Minimum-Fuel Optimization in the Circular Restricted Three-Body Problem*, *Journal of Guidance, Control, and Dynamics* **38**, 1501 (2015).
- M. T. Ozimek, *A Low-Thrust Transfer Strategy to Earth-Moon Collinear Libration Point Orbits*, Master thesis, Purdue University (2006).

- D. J. Grebow, M. T. Ozimek, K. C. Howell and D. C. Folta, *Multi-body orbit architectures for lunar south pole coverage*, *Journal of Spacecraft and Rockets* **45**, 334 (2008).
- D. J. Grebow, *Generating Periodic Orbits in the Circular Restricted Three-Body Problem with Applications to Lunar South Pole Coverage*, Master thesis, Purdue University (2006).
- F. Topputo, *Fast numerical approximation of invariant manifolds in the circular restricted three-body problem*, *Communications in Nonlinear Science and Numerical Simulation* **32**, 89 (2016).
- R. Thurman and P. A. Worfolk, *The geometry of halo orbits in the circular restricted three-body problem*, Tech. Rep. (The Geometry Center, University of Minnesota, 1996).
- G. Turner, *Results of Long-Duration Simulation of Distant Retrograde Orbits*, *Aerospace* **3**, 37 (2016).
- D. C. Folta, N. Bosanac, D. Guzzetti and K. C. Howell, *An earth-moon system trajectory design reference catalog*, *Acta Astronautica* **110**, 341 (2015).
- D. Guzzetti, N. Bosanac, A. Haapala, K. C. Howell et al., *Rapid trajectory design in the Earth-Moon ephemeris system via an interactive catalog of periodic and quasi-periodic orbits*, *Acta Astronautica* **126**, 439 (2016).
- J. R. Wertz, *Orbit & Constellation Design & Management* (Microcosm Press; Springer, 2009).
- H. Raab, *Detecting and measuring faint point sources with a CCD*, in *Proceedings of Meeting on Asteroids and Comets in Europe (MACE)* (2002).
- F. Topputo, M. Massari, A. Cervone, P. Sundaramoorthy et al., *LUMIO: Lunar Meteoroids Impact Observer, A Cubesat at Earth-Moon L2, Challenge Analysis*, Tech. Rep. (Politecnico di Milano, Delft University of Technology, École Polytechnique Fédérale de Lausanne, The University of Arizona, S[&]T Norway, and Leonardo SpA, 2017).
- S. Bouley, D. Baratoux, J. Vaubaillon, A. Mocquet et al., *Power and duration of impact flashes on the Moon: Implication for the cause of radiation*, *Icarus* **218**, 115 (2012).
- L. K. Harding, R. T. Demers, M. Hoenk, P. Peddada et al., *Technology advancement of the CCD201-20 EMCCD for the WFIRST coronagraph instrument: sensor characterization and radiation damage*, *Journal of Astronomical Telescopes, Instruments, and Systems* **2**, 11007 (2015), [arXiv:arXiv:1601.01761v1](https://arxiv.org/abs/1601.01761v1) .
- Politecnico di Milano, *Negotiation Meeting for the ITT 8643–Lunar Cubesats for Exploration (LUCE)*, (2017), Minutes of Meeting, MoM-ITT8643-Negotiation.
- R. M. Suggs, D. E. Moser, W. J. Cooke and R. J. Suggs, *The flux of kilogram-sized meteoroids from lunar impact monitoring*, *Icarus* **238**, 23 (2014), [arXiv:1404.6458](https://arxiv.org/abs/1404.6458) .
- W. R. Swift, D. E. Moser, R. M. Suggs and W. J. Cooke, *An Exponential Luminous Efficiency Model for Hypervelocity Impact into Regolith*, in *Proceedings of the Meteoroids 2010 Conference* (2011) pp. 125–141.
- J. Oberst, A. Christou, R. M. Suggs, D. Moser et al., *The present-day flux of large meteoroids on the lunar surface - A synthesis of models and observational techniques*, *Planetary and Space Science* **74**, 179 (2012).

- J. J. Rembold and E. V. Ryan, *Characterization and Analysis of Near-Earth Objects via Lunar Impact Observations*, *Planetary and Space Science* **117**, 119 (2015).
- R. Suggs, S. Ehlert and D. Moser, *A comparison of radiometric calibration techniques for lunar impact flashes*, *Planetary and Space Science* (2017), 10.1016/j.pss.2017.04.016.
- D. Koschny and J. McAuliffe, *Estimating the number of impact flashes visible on the Moon from an orbiting camera*, *Meteoritics and Planetary Science* **44**, 1871 (2009).
- P. Brown, R. E. Spalding, D. O. ReVelle, E. Tagliaferri *et al.*, *The flux of small near-Earth objects colliding with the Earth*. *Nature* **420**, 294 (2002).
- E. Grün, H. A. Zook, H. Fechtig and R. H. Giese, *Collisional balance of the meteoritic complex*, *Icarus* **62**, 244 (1985).

7

Coverage Analysis

This chapter concerns Step 4 of the methodology presented in Chapter 4. The goal is to perform a trade-off analysis of the candidate orbits, taking only into account evaluation criteria related to lunar meteoroid impacts. For that purpose, a meteoroid impact flashes coverage analysis will be performed. How such coverage analysis will be performed is detailed in Section 7.1. The validation of the MATLAB® tool developed is presented in Section 7.2 and the results obtained are presented in Section 7.3. Finally, the orbit trade-off is presented in Section 7.4.

7.1. Methodology

The coverage analysis that will be performed is characterised by the interaction between three main modules, given the inputs of the Payload and Candidate Orbits modules, as depicted in the scheme of Figure 7.1. These modules are:

- The **meteoroid environment module**, described in Chapter 6, Section 6.4. Given the range of signals detectable by the payload and an altitude profile, this module can independently determine the range of kinetic energies detectable by LUMIO, for each candidate orbit. Once this range is known, it is possible to predict the average lunar meteoroid impact flux;
- The **FOV-area module**, which is responsible for computing the Moon surface area observable by the LUMIO-Cam. The payload's FOV and the position of the spacecraft are the two main inputs. Furthermore, a certain attitude profile must also be assumed. This module is described in detail in Section 7.1.1;
- The **lunar nightside monitoring module**, which is responsible for determining the fraction of the FOV-area not illuminated by the Sun. Since lunar impact flashes can only be detected on the lunar nightside, this module allows the determination of what will be referred to as the *effective FOV-area*. This module is described in detail in Section 7.1.2.

Combining the outputs of these three modules, it is possible to determine the total number of meteoroids detectable by LUMIO, over the mission lifetime. How that and other meteoroid related evaluation parameters can be computed will be explained in Section 7.1.3.

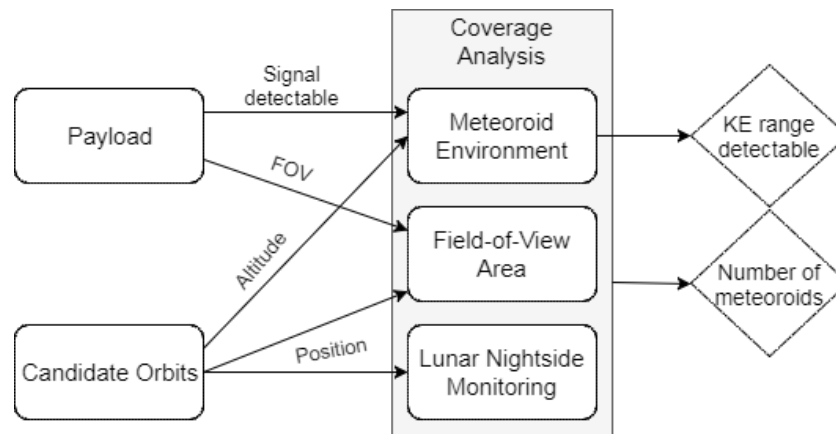


Figure 7.1: Scheme of the coverage analysis experimental set-up.

7.1.1.1. Field-of-View Area

The surface area that a spacecraft's instrument can observe, at one instant or extended period of time, defines the *coverage* of the central body. There are two main concepts associated with coverage analysis, which will be explained in detail in this section.

The first is the *footprint* or *FOV-area* of that instrument, which is the area that it can observe at a certain instant in time. On the other hand, the *Instantaneous Access Area (IAA)* is the total area that the instrument potentially could observe, if the spacecraft or instrument itself is turned. These concepts are both depicted in Figure 7.2, and, as can be observed, the *FOV-area* can be much smaller than the *IAA*. (Wertz, 2009, p.432-433,472-476)

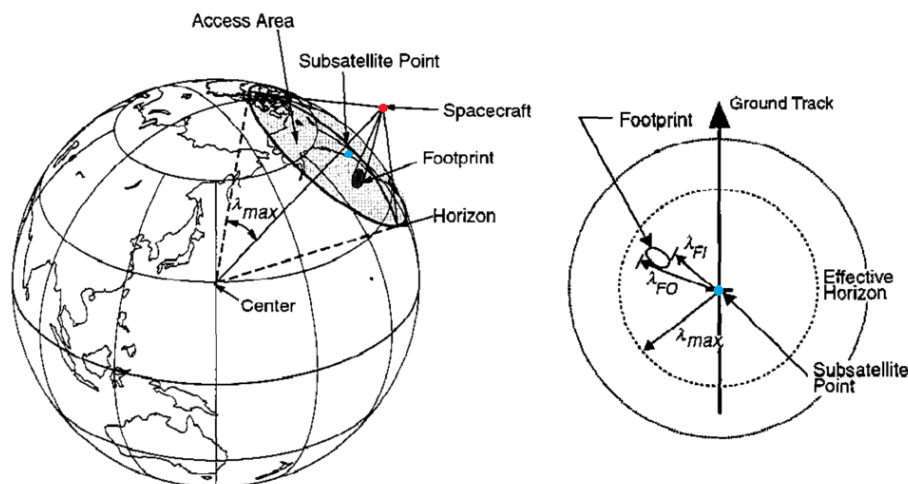


Figure 7.2: Instantaneous access area and footprint definition: 3D (left) and 2D (right) representations. From Wertz (2009, p.471,474).

The shape of the *FOV-area* on the central body's surface depends on several factors, such as the instrument's working principle. For an array sensor, such as the *LUMIO-Cam* detector, each of its straight edges projects onto the spacecraft's sky as a great-circle arc, as depicted in Figure 7.3 (left). Each of these great circles then project into space as a plane surface and intersects the celestial body as a small circle. These small circles define the edges of the instrument's *FOV-area*, within the spacecraft's *IAA*, as depicted in Figure 7.3 (right). In this figure, the projection of the array's *FOV* onto the central

body is clearly distorted, as the instrument is pointing off nadir. Otherwise, the array's FOV shape would be approximately maintained.

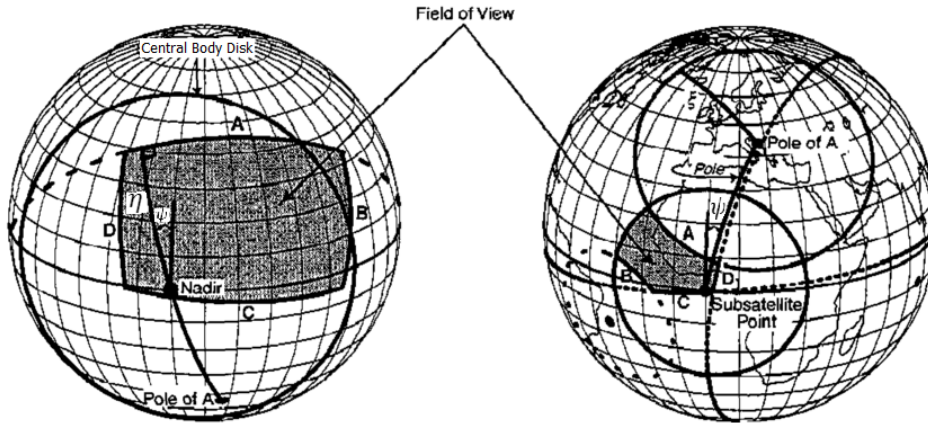


Figure 7.3: Projection of an array's FOV onto the spacecraft's sky (left) and onto the central body's surface (right). From Wertz (2009, p.433).

Figure 7.4 defines the main parameters required to compute the FOV-area, where:

- λ denotes the angle of a small circle of the central body, measured at the central body;
- ε denotes the elevation at the *toe* of the footprint;
- θ_{FOV} denotes the Field-of-View of the array sensor projected onto the spacecraft's sky;
- η denotes the off-nadir angle, measured at the spacecraft from the *subsatellite* point to the target.

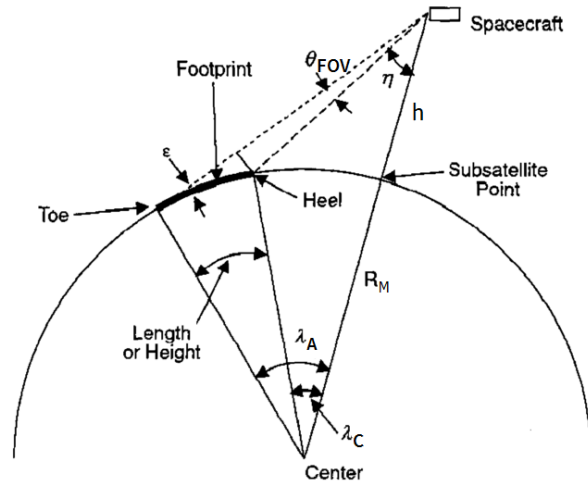


Figure 7.4: Definition of footprint parameters. From Wertz (2009, p.473).

Assuming that the centre of FOV-edges A and C (Figure 7.3) are aligned with nadir, from Figure 7.4, it can be deduced that the *footprint length* (L_F) is given by:

$$L_F^{AC} = R_M(\lambda_A - \lambda_C) \equiv R_M \Delta \lambda^{AC} \quad (7.1)$$

where λ_A is the central body angle at the *toe* of the footprint, corresponding to **FOV** edge A, and λ_C is the central body angle at the *heel* of the footprint, corresponding to **FOV** edge C. If, additionally, the instrument's **FOV** is pointing at nadir, $\eta = \theta_{FOV}/2$. In this case, the shape of the **FOV**-area can be assumed to approximate a rectangle and is given by:

$$FOV_{area} \approx L_F^{AC} \cdot L_F^{BD} = R_M^2 \Delta\lambda^{AC} \Delta\lambda^{BD} \quad (7.2)$$

where $\Delta\lambda^{BD}$ can be defined analogously to $\Delta\lambda^{AC}$. Furthermore, if the array's **FOV** is squared, $\Delta\lambda^{AC} = \Delta\lambda^{BD}$.

However, while this approximation is reasonable for low satellite altitudes, for higher altitudes, the curvature of the central body's surface must be taken into account. For a square array sensor, the **FOV**-area can then take three different shapes:

1. For $h < h_1$, all **FOV** corners and midpoints project onto the central body surface inside the **IAA**. In this case, the **FOV**-area has the shape depicted on the left side of Figure 7.5;
2. For $h_1 < h < h_2$, all **FOV** midpoints project onto the central body surface inside the **IAA**, but all corners project outside it. In this case, the **FOV**-area has the shape depicted on the right side of Figure 7.5;
3. For $h > h_2$, all **FOV** midpoints and corners project outside the **IAA**. In this case, the **FOV**-area is the **IAA** itself.

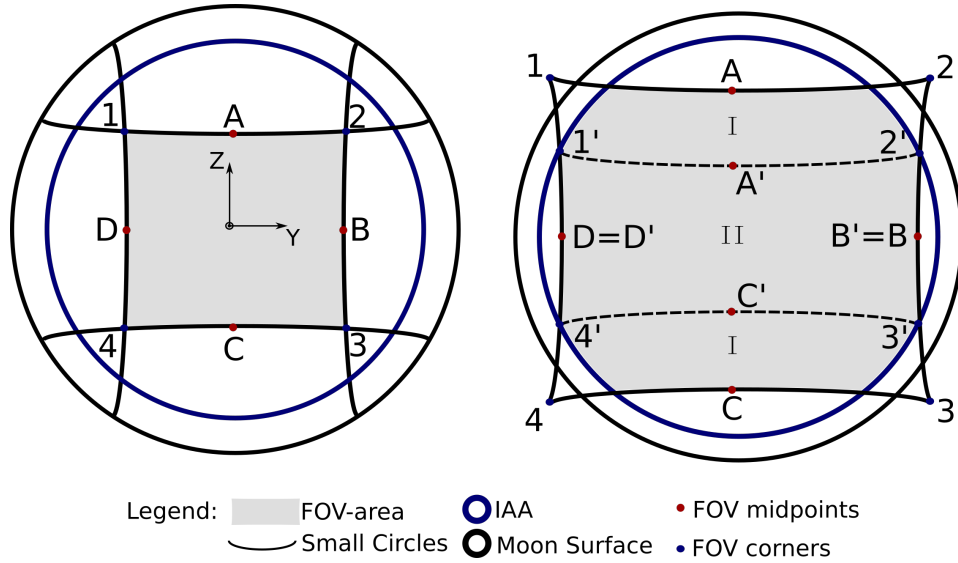


Figure 7.5: **FOV**-area of an array sensor for high altitudes. On the left, all **FOV** corners and midpoints project onto the central body surface inside the **IAA** and, on the right only the midpoints project inside the **IAA**.

In order to compute the **FOV**-area in cases 1 and 2, the reference frame depicted in Figure 7.5 is defined, centred at the Moon. The X-axis points towards the Sub-Satellite point, the Z-axis points to the centre of the small-circle correspondent to the projection of edge B and the Y-axis completes the right-handed frame.

Observing the left-side of Figure 7.5, one can conclude that the **FOV**-area is symmetric with respect to the XZ and XY-plane. Furthermore, the small-circles (correspondent to the projection of edges) A

and C are circles of constant latitude and the small-circles D and B are in a plane parallel to the XZ-plane (i.e. have a constant y-coordinate). As such, for case 1, it is possible to determine the FOV-area by integration, as follows:

$$\text{FOV}_{\text{area}} = \int_{\varphi_C}^{\varphi_A} \int_{\theta_D}^{\theta_B} R_M^2 \cos \varphi \, d\theta d\varphi \quad (7.3)$$

with:

$$\varphi_C = -\varphi_A = -\frac{\Delta\lambda^{AC}}{2} \quad (7.4)$$

$$\theta_D = -\theta_B = -\sin^{-1} \left(\frac{\sin(\Delta\lambda^{BD}/2)}{\cos \varphi} \right) \quad (7.5)$$

where Equation 7.5 has been deduced solving the following system for θ_B :

$$\begin{cases} y_B = R_M \sin(\Delta\lambda^{BD}/2) \\ y_B = R_M \sin \theta_B \cos \varphi \end{cases} \quad (7.6)$$

Observing the right-side of Figure 7.5, one can conclude that the FOV-area is given by the sum of three parts, two of which are equal (Parts I). The area given by Part II can be computed analogously to case 1, using Equations 7.3–7.5 and knowing $\Delta\lambda^{A'C'}$ and $\Delta\lambda^{B'D'}$. The area given by Part I is given by:

$$\text{FOV}_{\text{area}}^I = \int_{\varphi_{A'}}^{\varphi_A} \int_{\theta_{1'}}^{\theta_{2'}} R_M^2 \cos \varphi \, d\theta d\varphi \quad (7.7)$$

with:

$$\varphi_{A'} = \frac{\Delta\lambda^{A'C'}}{2}; \quad \varphi_A = \frac{\Delta\lambda^{AC}}{2} \quad (7.8)$$

$$\theta_{1'} = -\theta_{2'} = -\cos^{-1} \left(\frac{\cos(\lambda_{max})}{\cos \varphi} \right) \quad (7.9)$$

where Equation 7.9 has been deduced solving the following system for $\theta_{2'}$:

$$\begin{cases} x_{2'} = R_M \cos(\lambda_{max}) \\ x_{2'} = R_M \cos \theta_{2'} \cos \varphi \end{cases} \quad (7.10)$$

and λ_{max} is the central angle associated with the IAA. The total FOV-area in case 2 is then given by:

$$\text{FOV}_{\text{area}} = 2\text{FOV}_{\text{area}}^I + \text{FOV}_{\text{area}}^{\text{II}} \quad (7.11)$$

The IAA is defined by the *effective horizon*, which describes a small circle on the surface of the central body with central angle λ_{max} . This angle corresponds to a minimum elevation (ε_{min}) at which the spacecraft's instrument can work or the minimum elevation necessary to perform a certain observation. This concept is also depicted in Figure 7.2 (right). The IAA is given by:

$$\text{IAA} = 2\pi R_M^2 [1 - \cos(\lambda_{max})] = 2\pi R_M^2 \left(1 - \frac{R_M}{R_M + h} \right) \quad (7.12)$$

where it has been assumed that $\varepsilon_{min} = 0$. For large altitudes, it can happen that the instrument's FOV

covers the entire IAA. Hence, in case 3, $\lambda_A > \lambda_{max}$, and so, FOV-area = IAA. For a given instrument (i.e. fixed θ_{FOV}), total IAA coverage is guaranteed when:

$$h > R_M \left(\frac{1}{\sin(\theta_{FOV}/2)} - 1 \right) \equiv h_2 \quad (7.13)$$

As such the methodology applied in order to determine the FOV-area for each candidate orbit is as follows:

1. Define an attitude profile for LUMIO, assumed as constant nadir pointing. Since the LUMIO-Cam reference frame is fixed with respect to the spacecraft reference frame (see Chapter 6, Section 6.1), this can be done specifying that $+Z_{cam}$ points to the centre of the Moon and $+Y_{cam}$ points in the direction of the orbital velocity. For that purpose, the SPICE utility *prediCkt.exe* is used. The attitude profile for each orbit is then automatically stored in a C-matrix Kernel (CK). A CK is a file that contains a transformation (usually known as the ‘‘C-matrix’’) which provides time-tagged¹ orientation angles for a spacecraft bus;
2. Project the instrument’s FOV corners and midpoints of each edge onto the Moon’s surface. This can be done using SPICE’s function *cspice_sincpt*. The main inputs are the ephemeris of the spacecraft, the name of the target body and the corresponding body-fixed frame. The latter has been defined as the ME reference frame. The main output is the direction vector of the surface intercept point (\mathbf{r}_i), expressed in Cartesian coordinates, relative to the ME frame at the intercept epoch, or a flag indicating that the point does not project onto the selected body’s surface;
3. If all FOV midpoints project onto the Moon surface, $\Delta\lambda^{CA}$ and $\Delta\lambda^{DB}$ can be computed, as follows:

$$\begin{aligned} \Delta\lambda^{CA} &= \text{atan}_2(\|\mathbf{r}_A \times \mathbf{r}_C\|, \mathbf{r}_A \cdot \mathbf{r}_C) \\ \Delta\lambda^{DB} &= \text{atan}_2(\|\mathbf{r}_D \times \mathbf{r}_B\|, \mathbf{r}_D \cdot \mathbf{r}_B) \end{aligned} \quad (7.14)$$

where $\text{atan}_2(Y, X)$ is the four-quadrant inverse tangent and \mathbf{r}_i denotes the intersection direction vector of the midpoint of edge i . If all FOV corners also project onto the Moon, the FOV-area can then be computed using the approximation of Equation 7.2, for low altitudes, or Equation 7.3, for high altitudes (case 1). Otherwise, Equation 7.11 should be used (case 2). In this case, function *cspice_sincpt* can be used to determine the new intersection direction vectors, \mathbf{r}_i' . Finally, if no midpoints or corners project onto the lunar surface (case 3), the FOV-area is given by Equation 7.12.

7.1.2. Lunar Nightside Monitoring

In order to determine the effective FOV-area (FOV_{eff}) a different methodology is applied for TBP or CRTBP orbits. Both are based on the determination of the Sun–Moon–Spacecraft angle (β) in order to determine the illumination conditions of the FOV-area. However, for TBP orbits it is assumed that the FOV-area is either 100% or 0% illuminated, while for CRTBP orbits it is assumed that a fraction (f_{dark}) of the FOV-area is non-illuminated (as has been done in Chapter 5, Section 5.3). Figure 7.6 depicts some schematic illuminations of the FOV-area, for low or high altitudes and different angles β .

¹The time-tag associated with the attitude definition of a spacecraft implies also the definition of an on-board time count, i.e. a ‘‘spacecraft clock’’. This can be done using the SPICE utility *makclk.exe* and a Spacecraft Clock Kernel. This kernel only needs to be generated once for all orbits and only needs to be updated if the mission starting date (t_0) is altered.

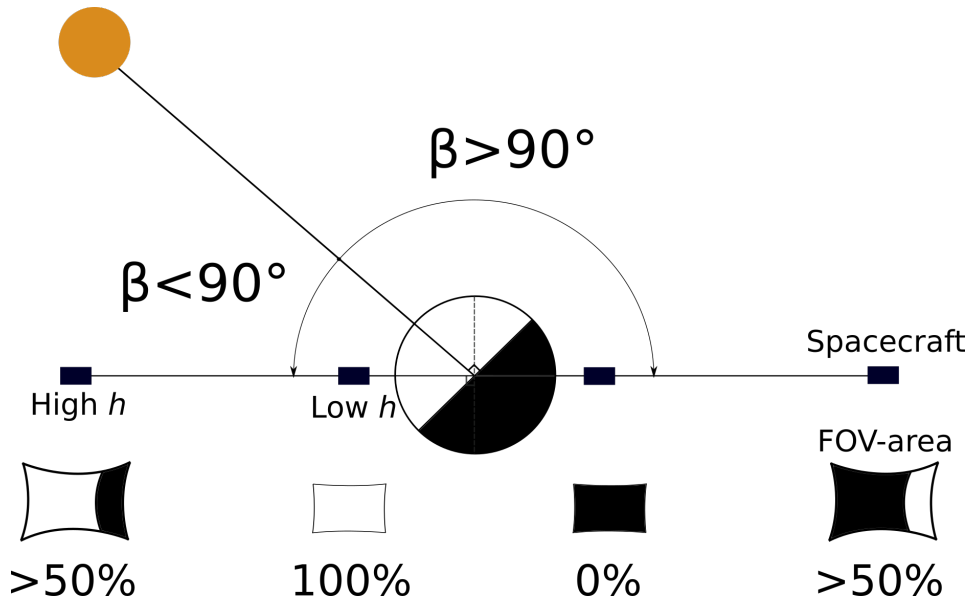


Figure 7.6: Scheme of the FOV-area illumination for low and high altitudes and different Sun-Moon-Spacecraft phase angles (β). The percentages denote the fraction of the FOV-area illuminated. Distances are not to scale.

Two-Body Problem Orbits

In order to determine the effective FOV-area, the following methodology is applied:

1. Determination of the Sun-Moon-Spacecraft angle at each epoch t , using SPICE function *cspice_phaseq*;
2. Determination of the effective FOV-area as follows:

$$\text{FOV}_{\text{eff}}(t) = \begin{cases} \text{FOV}_{\text{area}}, & \text{if } \beta(t) \geq 90^\circ \\ 0, & \text{if } \beta(t) < 90^\circ \end{cases} \quad (7.15)$$

since, as can be seen in Figure 7.6, for $\beta > 90^\circ$ the spacecraft observes the nightside of the Moon, and for $\beta < 90^\circ$ the dayside.

Circular Restricted Three-Body Problem Orbits

In order to determine the effective FOV-area, the following methodology is applied:

1. Determination of the Sun-Moon-Spacecraft angle at each epoch t , using SPICE function *cspice_phaseq*;
2. Determination of the fraction of the FOV-area non-illuminated, as follows:

$$f_{\text{dark}}(t) = \frac{\beta(t)}{180} \quad (7.16)$$

with $\beta \in [0, 180]^\circ$;

3. Determination of the effective FOV-area as follows:

$$\text{FOV}_{\text{eff}}(t) = \begin{cases} f_{\text{dark}} \cdot \text{FOV}_{\text{area}}, & \text{if } \beta(t) \geq 90^\circ \\ 0, & \text{if } \beta(t) < 90^\circ \end{cases} \quad (7.17)$$

where it has been assumed that if the illumination of the FOV-area is $< 50\%$ (i.e. $f_{\text{dark}} < 0.5 \Leftrightarrow \beta < 90^\circ$), no observations can be performed and, so, the effective FOV-area is zero.

7.1.3. Number of Meteoroid Detections

Once the effective FOV-area is known, the total number of meteoroids detected in the kinetic energy range $[KE_{min}, KE_{max}]$, over the mission lifetime, is determined as follows:

1. Estimation of the impact flux visible in the satellite's effective FOV-area, as function of time (see Chapter 6, Subsection 6.4.2):

$$f_{impacts}(t) = \frac{1}{2} \frac{FOV_{eff}}{4\pi R_M^2} [f_M(\geq KE_{min}) - f_M(\geq KE_{max})] \left[\frac{impacts}{year} \right] \quad (6.54)$$

where FOV_{eff} , KE_{min} and KE_{max} are a function of time;

2. Estimation of the average impact flux visible in the satellite's effective FOV-area, during one synodic month (S_M), as follows:

$$\begin{aligned} \bar{f}_{impacts} &= \frac{1}{S_M} \int_{t_0}^{t_0+S_M} f_{impacts}(t) dt \approx \frac{1}{S_M} \sum_{i=1}^{N_{SM}} (f_{impacts}(t_i) \cdot \Delta t_i) = \frac{\Delta t}{S_M} \sum_{i=1}^{N_{SM}} f_{impacts}(t_i) \\ \Rightarrow \bar{f}_{impacts} &= \frac{1}{N_{SM}} \sum_{i=1}^{N_{SM}} (f_{impacts}(t_i)) \end{aligned} \quad (7.18)$$

where N_{SM} denotes the number of points with which an orbit has been discretized in the period S_M and Δt denotes the step size, constant for each orbit. In order to guarantee that the coverage characteristics of an orbit are assessed properly, each orbit has been discretized with a personalized N_{rev} points per revolution. As such, N_{SM} has been determined for each orbit as follows:

$$N_{SM} = \frac{S_M}{P} N_{rev} \quad (7.19)$$

3. Estimation of the total number of meteoroids detected over the mission lifetime, as follows:

$$N_{impacts} = \bar{f}_{impacts} \cdot \text{Lifetime} \quad (7.20)$$

where it is assumed that $\bar{f}_{impacts}$ remains constant for the mission duration.

7.2. Verification and Validation

Figure 7.7 shows the altitude (left) and FOV-area (right) of a Frozen Orbit, computed for one orbital revolution. From the right-side plot, it can be observed that the result obtained with the planar approximation (Equation 7.2) is the same as the obtained with Equation 7.3, which takes into account the Moon's curvature. As such, it can be concluded that the planar approximation suffices for low altitudes.

The results obtained are also in accordance with a rough approximation of the FOV-area, given by:

$$FOV_{area} \approx \left[2h \tan\left(\frac{\theta_{FOV}}{2}\right) \right]^2 \quad (7.21)$$

The maximum difference with respect to this approximation is $\approx 9 \text{ km}^2$. By comparing the two plots of Figure 7.7, it can also be concluded that the FOV-area of low altitude satellites is mainly a function of altitude, as Equation 7.21 indicates. As such, the implementation of the method to determine FOV-area of low altitude orbits can be considered validated.

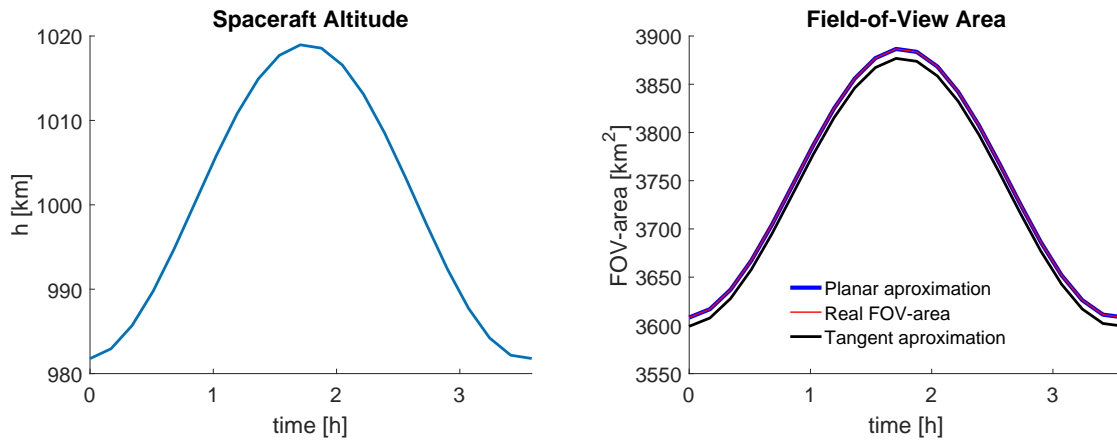


Figure 7.7: Altitude (left) and FOV-area (right) of a Frozen Orbit with $a = 2738$ km, $i = 50^\circ$ and $\omega = 90^\circ$, during one orbit revolution.

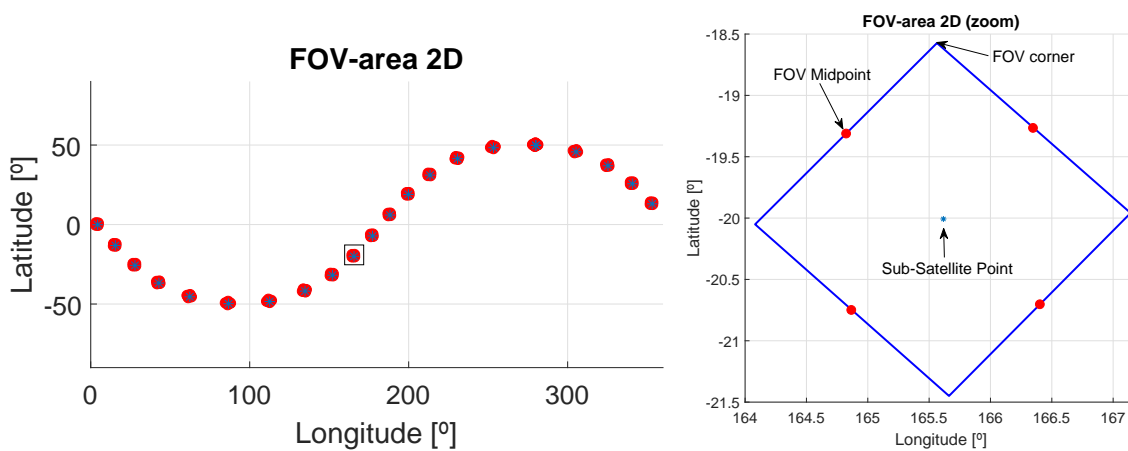


Figure 7.8: Frozen orbit FOV-area 2D representation, during one orbital revolution (left) and at one instant (right). Frozen Orbit with $a = 2738$ km, $i = 50^\circ$ and $\omega = 90^\circ$.

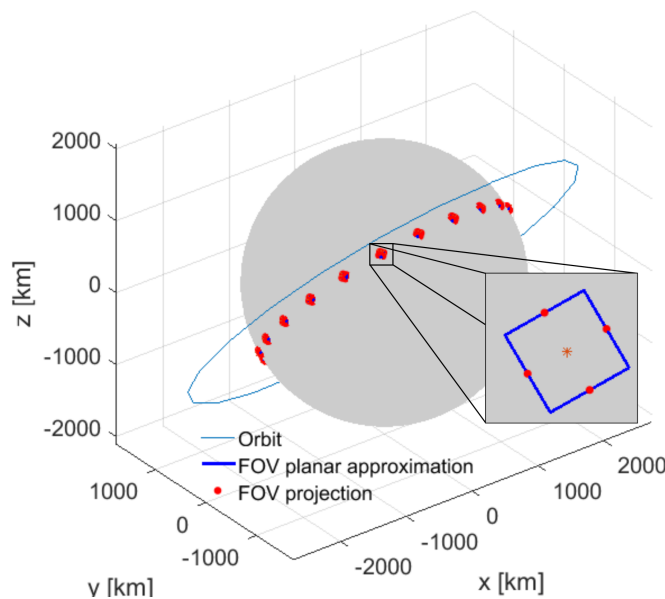


Figure 7.9: Frozen orbit FOV-area 3D representation, during one orbit revolution. Frozen Orbit with $a = 2738$ km, $i = 50^\circ$ and $\omega = 90^\circ$.

Figures 7.8 and 7.9 depict a representation of a Frozen Orbit's footprint in the Moon's surface in 2 and 3 Dimensions, respectively. From these representations one can observe that the FOV-area is indeed centred with the subsatellite point. As such, the spacecraft is pointing at nadir and the FOV has been correctly projected onto the Moon's surface. Furthermore, it is also possible to visually verify that the planar approximation is reasonable, as the projection of the FOV midpoints fall on the approximated FOV-area edges.

In order to validate the method applied for higher altitude orbits, a Lyapunov Orbit with $A_x = 21000$ km has been used. Figures 7.10 and 7.11 (left) show the altitude and FOV-area, respectively, computed for one synodic month. The right-side plot of Figure 7.11 depicts a warning flag which is 1 when a FOV point projects onto the Moon surface and 0 when it does not project.

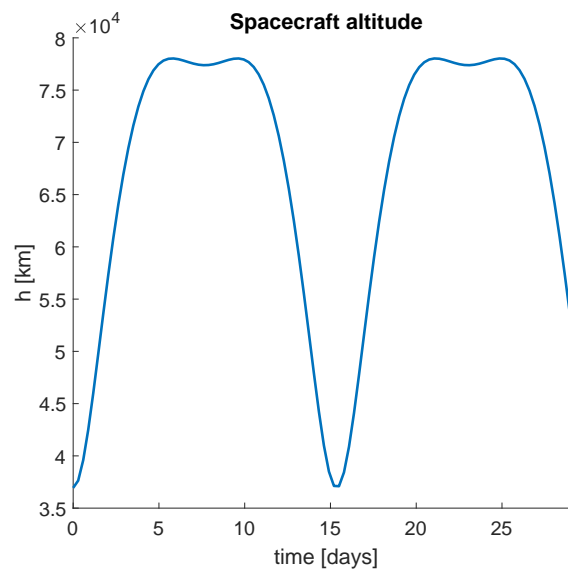


Figure 7.10: Altitude variation of a Lyapunov orbit with $A_x = 21000$ km during one synodic month.

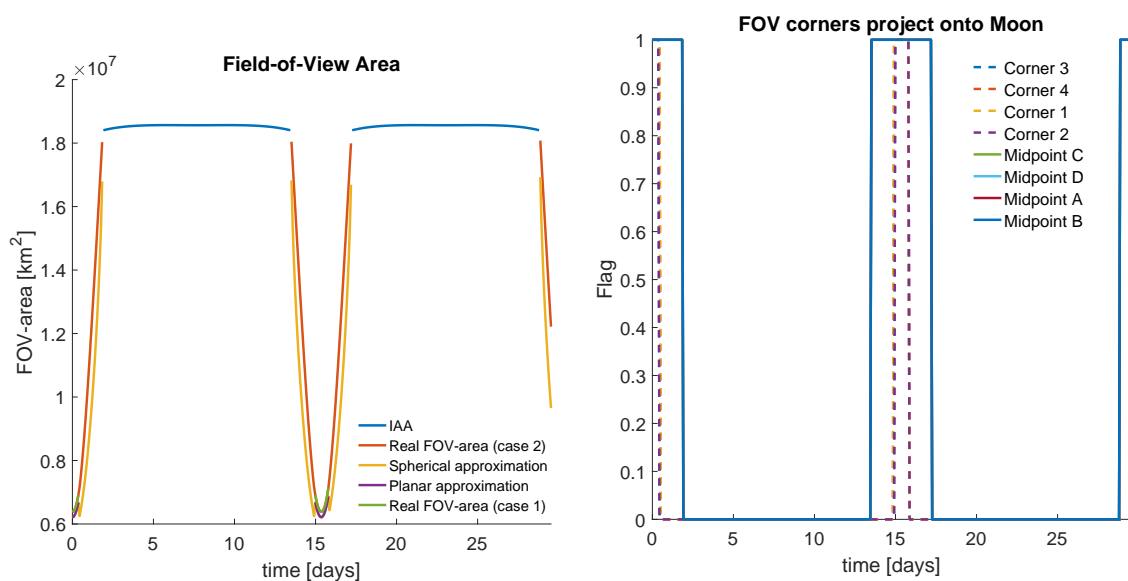


Figure 7.11: FOV-area (left) of a Lyapunov orbit with $A_x = 21000$ km for one synodic month. The right-side plot depicts a warning flag which is 1 when a FOV point projects onto the Moon surface and 0 when it does not project.

This flag can be used to validate the computation of the FOV-area for the three cases presented in Subsection 7.1.1. Given that for LUMIO, $\theta_{FOV} \approx 3.5^\circ$ and its FOV cross-diagonal is $\approx 4.95^\circ$, from Equation 7.13 it can be computed $h_1 \approx 38000$ km and $h_2 \approx 55000$ km. From the right-side plot of Figure 7.11 and Figure 7.10, it can be concluded that, as expected, when $h > 55000$ km, the FOV midpoints and corners do not project onto the Moon surface and when $h < 38000$ km all points do project. Simultaneously, it can be verified, on the left-side plot of Figure 7.11, that that is when the FOV-area is given by the IAA (case 3) or Equation 7.3 (case 1), respectively. On the other hand, when $h_1 < h < h_2$, it can be verified that only the midpoints project onto the lunar surface and that this is when the FOV-area is given by Equation 7.11 (case 2).

From Figure 7.11, it can also be verified that, for $h < h_1$, the FOV-area given by the planar approximation (Equation 7.2) is an underestimation. The maximum error of this approximation for these altitudes is ≈ 170000 km², for $t = 0$. As such, and as expected, the planar approximation is not appropriate for high altitudes.

Figure 7.12 depicts the FOV-area at $t = 0$. In this figure, the real FOV-area is delimited by the red small-circles and the planar approximation is represented by the square with blue lines. The black lines represent great-circles correspondent to edges B and D. Instead of using the planar approximation, a spherical approximation using these great-circles could also have been used to estimate the FOV-area. Since great-circles are circles of constant longitude, this can be done by fixing θ_B and θ_D in Equation 7.5. Figure 7.11 also shows this approximation for $h_1 < h < h_2$. Despite having the same variation with h as the real FOV-area, this approximation fails by $1.21 \cdot 10^6$ km² close to the discontinuity at h_2 . As such, it can be concluded the spherical approximation, despite being simpler, would also not have been appropriate to accurately determine FOV-area at high altitudes.

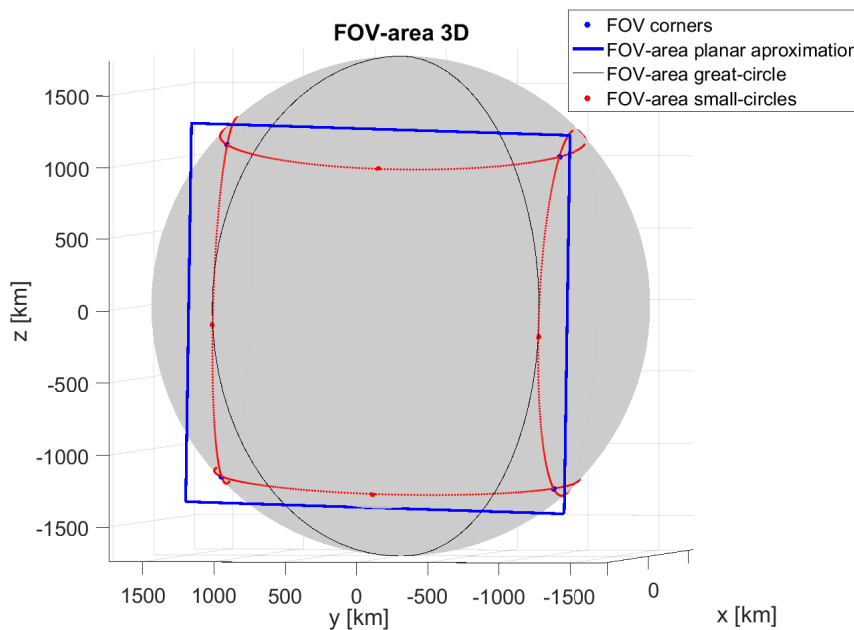


Figure 7.12: Lyapunov orbit ($A_x = 21000$ km) FOV-area 3D representation, when all FOV corners project onto the Moon surface.

From the left-side plot of Figure 7.11 and Figure 7.10 it is also possible to observe that, similarly to low altitude orbits, the FOV-area for $h < h_2$ is mainly a function of altitude. On the other hand, for $h > h_2$ the FOV-area is approximately constant. However, when computing the effective FOV-area, the latter is no longer verifiable. As can be observed in Figure 7.13, the FOV-area plotted in Figure 7.11

is reduced, proportionally to the Sun-Moon-Spacecraft angle, β . Furthermore, from Figure 7.13, it can also be verified that, for $\beta < 90^\circ$, there is no effective FOV-area. This occurs approximately for half of the synodic period ($t > 15$), as expected for an Earth-Moon L_2 orbit (see Chapter 5, Section 5.3). As such, the methodology presented in Section 7.1.2, for CRTBP orbits, can be considered validated.

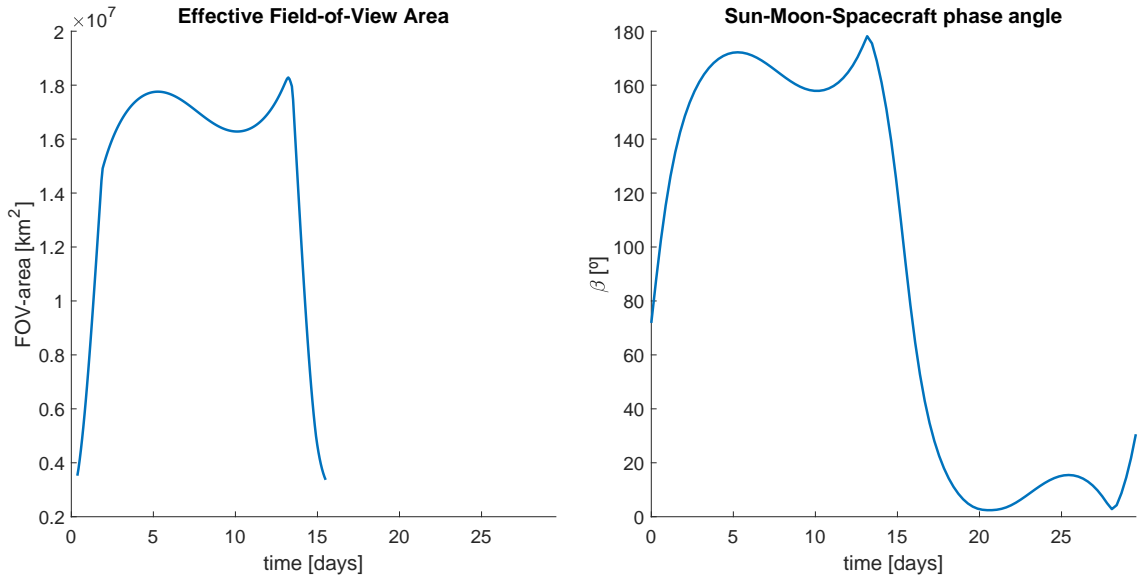


Figure 7.13: Effective FOV-area (left) and Sun-Moon-Spacecraft angle (right) in a Lyapunov orbit with $A_x = 21000$ km, for one synodic month, starting at $t_0 = 01$ Jan 2020 12:00:00.000 (TDB).

The plots of Figure 7.14 show the variation of altitude, effective FOV-area and Sun-Moon-Spacecraft angle of all Frozen Orbits with $a_0 = 2738$ km and $\omega_0 = 90^\circ$. The left-side plots correspond to the first two revolutions and the right-side plots to the last two revolutions, in one synodic month. Once again, it can be verified that, for $\beta < 90^\circ$, there is no effective FOV-area. Furthermore, for $\beta > 90^\circ$, the effective FOV-area is equal to the full FOV-area (cf. Figure 7.7, for $i_0 = 50^\circ$). Knowing that, for $a_0 = 2738$ km, the orbital period is ≈ 3.5 hours, from Figure 7.14 it can also be verified that no impact flashes observations can be made for approximately half period intervals. Since this was the expected for circular orbits (see Chapter 5, Section 5.3), the methodology presented in Section 7.1.2 for Frozen Orbits can be considered validated.

Comparing the β -angles for the first and last two revolutions, in the bottom plots of Figure 7.14, it can also be observed that the periodicity of β is not constant. Namely, all inclinations experience an increase of the amplitude of β . Hence, if the orbits were integrated for another synodic month, the effective FOV-area profile would most likely not be the same as the depicted in Figure 7.14. As such, assuming that the profile $f_{\text{impacts}}(t)$ repeats itself every synodic month, and, so, \bar{f}_{impacts} remains constant during the mission lifetime (see Section 7.1.3) is a rough estimation.

The same conclusion applies for CRTBP-orbits, but for a different reason. As can be seen in the right-side plot Figure 7.13, the periodicity of β is not completed in 29.5 days. Consequently, so is not the periodicity of the effective FOV-area. As such, assuming that a \bar{f}_{impacts} , computed for 29.5 days, remains constant during the mission lifetime is, once again, a rough estimation.

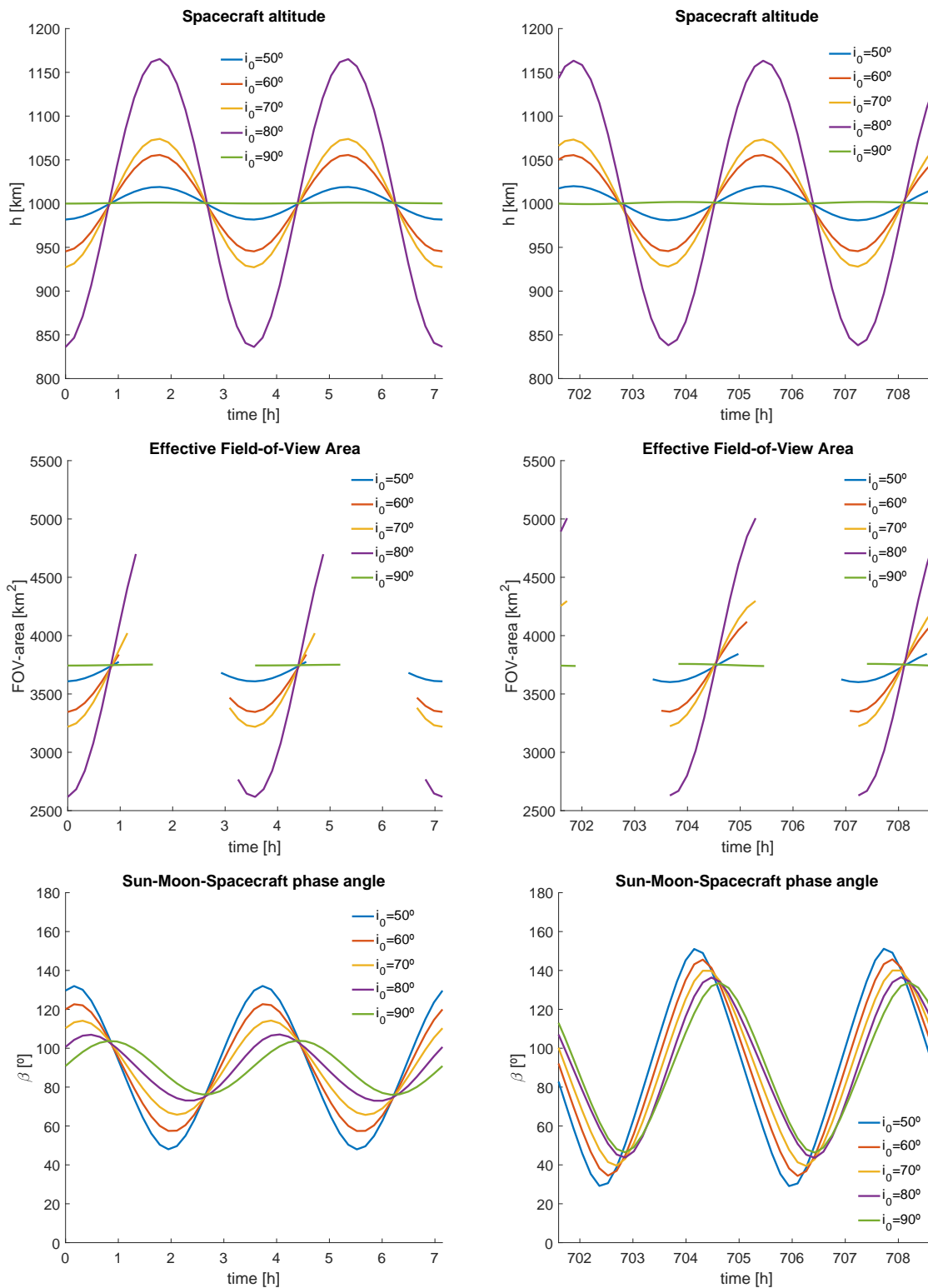


Figure 7.14: Altitude (top), effective FOV-area (centre) and Sun-Moon-Spacecraft angle (bottom) of a Frozen Orbit with $a = 2738$ km, $50^\circ < i < 90^\circ$ and $\omega = 90^\circ$. The left-side plots correspond to the first two revolutions and the right-side plots to the last two revolutions, in one synodic month, starting at $t_0 = 01$ Jan 2020 12:00:00.000 (TDB).

Finally, it should also be noted that, given the t_0 chosen, β is in phase with the FOV-area for the presented Lyapunov orbit, but out of phase for the Frozen Orbits. Given two spacecraft with similar FOV-area profiles, the one which is in phase with β has a larger cumulative effective FOV-area, during one synodic period. As such, the latter could possibly detect more meteoroid impacts. Ideally, all orbits should be assessed under equivalent illumination conditions. However, that would require optimising the phasing of the spacecraft in its orbit, with respect to the Sun, for each candidate orbit, which will not be taken into account in this study.

7.3. Results

7.3.1. Field-of-View 3.5°

Figure 7.15 shows the minimum and maximum kinetic energy detectable by the LUMIO-Cam from a Frozen Orbit, for the two methods presented in Chapter 6, Section 6.4. Only the inclinations which allow the maximum number of detections, per semi-major axis, are presented for brevity, but the results shown are representative of all inclinations. As expected, with both methods, KE_{min} and KE_{max} increase with altitude (larger a), but the methods considerably disagree in the KE ranges detectable for Frozen Orbits. The Luminous efficiency method estimates that $KE_{min} \in [10^{-13}, 10^{-9}]$ kton TNT and $KE_{max} \in [10^{-10}, 10^{-7}]$ kton TNT, while the the Blackbody method estimates that $KE_{min} \in [10^{-18}, 10^{-12}]$ kton TNT and $KE_{max} \in [10^{-12}, 10^{-8}]$ kton TNT.

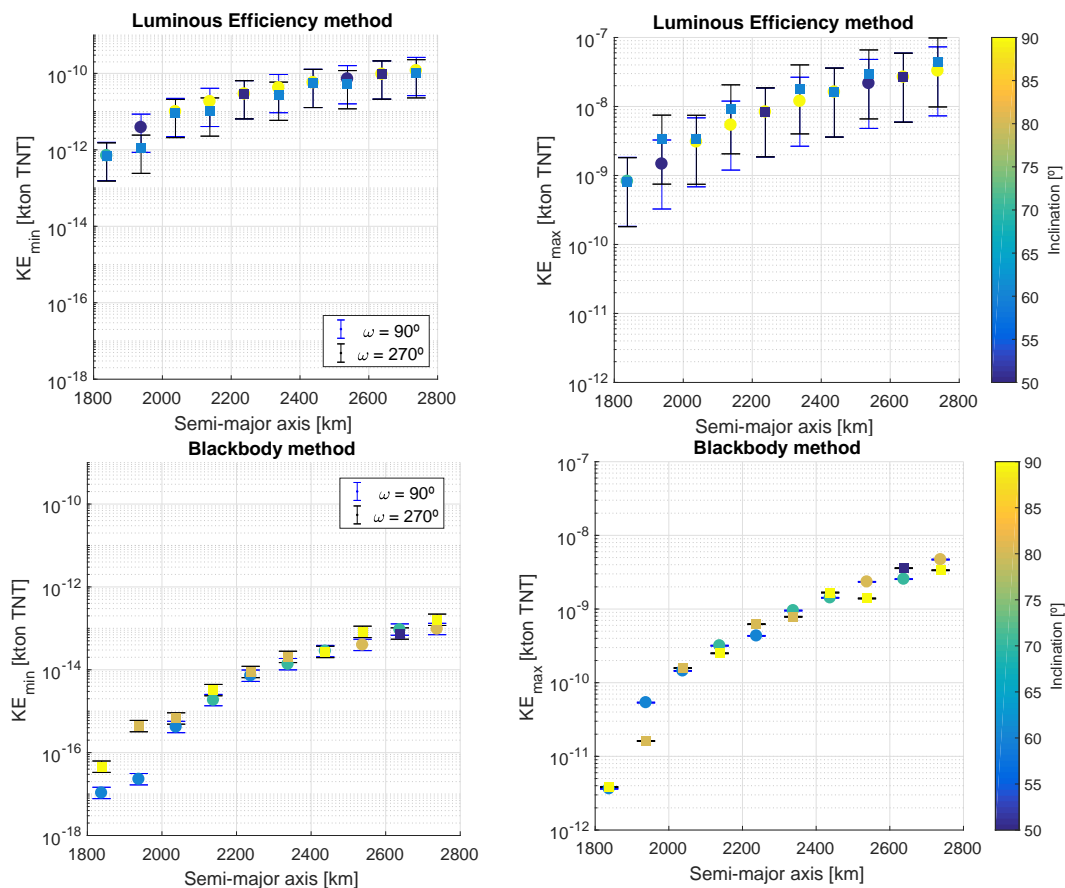


Figure 7.15: Estimated detectable kinetic energy range from Frozen Orbits, using two different methods. Only the inclination which allows the maximum number of detections, per semi-major axis, is presented. Circles and squares represent orbits with $\omega = 90^\circ$ and $\omega = 270^\circ$, respectively.

Figure 7.16 shows the corresponding total number of meteoroid detections during the mission lifetime. Also as expected from the analysis presented in Chapter 6, Subsection 6.4.1, the Luminous Efficiency method predicts more meteoroid detections for increasing altitude, while the Blackbody method predicts the contrary. Furthermore, due to the disagreement in the estimation of KE_{min} , the Luminous Efficiency method predicts the detection of much less meteoroids than the Blackbody method. The former estimates between ≈ 4000 and 9000 meteoroid detections during the mission lifetime for a [Frozen Orbit](#), while the later estimates between $\approx 2 \cdot 10^6$ and $2 \cdot 10^8$ meteoroids during the same period.

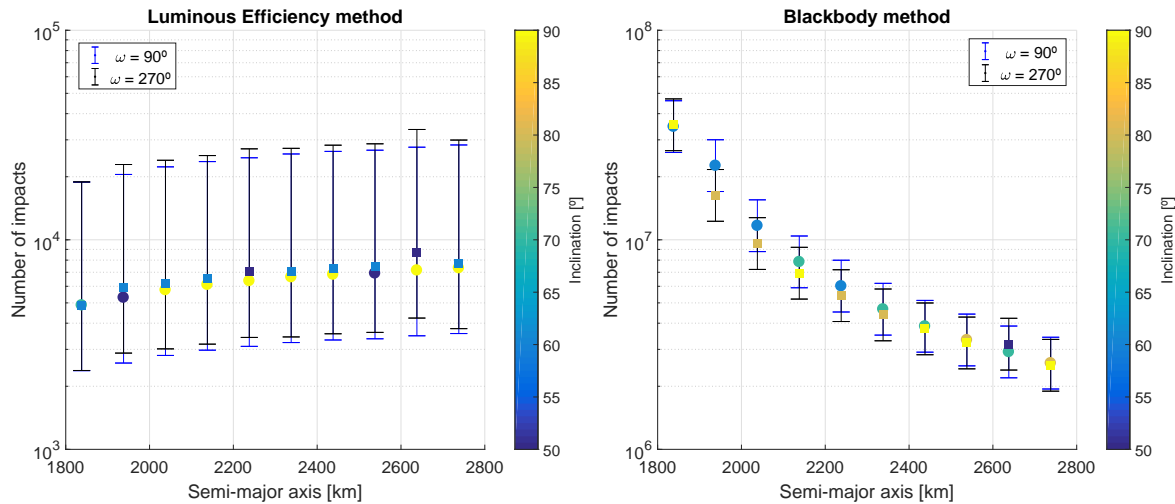


Figure 7.16: Estimated total number of meteoroid detections from Frozen Orbits during the mission lifetime, using two different kinetic energy estimation methods. Only the inclination which allows the maximum number of detections, per semi-major axis, is presented. Circles represent orbits with $\omega = 90^\circ$ and squares represent orbits with $\omega = 270^\circ$.

[Oberst et al. \(2011\)](#) mentions that the SPOSH camera² would be able to detect about “1–100 flashes in its field of view [90°] every day, [...] with magnitudes brighter than $m_V = +7$ ”, from a 50 km altitude lunar orbit. This means between 365 and 36500 impacts detections per year, or an average of 18250 impacts per year. Given that the LUMIO-cam has a FOV 16 times smaller than the SPOSH camera and at least twice the altitude, the estimation made by the Luminous Efficiency method is more in alignment with the presented in [Oberst et al. \(2011\)](#), than the Blackbody method. According to this data, the Blackbody method overestimates the number of impacts detectable from a [Frozen Orbit](#), by at least two orders of magnitude. Nonetheless, in [Oberst et al. \(2011\)](#), it is unclear which methodology has been applied to estimate SPOSH’s number of detections.

Figure 7.17 shows the minimum and maximum kinetic energy detectable by the LUMIO-Cam from each of the CRTBP studied and the two kinetic energy estimation methods applied. The black lines represent the kinetic energy requirements *SCI.01* and *SCI.02*, defined in Chapter 3. The energies defined at the Earth as 10^{-6} and 10^{-1} kton TNT have been redefined as energies at the Moon. Given the gravitational corrector factor at the Earth, $f_{KE} = 1.42$ (see Chapter 6, Subsection 6.4.2), the energies translate to $7 \cdot 10^{-7}$ and $7 \cdot 10^{-2}$ kton TNT at the Moon, respectively. Once again, the methods applied disagree with respect to the kinetic energy range estimated, specially with respect to KE_{max} . In general, the Blackbody method predicts a larger kinetic energy range, with smaller KE_{min} and larger KE_{max} .

²the LUMIO-cam design is based on the SPOSH camera

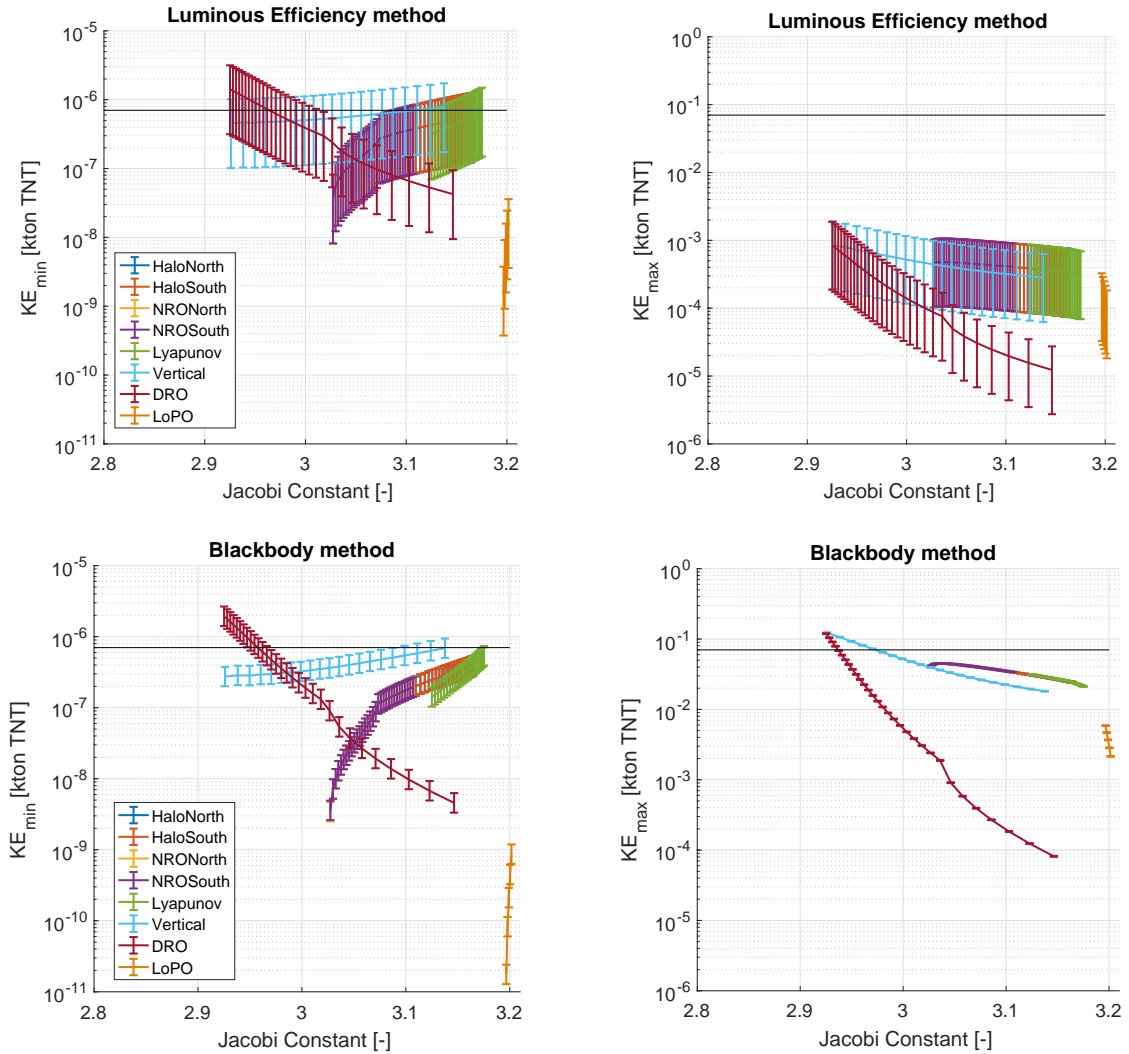


Figure 7.17: Estimated kinetic energy range detectable from CRTBP orbits, using two different methods. The black lines represent the kinetic energy limits set in the requirements (corrected for the Moon).

Nonetheless, the difference between the two methods, for CRTBP orbits, when it comes to the number of meteoroid detections, is not as prominent as for Frozen Orbits. Figure 7.18 shows the corresponding total number of meteoroid detections during the mission lifetime. As can be seen in this figure, for Lyapunov, Halo, Near-Rectilinear, Vertical and some Distant-Retrograde orbits, the number of impacts estimated by both methods is in the same order of magnitude (between 1000 and 10000). This is because, as already stated in Chapter 6, Subsection 6.4.1, for higher altitudes, the methods are in agreement with respect to KE_{min} , parameter which drives the number of meteoroid detections.

On the left-side plots of Figure 7.18, the total number of detections estimated for a satellite permanently at the Earth-Moon L_2 are also presented, for validation purposes. As expected, the results obtained for L_2 should be the limit case for all L_2 orbits (namely, LO, HO, NRO and VO). Furthermore, it should be noted that, in general, having a smaller minimum distance with respect to the Moon is beneficial. Nonetheless, and also as expected, the main exception to this rule are LoPOs, which do not have enough cumulative observation time at the lowest altitudes (see Chapter 6, Subsection 6.2.2).

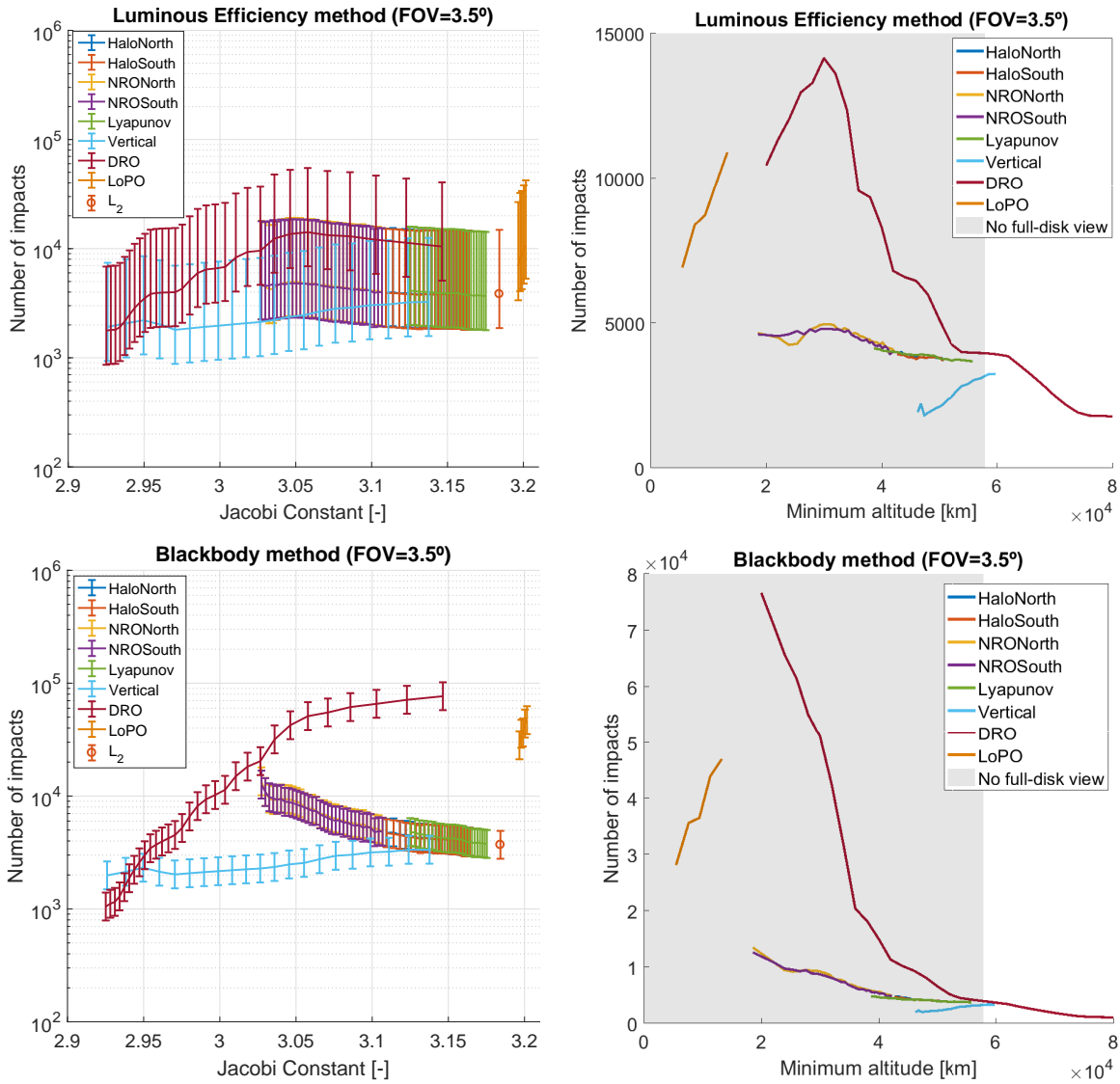


Figure 7.18: Estimated total number of meteoroid detections from CRTBP orbits during the mission lifetime, using two different kinetic energy estimation methods, for $\theta_{FOV} = 3.5^\circ$.

Finally, it should be noted in all plots presented in this section, the Blackbody method results have, in general, smaller error bars than the Luminous Efficiency results. However, the Blackbody method inherently has more assumptions than the Luminous Efficiency method (see Chapter 6, Subsection 6.4.1), and the possible errors associated with those assumptions are not represented in the results shown in this section.

7.3.2. Field-of-View 6°

At this stage of the orbital design, it was concluded that, in order to perform autonomous navigation and attitude and orbital control in lunar orbit, it would be required to have a full-disk view of the Moon. For a FOV of 3.5°, the required minimum altitude would be ≈ 58000 km, including a margin for possible attitude errors. From the left-side plots of Figure 7.18, it can be concluded that the orbital design space would be restricted to very few orbits (only some DROs and VOs). As such, it was decided by the LUMIO team to increase the payload’s FOV to $6^\circ \times 6^\circ$ and perform a second iteration of the

satellite's design. With this FOV, the minimum distance required to the Moon is 34902.8 km.

For $\theta_{FOV} = 6^\circ$, the Frozen Orbits results presented in the previous are still valid, for orbital design purposes. For CRTBP orbits, the new results are presented in Figures 7.19 and 7.20. Furthermore, Figure 7.21 shows the number of impacts detections in the two kinetic energy ranges defined by evaluation criteria EC.A.03 and EC.A.04.

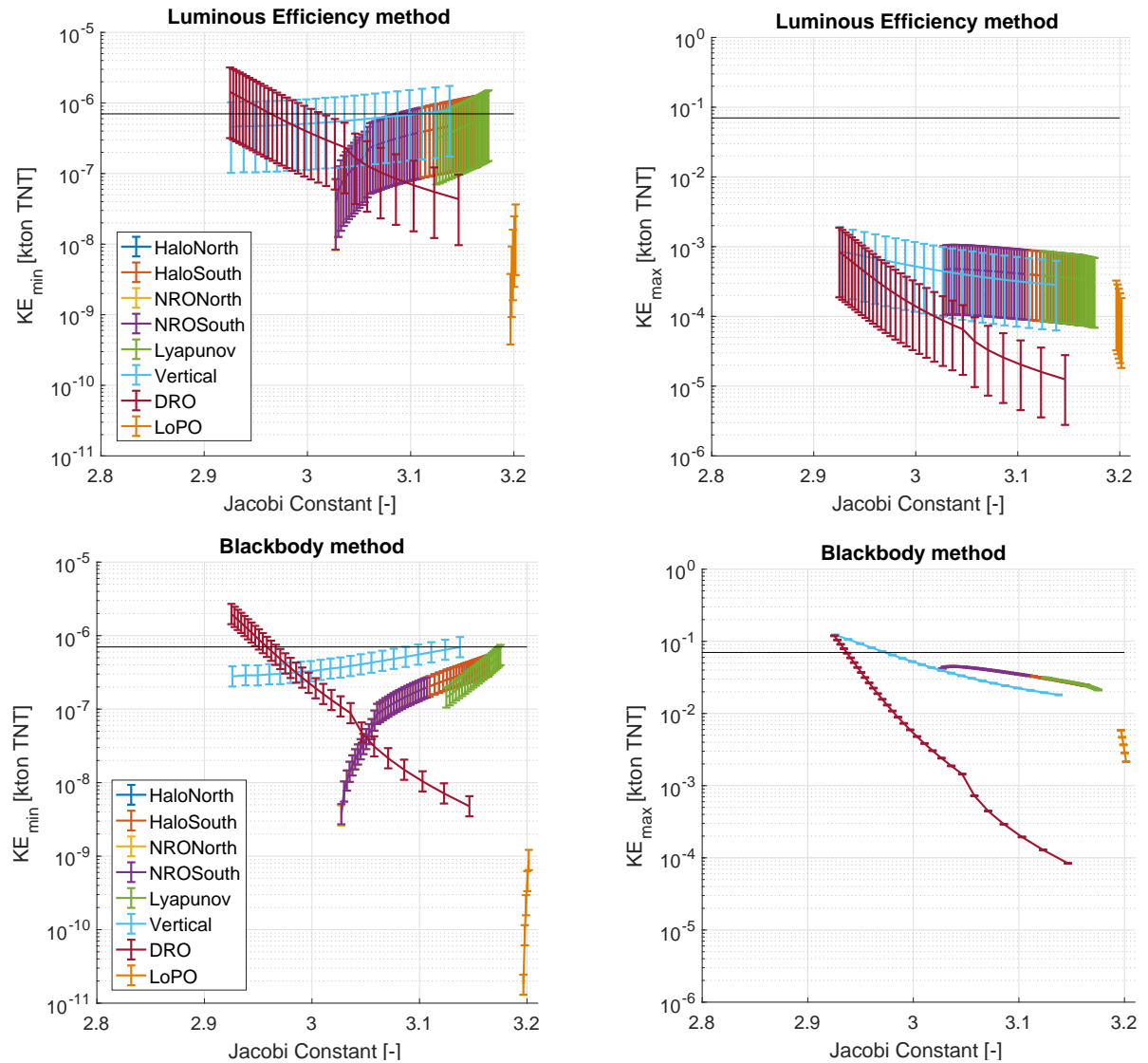


Figure 7.19: Estimated kinetic energy range detectable from CRTBP orbits, using two different methods, for $\theta_{FOV} = 6^\circ$. The black lines represent the kinetic energy limits set in the requirements (corrected for the Moon).

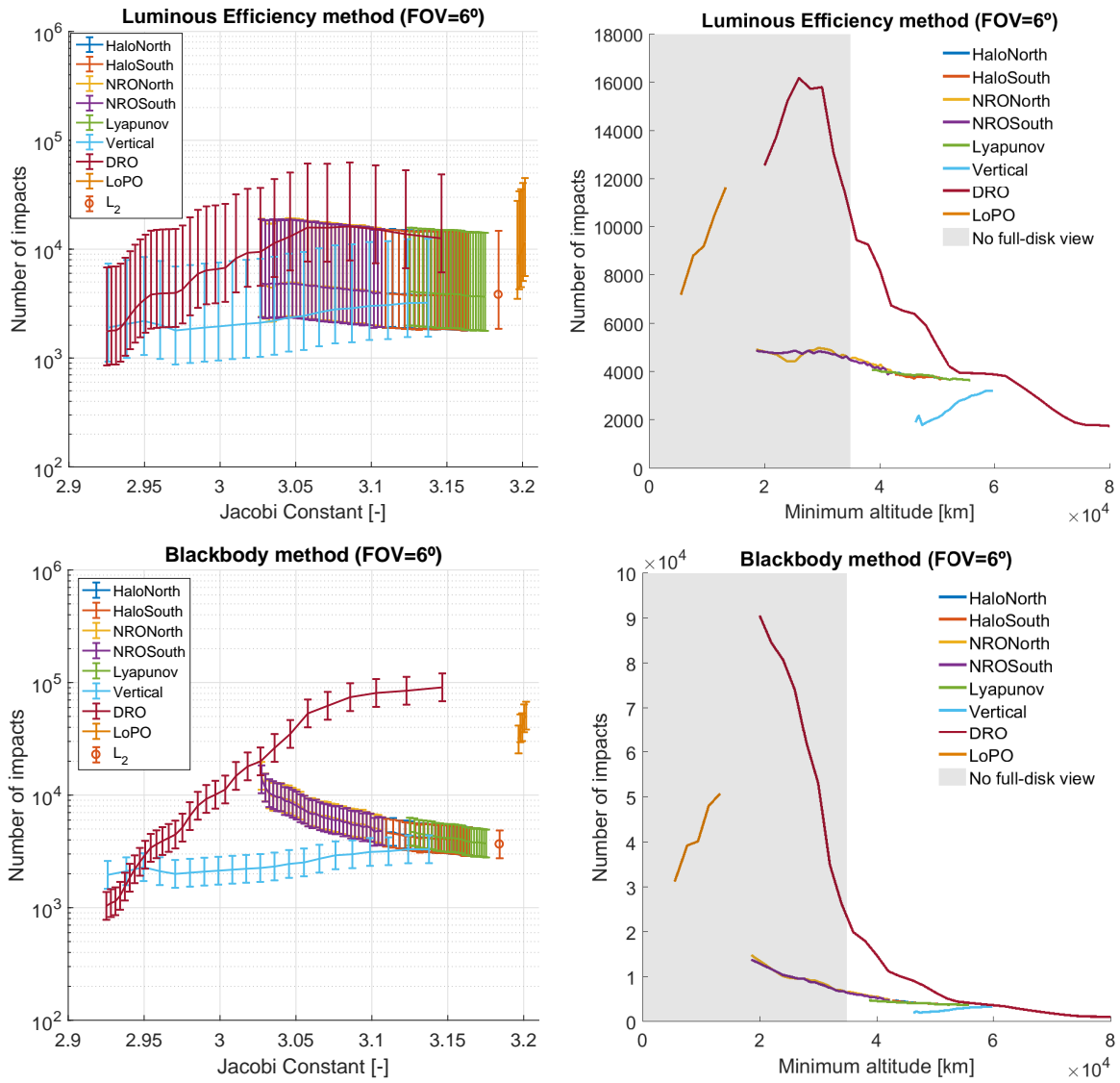


Figure 7.20: Estimated total number of meteoroid detections from CRTBP orbits during the mission lifetime, using two different kinetic energy estimation methods, for $\theta_{FOV} = 6^\circ$.

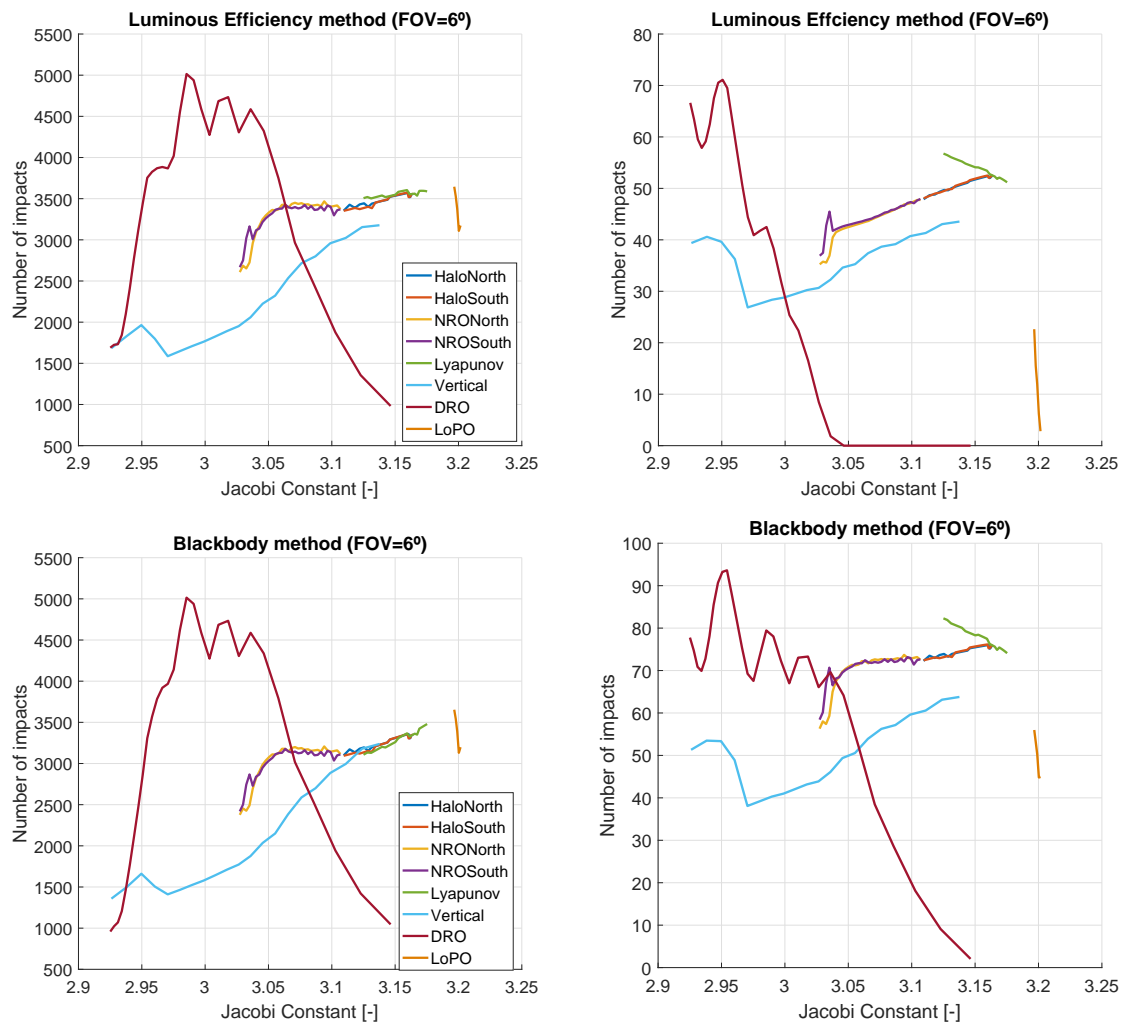


Figure 7.21: Estimated number of meteoroid detections during the mission lifetime, in the KE = $[10^{-6}, 10^{-4}]$ kton TNT (left-side plots) and KE = $[10^{-4}, 10^{-1}]$ kton TNT (right-side plots) ranges, using two different kinetic energy estimation methods.

7.4. First Orbit Trade-Off

The first orbit trade-off takes into account evaluation criteria *EC.A.01* to *EC.A.04*. The new requirement regarding the full-disk view of the Moon and respective evaluation criteria, as stated in Table 7.1, will also be taken into account.

Table 7.1: Additional LUMIO mission requirement and evaluation criteria, added during the second design iteration.

ID	Requirement	Parent ID
	...	
MIS.08	The mission shall have a full-disk view of the Moon at all times.	TLO.02

ID	Criteria	Parent ID
	...	
EC.A.08	The spacecraft shall have an altitude higher than 34902.8 km at all times.	MIS.08

Since two kinetic energy estimation methods have been used, two separate orbital trade-offs will be presented. Taking into account the results presented in Figures 7.15–7.16 and 7.19–7.20, Tables 7.2 and 7.3 present a graphical orbit trade-off for the results of the Luminous Efficiency method and Blackbody method, respectively.

Table 7.2: First orbit trade-off, given the results of the Luminous Efficiency method.

Orbit	Allows observations in $10^{-6} \leq KE \leq 10^{-1}$ kton TNT	$N_{\text{impacts}} \geq 240$	$N_{\text{impacts}} \geq 2$ for $KE \in [10^{-4}, 10^{-1}]$ kton TNT	$N_{\text{impacts}} \geq 100$ for $KE \in [10^{-6}, 10^{-4}]$ kton TNT	$h \geq 34902.8$ km
	EC.A.01	EC.A.02	EC.A.03	EC.A.04	EC.A.08
FO	<u>red</u> None	<u>green</u> All assessed	<u>red</u> None	<u>red</u> None	<u>red</u> None
LO	<u>green</u> All assessed	<u>green</u> All assessed	<u>green</u> All assessed	<u>green</u> All assessed	<u>green</u> All assessed
HO	<u>green</u> All assessed	<u>green</u> All assessed	<u>green</u> All assessed	<u>green</u> All assessed	<u>green</u> All assessed
NRO	<u>green</u> All assessed	<u>green</u> All assessed	<u>green</u> All assessed	<u>green</u> All assessed	<u>green</u> $C > 3.068$
VO	<u>green</u> All assessed	<u>green</u> All assessed	<u>green</u> All assessed	<u>green</u> All assessed	<u>green</u> All assessed
DRO	<u>green</u> All assessed	<u>green</u> All assessed	<u>green</u> $C < 3.036$	<u>green</u> All assessed	<u>green</u> $C < 3.027$
LoPO	<u>green</u> All assessed	<u>green</u> All assessed	<u>green</u> All assessed	<u>green</u> All assessed	<u>red</u> None

Legend: green Meets evaluation criteria red Does not meet evaluation criteria

Table 7.3: First orbit trade-off, given the results of the Blackbody method.

Orbit	Allows observations in $10^{-6} \leq KE \leq 10^{-1}$ kton TNT	$N_{\text{impacts}} \geq 240$	$N_{\text{impacts}} \geq 2$ for $KE \in [10^{-4}, 10^{-1}]$ kton TNT	$N_{\text{impacts}} \geq 100$ for $KE \in [10^{-6}, 10^{-4}]$ kton TNT	$h \geq 34902.8$ km
	EC.A.01	EC.A.02	EC.A.03	EC.A.04	EC.A.08
FO	red None	green All assessed	red None	red None	red None
LO	green All assessed	green All assessed	green All assessed	green All assessed	green All assessed
HO	green All assessed	green All assessed	green All assessed	green All assessed	green All assessed
NRO	green All assessed	green All assessed	green All assessed	green All assessed	green $C > 3.068$
VO	green All assessed	green All assessed	green All assessed	green All assessed	green All assessed
DRO	green All assessed	green All assessed	green All assessed	green All assessed	green $C < 3.027$
LoPO	green All assessed	green All assessed	green All assessed	green All assessed	red None

Legend: green Meets evaluation criteria red Does not meet evaluation criteria

As can be observed in Tables 7.2 and 7.3, the two trade-offs carried out are very similar, despite two different kinetic energy estimation methods having been used. Both methods lead to the conclusion that Frozen Orbits meet 1 out of the 4 acceptance criteria related to meteoroid impacts, while all CRTBP orbits assessed meet 4 out of 4. Nonetheless, it should be noted that the results obtained with the Luminous Efficiency method led to a restriction of the DRO family in order to meet criteria EC.A.03.

Furthermore, it should also be noted that these 4 criteria are not constraining enough in such a way that an operational orbit can be chosen or the design space significantly reduced, before the second orbit trade-off is carried out. In fact, it is the additional criteria EC.A.08 that reduces the design space to:

- Lyapunov orbits;
- Halo orbits;
- Near-Rectilinear Orbits, with $C > 3.068$;
- Vertical Orbits;
- Distant-retrograde Orbits, with $C < 3.027$.

eliminating Low-Prograde Orbits.

Taking into account selection criteria EC.S.01, which states that “the number of meteoroids detected during the mission lifetime shall be maximised”, out of this design space, the chosen orbit would be a

DRO. However, these orbits have a high transfer ΔV cost (see Table 5.4). As such, LUMIO's mission analysis team decided to focus the next orbital trade-off only on the second best orbital family, in terms of meteoroids detections: the **NRO family**. Small Halo orbits and Lyapunov orbits could also allow the detection of the same order of magnitude of meteoroids as the **NROs**. However, they were not considered for the second orbit trade-off due to the large stationkeeping costs, as their large stability index suggests (see Figure 6.18). Furthermore, the **NRO family** also has the advantage of allowing a constant visibility of the spacecraft from the Earth (see Table 5.2) and an easy concept of operations, due to having $P_M/P \approx 2$ (see Figure 6.16). Figure 7.22 shows the detectable kinetic energy as function of time, for all **NROs**, and Figure 7.23 shows the expected number of impact detections per hour.

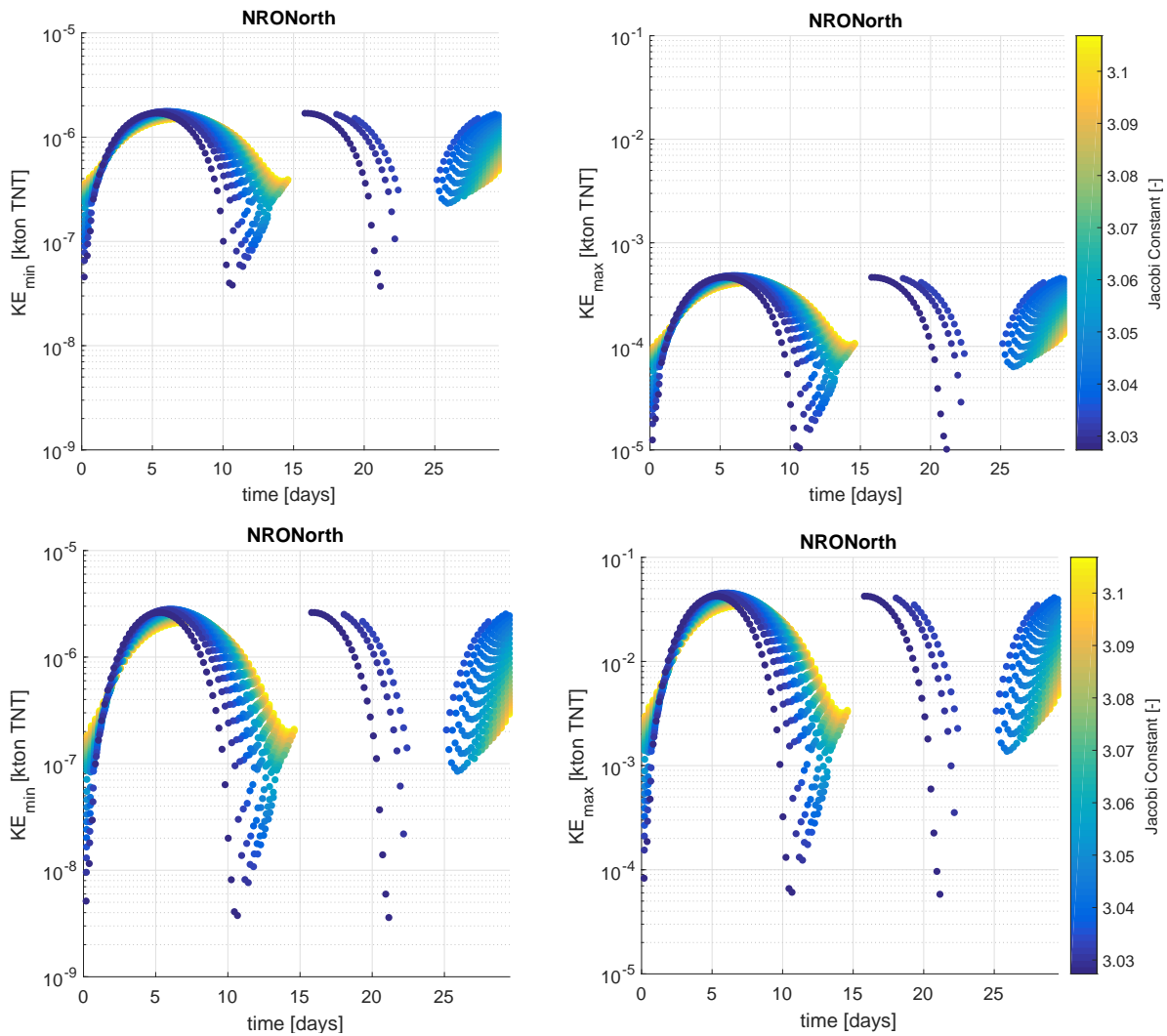


Figure 7.22: Detectable Kinetic energy range from **NROs** as function of time, using two different kinetic energy estimation methods: the Luminous Efficiency method (top) and the Blackbody method (bottom).

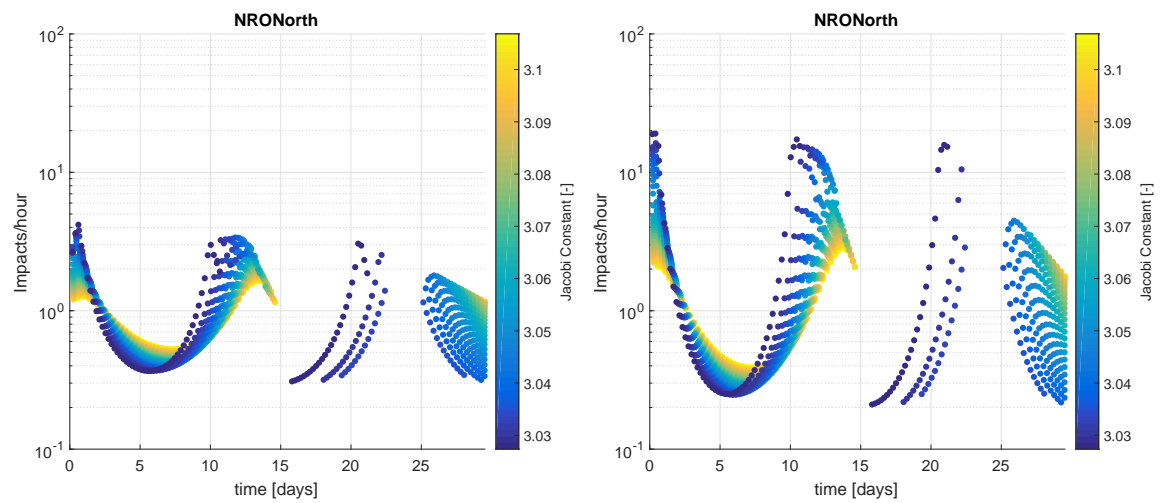


Figure 7.23: Number of expected meteoroid detections per hour, from an *NRO*, using two different kinetic energy estimation methods: the Luminous Efficiency method (left) and the Blackbody method (right).

References

- J. R. Wertz, *Orbit & Constellation Design & Management* (Microcosm Press; Springer, 2009).
- J. Oberst, J. Flohrer, S. Elgner, T. Maue et al., *The smart panoramic optical sensor head (SPOSH)A camera for observations of transient luminous events on planetary night sides*, *Planetary and Space Science* **59**, 1 (2011).

8

Conclusion

8.1. Operative Orbit and Considerations

The second orbit trade-off was carried out by LUMIO's Mission Analysis team. Taking into account both transfer and stationkeeping ΔV , an NRO with $C = 3.09$ was found to have the minimum ΔV budget, out of 14 orbits with $C \in [3.04, 3.16]$. As such, an NRO with $C = 3.09$ has been chosen as the operative orbit (Topputo *et al.*, 2017). The loss of meteoroid detections, with respect to the limit case ($C = 3.068$) determined in the first orbit trade-off (Chapter 7, Section 7.4), is ≈ 1400 or ≈ 280 , according to the Blackbody or Luminous Efficiency method, respectively. Table 8.1 summarises the meteoroid detection characteristics of the chosen orbit.

Table 8.1: Meteoroid detection characteristics of the operative orbit, a (Northern) Near-Rectilinear Orbit with $C = 3.0889$.

Characteristic	Luminous Efficiency method	Blackbody Method	Meets Requirement
KE_{min} [kton TNT]	$(3.301^{+4.041}_{-2.567}) \cdot 10^{-7}$	$(1.572^{+0.584}_{-0.425}) \cdot 10^{-7}$	–
KE_{max} [kton TNT]	$(4.242^{+5.193}_{-3.299}) \cdot 10^{-4}$	$(3.655^{+0.046}_{-0.045}) \cdot 10^{-2}$	–
$N_{impacts}$	4219^{+12103}_{-2164}	5475^{+1801}_{-1355}	SCI.05
$N_{impacts}$ for $KE \in [10^{-4}, 10^{-1}]$ kton TNT	46^{+13}_{-41}	$72.68^{+0.01}_{-0.01}$	SCI.01
$N_{impacts}$ for $KE \in [10^{-6}, 10^{-4}]$ kton TNT	3408^{+1124}_{-1413}	3147^{+427}_{-406}	SCI.02
Impacts per hour	[0.488, 1.8]	[0.350, 3.4]	–
m_{min} [kg]	$(1.009^{+1.24}_{-0.78}) \cdot 10^{-2}$	$(4.806^{+1.786}_{-1.302}) \cdot 10^{-3}$	–
m_{max} [kg]	$12.97^{+15.88}_{-10.09}$	$1117^{+13.92}_{-13.75}$	–

* Assumed impact velocity $v = 17$ km/s

As can be concluded from Table 8.1, the operational orbits meets science requirements *SCI.01*, *SCI.02* and *SCI.05*. Compliance with *SCI.06* – observation of the lunar farside – is also met, since

the orbit is an Earth-Moon L_2 orbit. However, it should be noted that the predicted number of new meteoroid impacts discovered in the range $[7 \cdot 10^{-5}, 7 \cdot 10^{-2}]$ kton TNT (i.e. Earth's equivalent range $[10^{-4}, 10^{-1}]$ kton TNT) are all contained in the range $[7 \cdot 10^{-5}, 4 \cdot 10^{-4}]$ or $[7 \cdot 10^{-5}, 3.6 \cdot 10^{-2}]$ kton TNT, according to the Luminous Efficiency or Blackbody method, respectively. Impact detections with energies larger than $4 \cdot 10^{-4}$ or $3.6 \cdot 10^{-2}$ kton TNT can also occur, but their real magnitudes cannot be measured with just one pixel, due to the saturation of the detector. As such, there might still be a gap in meteoroid detections with equivalent kinetic energies at Earth of $\sim 10^{-1}$ kton TNT, after the LUMIO mission is completed. Hence, compliance with mission objective *MO.02* – complement observations achievable via ground-based assets – is only partial.

Regarding the methodology employed, one of the main purposes of the sequential trade-offs applied was to reduce the design space in between trade-offs, as the analysis required became more complex. The drawback of this methodology could have been a false conclusion on the feasibility of the mission, given the evaluation criteria defined. However, since a feasible operational orbit has been found and no major iterations back to Step 1 of the methodology presented in Chapter 4 were required, it can be concluded that the evaluation criteria were appropriately defined. Nevertheless, the majority of the orbits met the (meteoroid related) acceptance criteria at the end of the first orbit trade-off (see Chapter 7, Section 7.4). As such, the reduction of the feasible design space before the second trade-off was done recurring to selection criteria *EC.S.02*. This means that some candidate orbits have not been evaluated with respect to acceptance criteria *EC.A.06* and *EC.A.07* ($\Delta V < 200$ m/s), namely DROs, LOs and VOs, some of which could potentially be feasible according to the requirements.

The choice of the final operational orbit also came from the application of the second selection criteria (smallest ΔV), in detriment of the first (largest number of meteoroid detections). Nonetheless, the final ΔV budget is smaller than 200 m/s, and, so, the mission could be extended for more than the nominal mission lifetime. The operational orbit has a budget of $\Delta V = 150$ (transfer) + 18 (maintenance) = 168 m/s. Given an additional 32 m/s, the mission lifetime could be extended for almost 2 years, which would mean that almost 3 times as many impacts could be detected.

Regarding the research question, the orbit selected can be considered as the “best orbit to detect meteoroid impact flashes on the lunar surface, with a CubeSat”. Nevertheless, as mentioned, some orbits of the design space at the end of the First Orbital Trade-off have not been assessed in terms of ΔV budget. Still, from the data presented in Table 8.1, it can be concluded that the orbit selected will contribute to the achievement of the research objective – help improve the detection of lunar meteoroid impact flashes, with a CubeSat.

Regarding the range of detectable kinetic energy, LUMIO detects approximately the same range as, for example, NASA's lunar impact flashes observation programme (see Chapter 2, Subsection 2.4.3). As such, there is no improvement with respect to Earth-based methods in this aspect. However, the cumulative number of meteoroid detections over the mission lifetime is at least 16 times greater than NASA's observation programme. Furthermore, it should be noted that the reported 240 observations of this programme were made in a period of 5 years, while LUMIO would be able to detect 240 impacts in approximately one month. Additionally, LUMIO would detect impact flashes on the lunar farside, where no detections of meteoroid impacts have ever been done, and potentially provide observations in the near to 10^{-1} kton TNT kinetic energy range.

8.2. Conclusion

The Earth's neighbourhood constantly encounters the more than 15,500 Near-Earth Objects (NEOs) currently catalogued and their respective fragments, known as meteoroids. As such, studying meteoroids can be valuable not only for the study of NEOs themselves, but can also serve a purpose on its own. For example, by constructing accurate Solar System meteoroid models, it is possible to predict the degradation of space-based equipment and instruments, and, so, create more sustainable designs. Currently, in order to improve meteoroid models, there are some Earth-based lunar monitoring programmes for the detection of meteoroid impact flashes, which is one of the most efficient meteoroid impact detection methods. However, Earth-based observations can only be made on the lunar nearside and are restricted by weather conditions at the observation site, conditions to which a lunar remote sensing mission would not be restricted to.

The goal of this thesis was to determine which orbit should the CubeSat [Lunar Meteoroid Impacts Observer \(LUMIO\)](#) fly in order to better detect lunar meteoroid impact flashes, while complementing Earth-based monitoring programmes. The main requirements were to detect meteoroid impact flashes at the lunar farside and detect at least 240 meteoroid impacts, with Earth equivalent kinetic energies between 10^{-6} and 10^{-1} kton TNT, during its one year mission lifetime, while having a restricted ΔV budget of at most 200 m/s. Furthermore, the detection of the impact flashes will be done with the [LUMIO-cam](#), which has a [FOV](#) of $6^\circ \times 6^\circ$ and includes a [CCD](#) sensor, operating in the visible spectrum.

In order to design the orbit of such a lunar remote sensing mission, a methodology of (3) sequential orbital trade-offs was followed, taking into account acceptance criteria based on the mission requirements and selection criteria based on the research objective. The latter ensure the maximization of the number of meteoroid detections, during the mission lifetime, and the minimization of the total mission ΔV budget.

Firstly, several types of possible orbital families were identified: the Keplerian, perturbed Keplerian or Libration point orbital families. Based on information already available in the literature, a Preliminary (graphical) Orbital Trade-off was carried out. Out of the first two families, only circular Frozen Orbits were selected as candidate orbits, due to their low stationkeeping budget and the possibility to monitor the lunar nightside regularly throughout the year. From the Libration point orbital family, only Lyapunov, Halo, Near-Rectilinear, Vertical, Distant-Retrograde and Low-Prograde orbits were selected as candidate orbits.

Secondly, the candidate orbits, the payload and the meteoroid environment were simulated, in order to check compliance with the meteoroid related acceptance criteria and perform the First Orbital Trade-off. The generation of both types of orbits selected implied first the determination of precise initial conditions. For Frozen Orbits, a computationally heavy numerical method, based on the minimisation of the osculating eccentricity variation, was applied, while for [CRTBP](#) orbits, a time-varying targetting scheme and a continuation procedure were followed. The [MATLAB](#)[®] codes developed were verified and the results obtained were validated against those presented in the literature. Nonetheless, the initial conditions obtained for Frozen Orbits require refinement for more precise applications, as the propagation time used is relative short compared to the mission lifetime.

The modelling of the payload implied both the modelling of its optics and detector. The first was implemented by defining its [FOV](#) in a [SPICE's IK](#) file, while the second was implemented by defining the [Signal-to-Noise Ratio](#) of the detector and, consequently, determining the minimum and maximum signal it can detect in one pixel. The noise budget took into account the Moon's surface background noise, cosmic noise, dark-current, read-out noise, off-chip noise and quantisation noise, but not motion blur, straylight, defocusing and Earthshine. It was concluded that, for a threshold [SNR](#) of 5, it should be

possible to detect signals between 290 and 80000 electrons, which corresponds to an apparent visual magnitude between +1.8 and +7.9.

The simulation of the meteoroid environment implied translating the signal detectable by the CCD sensor into a kinetic energy range of impacts detected. This was done resorting to two different methods: the Luminous Efficiency and the Blackbody method. The first assumes a directly proportional relation between light emitted in the visible spectrum and the impactor's kinetic energy, given an assumed luminous efficiency coefficient. The second assumes that the impact flash emits radiation as a blackbody and the emitting surface scales with the size of the impact crater. As such, the latter method required the assumption of the impact duration, temperature and a crater size scaling factor, among other parameters.

Using both methods, an approach to conservatively estimate the minimum kinetic energy was followed, in detriment of the estimation of the maximum kinetic energy, as it is the first parameter that mainly dictates the number of meteoroid impacts detected. The methods were found to agree with respect to the minimum kinetic energy detectable and disagree with respect to the maximum kinetic energy, for high altitudes. On the other hand, for low altitudes, the contrary was verified. Furthermore, it was also found that, for high altitudes, the assumed position of the impact on the lunar surface can significantly influence the number of detections estimated. As such, for the assessment of CRTBP orbits, it was assumed that the impact occurs between the edge of the FOV-area and subsatellite point, while for Frozen Orbits, it was assumed to occur at nadir.

The detectable kinetic energy ranges estimated were used to estimate the corresponding lunar meteoroid flux, using Brown's meteoroid model, gravitationally corrected. The flux was assumed uniform across the Moon surface and spread evenly throughout the year, i.e. no temporal peaks in flux, due to meteoroid showers, were considered. Furthermore, the meteoroid environment simulated was successfully validated with data from ESA's impact flash monitoring programme, NELIOTA.

Given the detectable kinetic energy range and correspondent lunar meteoroid flux, a coverage analysis tool was developed to determine the payload's FOV-area in the lunar nightside, and, so, determine how many impact flash detections are possible from a certain orbit. The FOV-area was computed using SPICE's MATLAB® toolbox and the estimation of the dark FOV-area was done resorting to the Sun-Moon-Spacecraft angle, also computed using the same toolbox. A total number of detections over the mission lifetime was computed, for each orbit, based on an average number of detections per synodic month and assuming that such average applies to the entire duration of the mission lifetime.

For Frozen Orbits, the results obtained with both kinetic energy estimation methods differed by at least three orders of magnitude. Comparing with results presented in the literature, the Luminous Efficiency method, which estimates less meteoroid detections, appears to be more accurate than the Blackbody method, at least for low altitudes. Nonetheless, both methods lead to the conclusion that these orbits would not allow the detection of kinetic energies larger than 10^{-6} kton TNT. As such, Frozen Orbits were eliminated from the orbital design space.

For CRTBP orbits, the results obtained with both methods are in accordance and most orbits meet the meteoroid related evaluation criteria. From Lyapunov, Halo, Near-Rectilinear and Vertical Orbits it would be possible to detect between 1000 and 10000 impacts during the mission lifetime, but detections from some DROs could be one order of magnitude larger. As such, from the First Orbital Trade-off, DROs would have been the preferential operational orbits. However, transfer costs to DROs are known to be high. Hence, the Second Orbital Trade-off, which took into account the ΔV budget, was instead focused on the second best orbital family in terms of meteoroid detections: Near-Rectilinear Orbits.

Finally, from the Second Orbital Trade-off, it was found that an orbit with $C = 3.09$ has the minimum

ΔV budget. In one year, it is expected that at least 4000 meteoroid impact flashes could be detected and eventual mission extensions could triple that amount. Furthermore, new impacts in never before observed kinetic energy ranges could be detected. As such, a mission like LUMIO can not only complement Earth-based observation methods, by observing the lunar farside, but also contribute with significant statistical information to the improvement of current Solar System meteoroid models.

8.3. Recommendations for Future Work

In order to further the work carried out in this thesis, one of the main drivers should be improving some of the assumptions made. In the Blackbody method, for example, it was assumed that, regardless of the kinetic energy of an impact, the impact duration is the same. However, from Earth-based observations, it has already been verified that there is a relation between impact duration and kinetic energy. As such, in order to proceed with this method it would be advised to implement a correlation between impact duration and kinetic energy, using the data gathered from Earth-based observations.

Otherwise, it is also possible to combine the Luminous Efficiency and Blackbody method, without having to assume an impact flash duration. The total energy emitted in the visible spectrum can be assumed given by:

$$E_T^V = \Delta t S \int_{\lambda_1}^{\lambda_2} L(\lambda, T_F) d\lambda \quad [J] \quad (8.1)$$

Using Blackbody method's Equations 6.35–6.37, Equation 8.1 can be re-written as follows:

$$E_T^V = 2\pi d^2 \frac{S_{\text{impact}}}{\tau A_{\text{lens}}} \frac{\int_{\lambda_1}^{\lambda_2} L(\lambda, T_F) d\lambda}{\int_{\lambda_1}^{\lambda_2} L(\lambda, T_F) \frac{qe(\lambda)}{E_V(\lambda)} d\lambda} \quad [J] \quad (8.2)$$

from which the kinetic energy of the impact can be computed, using Equation 6.34 and assuming a certain luminous efficiency.

Nevertheless, this method still requires the estimation of an impact flash temperature, which is also a function of kinetic energy. However, the modelling of this relation is not as straightforward as the impact duration correlation with kinetic energy. Only recently has the first Earth-based lunar impact flashes detection programme started measuring the magnitudes of flashes in two different bands (see Chapter 2, Subsection 2.4.3). The raw data is publicly available at NELIOTA's website¹, but would require processing in order to determine impact flashes' temperatures and their correlation with kinetic energy.

Finally, as DROs turned out to be the best orbits in terms of number of meteoroid detections, it would be useful to include Earthshine in the CCD's noise budget. If then, DROs are still the most advantageous for meteoroid detections, it should be confirmed with a more detailed analysis how much ΔV budget do they require. If a CubeSat could autonomously reach a DRO, this type of orbits could be an alternative to the operational orbit selected. Vertical orbits could also be a reasonable alternative to the operational orbit selected, although less optimal in terms of meteoroid detections and pending a detailed ΔV budget analysis. Furthermore, given a different mission baseline with the intent to detect micrometeoroids, for example, Frozen Orbits could be more appropriate than NROs. As such, these orbits should not be automatically excluded from future LUMIO-like missions' studies, based solely on the work here presented.

¹<https://neliota.astro.noa.gr> [Last accessed on: 13/08/2017]

References

- F. Topputo, M. Massari, A. Cervone, P. Sundaramoorthy *et al.*, *LUMIO: Lunar Meteoroids Impact Observer, A Cubesat at Earth-Moon L2, Challenge Analysis*, Tech. Rep. (Politecnico di Milano, Delft University of Technology, École Polytechnique Fédérale de Lausanne, The University of Arizona, S[&]T Norway, and Leonardo SpA, 2017).

A

Constants

Table A.1 presents the constants used throughout this thesis:

Table A.1: Constants

Parameter	Symbol	Value	Units
Earth–Moon mass parameter	μ	0.01215132	–
Sidereal month	P_M	27.321661	days
Synodic month	S_M	29.530589	days
Moon radius	R_M	1738	km
Earth radius	R_E	6378	km
Moon gravitational parameter	μ_M	4902.800305555400	km ³ s ⁻²
Earth gravitational parameter	μ_E	398600.4418	km ³ s ⁻²
Planck’s constant	h_P	$6.626 \cdot 10^{-34}$	J·s
Speed of light	c	$299.792 \cdot 10^6$	m s ⁻¹
Boltzman constant	k	$1.380 \cdot 10^{-23}$	J K ⁻¹
Moon gravitational acceleration	g	1.67	m s ⁻²
Kiloton of TNT	kton TNT	$4.418 \cdot 10^{12}$	J